

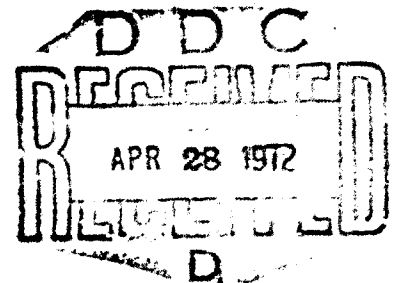
AD 740513

FAN/COMPRESSOR NOISE RESEARCH

Volume I - Detailed Discussion (I)

M.J. Benzakein R.M. Hochheiser
H.P. Claes S.B. Kazin
W.E. Coward P.R. Knott

Group Engineering Division
Aircraft Engine Group
General Electric Company
Evendale, Ohio



U.S. International Transportation Exposition
Dulles International Airport
Washington, D.C.
May 27-June 4, 1972

March 1972

FINAL REPORT

Availability is unlimited. Document may be released to the National Technical Information Service, Springfield, Virginia 22151, for sale to the public.

Reproduced by
NATIONAL TECHNICAL
INFORMATION SERVICE
Springfield, VA 22151

Prepared for

DEPARTMENT OF TRANSPORTATION
FEDERAL AVIATION ADMINISTRATION
Systems Research and Development Service
Washington, D.C. 20591

FROM	WHITE SECTION
TO	BUY SECTION
MAN. SEC.	
JUSTIFICATION	
DISTRIBUTION/AVAILABILITY CODES	
DIST.	AVAIL. AND SPECIAL
A	

The contents of this report reflect the views of the General Electric Company, which is responsible for the facts and the accuracy of the data presented herein. The contents do not necessarily reflect the official views or policy of the Department of Transportation. This report does not constitute a standard, specification, or regulation.

1. Report No. FAA-RD-71-85, I		2. Government Accession No.		3. Recipient Catalog No.	
4. Title and Subtitle FAN/COMPRESSOR NOISE RESEARCH, VOLUME I - DETAILED DISCUSSION (I)				5. Report Date OCTOBER 1971	
				6. Performing Organization Code	
7. Author(s) M.J. BENZAKEN, R.M. HOCHHEISER, H.P. CLAES, S.B. KAZIN W.F. COWARD, P.R. KNOTT, W.S. FISK				8. Performing Organization Report No.	
9. Performing Organization Name and Address GROUP ENGINEERING DIVISION/AIRCRAFT ENGINE GROUP GENERAL ELECTRIC COMPANY/ EVENDALE, OHIO				10. Work Unit No. 550-001-01H	
				11. Contract or Grant No. DOT FA63WA-1960	
12. Sponsoring Agency Name and Address FEDERAL AVIATION ADMINISTRATION SYSTEMS RESEARCH AND DEVELOPMENT SERVICE WASHINGTON D.C. 20591				13. Type of Report and Period Covered FINAL REPORT JUNE 1968 - OCTOBER 1971	
				14. Sponsoring Agency Code	
15. Supplementary Notes <i>Details of Illustrations in this document may be better studied on microfiche</i>					
16. Abstract Mechanisms of fan/compressor noise generation, transmission, radiation and propagation were physically defined and mathematically described in terms of functional relationships between acoustic, geometric and aerodynamic parameters. Based on these mechanisms, analytical and semi-empirical predictions of pure tone, broadband and multiple pure tone fan/compressor noise were established in terms of sound power spectra, directivity indices and the resultant sound pressure spectra. Test data on a variety of fan and compressor vehicles were used to verify the basic prediction techniques and to study the impact of specific design parameters upon fan/compressor noise, including vane-blade spacing, vane and blade numbers, tip speed, blade loading, rotor sweep, inlet guide vanes and vane lean. Effects of refraction on tone directivities were measured and compared with expectations. Propagation of acoustic waves were studied, with specific experiments conducted to investigate ground reflection phase factor and atmospheric absorption at high frequencies. The prediction systems were summarized in terms of flow charts and tables. Volumes I and II contain a detailed discussion of the experimentation and analysis. Volumes III and IV are a compilation of the acoustic test data in the form of computer print-out sheets.					
17. Key Words Acoustics Blade-passing noise Broadband noise Compressor noise Fan noise			18. Distribution Statement Availability is unlimited. Document may be released to the Clearinghouse for Federal Scientific and Technical Information, Springfield, Virginia 22151 for sale to the public.		
19. Security Classif. (of this report) UNCLASSIFIED		20. Security Classif. of this page UNCLASSIFIED		21. No. of Pages 300	22. Price \$6/pc \$.95/mc

APR 28 1972

ABSTRACT

Mechanisms of fan/compressor noise generation, transmission, radiation and propagation were physically defined and mathematically described in terms of functional relationships between acoustic, geometric and aerodynamic parameters. Based on these mechanisms, analytical and semi-empirical predictions of pure tone, broadband and multiple pure tone fan/compressor noise were established in terms of sound power spectra, directivity indices and the resultant sound pressure spectra.

Test data on a variety of fan and compressor vehicles were used to verify the basic prediction techniques and to study the impact of specific design parameters upon fan/compressor noise, including vane-blade spacing, vane and blade numbers, tip speed, blade loading, camber sweep, inlet guide vane and vane lean. Effects of refraction on tone directivities were measured and compared with expectations. Propagation of acoustic waves were studied, with specific experiments conducted to investigate ground reflection phase factor and atmospheric absorption at high frequencies.

The prediction systems were summarized in terms of flow charts and tables.

TABLE OF CONTENTS

	<u>PAGE</u>
<u>VOLUME I - DETAILED DISCUSSION (I)</u>	
ABSTRACT	I-iii
TABLE OF CONTENTS	I-v
LIST OF ILLUSTRATIONS	I-xi
LIST OF TABLES	I-xxii
 I. INTRODUCTION	 1
II. FAN/COMPRESSOR NOISE GENERATING MECHANISMS	3
A. Blade Passing Frequency Tones and Harmonics	3
1. Mathematical Model	3
2. Rotor Alone Noise	9
3. Viscous Wake Interaction Noise	11
4. Potential Interaction Noise	16
5. Wake Vortex Interaction Noise	33
6. Summary	35
Section II-A Nomenclature	38
Section II-A References	42
B. Analytical Prediction of Broadband Noise	43
1. General Formulation	43
2. Calculation of Broadband Noise Overall Acoustic Power	49
3. Spectral Distribution of Broadband Noise	54
Section II-B Nomenclature	62
Section II-B References	64
C. Experimental Investigation of Vortex Shedding Noise in Subsonic and Transonic Wind Tunnels	65
1. Test Facilities	65
2. Instrumentation	70
3. Subsonic Wind Tunnel Tests	75
4. Transonic Wind Tunnel Tests of Thin Airfoils	116
5. Summary of Wind Tunnel Results	125
6. Rotating Wake Measurements	125

TABLE OF CONTENTS (Continued)

	<u>PAGE</u>
Section II-C Nomenclature	166
Section II-C References	167
D. Multiple Pure Tones - Blade Passing Frequency Sub-Harmonics	168
1. General Descriptions of the Phenomena	168
2. Some Theoretical Considerations	168
3. Some Conclusions on MPT Generation	181
Section II-D Nomenclature	183
Section II-D References	184
III. FAN COMPRESSOR NOISE TRANSMISSION AND RADIATION MECHANISMS	185
A. Sound Transmission in a Turbomachinery Duct	185
1. The Three-Dimensional Acoustic Transmission and Radiation Program	185
2. Experimental Verification	194
Section III-A Nomenclature	204
Section III-A References	206
B. Sound Transmission Through Blade Rows	207
Section III-B Nomenclature	216
Section III-B References	217
C. Refraction Effect on Sound Directivity	218
1. Basic Mechanism of Refraction	218
2. Refraction Control of Exhaust Radiated Noise	225
3. Predicted Directivity Index Resulting from Refraction	232
4. Refraction From a Simple Engine Exhaust	233
5. Effect of Adding a Hot Shroud	237
Section III-C Nomenclature	241
Section III-C References	242
D. Propagation Effects	243
1. Inverse Square Law	243

TABLE OF CONTENTS (Continued)

	<u>PAGE</u>
2. Atmospheric Absorption	243
3. Ground Boundary Layer	243
4. Reflection of Sound Waves by the Ground	244
Section III-D Nomenclature	253
Section III-D References	254
IV. EXPERIMENTAL INVESTIGATION OF VANE/BLADE NUMBER EFFECTS	255
A. Vehicle and Test Descriptions	255
B. Discussion of the Test Results	262
V. EXPERIMENTAL INVESTIGATION OF IGV VS. NO IGV FAN	276
A. Vehicle and Test Descriptions	276
B. Discussion of the Test Results	282
<u>VOLUME II - DETAILED DISCUSSION (II)</u>	
ABSTRACT	II-iii
TABLE OF CONTENTS	II-v
LIST OF ILLUSTRATIONS	II-viii
LIST OF TABLES	II-
VI. EXPERIMENTAL INVESTIGATION OF REFRACTION/PROPAGATION EFFECTS	301
A. Refraction Effects	301
1. Experimental Rig, Test Conducted and Data Analysis	301
2. Results	308
Section VI-A Nomenclature	319
B. Experimental Investigation of Propagation Effects	320
1. Reflection Phase Factor	320
2. Atmospheric Absorption	392
VII. SEMI EMPIRICAL FAN NOISE PREDICTION	401
A. Introduction	401
B. Broadband Noise/Multiple Pure Tone Sound Power Levels Generated by IGV Less Fans	403
1. IGV ~ Less Fans	403
2. IGV Fans	403
3. Frequency Scaling	411

TABLE OF CONTENTS (Continued)

	<u>PAGE</u>
C. Fan Blade Passing Frequency Directivity	417
1. IGV-Less Fans	417
2. IGV Fans	417
D. Broadband and Multiple Pure Tone Noise Directivity	423
1. IGV-Less Fan	423
2. IGV Fans	423
3. Frequency Scaling	423
VIII. VERIFICATION OF FAN NOISE PREDICTION METHOD	487
A. Blade Passing Frequency Tones	487
1. CJ805-23 Fan	487
2. CF700 Fan	487
3. TF39 Fan "Family"	487
4. NASA Two-Stage Fan	510
Section VIII-A References	515
B. Broadband Noise Verification	516
1. LF336 Fans A and B	516
2. Development Vehicle IV	516
C. Verification of Size Parameter	556
Section VIII-C References	561
IX. SEMI-EMPIRICAL PREDICTION OF COMPRESSOR NOISE	562
X. VERIFICATION OF COMPRESSOR NOISE PREDICTION METHOD	585
A. Low Speed Single Stage Axial Flow Compressor Pure Tone Levels	585
B. High Speed Multistage Compressor Pure Tone Levels	585
C. Multistage Compressor Directivity Predictions	585

TABLE OF CONTENTS (Continued)

	<u>PAGE</u>
Section X-A References	590
XI. NOISE REDUCTION METHODS	591
A. Results of Analytical Studies	591
1. Rotor-Tip Speed	591
2. Pressure Ratio	594
3. Number of Rotor Blades	594
4. Vane-Blade Number Ratio	594
5. Blade-Vane Spacing	600
6. Vane Lean	600
7. Vane Sweep	603
8. Wake Control	603
9. Inlet Choking	603
Section XI-A References	605
B. Experimental Investigation	606
1. Rotor Speed	606
2. Pressure Ratio	606
3. Vane-Blade Number Ratio	611
4. Blade-Vane Spacing	611
5. Swept Rotor	611
6. Wake Control	615
XII. SUMMARY AND CONCLUSIONS	633
XIII. RECOMMENDATIONS	635
XIV. ACKNOWLEDGEMENT	636
 <u>VOLUME III - COMPILATION OF TEST DATA (I)</u>	
ABSTRACT	III-iii
TABLE OF CONTENTS	III-v
INTRODUCTION - APPENDICES A-C	637
LEGAND - APPENDICES	638

TABLE OF CONTENTS (Concluded)

	<u>PAGE</u>
APPENDIX A	A-1
APPENDIX B	B-1
APPENDIX C	C-1
<u>VOLUME IV - COMPILATION OF TEST DATA (II)</u>	
ABSTRACT	IV-iii
TABLE OF CONTENTS	IV-v
INTRODUCTION - APPENDICES D-E	640
LEGEND - APPENDICES	641
APPENDIX D	D-1
APPENDIX E	E-1

VOLUME I
LIST OF ILLUSTRATIONS

<u>Figure</u>		<u>Page</u>
II-A1	Duct Geometry for Blade Passing Frequency Tones and Harmonics Analysis	4
II-A2	Section AA of Duct	7
II-A3	Two Dimensional Cascade Airfoil Circulation Control Surface	10
II-A4	Blade Wake Profile	12
II-A5	Blade Row Geometry for Viscous Wake Interaction	13
II-A6	Blade Row Geometry for a Potential Interaction	17
II-A7	Axial Vector Dimensions for an Axisymmetric Potential Interaction	22
II-A8	Geometry for the Velocity at the Stator Induced by the Steady Circulation of the Rotor	24
II-A9	Geometry for the Velocity at the Rotor Induced by the Steady Circulation of the Stator	31
II-A10	Schematic of the Wake Vortex Interaction	34
II-A11	Vane-Blade Row Spacing -- The Effect of Viscous Wake, Potential and Vortex Wake Interactions	37
II-B1	General Coordinate System for Acoustic Radiation	46
II-B2	Broadband Noise from Rotor-OGV	52
II-B3	Broadband Noise Mechanisms on a High Speed Fan	53
II-B4	Control Volume for Flow Over an Isolated Airfoil	55
II-C1	Major Components of Subsonic Wind Tunnel	66
II-C2	Photograph of Subsonic Wind Tunnel	67
II-C3	Cross- Section of Transonic Cascade Tunnel	68
II-C4	Block Diagram of the Transonic Wind Tunnel	69
II-C5	Velocity Sensitivity Hot Film Probe	71

VOLUME I

LIST OF ILLUSTRATIONS (Continued)

<u>Figure</u>		<u>Page</u>
II-C6	Block Diagram of the Hot Film Instrumentation	72
II-C7	Photograph of the Hot Film Instrumentation	73
II-C8	Calibration Curve: Output of Sensor vs. Hot Flow Mach Number	74
II-C9	Data Acquisition Block Diagram	76
II-C10	Mean Velocity Profile of the Subsonic Wind Tunnel	77
II-C11	Inlet Turbulence of the Subsonic Wind Tunnel	78
II-C12	Test Section with Upstream and Downstream Measuring Stations	79
II-C13	Turbulence Intensity, Normalized to Local Mean Velocity of the Wake Behind a Cylinder	80
II-C14	Turbulence Intensity, Normalized to Undisturbed (Upstream) Mean Velocity of the Wake Behind a Cylinder	81
II-C15	Upstream Turbulence Intensity vs. Immersion	82
II-C16	Downstream Turbulence Intensity vs. Immersion, Two Diameters Downstream of a Cylinder	84
II-C17	Turbulence on the Wake Axis, Two Diameters Downstream of a Cylinder	85
II-C18	Turbulence Intensity vs. Immersion, Ten Diameters Downstream of a Cylinder	86
II-C19	Turbulence Intensity vs. Immersion, Eighteen Diameters Downstream of a Cylinder	87
II-C20	Turbulence Intensity vs. Immersion, Two Diameters Downstream of a Cylinder	88
II-C21	Turbulence Intensity vs. Immersion, Ten Diameters Downstream of a Cylinder	89
II-C22	Turbulence Intensity vs. Immersion, Eighteen Diameters Downstream of a Cylinder	90
II-C23	Vortex Shedding Frequency for 1/2" Cylinder, Two Diameters Downstream ($F_v = 520$ Hz)	91

VOLUME I

LIST OF ILLUSTRATIONS (Continued)

<u>Figure</u>		<u>Page</u>
II-C24	Vortex Shedding Frequency for 1/2" Cylinder, Two Diameters Downstream ($F_V = 990$ Hz)	92
II-C25	Vortex Shedding Frequency for 1/2" Cylinder, Two Diameters Downstream ($F_V = 1480$ Hz)	93
II-C26	1/3 Octave Sound Spectrum of a 1/2" Cylinder Immersed in an Airstream (1/2" Mike Downstream $M = 0.1$)	96
II-C27	1/3 Octave Sound Spectrum of a 1/2" Cylinder Immersed in an Airstream (1/4" Mike Below Cylinder - $M = 0.1$)	97
II-C28	1/3 Octave Sound Spectrum of a 1/2" Cylinder Immersed in an Airstream (Δ SPL Between the Noise with and without the Cylinder - $M = 0.1$)	98
II-C29	1/3 Octave Sound Spectrum of a 1/2" Cylinder Immersed in an Airstream (1/2" Mike Downstream $M = 0.2$)	99
II-C30	1/3 Octave Sound Spectrum of a 1/2" Cylinder Immersed in an Airstream (1/4" Mike Below Cylinder $M = 0.2$)	100
II-C31	1/3 Octave Sound Spectrum of a 1/2" Cylinder Immersed in an Airstream (Δ SPL between the Noise with and without the Cylinder $M = 0.2$)	101
II-C32	1/3 Octave Sound Spectrum of a 1/2" Cylinder Immersed in an Airstream (1/2" Mike Downstream $M = 0.3$)	102
II-C33	1/3 Octave Sound Spectrum of a 1/2" Cylinder Immersed in an Airstream (1/4" Mike Below Cy- linder $M = 0.3$)	103
II-C34	1/3 Octave Sound Spectrum of a 1/2" Cylinder Immersed in an Airstream (Δ SPL between the Noise with and without the Cylinder $M = 0.3$)	104
II-C35	1/3 Octave Sound Spectrum of a 1/2" Cylinder Immersed in an Airstream (1/2" Mike Downstream $M = 0.4$)	105
II-C36	1/3 Octave Sound Spectrum of a 1/2" Cylinder Immersed in an Airstream (1/4" Mike Below Cylinder)	106

VOLUME I

LIST OF ILLUSTRATIONS (Continued)

<u>Figure</u>		<u>Page</u>
II-C37	1/3 Octave Sound Spectrum of a 1/2" Cylinder Immersed in an Airstream (Δ SPL Between the Noise with and without the Cylinder $M = 0.4$)	107
II-C38	OASPL of Noise with and without a 1/2" Cylinder vs. Flow Mach Number	108
II-C39	Sound Pressure Level of Fundamental Tone vs. Flow Mach Number	109
II-C40	Test Section with Upstream and Downstream Measuring Stations	111
II-C41	Turbulence Intensity on the Wake Axis of a Symmetric Airfoil vs. Downstream Distance	112
II-C42	Turbulence on the Wake Axis, Two Chord Lengths Downstream of a Symmetric Airfoil	113
II-C43	Turbulence Intensity of a Symmetric Airfoil vs. Immersion	114
II-C44	Turbulence Intensity of a Symmetric Airfoil vs. Immersion	115
II-C45	Turbulence Intensity on the Wake Axis of a Symmetric Airfoil vs. Downstream Distance	117
II-C46	Turbulence Intensity of a Symmetric Airfoil vs. Immersion (Station 2)	118
II-C47	Turbulence Intensity of a Symmetric Airfoil vs. Immersion (Station 4)	119
II-C48	Total Pressure Profile Across the Duct	120
II-C49	Cascade Characteristics	121
II-C50	Mean Velocity Profile, One Chord Downstream of Cascade ($M = 0.4$)	122
II-C51	Mean Velocity Profile, One Chord Downstream of Cascade ($M = 0.5$)	123
II-C52	Mean Velocity Profile, One Chord Downstream of Cascade ($M = 0.7$)	124
II-C53	Turbulence Intensity vs. Position in Cascade Transonic Tunnel ($M = 0.4$)	127

VOLUME I
LIST OF ILLUSTRATIONS (Continued)

<u>Figure</u>		<u>Page</u>
II-C54	Turbulence Intensity vs. Position in Cascade Transonic Tunnel ($M = 0.5$)	128
II-C55	Turbulence Intensity vs. Position in Cascade Transonic Tunnel ($M = 0.7$)	129
II-C56	Turbulence Intensity vs. Position in Cascade Transonic Tunnel ($M = 0.4$)	130
II-C57	Turbulence Intensity vs. Position in Cascade Transonic Tunnel ($M = 0.5$)	131
II-C58	Turbulence Intensity vs. Position in Cascade Transonic Tunnel ($M = 0.7$)	132
II-C59	u' Turbulence Intensity Downstream of Cascade ($M = 0.4$)	133
II-C60	u' Turbulence Intensity Downstream of Cascade ($M = 0.7$)	134
II-C61	v' Turbulence Intensity Downstream of Cascade ($M = 0.4$)	135
II-C62	v' Turbulence Intensity Downstream of Cascade ($M = 0.7$)	136
II-C63	Noise for a Tip Section Airfoil of D/V #4 at $M = .4$ and $.7$	137
II-C64	u' Turbulence Spectra for a Tip Section Airfoil of D/V #4 $M = .4$ and $.7$	138
II-C65	v' Turbulence Spectra for a Tip Section Airfoil of D/V #4 $M = .4$ and $.7$	139
II-C66	Mean Velocity Profile Decrement for Two Incidence Angles	140
II-C67	Narrowband Frequency Analysis of the Turbulence Component u' for a Tip Section Airfoil of D/V #4	141
II-C68	Narrowband Frequency Analysis of the Turbulence Component v' for a Tip Section Airfoil of D/V #4	142
II-C69	Noise for a Tip Section Airfoil of D/V #4 at Incidence Angles 5° and 7.5° with Tunnel Background	143
II-C70	3-D Rotor Wake Narrowband Analysis of Turbulent Component v' at Immersion #1 - D/V #4	146

VOLUME I
LIST OF ILLUSTRATIONS (Continued)

<u>Figure</u>		<u>Page</u>
II-C71	3-D Rotor Wake Narrowband Analysis of Turbulent Component v' at Immersion #2 - D/V #4	147
II-C72	3-D Rotor Wake Narrowband Analysis of Turbulent Component v' at Immersion #3 - D/V #4	148
II-C73	3-D Rotor Wake Narrowband Analysis of Turbulent Component v' at Immersion #4 - D/V #4	149
II-C74	3-D Rotor Wake Narrowband Analysis of Turbulent Component v' at Immersion #5 - D/V #4	150
II-C75	3-D Rotor Wake Narrowband Analysis of Turbulent Component u' at Immersion #1 - D/V #4	151
II-C76	3-D Rotor Wake Narrowband Analysis of Turbulent Component u' at Immersion #2 - D/V #4	152
II-C77	3-D Rotor Wake Narrowband Analysis of Turbulent Component u' at Immersion #3 - D/V #4	153
II-C78	3-D Rotor Wake Narrowband Analysis of Turbulent Component u' at Immersion #4 - D/V #4	154
II-C79	3-D Rotor Wake Narrowband Analysis of Turbulent Component u' at Immersion #5 - D/V #4	155
II-C80	3-D OGV Wake Narrowband Analysis of Turbulent Component v' at Immersion #1 - D/V #4	156
II-C81	3-D OGV Wake Narrowband Analysis of Turbulent Component v' at Immersion #3 - D/V #4	157
II-C82	3-D OGV Wake Narrowband Analysis of Turbulent Component v' at Immersion #4 - D/V #4	158
II-C83	3-D OGV Wake Narrowband Analysis of Turbulent Component u' at Immersion #1 - D/V #4	159
II-C84	3-D OGV Wake Narrowband Analysis of Turbulent Component u' at Immersion #3 - D/V #4	160
II-C85	3-D OGV Wake Narrowband Analysis of Turbulent Component u' at Immersion #4 - D/V #4	161
II-C86	3-D OGV Wake Narrowband Analysis of Turbulent Component v' at Immersion #1 - D/V #4	162
II-C87	3-D OGV Wake Narrowband Analysis of Turbulent Component u' at Immersion #1 - D/V #4	163

VOLUME I
LIST OF ILLUSTRATIONS (Continued)

<u>Figure</u>		<u>Page</u>
II-D1	Typical Spectrum Containing Multiple Pure Tones Far Field Data	169
II-D2	Exhaust Probe Narrowband Spectral Analysis Indi- cating the Absence of MPT's	170
II-D3	Inlet Probe Narrowband Spectral Analysis Showing Multiple Pure Tones - 8989 RPM - 50 Hz B.W.	171
II-D4	Campbell Diagram of MPT's IGV and No IGV	172
II-D5	Tracking Filter Narrowband Spectrum of 10/Rev SPL vs. Fan Speed	173
II-D6	Multiple Pure Tone Occurrence	174
II-D7	Arbitrary Blade Loading Distribution	177
II-D8	Cut-off Mach Number for Spinning Modes	178
III-A1	Cylindrical Coordinate System	187
III-A2	Actual Configuration	189
III-A3	Analytical Model for Duct Sound Transmission	190
III-A4	Six-Lobe Pressure Pattern Rotating with Angular Velocity Rad./Sec.	192
III-A5	Phase Speaker Model	195
III-A6	Phased Speaker Model Results. Four Lobes, 70 Hz (Above Cut-Off), No Acoustic Lining (Rigid Walls). Radial Pressure Distribution at Axial Location 0 Inches	196
III-A7	Phased Speaker Model Results. Four Lobes, 700 Hz (Above Cut-Off), No Acoustic Lining (Rigid Walls). Radial Pressure Distribution at Axial Location 30 Inches	197
III-A8	Phased Speaker Model Results. Four Lobes, 700 Hz (Above Cut-Off) No Acoustic Lining (Rigid Walls). Radial Pressure Distribution at Axial Location 55 Inch	198

VOLUME I

LIST OF ILLUSTRATIONS (Continued)

<u>Figure</u>		<u>Page</u>
III-A9	Phased Speaker Model Results. Four Lobes, 700Hz (Above Cut-Off), No Acoustic Lining (Rigid Walls). Axial Pressure Distribution at R = 8.9 Inches	199
III-A10	26" Diameter Single Stage Research Compressor with the Angular Duct Extension	201
III-A11	Schematic View of 26-Inch-Diameter Research Compressor with 24-Inch Long Extension	202
III-A12	Comparison Between Calculated and Measured Far Field Sound Pressure Level for a 26" Diameter Research Compressor	203
III-B1	Laboratory Duct and Cascade Set-Up	208
III-B2	Air Flow Noise Reduction Through Cascade Vanes - Comparisons Between Measured and Calculated Results	209
III-B3	Model for Sound Wave Transmission Through a Blade Row	210
III-B4	Calculated Ratios of Transmitted to Incident Sound Wave Amplitudes for Various Blade Spacings and Incidence Angles	212
III-B5	Effect of Incident Sound Frequency and Flow Mach Number on Sound Attenuation by a Blade Row	213
III-B6	Sound Energy Reduction by a Blade Row as a Function of Sound Wave Angle of Incidence and Flow Mach Number	214
III-B7	Sound Energy Reduction by a Blade Row as a Function of Stagger Angle and Flow Mach Number	215
III-C1	Simple Model of Snell's Law of Refractive Index Using Air and Water as an Example	219
III-C2	Simple Model of Snell's Law Across the Shear Zone of Two Airstreams of Different Velocity and Temperature	221
III-C3	Possible Angles of Refraction and Occurrence of a Shadow Region	223
III-C4	Shadow Angle when the Fan Jet Exhaust Mach Number is 0.5	224
III-C5	Typical Inlet Potential Flow Lines and Constant Velocity Contours	226

VOLUME I
LIST OF ILLUSTRATIONS (Continued)

<u>Figure</u>		<u>Page</u>
III-C6	Characteristic Refraction Effect for the Inlet	227
III-C7	Simplified Illustration of Characteristic Refraction Effect at the Inlet	228
III-C8	Critical Angle for Internal Reflection	229
III-C9	Effect of Temperature and Velocity Difference in Two Adjacent Gas Streams on Acoustic Transmission	231
III-C10	Effect of Airflow Mach Number on Aft Quadrant Directivity Index	236
III-C11	Typical Ray Path through Shroud When Internal Reflection Does Not Occur	238
III-C12	Example of Effect on Directivity Index of Enclosing Exhaust with Hot Shroud	240
III-D1	Illustration of Reflection Problem	245
III-D2	Illustration of the Effect of Reflection Absorption on Sound Pressure Level for 1/3 Octave Band Analysis	251
III-D3	Illustration of the Effect of Reflection on Measurement of Pure Tones	252
IV-A1	80 OGV Vehicle (D/V I)	256
IV-A2	Configuration Sketch (D/V I)	257
IV-A3	OGV for D/V II - Front View	258
IV-A4	OGV for D/V II - Rear View	259
IV-A5	Fan Operating Map D/V I and D/V II Comparison	260
IV-A6	D/V II Test Far Field Acoustic Test Microphone Locations	261
IV-B1	Comparison of Fundamental PWL's from 50-Cycle Narrowbands 80 Vane Configuration vs. 48-Vane Configuration	264
IV-B2	2nd Harmonic PWL's from 50 Cycle Narrowband 48 Vane and 80 Vane Configurations	265

LIST OF ILLUSTRATIONS (Continued)

<u>Figure</u>		<u>Page</u>
IV-B3	Comparison of 1/3 Octave Power Spectrum for 48-Vane and 80-Vane Vehicles (5089 RPM)	266
IV-B4	Comparison of Blade Passing Frequency Arc SPL for 48 OGV and 80 OGV Vehicles (5750 RPM)	268
IV-B5	Comparison of BPF Arc SPL for 48 OGV and 80 OGV Vehicles (8500 RPM)	269
IV-B6	Comparison of 2nd Harmonic Arc SPL for 48 OGV and 80 OGV Vehicles (5750 RPM)	270
IV-B7	Comparison of 2nd Harmonic Arc SPL for 48 OGV and 80 OGV Vehicles (8500 RPM)	271
IV-B8	Narrowband Analysis of 48 OGV Vehicle Far Field Data - 110°	272
IV-B9	Narrowband Analysis of 80 OGV Vehicle Far Field Data - 110°	273
IV-B10	Narrowband Analysis of 48 OGV Vehicle Far Field Data - 120°	274
IV-B11	Narrowband Analysis of 80 OGV Vehicle Far Field Data - 120°	275
V-A1	IGV - Vehicle D/V III	277
V-A2	Schematic of IGV Test Vehicle D/V III	278
V-A3	IGV Set for D/V III	279
V-A4	Rotor for D/V III	280
V-A5	OGV's and Inner Fan Stage D/V III	281
V-A6	Comparison of D/V II and D/V III Weight Flow vs. Speed	283
V-A7	Comparison of D/V II and D/V III Operating Line Data	284
V-E1	Comparison IGV and No IGV Fans with Variable Rotor Stator Spacing	285
V-B2	Comparison of Fundamental PWL IGV and No IGV Vehicles	286
V-B3	Blade Passing Frequency Directivity Comparison IGV and 28° No IGV Vehicles - 6150 RPM Corrected Speed	

VOLUME I
LIST OF ILLUSTRATIONS (Concluded)

<u>Figure</u>		<u>Page</u>
V-B4	Blade Passing Frequency Directivity Comparison IGV and No IGV Vehicles - 7600 RPM Corrected Speed	288
V-B5	1/3 Octave Power Level Spectra Comparison IGV and No IGV Vehicles - 6150 RPM Corrected Speed	290
V-B6	1/3 Octave Power Level Spectra Comparison IGV and No IGV Vehicles - 7600 RPM Corrected Speed	291
V-B7	PNdB Directivity Comparisons IGV and No IGV Vehicles - 6150 RPM Corrected Speed	292
V-B8	PNdB Directivity Comparisons IGV and No IGV Vehicles - 7600 RPM Corrected Speed	293
V-B9	Comparison of Blade Passing Frequency PWL - IGV's Nominal and IGV's 9° Closed	294
V-B10	Comparison of 1/3 Octave Power Level Spectra IGV's Nominal and IGV's 9° Open - 7900 RPM	295
V-B11	Comparison of Blade Passing Frequency PWL - IGV's Nominal and IGV's 9° Closed	296
V-B12	Comparison of 1/3 Octave Power Level Spectra IGV's Nominal and IGV's 9° Closed - 5750 RPM	297
V-B13	Comparison of 1/3 Octave Power Level Spectra IGV's Nominal and IGV's 9° Closed - 6900 RPM	298
V-B14	Comparison of Blade Passing Frequency PWL No IGV's and IGV's 9° Closed	299
V-B15	Comparison of 1/3 Octave Power Level Spectra No IGV's and IGV's 9° Closed - 7900 RPM	300

VOLUME I
LIST OF TABLES

<u>TABLE NO.</u>		<u>PAGE</u>
II-A1	Subscript Changes for Multiple Potential Interaction	21
II-A2	Data Required for a Blade Passing Frequency PWL	36
II-C1	Comparison Between Hot Film and Microphone Vortex Shedding Frequency	95
II-C2	Probe Positions and Immersion Depths	126
II-C3	Radial Design Points $\Delta P/q$ Distribution for D/V #4	145
II-C4	Comparison of Peak Turbulence Level Amplitudes for the Cascade and D/V #4	165
IV-B1	Fundamental Blade Passing Frequency Cutoff Speeds with 48 and 80 Vane Stators	263

I. INTRODUCTION

As recently as 1960, very little was known about the basic mechanisms of fan noise generation and transmission. In the absence of well validated causal relationships between parameters and noise characteristics, researchers in the field first set out to determine such relationships by observation and empiricism.

With this technique, each observer drew his own conclusions from analysis of data on either one specific type and size of fan or at best a limited range of fan types and sizes. Since the relationships determined between noise and design or performance characteristics were based largely upon observed data trends, the validity of those relationships was limited by the ability of the observer to be aware of and properly account for all of the factors which should be observed for meaningful correlations. The basic problem with the empirical approach was that it was virtually impossible to predict with confidence the acoustical characteristics of a fan prior to building the vehicle and obtaining full-scale test data. Another problem was that one would tend to assume that design changes resulting in a noise change on one fan or type of fan would result in a similar noise change on other types of fans. Such assumptions are, of course, extremely tenuous, and quite often erroneous!

This program was established in order to develop meaningful fan/compressor noise prediction methods which were based on an understanding of fundamental noise generation and transmission mechanisms, and verified by tests and measurements on several different scales and types of vehicles. The experiments were chosen not only to establish functional relationships between the basic mechanisms and the resultant noise levels, but also to evaluate the effects of a series of design parameters and concepts upon noise generation and reduction, and to demonstrate the accuracy of the prediction methods.

This report documents the results of the program, starting with the derivation of the theoretical and semi-empirical relationships which describe the mechanisms of fan and compressor noise generation, transmission, radiation and propagation. These mechanisms are described in terms of aerodynamic and geometric design parameters and are quantitatively related to noise in terms of sound power spectra, directivity indices, and the resultant sound pressure spectra.

The verification of the validity of the inter-relationships between these mechanisms in terms of pure tone and broadband spectra and directivities is provided on a number of different fan and compressor vehicles. Effects of specific design parameters, such as blade-vane numbers, blade-vane spacing, loading, tip speed, etc. are analytically evaluated and experimentally verified.

Major subjects treated in the report include:

- The measured acoustic relationship between pure tone noise and blade/vane numbers on a controlled basis.

- The measured acoustic comparison between an IGV fan and an IGV-less fan designed for essentially the same aerodynamic performance.

- The two and three dimensional cascade measurements enabling relationships to be derived between broadband fan noise and turbulence intensities.

- The measured relationship between refraction phenomena and directivity from a tone generated in a co-annular bypass duct.

- The measured acoustic effects of "wake-filling" relative to wakes generated upstream of a rotor.

- The demonstration of the applicability of the basic mechanisms over a 16:1 size range.

- The relative importance of blade loading and tip speed on fan noise.

- The correlation of the effects of wave cancellation and reinforcement propagation phenomena as a function of microphone height, fan height, terrain effects and frequency.

The analytical and experimental investigations in this report result in comprehensive fan and compressor noise prediction systems which are shown to be reasonably accurate and which can provide a useful tool to the engineer in designing low noise fans and compressors.

II. FAN/COMPRESSOR NOISE GENERATING MECHANISMS

The acoustic signature of modern high speed fans and compressors engine consists essentially of three different types of noise components.

- . Blade passing frequency tones and higher harmonics.
- . Broadband noise.
- . Multiple pure tones - blade passing frequency sub-harmonics.

This section will describe the different generating mechanisms for the three noise components as well as the mathematical models that were developed to explain and evaluate quantitatively the fan/compressor generated noise spectra.

(A) Blade Passing Frequency Tones and Harmonics

(1) Mathematical Model. The basis for the analysis of pure tone generation is a solution to the linearized wave equation in an annular duct (see Figure II-A1) with uniform axial flow and solid body rotational fluid motion. The equation can be expressed in non-dimensional form as

$$\nabla^2 p = \left(\frac{\partial}{\partial t} + M_z \frac{\partial}{\partial t} + \bar{M}_\theta \frac{\partial}{\partial \theta} \right)^2 p \quad (\text{II-A1})$$

where

p - sound pressure

z - axial distance

M_z - axial Mach number

\bar{M}_θ - tip swirl Mach number

θ - circumferential angle

t - time

and where

$$\nabla^2 = \frac{\partial^2}{\partial r^2} + \frac{1}{r} \frac{\partial}{\partial r} + \frac{1}{r^2} \frac{\partial^2}{\partial \theta^2} + \frac{\partial^2}{\partial z^2} \quad (\text{II-A2})$$

The solution to this equation can be expressed as

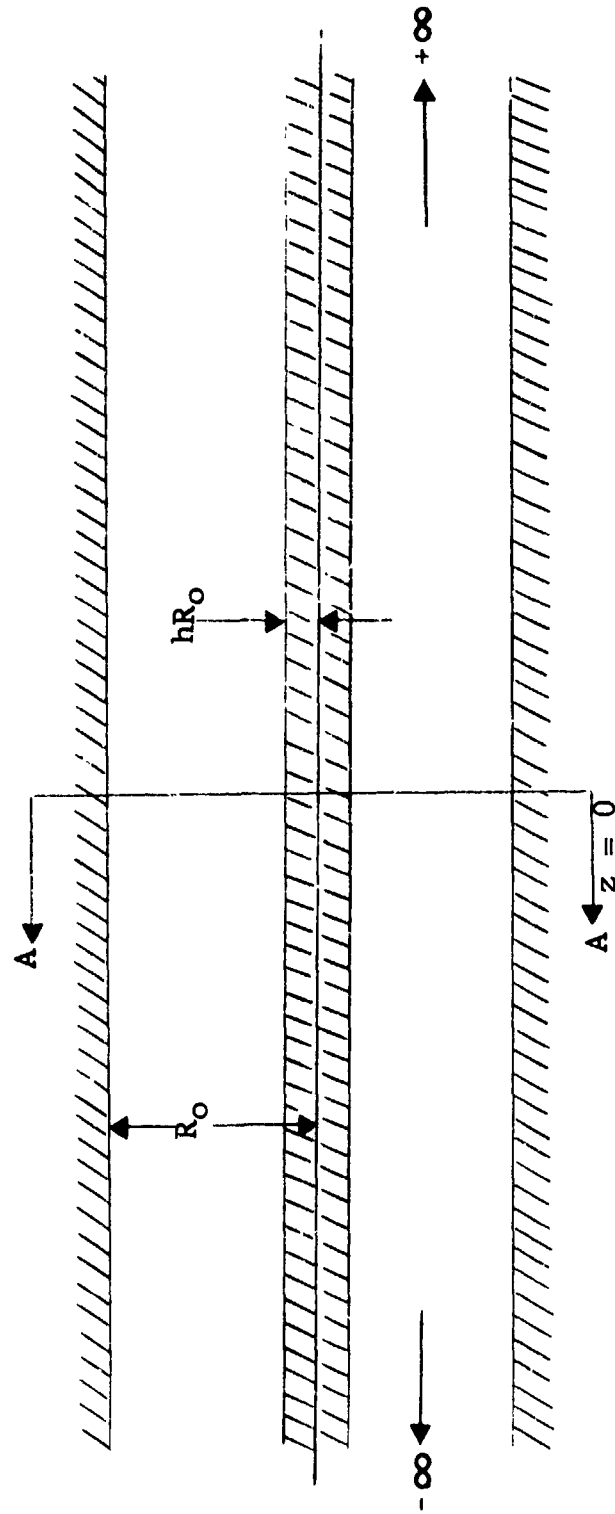


FIGURE II-A1 DUCT GEOMETRY FOR BLADE PASSING FREQUENCY TONES AND HARMONICS ANALYSIS

$$p = \sum_{n=-\infty}^{+\infty} \sum_{m=0}^{\infty} \rho c^2 n \omega e^{in(\theta - \omega t)}.$$

$$R_n(\lambda_{nm} r) e^{i\alpha z} \left[K_1 e^{\beta z} + K_2 e^{-\beta z} \right] \quad (II-A3)$$

where

$$\alpha = \frac{-n M_z (\omega - M_\theta)}{1 - M_z^2} \quad (II-A4)$$

$$\beta = \frac{\sqrt{n^2 (\omega - M_\theta)^2 - \lambda_{nm}^2 (1 - M_z^2)}}{1 - M_z^2} \quad (II-A5)$$

and where

ρ - density

c - speed of sound

n - spinning lobe number

ω - mode tip Mach number

λ_{nm} - eigenvalue

K_1, K_2 - constants

$R_n(\lambda_{nm} r)$ - linear combination of first and second kind Bessel functions

The eigenvalues, λ_{nm} , may be determined from the equation

$$Y'_n(\lambda_{nm} h) J'_n(\lambda_{nm}) - Y'_n(\lambda_{nm}) J'_n(\lambda_{nm} h) = 0 \quad (II-A6)$$

where

h - radius ratio of the annulus

J' - derivative of a first kind Bessel function

Y' - derivative of a second kind Bessel function

The constants K_1 and K_2 are determined from boundary conditions at the plane $z = 0$. These boundary conditions are based on the annular duct geometry shown in Figure II-A1.

It may be assumed that at the plane $z = 0$ there exists a rotating line vortex as shown in Figure II-A2. It may also be assumed that each time the vortex passes the angular position θ there will be an impulsive change in tangential velocity. That is,

$$v = f(r) \delta(\theta - \omega t) \quad (\text{II-A7})$$

where

$$\delta(\theta - \omega t) = \begin{cases} 1 & \text{when } \theta = \omega t \\ 0 & \text{when } \theta \neq \omega t \end{cases}$$

and where $f(r)$ is the radial distribution of tangential velocity. From equation (II-A7) a radial circulation may be computed as

$$\Gamma(r) = R_0 \text{ cr } f(r) \quad (\text{II-A8})$$

Therefore, a boundary condition of the form

$$v/z=0 = \frac{\Gamma(r)}{R_0 \text{ rc}} \delta(\theta - \omega t) \quad (\text{II-A9})$$

can be formulated.

For M such rotating line vortices equally spaced, equation (II-A9) can be expressed as

$$v/z=0 = \frac{\Gamma(r)}{R_0 \text{ c}} \sum_{k=1}^M \delta(\theta - \omega t + \frac{2\pi k}{M}) \quad (\text{II-A10})$$

Another boundary condition at the plane $z = 0$ is imposed by mass continuity. Since there is no discontinuous density or area change at $z = 0$, the axial velocity must be continuous. That is

$$u/z=0 \equiv \text{continuous} \quad (\text{II-A11})$$

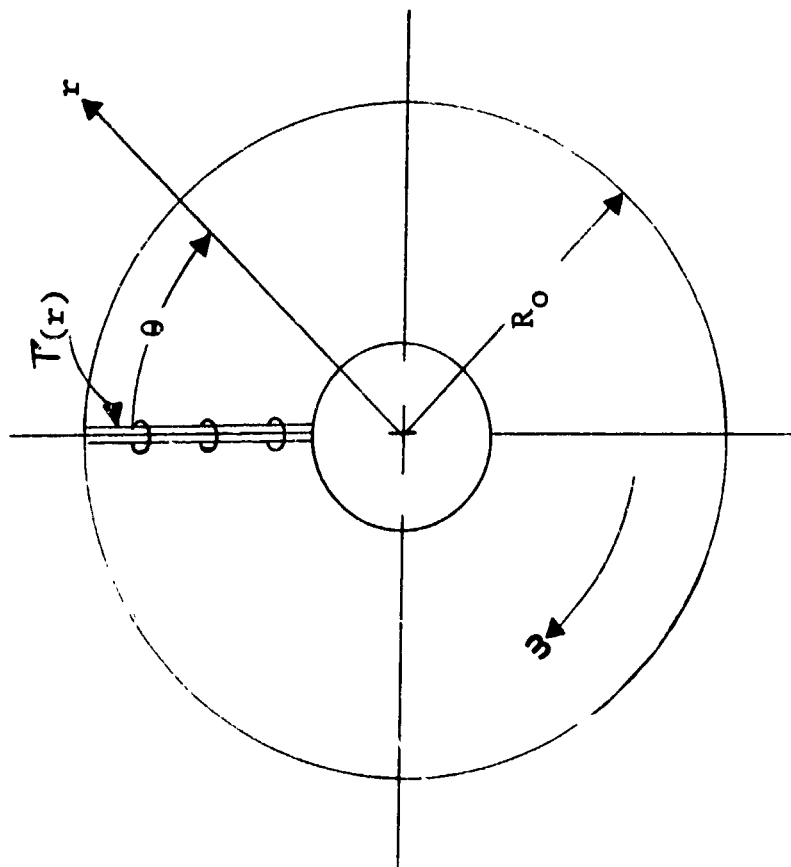


FIGURE II-A2 SECTION AA OF DUCT

If a velocity potential is defined in the annular duct as

$$\phi_{nm} = e^{in(\theta - \omega t)} R_n(\lambda_{nm} r) e^{i\alpha z} \left[K_1 e^{i\beta z} + K_2 e^{-i\beta z} \right] \quad (II-A12)$$

then the non-dimensional velocities may be defined as

$$v = \frac{1}{r} \frac{\partial \phi}{\partial \theta} \quad (II-A13)$$

and

$$u = \frac{\partial \phi}{\partial z} \quad (II-A14)$$

Applying the boundary condition of equation (II-A11) to equation (II-A12) it is found that

$$K_1 = -K_2 \quad (II-A15)$$

Combining equations (II-A10), (II-A12), and (II-A13) it can be shown that

$$\Gamma(r)M = 4 i n \pi R_o c A_{nm} R_n(\lambda_{nm} r) \quad (II-A-16)$$

for each n, m mode. Multiply both sides of equation (II-A-16) by $r R_n(\lambda_{nm} r)$ and integrating from h to 1 , it is found that

$$A_{nm} = \frac{M}{4 i \pi R_o c n \eta_{nm}} \int_h^1 \Gamma(r) r R_n(\lambda_{nm} r) dr \quad (II-A17)$$

where η_{nm} is the norm of $R_n(\lambda_{nm} r)$ is the region h to 1 .

Therefore, the acoustic pressure in the duct may be expressed as

$$P = \sum_{n=-\infty}^{+\infty} \sum_{m=0}^{\infty} A_{nm} \rho c^2 n \omega e^{in(\theta - \omega t)} R_n(\lambda_{nm} r) e^{i\alpha z} e^{i\beta z} \quad (II-A18)$$

The index n is determined by the well known lobe number equation

$$n = \bar{n} B - kV$$

where

\bar{n} - harmonic number

B - number of blade

k - integer

V - number of vanes

The index m represents the radial mode structure within the duct.

The major unknown in equation (II-A18) is A_{nm} which in turn depends on $\Gamma(r)$ in equation (II-A17). In the following sections this unsteady circulation is defined for various noise generating mechanisms.

(2) Rotor Alone Noise. The rotor alone noise is a result of the rotation of the steady (in the rotating reference frame) rotor pressure field which is seen by the stationary observer as a periodically varying (at the blade passing frequency) pressure pulse.

An approximate calculation of the circulation about a two dimensional airfoil can be obtained as follows:

Consider the cascade of airfoils shown in Figure II-A3.

The circulation is defined as:

$$\Gamma = \oint V \cdot ds \quad (\text{II-A19})$$

From Figure II-A3

$$\Gamma = \int V ds + \int_0^d C_{u2} ds - \int V ds - \int_0^d C_{u1} ds \quad (\text{II-A20})$$

Then

$$\Gamma = d (C_{u2} - C_{u1}) = d \Delta C_u \quad (\text{II-A21})$$

The ΔC_u is generally known from the rotor aerodynamic calculations. If equation (II-A21) is applied at several radial stations along the rotor, a distribution of circulation, $\Gamma(r)$, can be obtained. This distribution can then be used in equation (II-A17) to obtain the amplitude coefficient, A_{nm} .

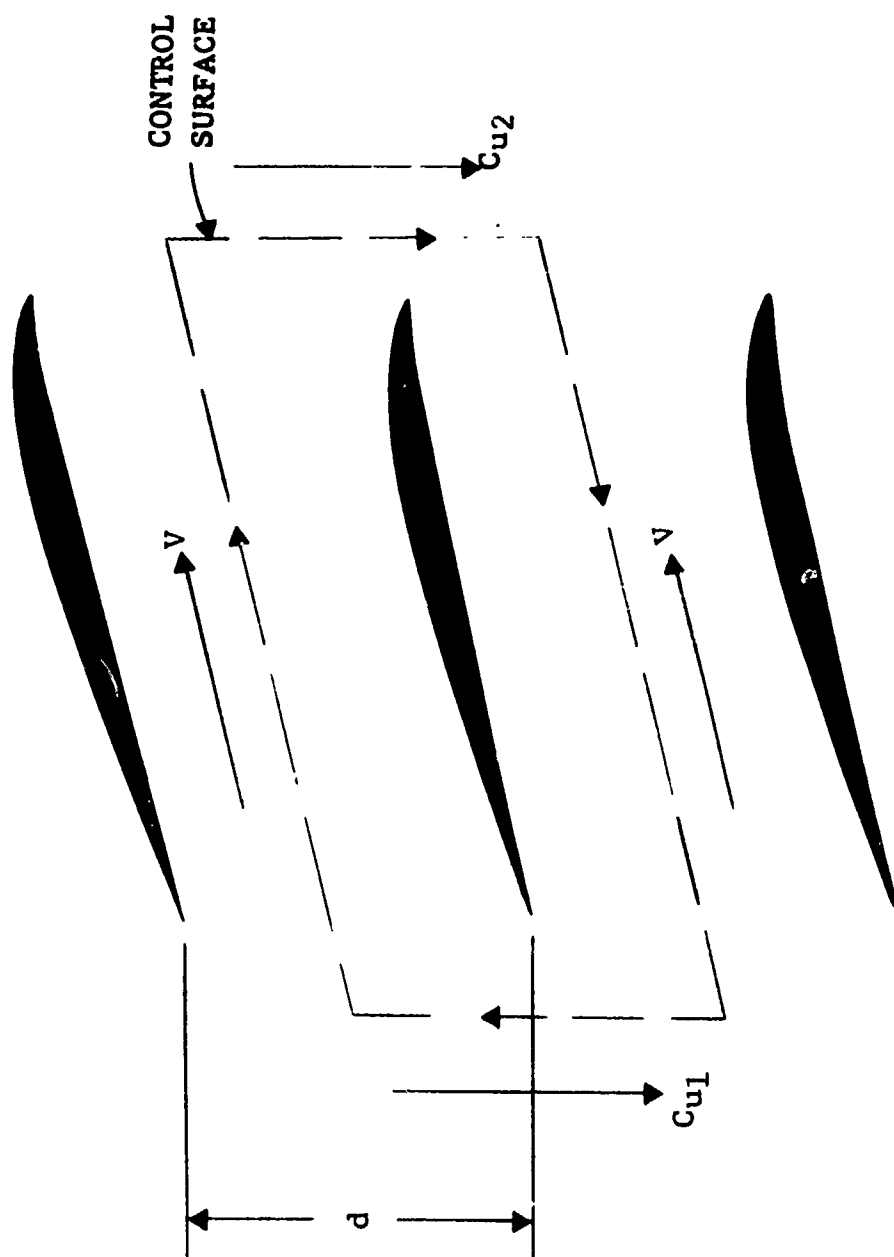


FIGURE II-A3 TWO DIMENSIONAL CASCADE AIRFOIL CIRCULATION CONTROL SURFACE

(3) Viscous Wake Interaction Noise. A viscous wake interaction results when the wakes from an upstream blade row impinge on a downstream blade moving relative to the upstream blades. The reaction of the downstream blade to the wake is a fluctuation of its loading (circulation) which in turn presents a periodically varying pressure source to the stationary reference frame. This pressure fluctuation is, therefore, a source of blade passing frequency noise.

The analysis of viscous wake interaction generated pure tone noise is based on reference 1. The analysis depicts the two blade rows as made up of a tandem cascade of thin airfoils in an inviscid two dimensional shear flow with the wake shape empirically determined.

Figures II-A4 and II-A5 contain the basic geometric configuration used. The wake shape can be represented by

$$Y = .962 C_d^{1/2} c \left(\frac{x}{c} - .7 \right)^{1/2} \quad (\text{II-A22})$$

where

Y - wake semi-width

c - blade semi-chord

C_d - drag coefficient

x - distance downstream from the upstream
blade row mid-chord

Using the geometry of Figure II-A5 and taking the relative motion of the two blade rows into account the unsteady upwash on the rotor can be expressed as

$$v = \frac{1}{2\pi} v_r \sum_{n=1}^{\infty} \frac{G_n^s}{n} \exp \left[i v_r \bar{n} \left(t - \frac{x_r}{v_r} \right) \right] \quad (\text{II-A23})$$

where

$$v_r = \frac{2\pi U}{d_s} \quad (\text{II-A24})$$

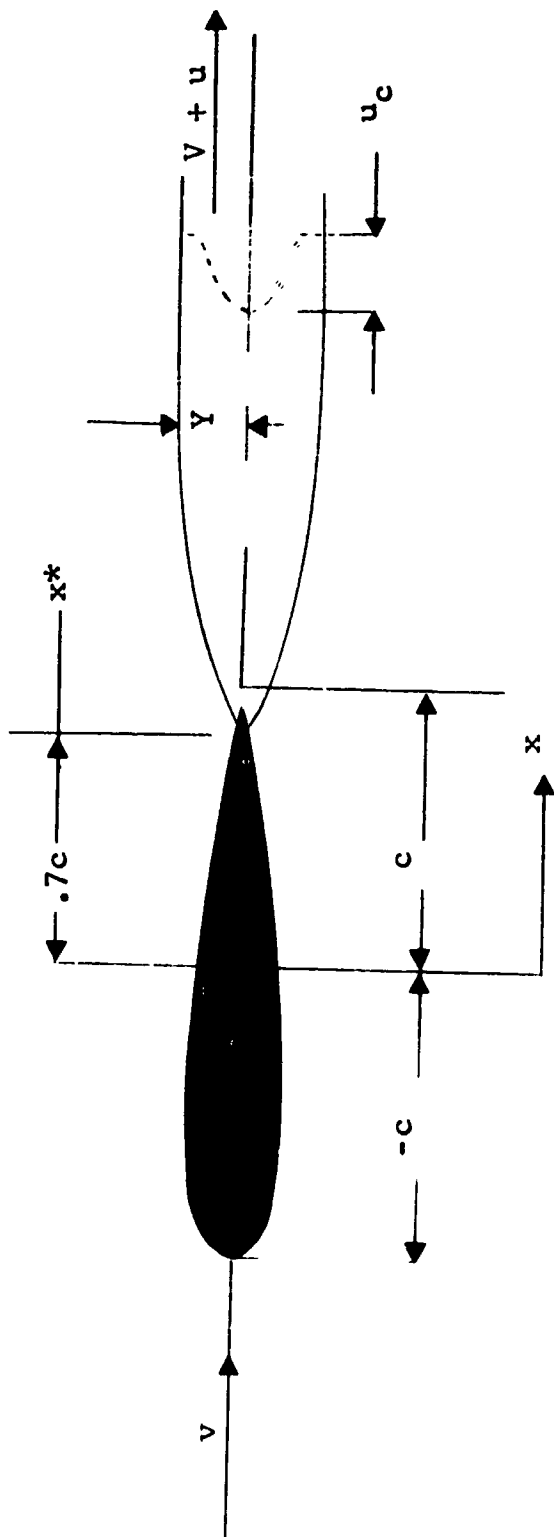


FIGURE II-A4 BLADE WAKE PROFILE



$$\frac{G_n^s}{n} = 14.622 \frac{V_s}{V_r} \frac{C_d \sin \bar{\beta}_s}{\left(\frac{x'_r}{c_s} + .3\right) \cos \alpha_s} \sqrt{\frac{x'_r}{c_s}} \exp \left[-\pi n^2 \left(\frac{.68 \sigma_s}{\sqrt{2} \cos \alpha_s} \right)^2 \frac{C_d x'_r}{c_s} \right] \quad (\text{II-A25})$$

$$\frac{x'_r}{c_s} = \frac{c_r}{c_s} \left(\frac{b}{c_r} \sec \alpha_s + \frac{x_r}{c_r} \frac{V_s}{V_r} \right) - .7 \quad (\text{II-A26})$$

$$\frac{x_r}{c_r} = 1/2 \quad (\text{II-A27})$$

and where σ_s is the stator solidity (all other variables are defined in Figure II-A5)

It might be interesting to note that equation II-A27 implies that the wake width and velocity u_c are measured at the quarter chord point on the rotor. Variations in this point, however do not affect the results significantly.

Using the results of thin airfoil theory, (reference 2) the unsteady circulation can be obtained from the upwash velocity as

$$|\Gamma| = c_r V_r \sum_{\bar{n}=1}^{\infty} \left| \frac{G_n^s}{n} \right| |J(\bar{n} \omega)| |S(\bar{n} \omega)| \quad (\text{II-A28})$$

$$|J(\bar{n} \omega)| = \left[J_0^2(\bar{n} \omega) + J_1^2(\bar{n} \omega) \right]^{1/2} \quad (\text{II-A29})$$

$$\omega = \frac{c_r \pi U_s}{c_s V_r} \quad (\text{II-A30})$$

and where $|S(\bar{n}\omega)|$ can be approximated by

$$|S(\bar{n}\omega)| \approx \left[\frac{a + \bar{n}\omega}{a + (\pi a + 1) \bar{n}\omega + 2\pi \bar{n}^2 \omega^2} \right]^{1/2} \quad (\text{II-A31})$$

where

$$a = .1811$$

The circulation calculated by equation (II-A28) is the required unsteady circulation due to the interaction of the wake of an upstream stator with a downstream rotor at a given radius. Similar equations can be derived for the interaction of a rotor and downstream stator by interchanging the subscripts r and s in equations IIA-23 through IIA-30.

In order to get an approximate radial distribution of unsteady circulation, the calculation can be made at three radial stations: hub, pitch and tip, and a curve fit through the results. Then the radial distribution can be expressed as

$$\Gamma(r) = a_0 + a_1 r + a_2 r^2 \quad (\text{II-A32})$$

In summary, the unsteady circulation has been cast in such a form that it can be directly related to the parameters which describe the geometric and aerodynamic configuration of the blade rows.

Equation (II-A32) can be substituted in equation (II-A17) to obtain the amplitude coefficient A_{nm} .

(4) Potential Interaction Noise. A potential interaction between blade rows produces a mutual disturbance and thus two noise sources are generated. That is, the pressure field of the rotor disturbs the stator and the pressure field of the stator disturbs the rotor. To a good approximation these two noise sources can be thought of as independent. These disturbances also lead to periodic blade loading (circulation) variations which produce pure tone acoustic waves.

Two analyses were developed for potential interaction. One two dimensional and the other axisymmetric.

The two dimensional analysis was adapted from reference 2. The intent of this work was to determine the upwash (or downwash) on a blade due to the potential field of a neighboring blade row moving relative to the blade. The resulting upwash velocity can then be used in a calculation of the unsteady circulation.

The analysis is for a two dimensional cascade of thin airfoils in a non-viscous incompressible flow. An approximate three dimensional solution can be obtained by making a two dimensional calculation at several radial locations and fitting a curve through the results.

Consider the two cascades shown in Figure II-A6. The upwash velocity on an upstream blade due to a point vortex of strength Γ' on each downstream blade can be expressed as

$$v^s = - \frac{\Gamma'}{2\pi} \sum_{j=1}^N \frac{1}{x_s - \zeta_j} \quad (\text{II-A33})$$

The point vortex can, however, be replaced by a line vortex distributed along the downstream blade row chord where

$$\Gamma_r = \int_{-c_r}^{+c_r} \gamma_r(x_r) dx_r \quad (\text{II-A3})$$

and γ_r is the distributed vortex strength. This strength in turn may be expressed in terms of a flat plate or elliptic distribution along the chord. That is

$$\gamma_r = 2V_r A_r \frac{1 - \cos \hat{\theta}}{\sin \hat{\theta}} \quad (\text{flat plate}) \quad \text{II-A35}$$

or

$$\gamma_r = 4V_r A_r \sin \hat{\theta} \quad (\text{elliptical}) \quad (\text{II-A36})$$

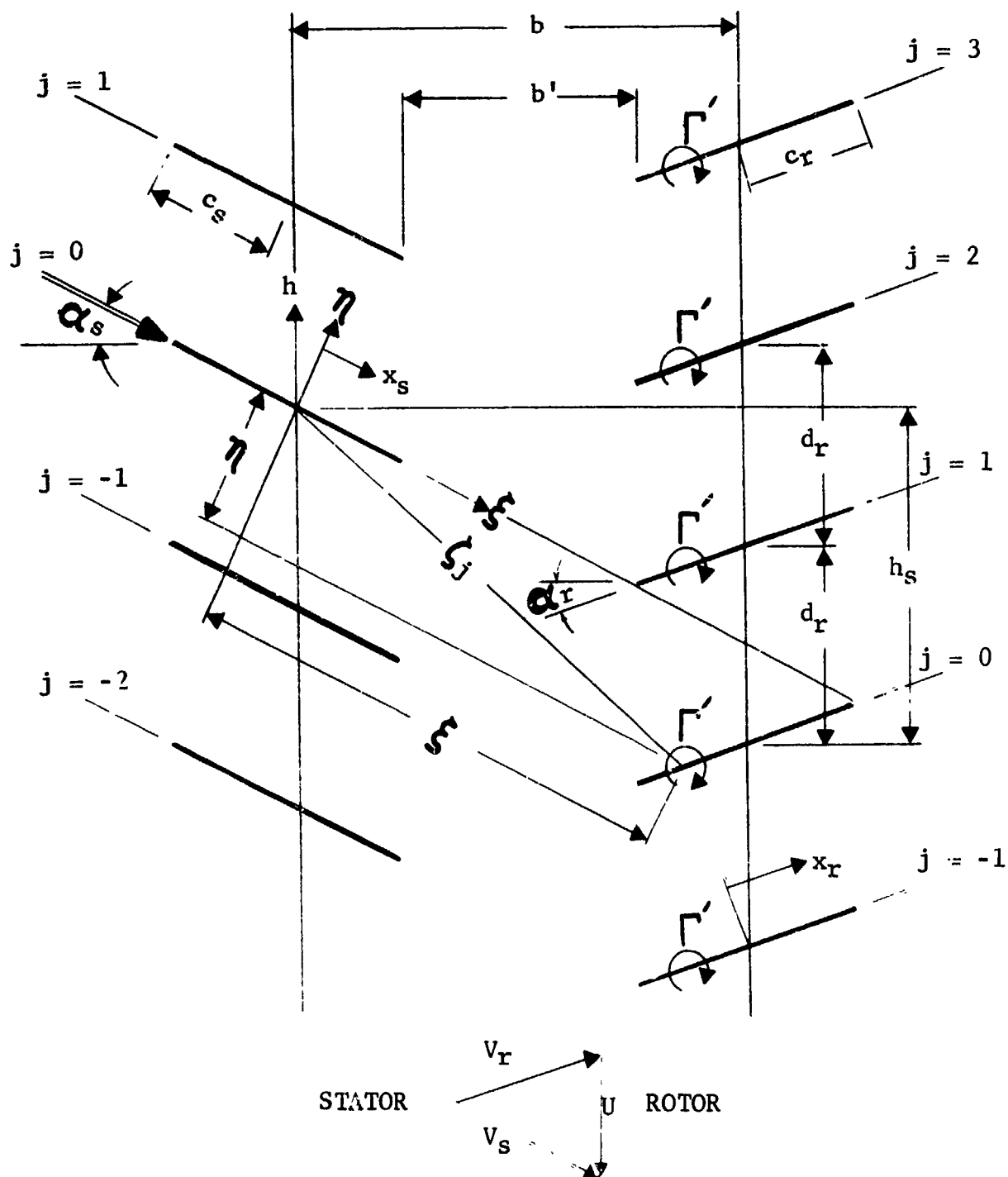


FIGURE II-A6 BLADE ROW GEOMETRY FOR A POTENTIAL INTERACTION

where the transformation

$$x_r = c_r \cos \hat{\theta} \quad (\text{II-A37})$$

has been made and where A_0^r and A_1^r are determined by the blade loading.

Substituting equations (II-A34-37) into equation (II-A33), introducing the geometry of Figures II-A6 and integration over the downstream blade row chord, the upwash velocity can be expressed as

$$v^s = \frac{\Gamma_r e^{-i\alpha_s}}{2d_r} \left\{ 1 + 2 \sum_{n=1}^{\infty} \frac{H_n^r}{n} \exp \left[-\frac{2\pi n}{d_r} \left(b + ih_s - x_s e^{-i\alpha_s} \right) \right] \right\} \quad (\text{II-A38})$$

where

$$H_n^r = J_0(z_r) + i J_1(z_r) \quad (\text{II-A39})$$

for a flat plate vorticity distribution and

$$H_n^r = \frac{2ie^{i\alpha_r}}{\pi c_r} J_1(z_r) \quad (\text{II-A40})$$

for an elliptic distribution. The argument is expressed as

$$z_r = \pi n \sigma_r e^{-i[\pi/2 + \alpha_r]} \quad (\text{II-A41})$$

Thus far the airfoils have been assumed to be stationary relative to one another. Introducing moving coordinates the upwash can be expressed as

$$v^s = \frac{\Gamma_r e^{-i\alpha_s}}{2d_r} + \frac{\Gamma_r}{2\pi c_s} \sum_{\bar{n}}^{\infty} G_{\bar{n}}^s \exp \left(\frac{2\pi \bar{n}}{d_r} e^{-i\alpha_s} x_{\bar{n}} \right) \quad (\text{II-A42})$$

where

$$G_{\bar{n}}^s = \frac{\pi \sigma_s d_s}{d_r} e^{-i\alpha_s} H_{\bar{n}}^r \exp \left\{ -\pi \bar{n} \sigma_r \left[\frac{b}{c_r} \left(1 + i \tan \alpha_r - \frac{iU}{v_s \cos \alpha_s} \right) - \frac{iU}{v_r} \right] \right\} \quad (\text{II-A43})$$

It can be shown (references 3 and 4) that the magnitude of the unsteady circulation for sinusoidal motion is given by

$$\Gamma = \Gamma_r \sum_{\bar{n}}^{\infty} |G_{\bar{n}}^s| |J(\lambda_s \bar{n})| |S(\bar{n}\omega_s)| \quad (\text{II-A44})$$

where

$$\lambda_s = \frac{2\pi c_s}{d_r} e^{i[\pi/2 - \alpha_s]} \quad (\text{II-A45})$$

$$\omega_s = \frac{2\pi U c_s}{v_s d_r} \quad (\text{II-A46})$$

$$|J(\lambda_s \bar{n})| = |J_0(\lambda_s \bar{n}) - 1 J_1(\lambda_s \bar{n})| \quad (\text{II-A47})$$

$$|S(\bar{n}\omega_s)| = \left[\frac{a + \bar{n}\omega_s}{a + (\pi a + 1) \bar{n}\omega_s + 2\pi \bar{n} \omega_s^2} \right]^{1/2} \quad (\text{II-A48})$$

and where

$$a = .1811 \quad (\text{II-A49})$$

Therefore, the unsteady circulation can be calculated from equation (II-A44). For an axisymmetric cascade, the circulation can be obtained approximately by applying equation (II-A44) at several radial locations. The resulting circulation distribution can then be applied to equation (II-A17) to determine A_{nm} .

Table II-A1 indicates the changes to be made in equations (II-A39-46) to obtain the remaining three types of potential interactions.

For the axisymmetric analysis consider an element dR_r of a vortex line of strength Γ_r' located at a point R_r on the rotor. Due to this vortex element, the induced velocity at a point R_s on the stator is given by (Figure II-A7)

$$d\vec{q}_s = \frac{\Gamma_r' d\vec{R}_r \times \vec{p}}{4\pi p^3} \quad (\text{II-A50})$$

or in scalar form

$$dq_s = \frac{\Gamma_r'(x_r, R_r) \sin\delta}{4\pi \left(\frac{r_s}{\sin\delta}\right)^2} dR_r \quad (\text{II-A51})$$

The induced velocity component vertical to the chord of the stator blade Figure (II-A8) is then

$$du_s = \frac{\Gamma_r'(x_r, R_r) \sin\delta}{4\pi \frac{r_s}{\sin\delta}} \sin\eta dR_r \quad (\text{II-A52})$$

	SUBSCRIPTS <u>r or s</u>	FLOW ANGLES <u>α</u>	WHEEL SPEED <u>U</u>
IGV - Rotor Potential	(as shown)	(as shown)	(as shown)
Rotor - IGV Potential	$r \rightarrow s$	$\alpha \rightarrow -\alpha$	$U \rightarrow -U$
OGV - Rotor Potential	(as shown)	$\alpha \rightarrow -\alpha$	$U \rightarrow -U$
Rotor - OGV Potential	$r \rightarrow s$	(as shown)	(as shown)

TABLE II-A1

Subscript Changes for Multiple Potential
Interactions

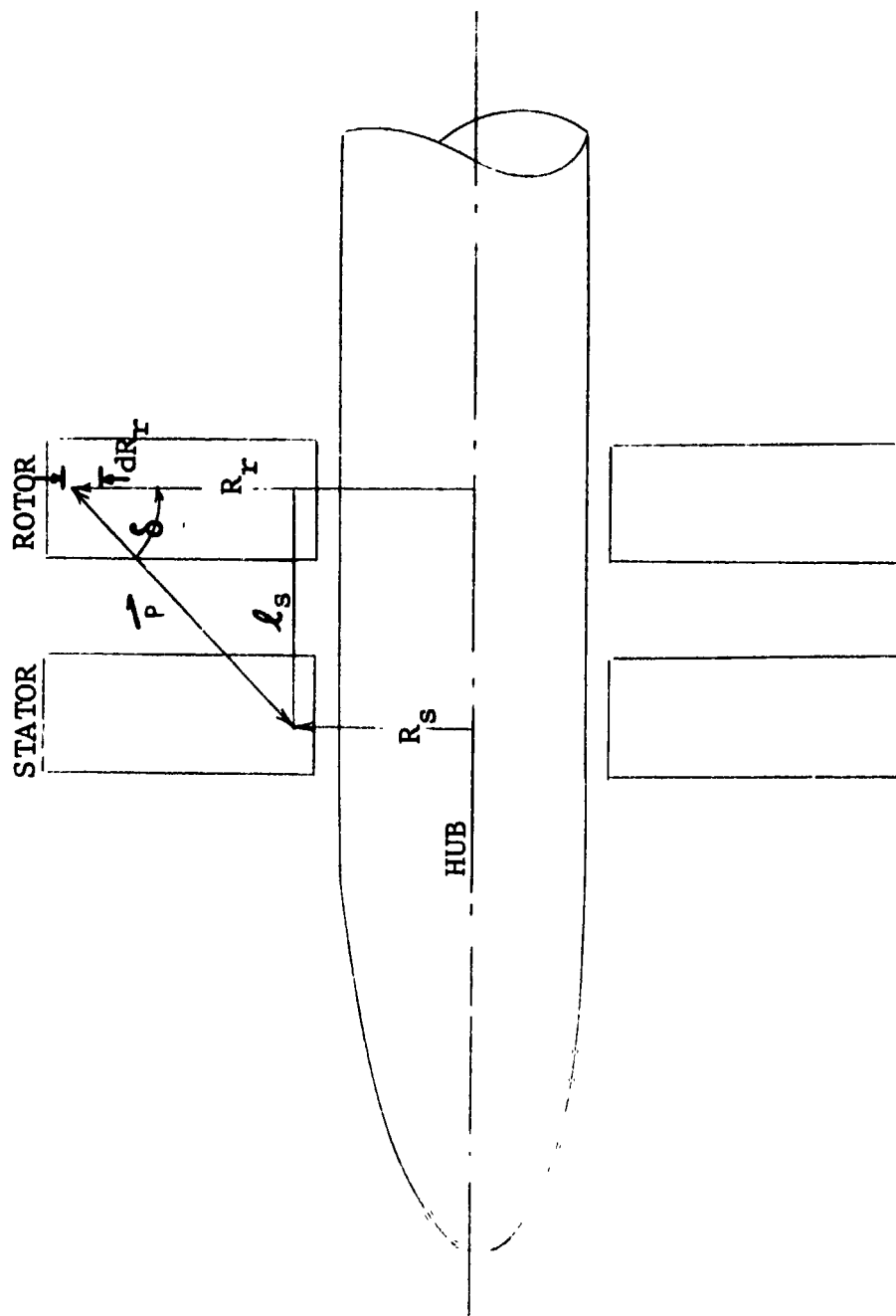


FIGURE II-A7 AXIAL VECTOR DIMENSIONS FOR AN AXISYMMETRIC POTENTIAL INTERACTION

where

$$\sin \delta = l_s / [l_s^2 + (R_r - R_s)^2]^{1/2} \quad (\text{II-A53})$$

$$l_s = \sqrt{(l_s)_1^2 + (l_s)_2^2} \quad (\text{II-A54})$$

$$(l_s)_1 = (C_r + x_r) \cos \alpha_r + (C_s - x_s) \cos \alpha_s + b' \quad (\text{II-A55})$$

$$(l_s)_2 = (C_r + x_r) \sin \alpha_r - (C_s - x_s) \sin \alpha_s + nd_r - Ut \quad (\text{II-A56})$$

l_s is the distance between a point on the stator and a point on the rotor. U is the speed of the rotor, positive down (Figure II-A8).

The following relations will be used in the later development:

$$V_s \sin (\alpha_r + \alpha_s) = U \cos \alpha_r \quad (\text{II-A57})$$

$$V_r \sin (\alpha_r + \alpha_s) = U \cos \alpha_s$$

The angle η between the chord of the stator blade and the velocity q_s can be expressed in terms of α_s , $(l_s)_1$, and $(l_s)_2$,

$$\eta = \frac{\pi}{2} - \left[\alpha_s + \tan^{-1} \frac{(l_s)_2}{(l_s)_1} \right]$$

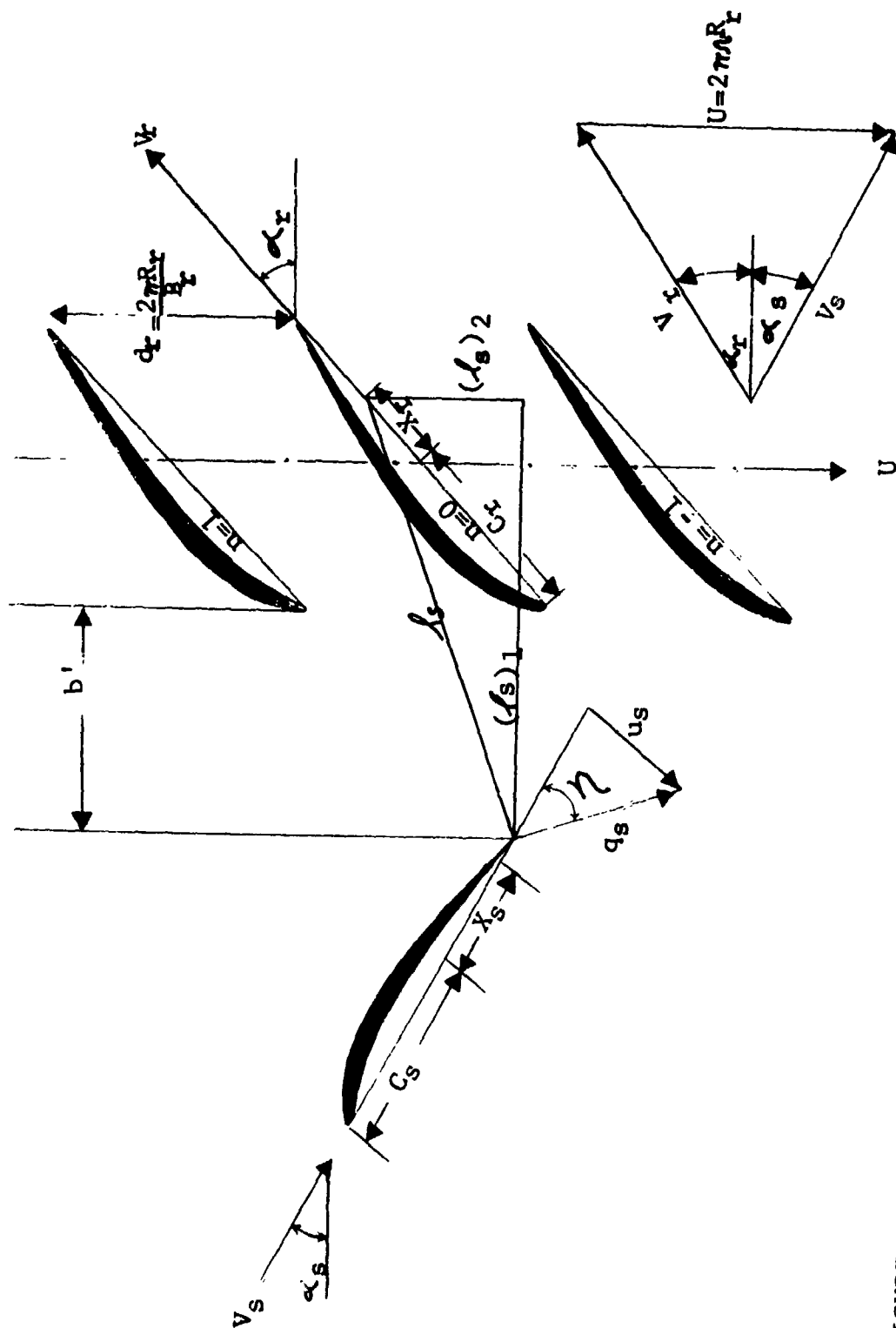


FIGURE II-A8 GEOMETRY FOR THE VELOCITY AT THE STATOR INDUCED BY THE STEADY CIRCULATION OF THE ROTOR

now

$$\sin \eta = \{ (C_r + x_r) \cos(\alpha_r + \alpha_s) + b' \cos \alpha_s + C_s - x_s - n d_r \sin \alpha_s + U t \sin \alpha_s \} / l \quad (\text{II-A58})$$

The vertical velocity at the stator induced by the steady non-uniform circulation distributed along the radial direction of the rotor blade, is obtained by integration equation (II-A52) from $R_r = R_1$ to R_2 .

$$u_s = \frac{1}{4\pi} \int_{R_1}^{R_2} \frac{\Gamma_r'(x_r, R_r) \sin \delta}{\left(\frac{l_s}{\sin \delta}\right)^2} \sin \eta \, dR_r \quad (\text{II-A59})$$

Substitution leads to

$$u_s = \frac{1}{4\pi} \int_{R_1}^{R_2} \Gamma_r'(x_r, R_r) \frac{(\ell_s)_1 \cos \alpha_s - (\ell_s)_2 \sin \alpha_s}{[\ell_s^2 + (R_r - R_s)^2]^{3/2}} \, dR_r \quad (\text{II-A60})$$

If, now, Γ_r' is replaced by the distribution of vortices $\gamma_r(x_r, R_r) \, dx_r$ along a line representing a typical rotor blade, the induced vertical velocity at the stator due to a single rotor blade is obtained by integrating over x_r from $-C_r$ to C_r .

$$u_s = \frac{1}{4\pi} \int_{-C_r}^{C_r} \int_{R_1}^{R_2} \gamma_r(x_r, R_r) \frac{(\ell_s)_1 \cos \alpha_s - (\ell_s)_2 \sin \alpha_s}{[\ell_s^2 + (R_r - R_s)^2]^{3/2}} \, dR_r \, dx_r \quad (\text{II-A61})$$

By assuming for the present computation

$$\gamma_r = (a_1 + a_2 R_r + a_3 R_r^2) \frac{1 - \cos \hat{\theta}_r}{\sin \hat{\theta}_r} \quad (\text{II-A62})$$

where the relationship between x_r and $\hat{\theta}_r$ is given by

$$x_r = C_r \cos \hat{\theta}_r \quad (\text{II-A63})$$

Equation (II-A61) can be written as

$$u_s = \frac{1}{4\pi} \int_0^\pi \int_{R_1}^{R_2} (a_1 + a_2 R_r + a_3 R_r^2) \frac{(\ell_s)_1 \cos \alpha_s - (\ell_s)_2 \sin \alpha_s}{[\ell_s^2 + (R_r - R_s)^2]^{3/2}} \cdot$$

$$(1 - \cos \hat{\theta}_r) C_r dR_r d\hat{\theta}_r \quad (\text{II-A64})$$

Summing up the contributions of all rotor blades, the induced vertical velocity at the stator blade due to the whole row of rotor blades, is given by

$$u_s = \frac{1}{4\pi} \sum_{n=n_1}^{n_2} \int_{\theta_r=0}^\pi \int_{R_r=R_1}^{R_2} (a_1 + a_2 R_r + a_3 R_r^2) \cdot$$

$$\frac{(\ell_s)_1 \cos \alpha_s - (\ell_s)_2 \sin \alpha_s}{[\ell_s^2 + (R_r - R_s)^2]^{3/2}} (1 - \cos \hat{\theta}_r) C_r dR_r d\hat{\theta}_r \quad (\text{II-A65})$$

where

$$n_1 = -\frac{B_r - 1}{2} \quad n_2 = \frac{B_r - 1}{2} \quad \text{if } B_r \text{ is an odd number}$$

$$n_1 = -\frac{B_r - 2}{2} \quad n_2 = \frac{B_r}{2} \quad \text{if } B_r \text{ is an even number}$$

Observing that $(\ell_s)_1, (\ell_s)_2, \ell_s$ are quantities evaluated at $R_r = R_s$, the R_r integration can be carried out analytically.

$$u_s(\hat{\theta}_s, R_s, t) = \frac{1}{4\pi} \sum_{n=n_1}^{n_2} \int_0^\pi H_r(\hat{\theta}_r, \hat{\theta}_s, R_s, t) [(\ell_s)_1 \cos \alpha_s - (\ell_s)_2 \sin \alpha_s] \cdot$$

$$(1 - \cos \hat{\theta}_r) C_r d\hat{\theta}_r \quad (\text{II-A66})$$

where

$$x_s = C_s \cos \hat{\theta}_s$$

$$H_r(\hat{\theta}_r, \hat{\theta}_s, R_s, t) = \frac{a_1}{\ell_s^2} \left[\frac{R_2 - R_s}{\rho_2} - \frac{R_1 - R_s}{\rho_1} \right] + \frac{a_2}{\ell_s^2} \left[\frac{R_2 R_s - R_s^2 - \ell_s^2}{\rho_2} \right. \\ \left. - \frac{R_1 R_s - R_s^2 - \ell_s^2}{\rho_1} \right] + a_3 \left\{ \frac{1}{\rho_2} \left[\frac{R_s^2 - \ell_s^2}{\ell_s^2} (R_2 - R_s) - 2R_s \right] \right. \\ \left. - \frac{1}{\rho_1} \left[\frac{R_s^2 - \ell_s^2}{\ell_s^2} (R_1 - R_s) - 2R_s \right] + \log \left| \frac{R_2 - R_s + \rho_2}{R_1 - R_s + \rho_1} \right| \right\} \quad (\text{II-A67})$$

$$\rho_1 = \sqrt{\ell_s^2 + (R_1 - R_s)^2} \quad (\text{II-A68})$$

$$\rho_2 = \sqrt{\ell_s^2 + (R_2 - R_s)^2} \quad (\text{II-A69})$$

In order to evaluate the circulation of the stator blade due to the effect of the rotor, equation (II-A66) may be written in the form:

$$u_s(\hat{\theta}_s, R_s, t) = V_s \left\{ C_0 + \sum_{m=-\infty}^{\infty} C_m e^{imv_s t} \right\} \quad (\text{II-A70})$$

where \sum'_m indicates the summation over m omitting $m = 0$ term.

$$C_m = \frac{1}{2p} \int_0^{2p} \frac{U_s}{V_s} e^{-imv_s t} dt, \quad p = \pi/v_s, \quad v_s = 2\pi U/d_r$$

The time-independent term in u_s of equation (II-A70) represents the steady induction effect of the rotor on a stator blade. It will be omitted in the later development for only the unsteady effects are of interest here.

The coefficients C_m which are functions of α_s , can be represented by a cosine series:

$$C_m = A_{m0} + 2 \sum_{q=1}^{\infty} A_{mq} \cos q \hat{\theta}_s \quad (\text{II-A71})$$

where

$$A_{mq} = \frac{1}{2\pi p} \int_{\hat{\theta}_s=0}^{\pi} \int_{t=0}^{2p} \frac{U_s}{V_s} e^{-imv_s t} \cos q \hat{\theta}_s dt d\hat{\theta}_s$$

Substitution of equation (II-A71) into equation (II-A70), (omitting the term C_0), leads to

$$u_s = V_s \sum_{m=-\infty}^{\infty} \left\{ A_{m0} + 2 \sum_{q=1}^{\infty} A_{mq} \cos \hat{\theta}_s \right\} e^{imv_s t} \quad (\text{II-A72})$$

Sears (reference 4) has shown that when the relative vertical velocity $u(x)$ of the airfoil is given in the form

$$u = \left\{ A_0 + 2 \sum_{q=1}^{\infty} A_q \cos q\hat{\theta} \right\} V e^{i\nu t} \quad (\text{II-A73})$$

the lift is given by

$$L = 2\pi\rho CV^2 e^{i\nu t} \left\{ (A_0 + A_1) C(\omega) + (A_0 - A_2) \frac{i\omega}{2} \right\} \quad (\text{II-A74})$$

where

$$x = C \cos \hat{\theta}$$

V = the incoming air velocity

ρ = the density of air

C = the semi-chord of the airfoil

ω = the reduced frequency = $\nu c/V$

ν = the frequency of oscillation in radians per second

$$C(\omega) = \frac{K_1(i\omega)}{K_0(i\omega) + K_1(i\omega)}$$

In order to obtain the quasi-steady circulation, the results of Von Karman and Sears (reference 7) will be utilized. It states that, if the motion of the airfoil is such that its quasi-steady circulation is given by

$$\Gamma^q(t) = F e^{i\nu t} \quad (\text{II-A75})$$

then

$$L^q + L^{(2)} = L^q C(\omega) \quad (\text{II-A76})$$

where L^q is the quasi-steady lift and $L^{(2)}$ is the lift due to wake effects. Comparison of equation (II-A74) with equation (II-A76) reveals

$$L^q = 2\pi\rho C V^2 e^{i\nu t} (A_0 + A_1) \quad (\text{II-A77})$$

Since

$$L^q = \rho \Gamma^q V \quad (\text{II-A78})$$

the quasi-steady circulation is given by

$$\Gamma^q = 2\pi C V e^{i\nu t} (A_0 + A_1) \quad (\text{II-A79})$$

As mentioned in reference 6, using the results of Von Karman and Sears (reference 7), it is easy to show that the total circulation is given by

$$\Gamma(t) = \Gamma^q(t) e^{-i\omega t} S(\omega) \quad (\text{II-A80})$$

Comparison of equation (II-A72) with equation (II-A73) and using equation (II-A80) gives

$$\begin{aligned} \Gamma_s = 2\pi C_s V_s \sum_{m=1}^{\infty} \left\{ e^{im(\nu_s t - \omega_s)} S(m\omega_s) (A_{m0} + A_{m1}) \right. \\ \left. + e^{-im(\nu_s t - \omega_s)} S(-m\omega_s) (A_{-m0} + A_{-m1}) \right\} \quad (\text{II-A81}) \end{aligned}$$

The velocity at the rotor induced by the steady circulation of the stator can be obtained in a similar manner as that used to determine the induced velocity at the stator, Figure II-A9.

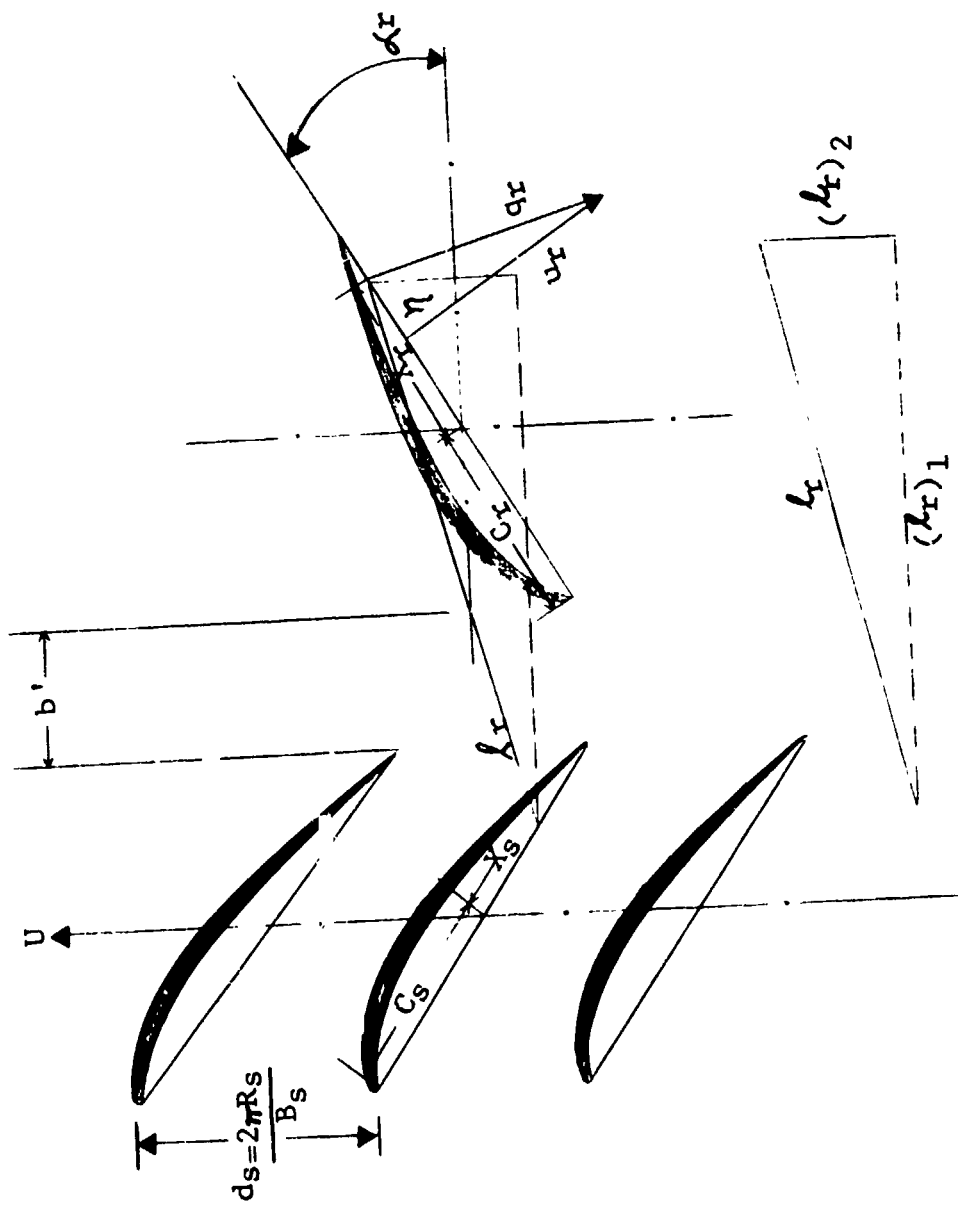


FIGURE 11-A9 GEOMETRY FOR THE VELOCITY AT THE ROTOR INDUCED BY THE STEADY CIRCULATION OF THE STATOR

The result is

$$\Gamma_r = 2\pi C_r V_r \sum_{m=1}^{\infty} \left\{ e^{im(\nu_r t - \omega_r)} S(m\omega_r) (B_{m0} + B_{m1}) + e^{-im(\nu_r t - \omega_r)} S(-m\omega_r) (B_{-m0} - B_{-m1}) \right\} \quad (II-A82)$$

where B_{mq} 's are the coefficients of

$$u_r = V_r \sum_{m=-\infty}^{\infty} \left\{ B_{m0} + 2 \sum_{q=1}^{\infty} B_{mq} \cos q\theta_r \right\} e^{im\nu_r t} \quad (II-A83)$$

$$B_{mq} = \frac{1}{2\pi p} \int_{\theta=0}^{\pi} \int_{t=0}^{2p} \frac{u_r}{V_r} e^{-im\nu_r t} \cos q\theta_r dt d\theta_r \quad (II-A84)$$

$$p = \pi/\nu_r$$

$$\nu_r = 2\pi U/d_s$$

$$\omega_r = \nu_r C_r / V_r$$

Application of equations (II-A81) or (II-A84) at several radial stations along the rotor's span will provide a distribution of unsteady circulation which can be used to evaluate A_{nm} .

The application of the analytical results indicate that in most cases the two dimensional and the axisymmetric analyses yield comparable data. It is only for very closely spaced rotors and stators (less than 0.1 chord spacing) that the axisymmetric analysis is required.

(5) Wake Vortex Interaction Noise. A secondary effect of the blade row interactions is a periodic wake vortex interaction. A schematic of this phenomenon is shown in Figure (II-A10). The shed vortex is usually termed a "starting vortex" and is a necessary result of the conservation of vorticity in a closed conservative system. Thus, when two blade rows interact two starting vortices are shed into their wakes. The vortices in turn impinge on the downstream blade row and set-up still another circulation fluctuation.

It can be shown (reference 2) that the wake vortex strength due to the potential interaction of a rotor pressure field with an upstream stator is given by

$$\varepsilon^S(x_s^0, t) = -\Gamma_r/c_s \sum_{\bar{n}=1}^{\infty} G_{\bar{n}}^S K(\bar{n}\omega_s) J(\bar{n}\lambda_s) e^{i\bar{n}\gamma_s} (t - x_s^0/V_s) \quad (\text{II-A85})$$

where $G_{\bar{n}}^S$ is given by equation (II-A43) and x_s^0 is a distance measured along the stator chord.

This strength may then be translated into an effective induced velocity at the leading edge of the rotor. The induced velocity can be expressed as

$$w = \sum_{\bar{n}=1}^{\infty} \sum_{k=-\infty}^{\infty} w_{\bar{n}k} \exp \left[i\gamma_r k \left(t - \frac{x_r^0}{V_r} \right) \right] \quad (\text{II-A86})$$

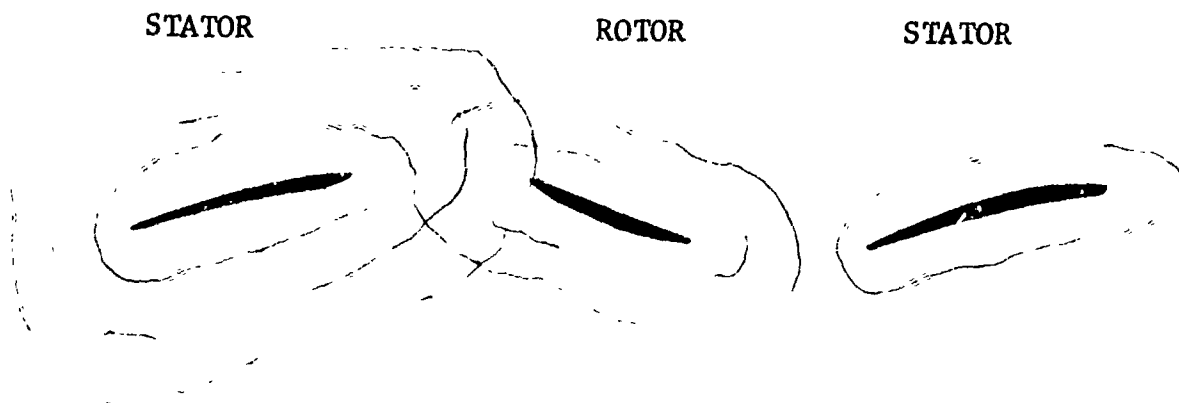
where

$$w_{\bar{n}k} = - \left\{ \Gamma_r G_{\bar{n}}^S K(\bar{n}\omega_s) J(\bar{n}\lambda_s) \exp \left[-i\bar{n}\pi\sigma_r \left(bU/c_s V_s \cos \beta + \frac{U}{V_r} \right) + i\omega_r k \right] \right\}.$$

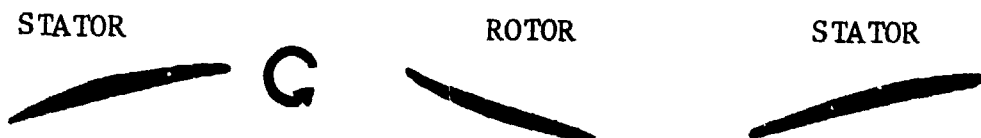
$$\frac{1}{d_s \cos \alpha_s} \left[\frac{(V_{sdr}/V_{rd_s})(k/\bar{n})}{1 + \cot^2 \beta [1 - (V_{sdr}/V_{rd_s})(k/\bar{n}) \sec \beta]^2} \right] \quad (\text{II-A87})$$

It may be noted that the sum over k excludes the term $k = 0$.

A POTENTIAL INTERACTION TAKES PLACE



A VORTEX IS SHED FROM THE UPSTREAM STATOR



VORTEX CHANGES THE DOWNWASH VELOCITY ON
DOWNSTREAM ROTOR



FIGURE II-A10 SCHEMATIC OF A WAKE VORTEX INTERACTION

Using the results of thin airfoil theory, the unsteady induced velocity may be expressed in terms of an unsteady circulation magnitude.

$$|\Gamma| = \sum_{n=1}^{\infty} \sum_{k=-\infty}^{\infty} 2\pi c_r |w_{nk}| |J(\omega_r k)| |S(\omega_s k)| \quad (\text{II-A88})$$

Equation (II-A88) can then be applied at the hub, midspan, and tip of the rotor to obtain a radial unsteady circulation distribution which in turn may be used to calculate A_{nm} in equation (II-A17)

A similar result can be derived for an upstream rotor-downstream stator combination. It is only necessary to reverse the r and s subscripts in all the equations.

(6) Summary. Table II-A2 summarizes the information required to make a calculation of blade passing frequency and harmonic noise.

Figure (II-A11) shows a typical calculated result of spacing versus noise for the four types of interaction noise possible for a rotor and OGV. In this case viscous wake interaction is dominant for about .15 chord spacing or greater. The viscous wake interaction also shows the slowest decay rate with spacing.

It must be pointed out that different aerodynamic designs will have different spacing decay rates. The parameters listed in Table II-A2 and the equation for the unsteady circulation clearly show the importance of the details of the aerodynamic design on the tone noise generation. The mathematical models described above were very successful in providing a good quantitative prediction of blade passing frequency tones and their higher harmonics. Detailed comparisons between prediction and experimental data obtained on a number of vehicles are presented in Section VIII.

Geometric	Aerodynamic
*blade row solidities	rotor speed
tip radius	speed of sound
hub radius	density
number of blades	*relative and absolute air angles entering and leaving each blade row
number of vanes	*section drag coefficient
number of spinning lobes	
harmonic number (1 = fundamental)	
axial distance from the plane of generation	
*axial spacing between blade rows	
* required at hub, midspan and tip radii	

TABLE II-A2

Data Required for a Blade Passing Frequency

PWL Prediction

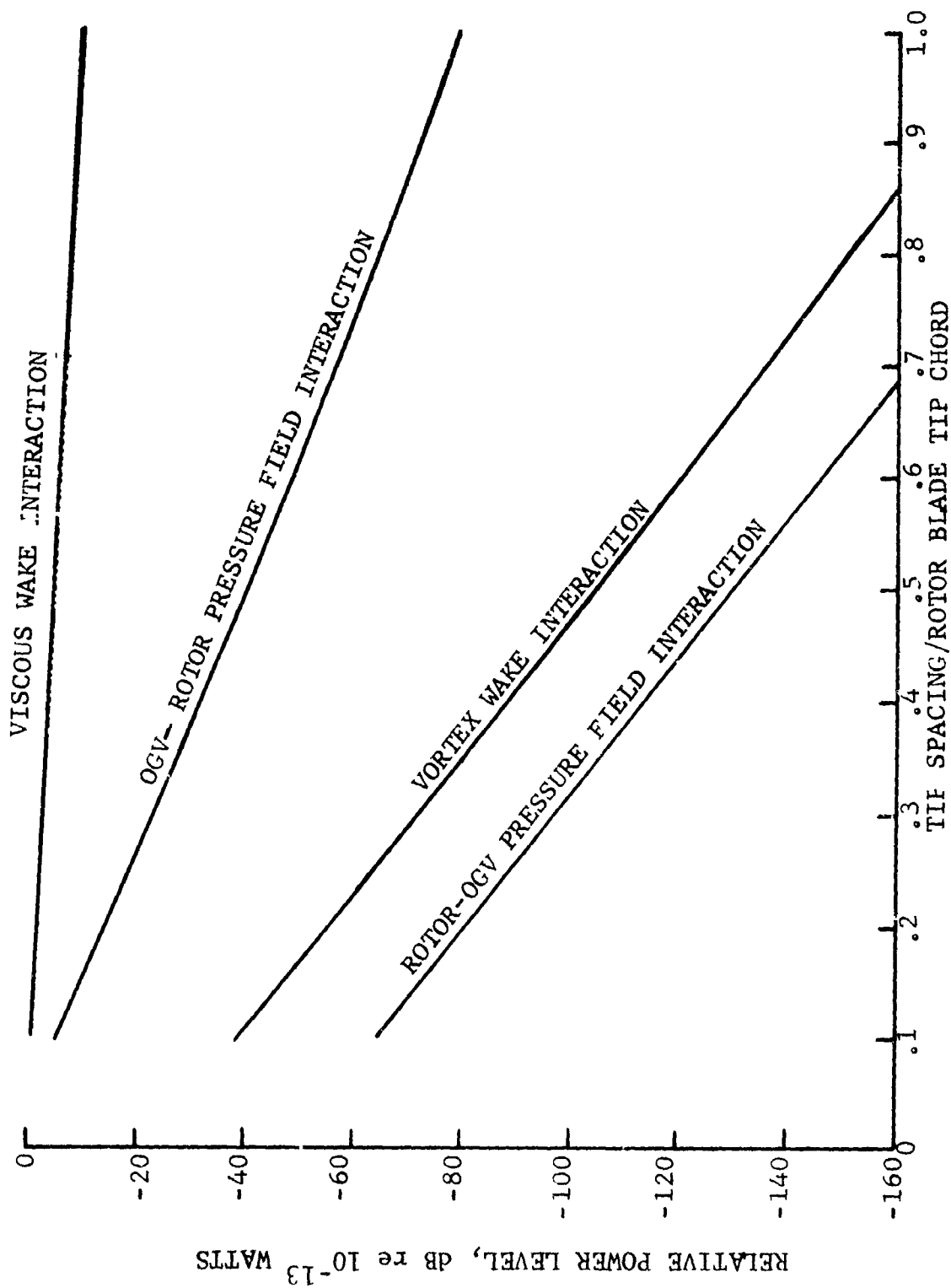


FIGURE II-A11 VANE-BLADE ROW SPACING - THE EFFECT OF VISCOUS WAKE, POTENTIAL, AND VORTEX WAKE INTERACTIONS.

NOMENCLATURE SECTION II-A

A_{mq}	coefficients of relative vertical velocity distribution - equation (22)
A_n	coefficients of the chordwise vorticity distribution
A_{nm}	n, m mode amplitude constant
b	blade row axial spacing, mid-chord to mid-chord
b'	blade row axial spacing, trailing edge to leading edge
c	speed of sound or airfoil semi-chord
C_d	drag coefficient
C_u	steady tangential velocity
$C(w)$	Theodorsen function
d	blade to blade spacing
e	natural log base
$f(r)$	radial distribution of tangential perturbation velocity
G_n	coefficient of unsteady wash
h	radius ratio of the annulus
h_s	see Figure II-A6
H_n^r	see equations (II-A39) and (II-A40)
i	imaginary number indicator
J	see equation (II-A47)
J_1	first kind Bessel function of first order
J_0	first kind Bessel function of zeroth order
K_1, K_2	constants
ℓ	distance between a point on the stator to a point on the rotor at the same radial distance

L	lift
m	radial pressure mode index
M	number of rotating line sources
M_z	axial Mach number
\overline{M}_0	tip swirl Mach number
n	spinning lobe number
\overline{n}	harmonic number
p	pressure
r	radial distance
R	radial dimension
R_1	hub radius
R_0	tip radius
$R_n(\lambda_{nm} r)$	linear combination of first and second kind Bessel function
S	see equation (II-A31)
t	time
u	axial perturbation velocity
u_c	wake velocity decrement
U	linear rotor speed
v	tangential perturbation velocity or upwash velocity
V	free stream steady velocity
X	distance measured parallel to the blade chord
y	distance measured perpendicular to the wake
Y	wake semi-width
Y_n	second kind Bessel function of order n
z_r	see equation (II-A41)
Z	axial distance

α - angle
 β - see equation (II-A5)
 $\bar{\beta} = \alpha_s + \alpha_r$
 Γ - circulation
 Γ' - point vortex circulation
 γ_r - vortex distribution along the rotor chord
 δ - Kronecker delta function
 ϵ - see equation (II-A85)
 ζ - complex distance from rotor to stator
 η - distance measured tangentially along the blade rows
 η_{nm} - norm of the cylinder function
 θ - circumferential angle
 $\hat{\theta}$ - transformed coordinate along the airfoil chords
 λ_{nm} - eigenvalue
 λ_s - see equation (II-A45)
 ω - circular frequency of motion in time = $2\pi U/d$
 ξ - axial distance from a point on the rotor to a point on the stator
 ρ - density
 $\rho_1 \rho_2$ - see equations (II-A68) and (II-A69)
 σ - solidity
 ϕ - velocity potential
 ϕ_r - circular arc camber
 Ω - rotational speed of rotor in rpm
 ω - mode tip Mach number or reduced frequency
 σ - stator solidity

SUBSCRIPTS

r	rotor
s	stator

SUPERSCRIPTS

r	rotor
s	stator
q	quasi-steady
(2)	wake effects

REFERENCES SECTION II-A

1. Kemp, N.H., W.R., "The Unsteady Forces due to Viscous Wakes in Turbo-machinery" Journal of the Aeronautical Sciences, July 1965.
2. Kemp, N.H., Sears, W.R., "Aerodynamic Interference Between Moving Blade Rows," Journal of the Aeronautical Sciences, September 1953.
3. Karman, Theodore Von, Sears, W.R., "Airfoil Theory for Non-Uniform Motion," Journal of the Applied Sciences, Vol. 5, No. 10, Page 379, August 1938.
4. Sears, W.R., "Some Aspects of Non-Stationary Airfoil Theory and its Practical Application," Journal of the Aeronautical Sciences, Vol. 8, No. 3, Page 104, January 1941.
5. Bateman, D.A., Chang, S.C., Hulse, B.T. and Large, J.B., "Compressor Noise Research," Technical Report - FAA-ADS-31, Commercial Airplane Division, The Boeing Company, January 1965.
6. Kemp, N.H., "On the Lift and Circulation of Airfoils in Some Unsteady Flow Problems," Journal of the Aeronautical Sciences, October 1952.
7. Karman, Theodore Von, Sears, W.R., "Airfoil Theory for Non-Uniform Motion," Journal of the Aeronautical Sciences, August 1938.

(B) Analytical Prediction of Broadband Noise. Modern aircraft engines are characterized by numerous noise sources. One category of noise which is of considerable importance, especially for noise evaluation of the high by-pass turbofan engine, is broadband noise. The name "broadband" noise is derived because of the broad frequency range associated with the sound pressure level spectra of aircraft fans and axial compressors.

It is known that there are two significant sources of broadband noise in fans. One arises in any type of flow from the vortex shedding at the airfoil trailing edge which induces local surface pressure fluctuations on the blade. The other is the broadband noise generated when the blade moves in a turbulent airflow. Under inlet turbulent flow conditions, the turbulent velocity fluctuations ahead of the blade cause random changes of incidence of the relative flow and hence a randomly fluctuating lift on the blade.

The two broadband noise mechanisms have the basic common feature of being generated by a random noise source distribution on and in the vicinity of a rotating blade. The basic acoustic source model associated with the two types of mechanisms discussed above is the dipole noise source. In addition to a dipole random distribution which results in a broadband noise spectra, there is also a random quadrupole contribution resulting from the turbulence presence in a wake. The following discusses a number of theories based on the noise mechanisms discussed above. Two main categories will be considered. Broadband formulations for predicting overall sound powers and formulations for predicting spectral sound level contributions of broadband noise.

(1) General Formulation. In a completely general way the wave equation for broadband noise can be obtained from the following conservation equations:

Continuity Equation

$$\frac{\partial \rho}{\partial t} + \text{Div } \rho \vec{u} = 0 \quad (\text{II-B1})$$

Momentum Equation

$$\frac{\partial \rho \vec{u}}{\partial t} + \text{Div } (\rho \vec{u}) \vec{u} = \text{Div } \vec{\tau} \quad (\text{II-B2})$$

$$\text{where } \vec{\tau} = -p \vec{I} + \vec{\tau}'$$

$$\vec{\tau}' = \text{Viscous Stress Tensor } [\mu \text{def } \vec{u} + \lambda \text{div } \vec{u}]$$

μ = First viscosity coefficient

λ = Second viscosity coefficient ($\lambda = 2/3\mu$)

\bar{I} = Unity tensor

def \vec{u} = Deformation tensor ($\text{grad } \vec{u} + (\text{grad } \vec{u})^T$)

By using the time derivative of equation (II-B1) and the divergence of equation (II-B2) and elimination of the momentum flux term $\rho \vec{u}$ one obtains

$$\nabla^2 p - \frac{\partial^2 \rho}{\partial t^2} = \text{Div Div} [\bar{\tau}' - (\rho \vec{u}) \vec{u}] \quad (\text{II-B3})$$

If p_0 and ρ_0 are considered as constant reference values such that reference speed of sound $C_0 = \gamma p_0 / \rho_0$, then equation (II-B3) may be written as

$$\begin{aligned} \nabla^2 (p - p_0) - \frac{1}{C_0^2} \frac{\partial^2 (p - p_0)}{\partial t^2} &= \text{Div Div} [\bar{\tau}' - (\rho \vec{u}) \vec{u}] \\ &- \frac{1}{C_0^2} \frac{\partial^2}{\partial t^2} (p - C_0^2 \rho) \end{aligned}$$

This relationship represents the inhomogeneous wave equation for pressure fluctuations. Lighthill (reference 1) has shown that except perhaps in exceptional circumstances, the source term $-\frac{1}{C_0^2} \frac{\partial^2 \rho}{\partial t^2} (p - C_0^2 \rho)$ is negligible. Thus, to this approximation one has

$$\nabla^2 p - \frac{1}{C_0^2} \frac{\partial^2 p}{\partial t^2} = \text{Div Div} (\bar{\tau}' - (\rho \vec{u}) \vec{u}) \quad (\text{II-B4})$$

The solution of equation (II-B4) may be obtained in a closed form by the method of "Green's Function" (reference 2). Let $G(\vec{r}, t/\vec{r}_0, t_0)$ be a solution to

$$\nabla^2 G - \frac{1}{C_0^2} \frac{\partial^2 G}{\partial t^2} = -4\pi \delta(\vec{r} - \vec{r}_0) \delta(t - t_0)$$

where $\delta(\vec{r} - \vec{r}_0)$ is the three-dimensional spacial Dirac-delta function and $\delta(t - t_0)$ is the time dependent form of the Dirac-delta function.

Then, if $p(\vec{r}, t)$ is a solution of the following non-homogeneous wave equation with a source function $\rho(\vec{r}, t)$

$$\nabla^2 p(\vec{r}, t) - \frac{1}{c^2} \frac{\partial^2}{\partial t^2} p = -4\pi \rho(\vec{r}, t)$$

for $t > 0$ within and on the surface S as shown in Figure (II-B1) one has

$$p(\vec{r}, t) = \int_{t_0} \iiint_{V_0} G(\vec{r}, t/\vec{r}_0, t_0) \tilde{\rho}(\vec{r}_0, t_0) dV_0 dt_0 + \frac{1}{4\pi} \int_{t_0} \iint_{S_0} \left\{ G(\vec{r}, t/\vec{r}_0, t) \nabla_0 p(\vec{r}_0, t_0) - p(\vec{r}_0, t_0) \nabla_0 G(\vec{r}, t/\vec{r}_0, t_0) \right\} \cdot \vec{n} dS_0 - \frac{1}{4\pi c^2} \int_{t_0} \iiint_{V_0} \left\{ \frac{\partial G}{\partial t_0} \right\}_{t_0=0} p(\vec{r}_0, t_0) - G_{t_0} \left\{ \frac{\partial \rho}{\partial t_0} \right\}_{t_0=0} dV_0 dt_0 \quad (II-B5)$$

where the subscript, o , on the vector "del" operator specifies differentiation with respect to the source position coordinates.

Since the source term, $\tilde{\rho}(\vec{r}, t)$, and the surface effects are of primary interest, the volume integral expressing initial effects will be considered negligible. Equation (II-B5) becomes then

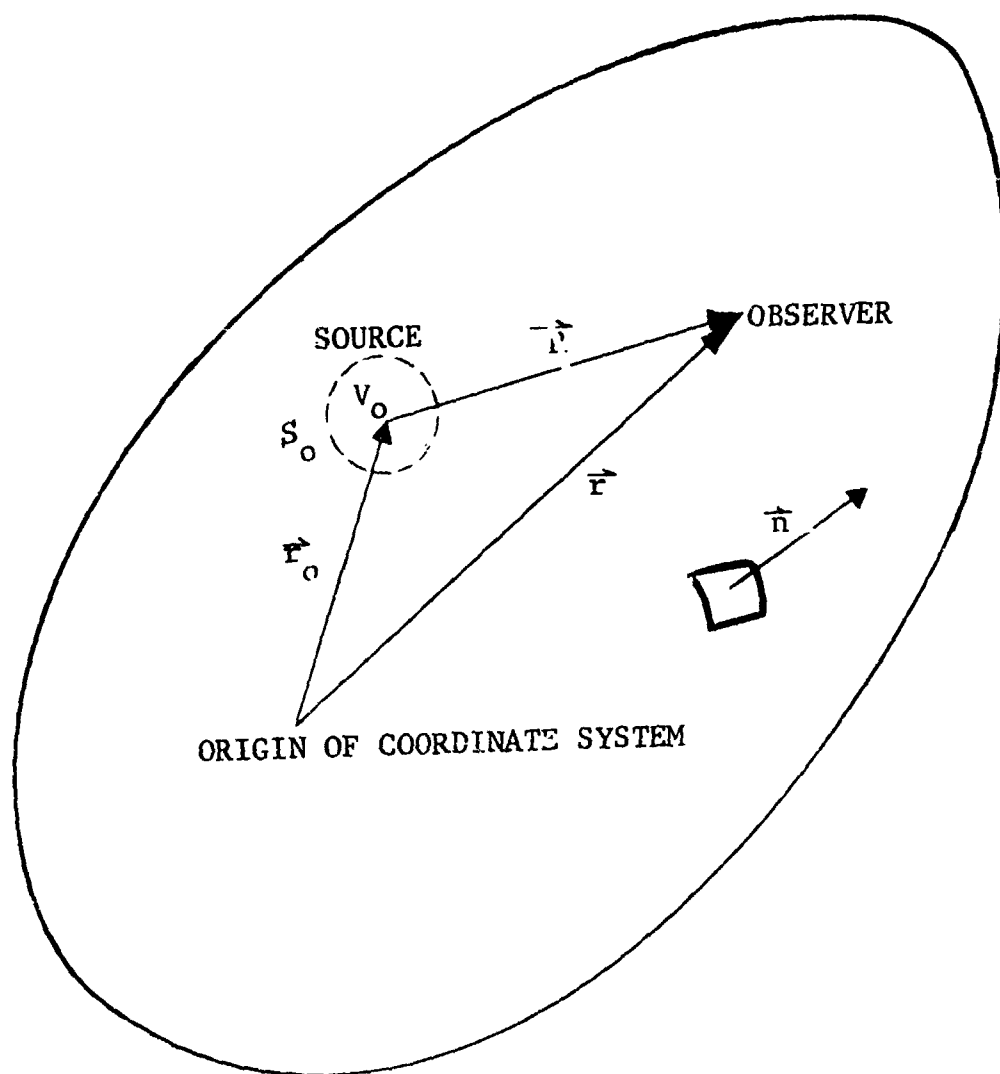


FIGURE I-B1 GENERAL COORDINATE SYSTEM FOR
ACOUSTIC RADIATION

$$p(\vec{r}, t) = \int_{t_0} \iiint_{V_0} G(\vec{r}, t/\vec{r}_0, t_0) \rho(\vec{r}_0, t_0) dV_0 dt_0 + \frac{1}{4\pi} \int_{t_0} \iint_{S_0} .$$

$$\left\{ G(\vec{r}, t/\vec{r}_0, t_0) \nabla_0 p(\vec{r}_0, t_0) - p(\vec{r}_0, t_0) \nabla_0 G(\vec{r}, t/\vec{r}_0, t_0) \right\} \cdot \vec{n} dS_0 dt_0 \quad (\text{II-B6})$$

where \vec{n} , is the unit normal vector pointing outward from the surface S. In three-dimensions, the Green's function is

$$G(\vec{r}, t/\vec{r}_0, t_0) = \frac{1}{R} \delta[R/C - (t - t_0)]; \quad R^2 \equiv (x - x_0)^2 + (y - y_0)^2 + (z - z_0)^2$$

Therefore for the source term as given in equation (II-B4) one has

$$\begin{aligned} p(\vec{r}, t) = & \int_{t_0} \iiint_{V_0} \frac{1}{R} \delta[t_0 - (t - R/C)] \text{Div}_0 \text{Div}_0 (\vec{r}' - (\rho \vec{u}) \vec{u}) / 4\pi] dV_0 dt_0 \\ & + \frac{1}{4\pi} \int_{t_0} \iint_{S_0} \left\{ \frac{1}{R} \delta[t_0 - (t - R/C)] \frac{\partial p(\vec{r}_0, t_0)}{\partial n_0} - p(\vec{r}_0, t_0) \frac{\partial}{\partial n_0} \right. \\ & \left. \left(\delta \frac{(t_0 - (t - R/C))}{R} \right) \right\} dS_0 dt_0 \end{aligned} \quad (\text{II-B7})$$

Integrating over time* yields

*Brackets about terms signify the term is evaluated at a retarded time $(t - R/C)$

$$p(\vec{r}, t) = \frac{1}{4\pi} \iiint_{V_0} \frac{1}{R} \text{Div}_0 \text{Div}_0 [\vec{\tau}' - (\rho \vec{u}) \cdot \vec{u}] dV_0 + \frac{1}{4\pi} \iint_{S_0} \frac{1}{R} \quad .$$

$$\left[\frac{\partial p}{\partial n_0} \right] dS_0 - \frac{1}{4\pi} \iint_{S_0} [p(r_0, t_0)] \frac{\partial}{\partial n_0} \left(\frac{1}{R} \right) dS_0 - \int_{t_0} \iint_S \quad .$$

$$\left[\frac{p(r_0, t)}{R} \right] (-1) \frac{\partial \delta}{\partial t} \frac{\partial (t-R/C)}{\partial R} \cdot \frac{\partial R}{\partial n_0} dS_0 dt_0$$

or

$$p(\vec{r}, t) = \frac{1}{4\pi} \iiint_{V_0} \frac{1}{R} \text{Div}_0 \text{Div}_0 [\vec{\tau}' - (\rho \vec{u}) \cdot \vec{u}] dV_0 + \frac{1}{4\pi} \iint_{S_0} \frac{1}{R} \left[\frac{\partial p}{\partial n_0} \right] dS_0 \\ - \frac{1}{4\pi} \iint [p] \frac{\partial}{\partial n_0} \left(\frac{1}{R} \right) dS_0 - \iint \left[\frac{\partial p}{\partial t} \right] (-1) \frac{1}{C} \frac{\partial R}{\partial n_0} dS_0 \quad (\text{II-B8})$$

For far field terms:

$$p(\vec{r}, t) = \frac{1}{4\pi r} \underbrace{\iiint_V \text{Div}_0 \text{Div}_0 [\vec{\tau}' - (\rho \vec{u}) \cdot \vec{u}] dV_0}_{\text{Noise resulting from fluctuating shearing stresses}}$$

Noise resulting from fluctuating shearing stresses

$$+ \frac{1}{4\pi r} \underbrace{\iint \left\{ \left[\frac{\partial p}{\partial n_0} \right] + \frac{[p]}{R} \frac{\partial R}{\partial n_0} + \frac{1}{C} \left[\frac{\partial p}{\partial t} \right] \frac{\partial R}{\partial n_0} \right\} dS_0}_{\text{Noise resulting from the effect of solid boundaries upon the flow}} \quad (\text{II-B9})$$

Noise resulting from the effect of solid boundaries upon the flow

Thus equation (II-B9) represents the acoustic pressure in the far field measured by an observer at r, t due to fluctuating shearing stresses and due to the reactive effect of solid boundaries upon the fluid at r_o, t_o .

The above formulation is derived from Curle, who performed the first theoretical work dealing with sound radiation from rigid boundaries. Based on dimensional arguments Curle had shown, that for surfaces small compared with a wave length, the total dipole acoustic power radiating from a solid surface in a flow was:

$$W = \frac{1}{12\pi\rho C^3} \left[\int_S \frac{\partial p}{\partial t} dS \right]^2 \quad (\text{II-B10})$$

Based on equation (II-B10), quantitative estimates of the output from a fan blade can be made by considering the mechanisms involved and by properly evaluating the integral.

(2) Calculation of Broadband Noise Overall Acoustic Power. In order to evaluate equation (II-B10), Sharland (reference 3) performed dimension arguments which lead to expressions for the total acoustic power for noise generated from blades operating in laminar and turbulent inlet flow. The following paragraphs discuss Sharland's approach and the application of the analysis to engine noise calculations.

(a) Noise from a Blade Operating in Laminar Flow. Implicit in the derivation of equation (II-B10) is the assumption that it is normal pressure fluctuation on the surface which are dominant. The fluctuations due to tangential stresses are assumed to be negligible in comparison to the normal pressure fluctuations. Thus the fluctuating pressure difference can be thought of as a local lift fluctuation per unit area. Writing the pressure distribution in terms of a local lift acting on a two-dimensional section of the blade one has

$$p = 1/2 \rho_o U^2 C_L$$

where U is the local mean velocity parallel to the surface of consideration. Then

$$\frac{\partial p}{\partial t} = 1/2 \rho_o U^2 \frac{\partial C_L}{\partial t}$$

Upon substitution into equation (II-B10) and integrating in the streamwise direction, the expression for the total acoustic power becomes

$$W = \frac{\rho}{48\pi c^3} \int_{\text{span}} C U^4 S_c \left[\frac{\partial C_L}{\partial t} \right]^2 dy \quad (\text{II-B11})$$

where C is the blade chord at spanwise coordinate y , C_L is the fluctuating lift coefficient on the section, S_c is the correlation area for the local instantaneous pressure fluctuation, and U is the relative mean velocity of the blade at y .

The order of magnitude of the source strength was suggested by Lilley. It was suggested that the lift fluctuations are related to time fluctuations in the boundary layer thickness at the blade trailing edge. Thus, it is argued that for typical fan conditions, the fluctuating lift coefficient should be of the order of $R_e^{-1/5}$ - where R_e is the Reynolds number based on the chord. Further the frequency of lift fluctuation of the same order as the vortex shedding frequency, which is approximately $0.2 U/C$. In addition, the correlation area which is governed by the large scale eddies is assumed to be of the order $10^{-1} C/2$. Using these orders of magnitude estimates, equation (II-B11) becomes

$$W = \frac{\rho_0}{120\pi c^3} \int_{\text{span}} C \cdot U^6 R_e^{-0.4} dy \quad (\text{II-B12})$$

(b) Noise from a Blade Operating in Turbulent Flow. For a blade operating in a turbulent flow a convenient form can be obtained by introducing an average lift curve slope, ϕ , such that $C_L = \phi v/U$ (v being the component of turbulent velocity normal to the chord). Then

$$\overline{\left[\frac{\partial C_L}{\partial t} \right]^2} = \frac{\phi^2}{U^2} \overline{\frac{\partial v^2}{\partial t}}$$

Assuming a harmonic form for the turbulent velocity component

$$\overline{\frac{\partial v^2}{\partial t}} = \omega^2 v^2$$

where, ω , is the angular center frequency, and that $S_c \omega^2$ is of the order of U^2 , the acoustic power from equation (II-B11) becomes

$$W = \frac{\rho_o}{48\pi C_o^3} \int_{\text{span}} \phi^2 C U^4 v^2 dy \quad (\text{II-B13})$$

(c) Comparison with Experimental Results. Equations (II-B12) and (II-B13) were developed for an isolated airfoil. For axial flow fan engines there are, B, blades contributing to the overall acoustic power, and the blade span is the extent between the hub and the tip of the rotor. Thus equations (II-B12) and (II-B13) may be written as

$$W = \frac{B \rho_o}{120\pi C_o^3} \int_{\text{Hub}}^{\text{Tip}} C U^6 R_e^{-0.4} dy \quad \text{Laminar Flow}$$

$$W = \frac{B \rho_o}{48\pi C_o^3} \int_{\text{Hub}}^{\text{Tip}} \phi^2 C U^4 v^2 dy \quad \text{Turbulent Flow}$$

The total acoustic power levels calculated from the equations above for a fan with outlet guide vanes are shown in Figure (II-B2). The data/theory comparisons are based on General Electric development vehicle (D/V 1) with the following parameters.

Number of rotor blades	38
Number of inlet guide vanes	80
Chord of rotor blade (tip)	4.05 in.
Chord of vane	1.81 in.
Average tip radius of rotor	17.475 in.
Average tip radius of OGV	16.975 in.
Average hub radius of OGV	10.325 in.
Design tip speed of rotor	1388 fps
Average lift curve slope	0.9 π

The mean velocity relative to the blade at each radial position was taken as the average mean velocity at the leading edge and that is the trailing edge.

The measured and predicted values shown in Figure (II-B2) are in remarkable agreement with each other. The sound power level due to each mechanism is plotted in Figure (II-B3). Vortex shedding from the rotor is seen to be the dominant noise source.

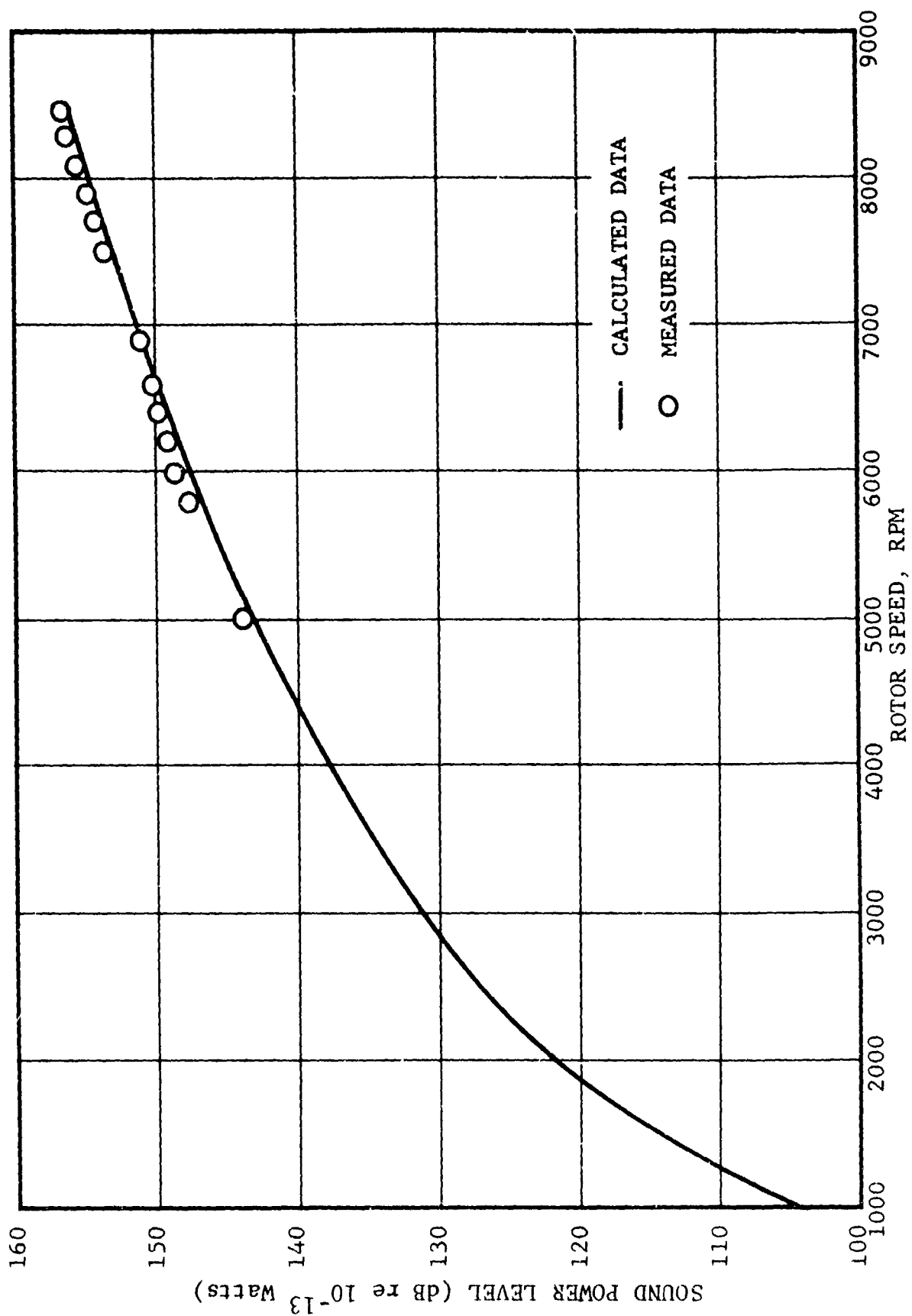


FIGURE II-B2 BROAD BAND NOISE FROM ROTOR-OGV

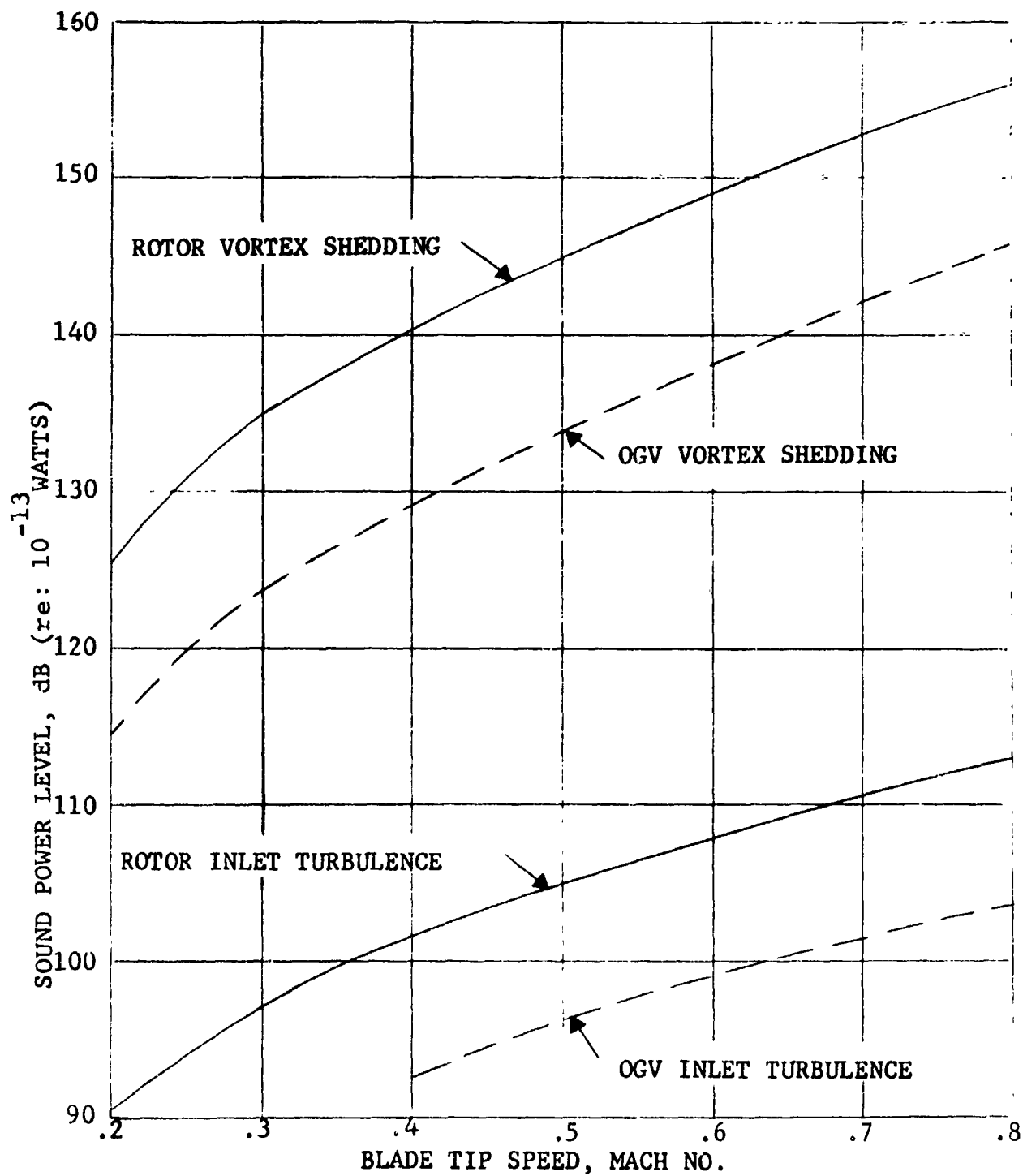


FIGURE II-B3 BROADBAND NOISE MECHANISMS ON A HIGH SPEED FAN

(3) Spectral Distribution of Broadband Noise. The text above illustrated what key aerodynamic parameters affect the overall acoustic sound power and a method for predicting the overall level of noise due to vortex shedding and due to inlet turbulence. The following will describe a method which extends the above analysis to include the predicting spectral distribution of noise, and the influence of aerodynamic parameters.

Hence, consider the integral equation for acoustic pressure given by equation (II-B9)

$$p(\vec{r}, t) = \underbrace{\frac{1}{4\pi r} \iiint_{V_0} \dot{\rho}(\vec{r}_0, t_0) dV_0}_{\text{Noise resulting from fluctuating shearing stresses}} + \underbrace{\iint_{S_0} \left\{ \left[\frac{\partial p}{\partial n} \right]_0 + \frac{[p]}{R} + \frac{1}{c} \left[\frac{\partial p}{\partial t} \right] \right\} dS_0}_{\text{Noise resulting from the effect of solid boundaries upon the flow field}}$$

The first term of the above equation represent Lighthill's classical quadrupole noise term, and thus may be neglected since we are considering dipole contributions alone. In a like vein, by dimensional considerations, the first two terms of the surface integral may be neglected since they represent monopole noise contributions. The resulting equation is then

$$p(\vec{r}, t) = \frac{1}{4\pi rc} \iint_{S_0} \frac{\partial p}{\partial t} dS_0 \quad (\text{II-B14})$$

(a) Fluid Dynamics Related to Dipole Noise. In order to obtain the relationship between the acoustic field and the detailed aerodynamic parameters, one can consider the integral form of the conservation of momentum for flow over an isolated airfoil as shown in Figure (II-B4).

$$\frac{\partial}{\partial t} \iiint_V \rho \vec{u} dV + \iint_S \rho \vec{u} (\vec{u} \cdot \vec{n}) dS = \iint_S \vec{\tau} \cdot \vec{n} dS \quad (\text{II-B15})$$

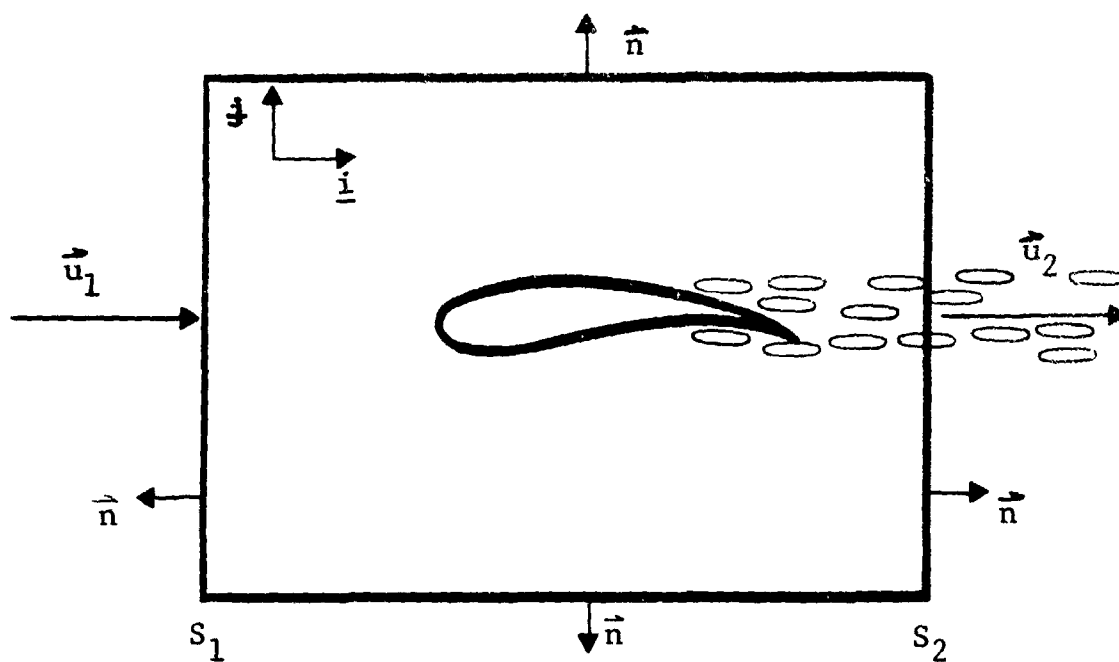


FIGURE II-B4 CONTROL VOLUME FOR FLOW
OVER AN ISOLATED AIRFOIL

where

V Control volume fixed in space

S Surface area of control volume

n Unit outer normal vector

$\bar{\tau}$ Stress Tensor $(-pI + \bar{\tau}')$

or upon expansion of the stress tensor

$$\frac{\partial}{\partial t} \iiint_V \rho \vec{u} \, dV + \iint_S \rho \vec{u} (\vec{u} \cdot \vec{n}) \, dS = - \iint_S p \vec{n} \, dS + \iint_S \bar{\tau} \cdot \vec{n} \, dS \quad (\text{II-B16})$$

Further, by assuming that the transverse components of the fluctuations of mass flux are large compared to the tangential components, equation (II-B16) may be written as

$$\begin{aligned} \frac{\partial}{\partial t} \iiint_V \rho \vec{u} \cdot \vec{j} \, dV + \iint_{S_1} \rho_1 \vec{u}_1 \cdot (-1) \vec{u}_0 \cdot \vec{j} \, d_1 S_1 + \iint_{S_2} \rho_2 \vec{u}_2 \cdot \vec{j} \, (U_2 + u_2') \, dS_2 \\ = - \iint_S p \vec{n} \cdot \vec{j} \, dS + \iint_S (\bar{\tau}' \cdot \vec{n}) \cdot \vec{j} \, dS \end{aligned}$$

where

$$\vec{u}_1 = U_0 \vec{i}$$

$$\vec{u}_2 = (U_2 + u_2') \vec{i} + v_2' \vec{j}$$

Therefore, performing the indicated vector operations yields

$$\begin{aligned} \frac{\partial}{\partial t} \iiint_{Vol} \rho v' dV + \iint_{S_2} \rho_2 v'_2 (U_2 + u'_2) dS_2 = \\ \iint_{Airfoil} p dS' + \iint_S (\bar{\tau}' \cdot \hat{n}) \cdot \hat{j} \cdot dS \end{aligned} \quad (II-B17)$$

Hence

$$\begin{aligned} \iint_{Airfoil} p dS = \frac{\partial}{\partial t} \iiint_{Vol} \rho v' dV + \iint_{S_2} \rho_2 v'_2 (U_2 + u'_2) \\ dS_2 - \iint_S (\bar{\tau}' \cdot \hat{n}) \cdot \hat{j} dS \end{aligned}$$

Differentiating with respect to time, a form is obtained which is directly applicable to equation (II-B14) i.e.

$$\begin{aligned} \frac{\partial}{\partial t} \iint_{Airfoil} p dS = \underbrace{\frac{\partial^2}{\partial t^2} \left(\iiint_{Vol} \rho v' dV \right)}_{\text{Dipole noise due to fluctuations of mass flux within the control volume}} + \underbrace{\frac{\partial}{\partial t} \iint_{S_2} \rho_2 v'_2 (U_2 + u'_2) dS_2}_{\text{Dipole noise due to fluctuation of momentum flux through the wake surface area } S_2} - \underbrace{\frac{\partial}{\partial t} \iint_S (\bar{\tau}' \cdot \hat{n}) \cdot \hat{j} dS}_{\text{Dipole noise due to fluctuation of viscous stresses}} \end{aligned}$$

Hence

$$p(\vec{r}, t) = \frac{1}{4\pi rc} \frac{\partial}{\partial t^2} \iiint_V \rho v' dV + \frac{\partial}{\partial t} \iint_{S_2} \rho_2 v'_2 (U + u'_2) dS_2 - \frac{\partial}{\partial t} \iint_S$$

$$(\vec{\tau}' \cdot \vec{n}) \cdot \frac{1}{c} dS \quad (\text{II-B18})$$

Equation (II-B18) represents the dipole noise resulting from the effect of solid boundaries upon the flow. The dipole noise thus represented is due to three phenomenon. The first dipole source is due to volumetric contributions to fluctuations of mass flux, the second dipole source is due to the fluctuations of transverse momentum flux through the surface area of the wake, the third term is dipole noise due to fluctuation in the transverse components of shear stress. In what follows, the assumption will be made that the shear stress fluctuations are negligible in comparison to the volume contributions, and fluctuations of momentum flux.

(b) Volume Contributions to Dipole Noise. The total radiated energy in the free field for the volume contributions of dipole noise is, for a surface whose dimensions are considered small in comparison with wave length.

$$W = \frac{4}{3} \pi \frac{r^2}{\rho_0 c_0} \left(\frac{1}{4\pi r c_0} \right)^2 \iint_{VV'} \overline{\frac{\partial^2}{\partial t^2} (\rho v') \cdot \frac{\partial^2 (\rho v')}{\partial t^2}} dV dV' \quad (\text{II-B19})$$

Thus a correlation volume may be defined as

$$\left[\overline{\frac{\partial^2}{\partial t^2} (\rho v')} \right]^2 \cdot V_c = \int_{V'} \left[\frac{\partial^2}{\partial t^2} (\rho v') \right]^2 dV'$$

Therefore:

$$W \sim \frac{1}{12\pi\rho_o C_o^3} V_c \int_{\text{Wake Vol}} \left[\frac{\partial^2}{\partial t^2} (\rho v') \right]^2 dV'$$

or neglecting second order effects

$$W \sim \frac{1}{12\pi\rho_o C_o^3} V_c V_w \overline{\left[\rho \frac{\partial^2 v'}{\partial t^2} + 2 \frac{\partial \rho}{\partial t} \frac{\partial v'}{\partial t} + v' \frac{\partial^2 \rho}{\partial t^2} \right]}^2 \quad (\text{II-B20})$$

where

$V_c \equiv$ Correlation Volume

$V_w \equiv$ Wake Volume

Further consider that it is the first term which reflects the character of the entire term in the brackets, then equation (II-B20) reduces to

$$W(\vec{r}, t) \sim \frac{1}{12\pi\rho_o C_o^3} V_c \left[\rho \frac{\partial^2 v'}{\partial t^2} \right]^2 V_w$$

or using the isentropic flow relations

$$W \sim \left(\frac{V_c V_w}{12\pi} \right) (\rho_o/a_o) \frac{M^2}{\left[1 + \frac{\gamma-1}{2} M^2 \right]^{\frac{\gamma+1}{\gamma-1}}} \left[\frac{\partial^2}{\partial t^2} (v'/U) \right]^2 \quad (\text{II-B21})$$

where M is the local Mach number in the wake region, U is the local mean axial speed in the wake, v' is the local turbulent transverse velocity component and γ is the ratio of specific heats.

The spectral distribution of acoustic power may be found by taking the Fourier Transform of equation (II-B21) yielding

$$W(f) \sim (\rho_o/a_o) \left(\frac{V_c V_w}{12\pi} \right) \frac{M^2}{\left[1 + \frac{\gamma-1}{2} M^2 \right]^{\frac{\gamma+1}{\gamma-1}}} f^4 [v'/U(f)]^2 \quad (\text{II-B22})$$

By assuming that the correlation volume, V_c , is proportional to a characteristic dimension of the wake, to the third power, namely the wake thickness, and that the wake volume V_w , is proportional to $Xb\Delta y$, where X is a reference longitudinal dimension, b the blade span, and Δy the wake thickness, equation (II-B22) may be written as

$$W(f) \sim (\rho_o/a_o) \frac{1}{12\pi} \frac{M^2}{\left\{1 + \frac{\partial-1}{2} M^2\right\}^{\frac{\gamma+1}{\gamma-1}}} Xb(\Delta y)^4 f^4 [v'/U(f)]^2 \quad (\text{II-B23})$$

Thus, equation (II-B23) represents the spectral energy distribution due to the volume contributions of the fluctuations of mass flux. Further the spectral distribution is seen to be proportional to the fourth power of wake thickness, the fourth power of frequency, the second power of the transverse component of turbulent intensity and local wake Mach number, and linearly proportional to the blade span.

(c) Surface Contributions to Dipole Noise. If one considers the form of the spectral distribution of acoustic power due to the surface contributions represented by the second integral of equation (II-B18), one can use for this limiting case the equation for acoustic pressure

$$p(\vec{r}, t) = \frac{1}{4\pi rc} \iint_{S_2} U_2 \frac{\partial}{\partial t} (\rho_2 v_2') dS_2 \quad (\text{II-324})$$

There exists a correlation area S_c , such that equation (II-B24) may be written as

$$p(\vec{r}, t) \sim \frac{1}{4\pi rc} S_c U_2 \frac{\partial}{\partial t} (\rho_2 v_2') A_w \quad (\text{II-B25})$$

Using the expression for the acoustic power for a dipole, the isentropic flow relations, and the Fourier transform of the resulting dipole power expression yields the following spectral distribution of acoustic energy due to surface contributions for wake noise.

$$W(f) = \frac{\rho c}{12\pi} (S_C A_w) \frac{M_2^4}{\left(1 + \frac{\gamma-1}{2} M_2^2\right)^{\frac{2\gamma}{\gamma-1}}} f^2 \left(\frac{v_2'}{U_2}(f)\right)^2 \quad (\text{II-B26})$$

By assuming that the correlation area, S_C is proportional to the wake thickness squared y^2 , and that the wake area, A_w is proportional to the span times the wake thickness ($b\Delta y$) equation (II-B26) becomes

$$W(f) = \frac{\rho c C_o}{12\pi} \frac{\Delta y^3 b}{\left[1 + \frac{\gamma-1}{2} M_2^2\right]^{\frac{2\gamma}{\gamma-1}}} \left(M_2^4 f^2\right) \left(\frac{v_2'}{U_2}(f)\right)^2 \quad (\text{II-B27})$$

Here it is seen that the spectral acoustic power distribution is proportional to wake thickness cubed, Δy^3 , local Mach number to the fourth, M_2^4 , frequency squared, f^2 , and the square of the transverse turbulent velocity component in the wake.

It can be shown that the acoustic energy intensity and acoustic power for a generalized dipole noise source varies as f^4 , i.e., for the acoustic power π

$$\pi \sim 4/3 (\pi/c)^3 f^4 \rho D_w$$

where D_w is the strength of the dipole. Hence the formulation presented for volume contributions to dipole noise is seen to check with the frequency to the fourth power law for a radiating transverse dipole.

It can be seen from the above that the airfoil broadband noise generation is directly linked to the velocity fluctuations around the airfoil. The limited knowledge of airfoil wake characteristics is however very restricted. A tunnel test program was therefore undertaken to permit a better understanding of unsteady aerodynamic phenomena around airfoils and subsequently broadband noise. The program is described in the next section of the report.

NOMENCLATURE SECTION II-B

b	blade span
c	speed of sound
C	blade chord
C_L	local two-dimensional lift coefficient
f	frequency
$G(\vec{r}, t / \vec{r}_0, t_0)$	Green's Function
\bar{I}	unity tensor
\hat{i}, \hat{j}	unit vectors in longitudinal and transverse directions
M	local Mach number
\hat{n}	unit outer normal vector
p	pressure
\vec{r}	radial vector from origin of coordinate system to point of observation (see Figure II-B1)
R	position vector from source location to observer (See Figure II-B1)
R_e	Reynold's number based on chord length
S	surface area
t	time
U	local longitudinal mean velocity component in the wake
\vec{u}	vector velocity
u	longitudinal turbulent velocity component
V	volume
v, v'	transverse turbulent velocity component
W	acoustic power
X	longitudinal distance from airfoil

γ	ratio of specific heats
Δ	increment of distance
δ	Dirac delta function
λ	second viscosity coefficient
μ	first viscosity coefficient
π	acoustic power
ρ	density
$\tilde{\rho}$	acoustic source function
$\overline{\tau}$	stress tensor
$\overline{\tau}'$	viscous stress tensor
ϕ	average lift curve slope
ω	angular frequency

SUBSCRIPTS

0	Ambient conditions, reference to source coordinate system (See Figure II-B1)
1	Station one (See Figure II-B4)
2	Station two in wake region (See Figure II-B4)

REFERENCES SECTION II-B

1. Lighthill, M.J. Proc. Roy. Soc. A211 (1952), A222 (1954).
2. Morse, P.M., Feshback, H., Methods of Theoretical Physics, Part I, McGraw Hill Book Company, Chapter 6, 1953.
3. Sharland, I.J., J. Sound Vib. 1, 302 (1964).

(C) Experimental Investigation of Vortex Shedding Noise in Subsonic and Transonic Wind Tunnels. Experiments were conducted to gain knowledge of the broadband noise generating mechanisms. Attention was focused on vortex shedding noise which was determined (see Figure II-B3) to be the major broadband noise contributor. Basic experiments were conducted in subsonic and transonic wind tunnels to investigate vortex shedding from simple geometric objects such as cylinders and isolated airfoils. Data was also obtained on loaded airfoils in two dimensional cascades. Hot film anemometers were used to determine aerodynamic properties. Attempts were made to correlate, wherever possible, the velocity fluctuations with the generated noise.

(1) Test Facilities.

(a) Subsonic Wind Tunnel. The subsonic wind tunnel is shown in Figures II-C1 and II-C2. The tunnel consists of a rectangular, acoustically treated muffler and a test section bolted on to a 29.5 inch circular plenum chamber. Interior dimensions of the muffler are: 47.5 x 4 x 16 inches and of the test section 21 x 4 x 16 inches. (Dimensions are given as: length, width and height respectively).

The plenum chamber, acting as a settling reservoir, was provided with four stainless steel screens; one of which was a heavy gauge screen with about 50% open area. The three others contained fine 20 mesh screening. The muffler was incorporated in the system to eliminate upstream piping noise. The acoustic treatment linings on two sidewalls of the muffler section consisted of 1 inch thick Scottfelt, located between the muffler wall and a stainless steel perforated plate (22% open area, 0.03 inches thick). Before the flow enters the test section it meets two contraction blocks which form a bellmouth inlet to the test section. The air is exhausted to atmospheric conditions. The exhaust cross sectional area was larger than the cross sectional area of the test section (5/1 expansion area) so that the exhausted air could expand.

(b) Transonic Wind Tunnel. A cross section of the transonic wind tunnel facility is shown in Figure II-C3. Inside the tank a cascade, placed between two Plexiglas sidewalls, was mounted in a moveable drum. This drum can rotate in relation to the oncoming flow, thereby varying the inlet air angle to the cascade. The tunnel was equipped with instrumentation to obtain aerodynamic and turbulence data. Upstream and downstream pressure and hot film traverses were executed using actuators. The actuators are remotely controlled, and are movable in all directions. Noise data was recorded on a microphone located 6 feet away from the cascade inside the wind tunnel.

A bloc' diagram of the piping system for the transonic wind tunnel is shown in Figure II-C4. The test section of the wind tunnel is at the end of the pipe entering the test tank. Atmospheric air enters the system at (A) and can be routed through the air dryer or sent directly to the test tank. This inlet air then passes through a plenum chamber and a bellmouth before entering the test section. After exhausting into the tank the air is drawn out the bottom of the tank through valve (C) to the inlet of the compressor. Valve (C) regulates the flow velocity by controlling the back pressure in the tank. From the discharge of the compressor most of the air is exhausted to the atmosphere but a portion of it is recirculated through the system by valve (B).

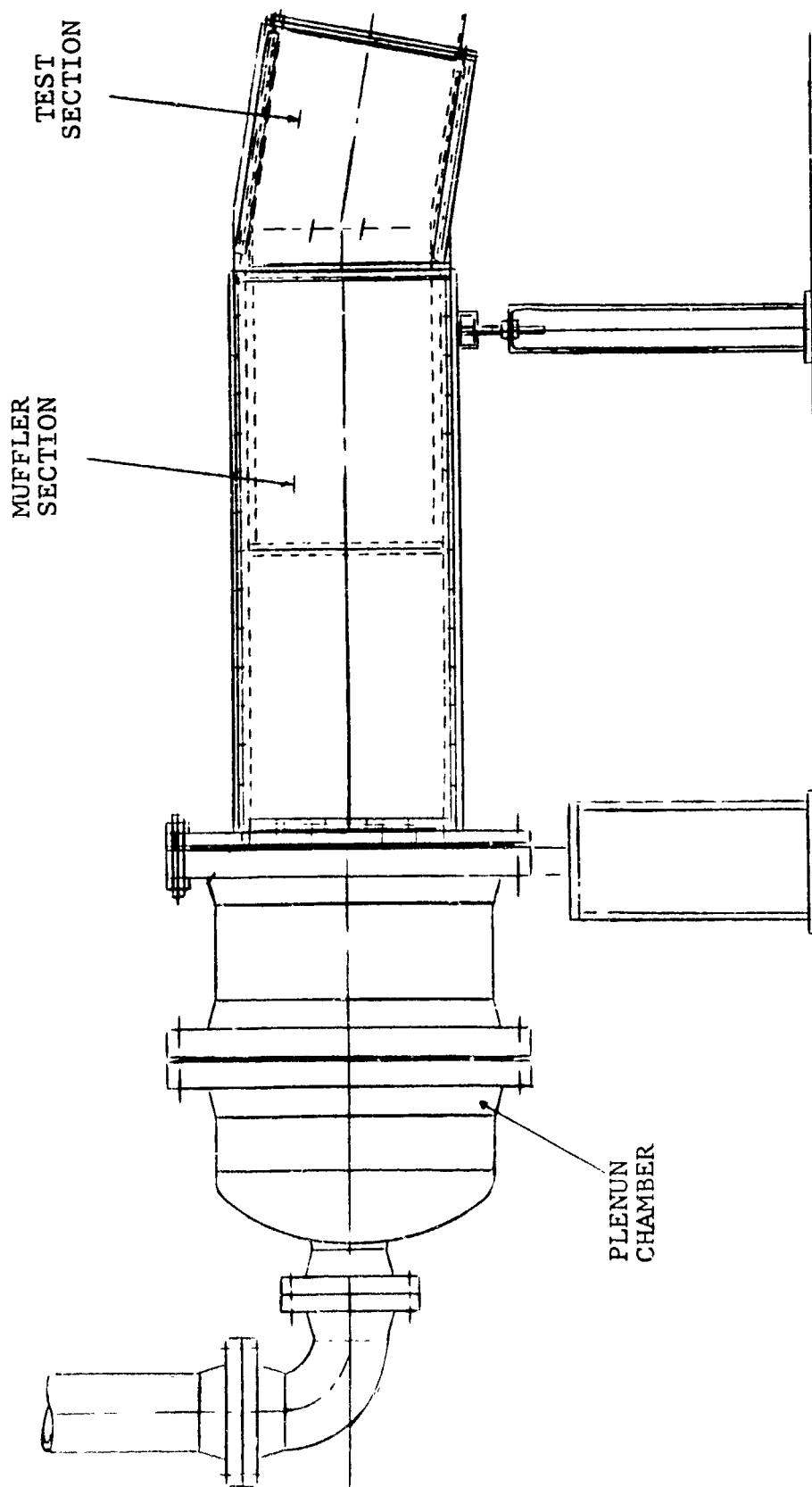


FIGURE II-C1. MAJOR COMPONENTS OF THE SUBSONIC WIND TUNNEL

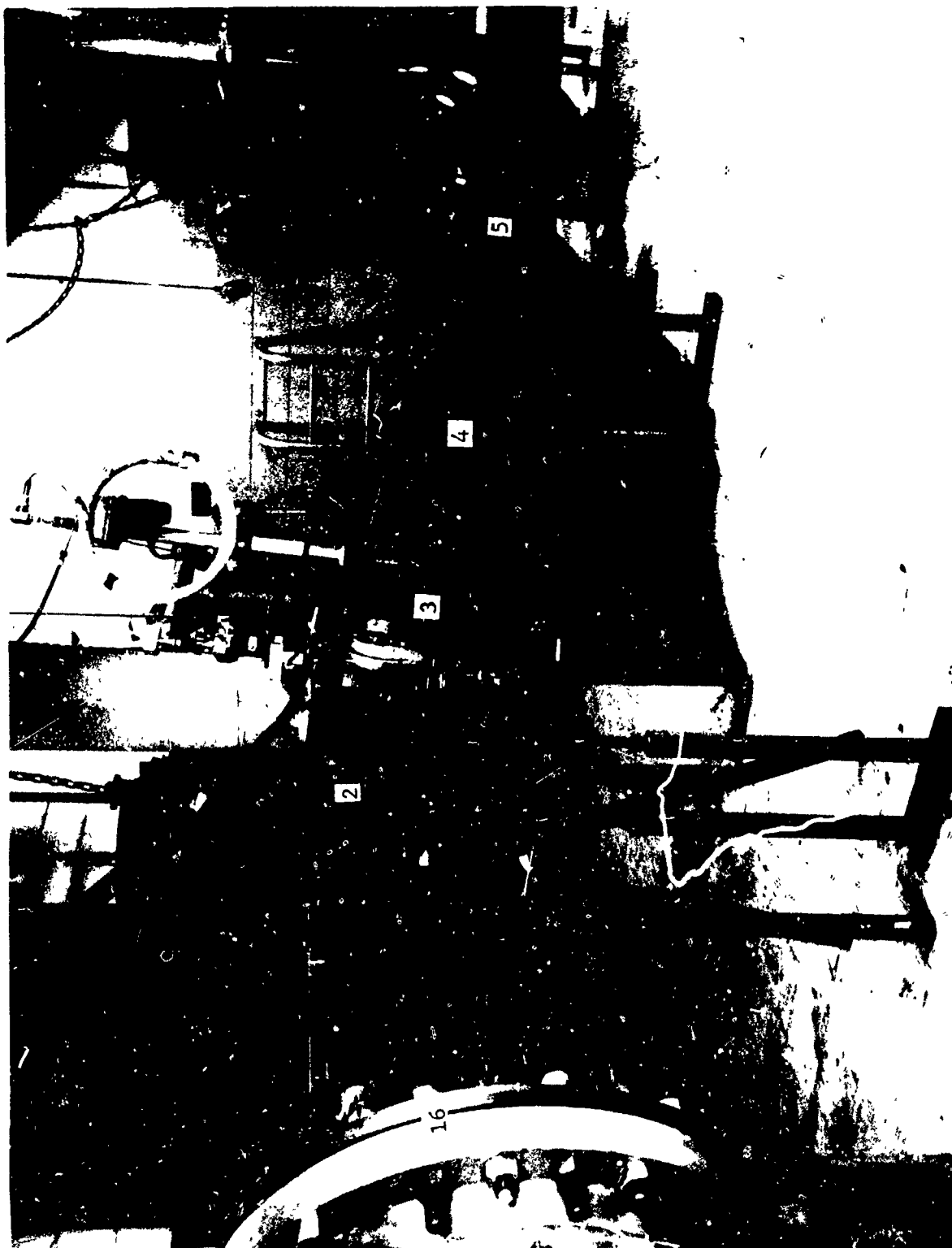


FIGURE II-C2 PHOTOGRAPH OF THE SUBSONIC WIND TUNNEL

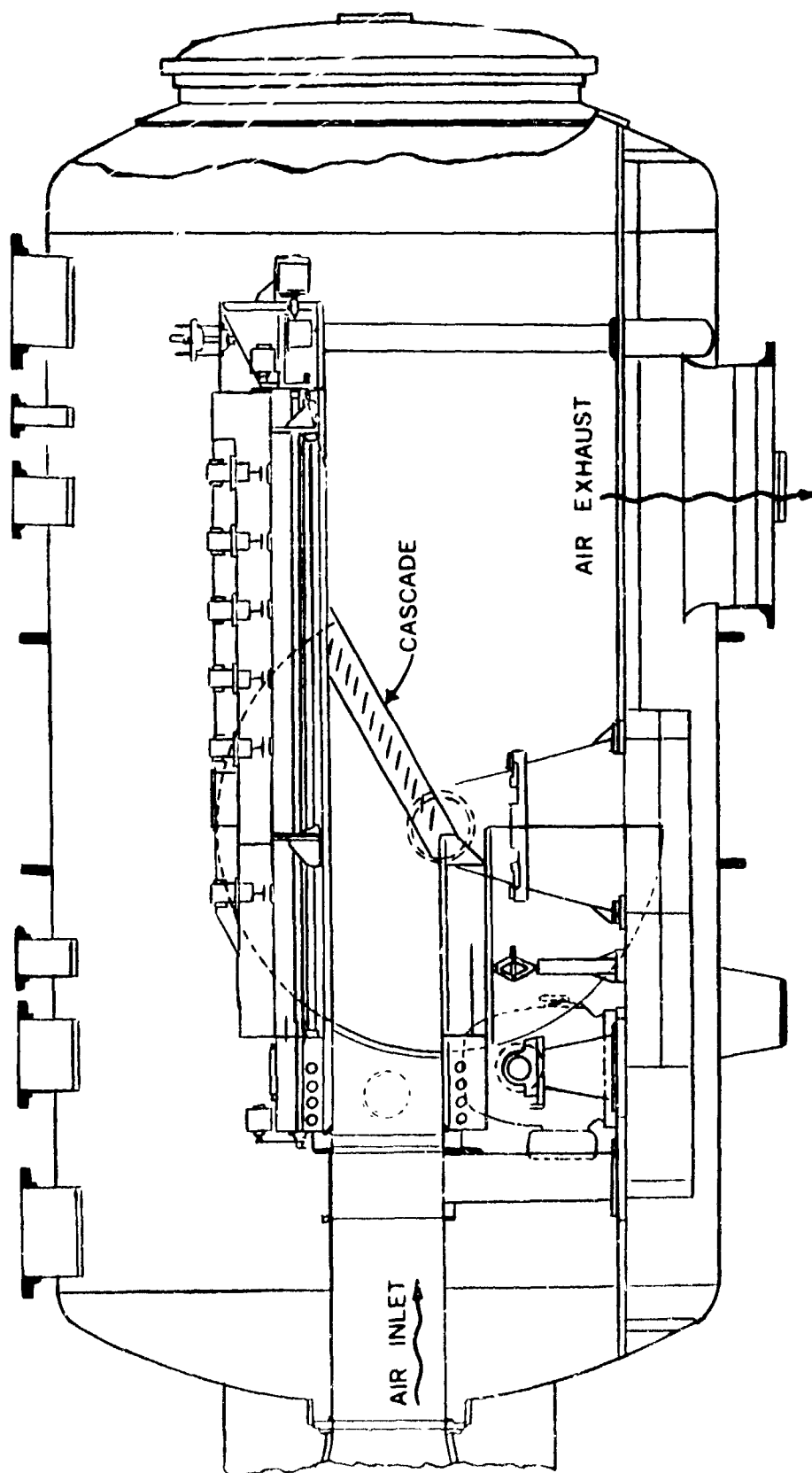


FIGURE 11-C3. CROSS-SECTION OF TRANSONIC CASCADE TUNNEL.

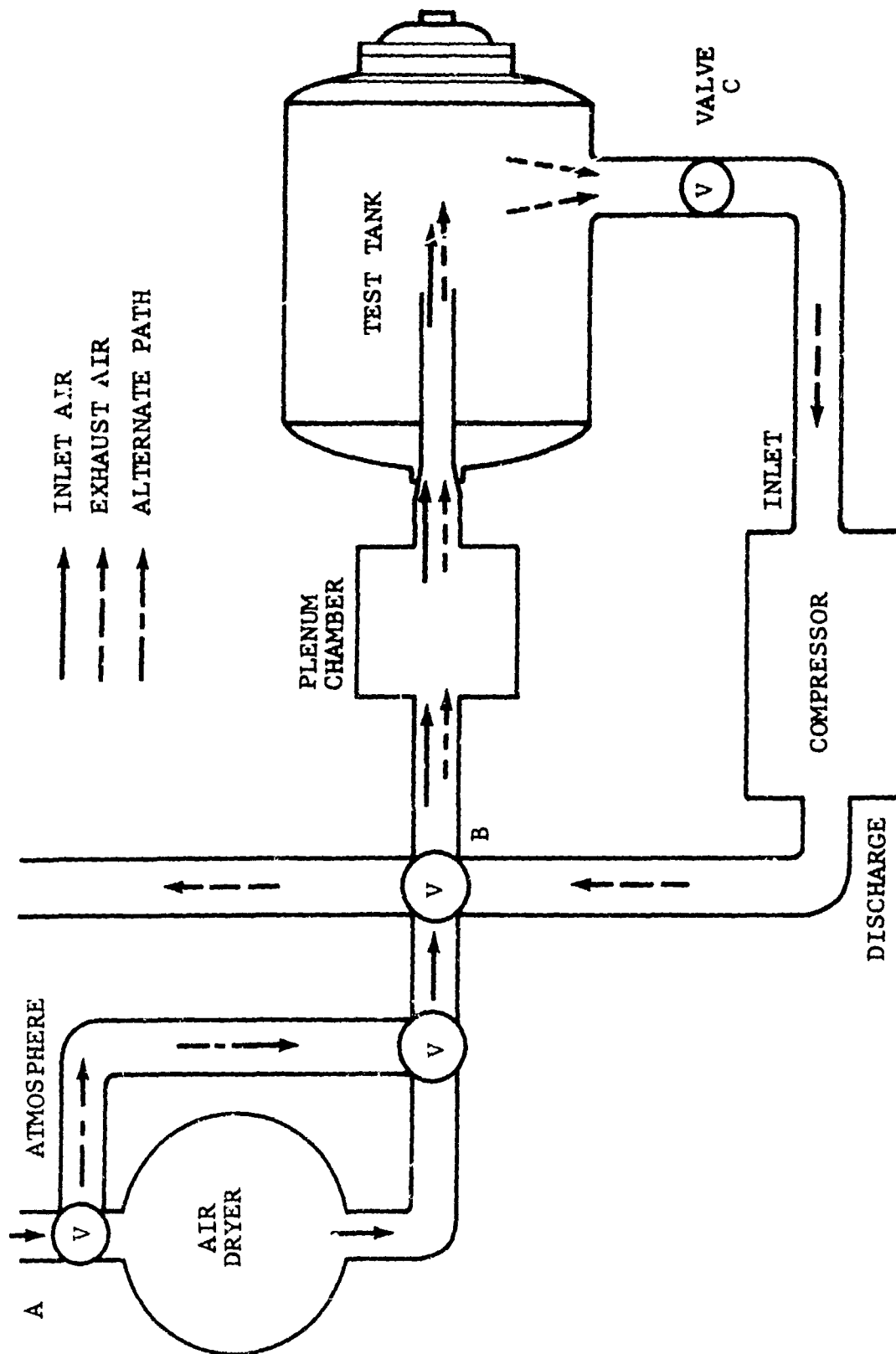


FIGURE II-C4. BLOCK DIAGRAM OF THE TRANSONIC WIND TUNNEL

Velocities in the tunnel are set by using a mechanical pressure gauge to record plenum chamber total pressure and static pressure upstream of the test section and forming the ratio P_s/P_o where P_s is static pressure and P_o is total pressure. Manometer banks filled with TBE manometer fluid are provided to measure an upstream and downstream pressure.

(2) Instrumentation.

(a) Hot Film Anemometers - Velocity Measurements. It is advantageous to obtain velocity data by hot film probes since the compactness of such probes minimizes the disturbance to the flow and also because of the fast response time of the probe to flow changes. The hot film sensors are an improved version of the hot wire in that they are more rigidly constructed. The hot film sensor consists of a thin film of metal deposited onto a ceramic substrate held by needle shaped supports which in turn are attached to the stem of the probe. An X-array of sensors and probe assembly is shown in Figure II-C5. Sensors, probes and associated instrumentation were purchased from Thermo Systems, Inc.

In operation, each sensor is part of a Wheatstone bridge. The sensors are kept at constant temperature by the anemometers, shown in the block diagram of Figure II-C6. The equipment used is shown on Figure II-C7. They instantaneously measure fluid flow parameters, by sensing the heat transfer rate between the electrically heated sensor and the flow. When the flow velocity changes, compensation is provided to maintain a constant temperature difference. Since the resistances in the Wheatstone bridge are kept constant, through a feedback control in the circuitry, the voltage across the bridge is directly proportional to the current, I , through the sensor and the power, P , is equal to the product of the square of the current and the resistance, R ($P = I^2 R$). Therefore, the square of the voltage, measured on top of the bridge is directly proportional to the instantaneous heat transfer between the sensor and its environment. This heat transfer is proportional to the fluid velocity.

The output of the sensor amplified by the bridge is not linear with flow velocity changes; therefore, a linearizer was incorporated in the system (See Figure II-C6 and II-C7) for convenience. An example of a linearized calibration curve for an X-array sensor is shown in Figure II-C8. To obtain calibration of sensors and flow parameters a correlator was used. This device is able to perform additions and subtractions or alternatively present the output of the sensors to a DC Voltmeter and a set of four "true root mean square" voltmeters (TRMS). These voltmeters display mean, mean square, and RMS values of the sensor outputs. The voltmeters were altered to merge with a Honeywell digitizing system. This system consists of a multipoint analog scanner which sequentially scans the outputs of the various voltmeters. These outputs are then sequentially processed, displayed on the digital voltmeter, converted to digital form and fed to the teletype. It was convenient to do so, since the teletype provided a printed copy of the data and a punched paper tape.

(b) Condenser Microphone - Sound Measurements. Sound measurements were obtained during testing in the cascade using a 1/4 inch Bruel and Kjaer (B&K) condenser microphone. The microphone was located 6 feet away from the exit measuring station in the cascade tunnel. Long extension cables made it necessary to use a power supply (B&K 2801) in conjunction with the microphone (See Figure

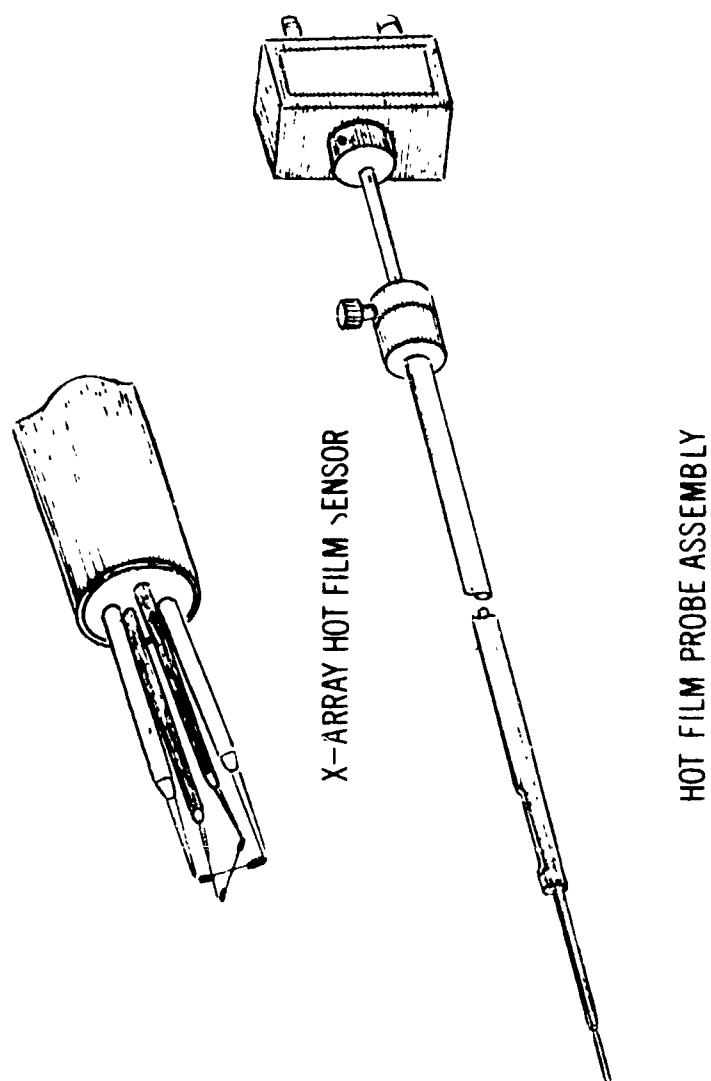


FIGURE II-C5. VELOCITY SENSITIVE HOT FILM PROBE.

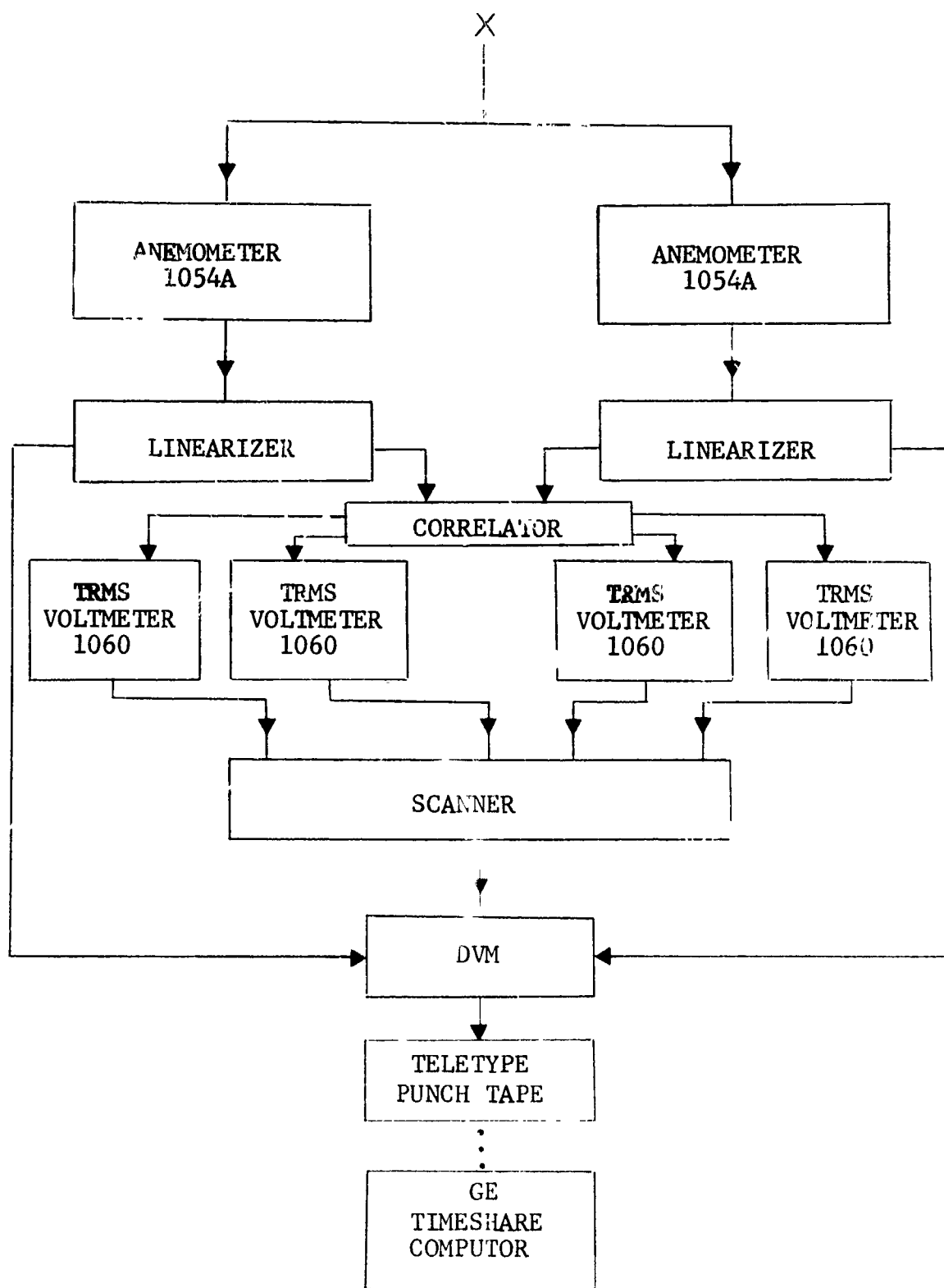


FIGURE II-C6. BLOCK DIAGRAM OF THE HOT FILM INSTRUMENTATION.

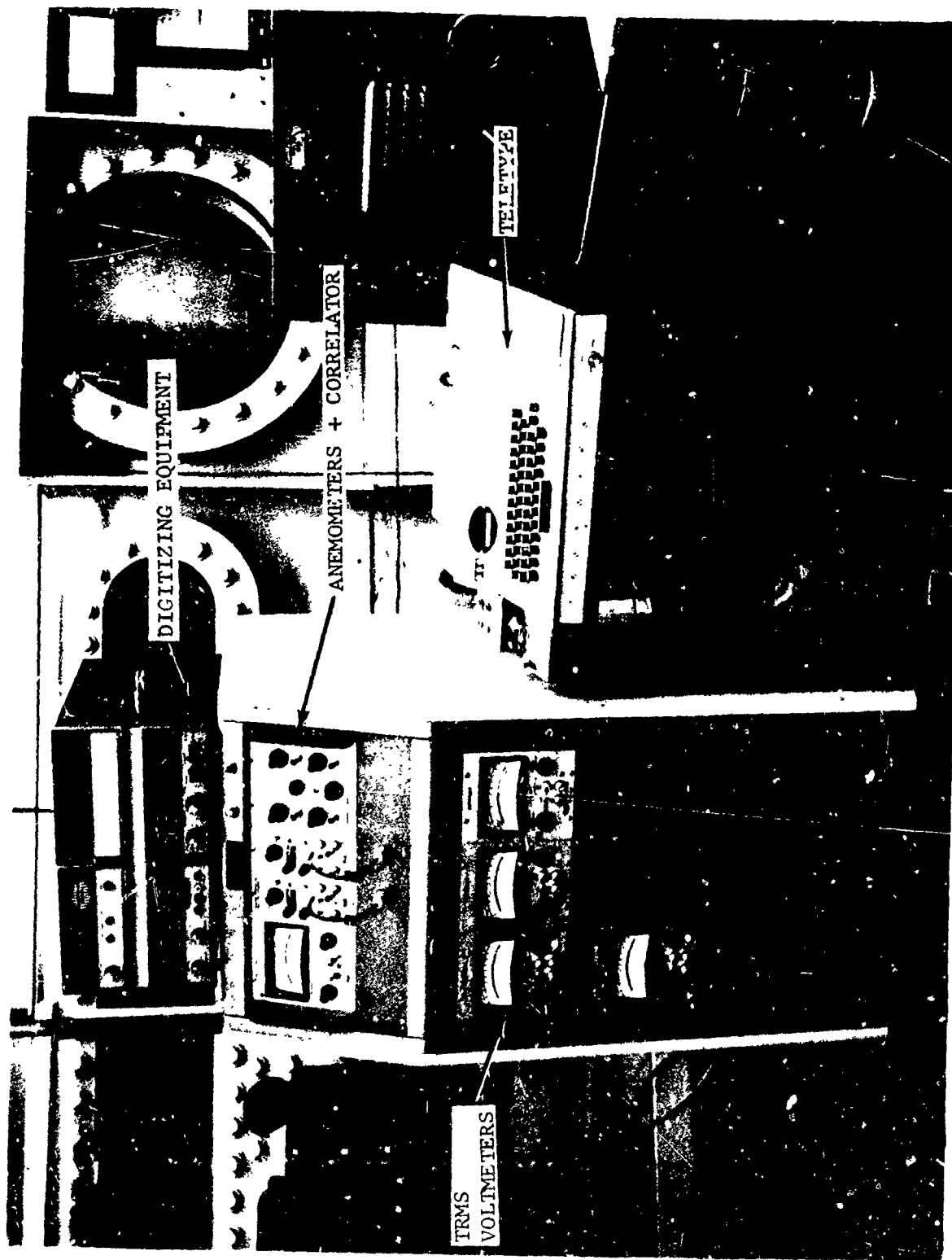


FIGURE II-C7 PHOTOGRAPH OF THE HOT FILM INSTRUMENTATION

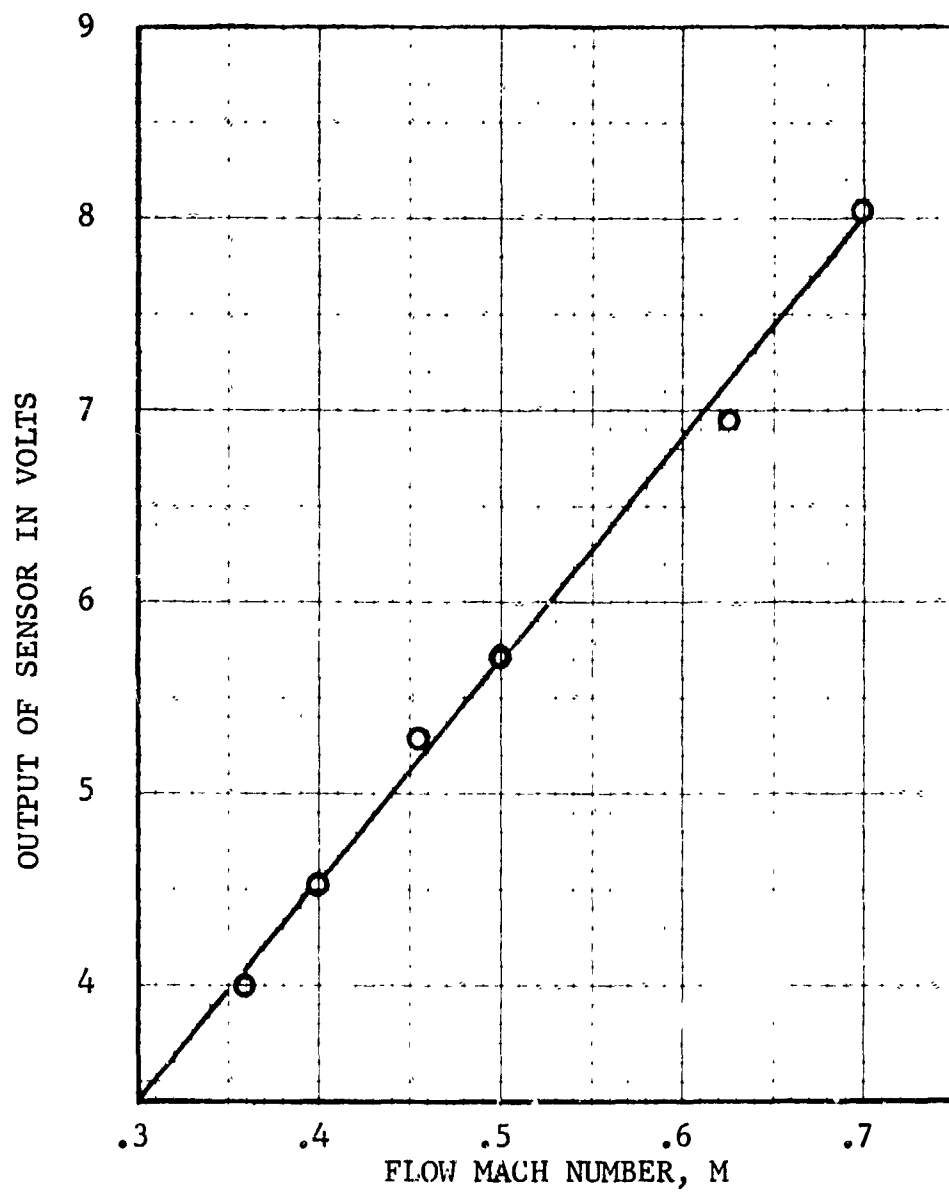


FIGURE II-C8. CALIBRATION CURVE: OUTPUT OF SENSOR VS. FLOW MACH NUMBER

II-C9). This apparatus supplied ample voltage to the microphone's cathode follower and also provided the necessary polarization voltage to the condenser microphone. Calibration of the microphone was accomplished by temporarily attaching a B&K Pistonphone (Type 4220) to the microphone. The sound pressure level of this source was 124 dB within ± 0.2 dB.

The output signal of the microphone was connected to a B&K Wave Analyzer (Type 2107). This analyzer utilizes a 6% constant percentage bandwidth. It performed on line to produce narrowband analysis of the noise. A built-in mechanical device (combination of gears) provided automatic turning when coupled to the motor of the B&K level Recorder (Type 2305). Combined in this manner, frequency amplitude diagrams of the sound spectrum were obtained. An alternate routing was made using a Lockheed 411B, 4 channel AM Tape Recorder which preserved the noise signal for off line narrowband analysis.

(3) Subsonic Wind Tunnel Tests. The inlet turbulence and the inlet velocity profile were checked at $M = 0.4$ using a hot film traverse. The traverse originated at the center of the duct, represented by $Y = 0$, and ended near the top wall, indicated by $Y = 8$. Data reduction of the hot film output yielded turbulence intensity in the axial flow direction (u'/\bar{U}) and the mean velocity \bar{U} for each probe position. Figure II-C10 shows the mean velocity profile for the air flowing through the duct. The shape of the mean velocity profile was flat except at $Y = 5$ inches where the mean velocity decreased due to the influence of the solid boundary (top wall). As can be seen in Figure II-C11 the turbulence intensity u'/\bar{U} in the center of the duct is less than 4%. About one inch away from the top wall the $u'/\bar{U} = 7.7\%$.

(a) Cylinder Wake Investigation. The wake of a one-inch cylinder was explored by means of the hot film anemometers, described in Section II-C2a. Turbulence intensity measurements were made for upstream and downstream stations relative to the cylinder with flow Mach numbers 0.1, 0.2 and 0.3.

Figure II-C12 depicts the test section in which the cylinder was mounted. Figure II-C13 shows the turbulence intensity u'/\bar{U} on the wake axis of the cylinder as a function of downstream distance for various Reynolds numbers. As expected, the turbulence intensity decreased for increasing downstream distances. The turbulence intensity increased for increasing flow Mach number. While Figure II-C13 indicates the turbulence intensity normalized to the local mean velocity (\bar{U}); Figure II-C14 shows the turbulence intensity normalized to the undisturbed (i.e., upstream) mean velocity (\bar{U}_0) of the flow versus downstream positions. The results were compared to experiments of Kovasnay (Reference 1) and show that there is a point on the wake axis of the cylinder where the turbulence intensity peaks. results indicate this point to be 5 diameters downstream of the cylinder while lower Reynold's number experiments put it at 7.

Figure II-C15 shows the turbulence intensities in the flow direction (u'/\bar{U}) two inches upstream of the cylinder for several positions in the duct and for three flow Mach numbers. The turbulence intensity is less than 5% in the center of the duct and is shown to increase rapidly when approaching the duct walls.

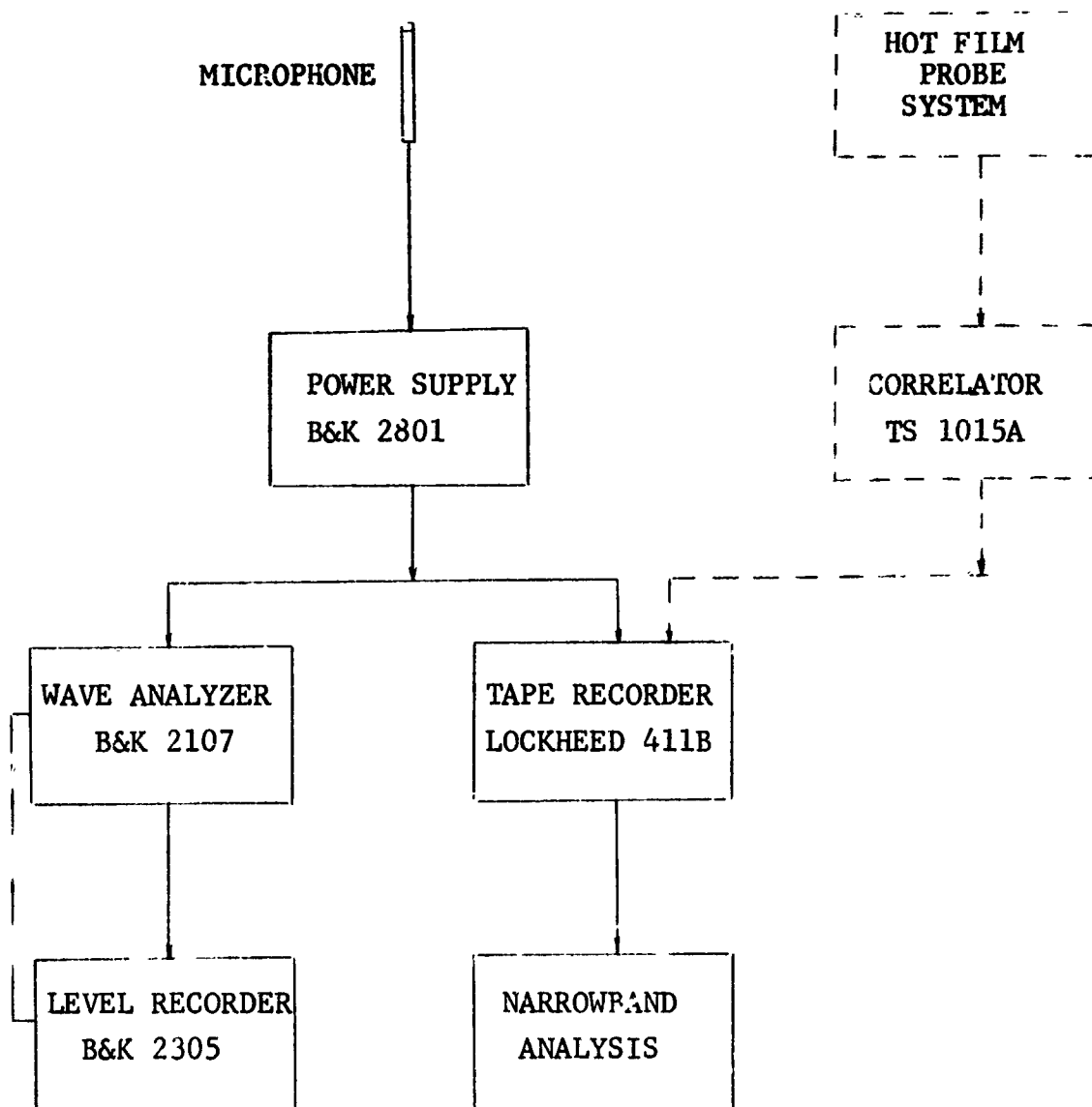


FIGURE II-C9. DATA ACQUISITION BLOCK DIAGRAM.

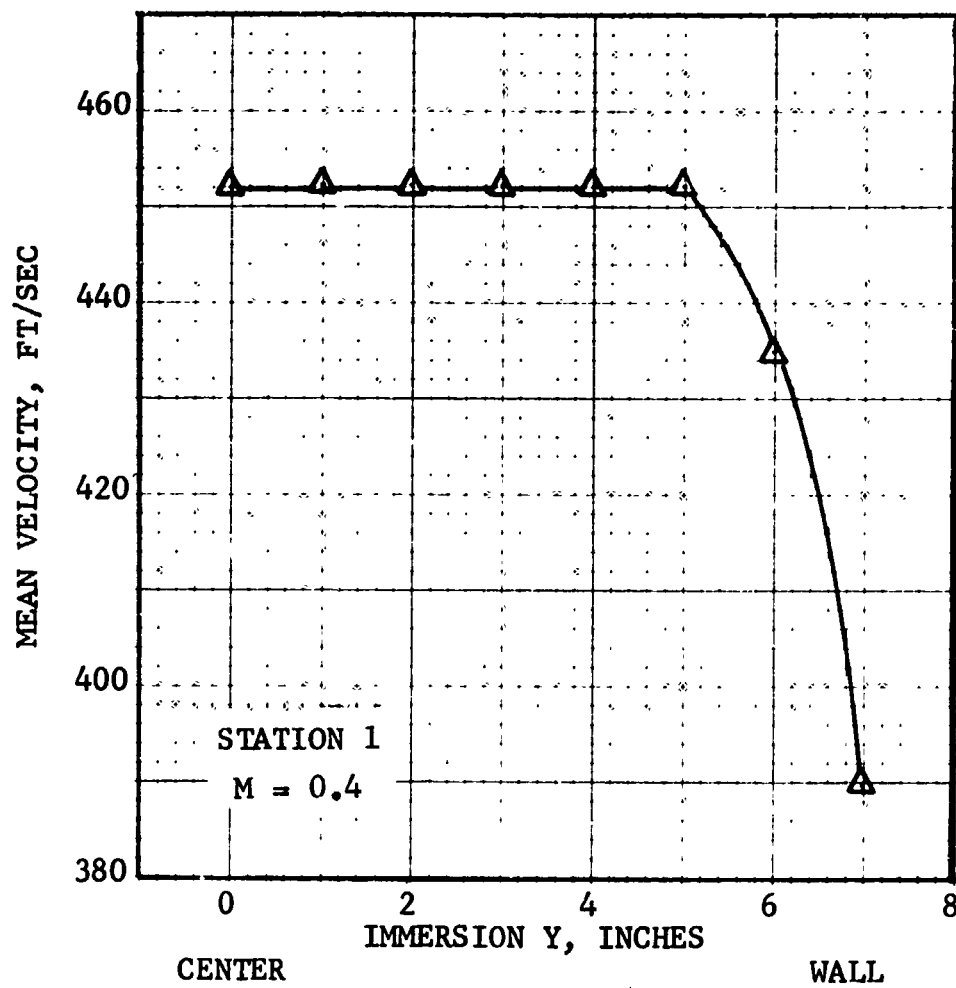


FIGURE II-C10. MEAN VELOCITY PROFILE OF THE SUBSONIC WIND TUNNEL.

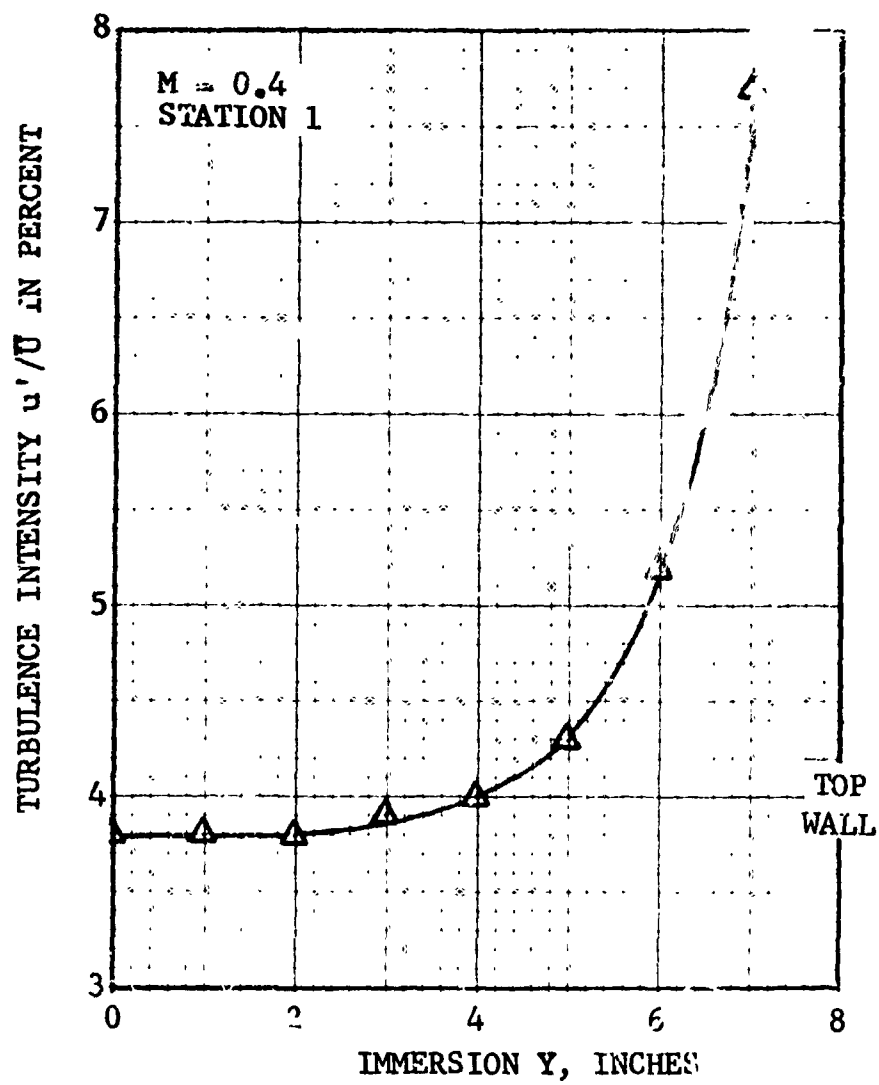


FIGURE II-C11. INLET TURBULENCE OF THE SUBSONIC WIND TUNNEL.

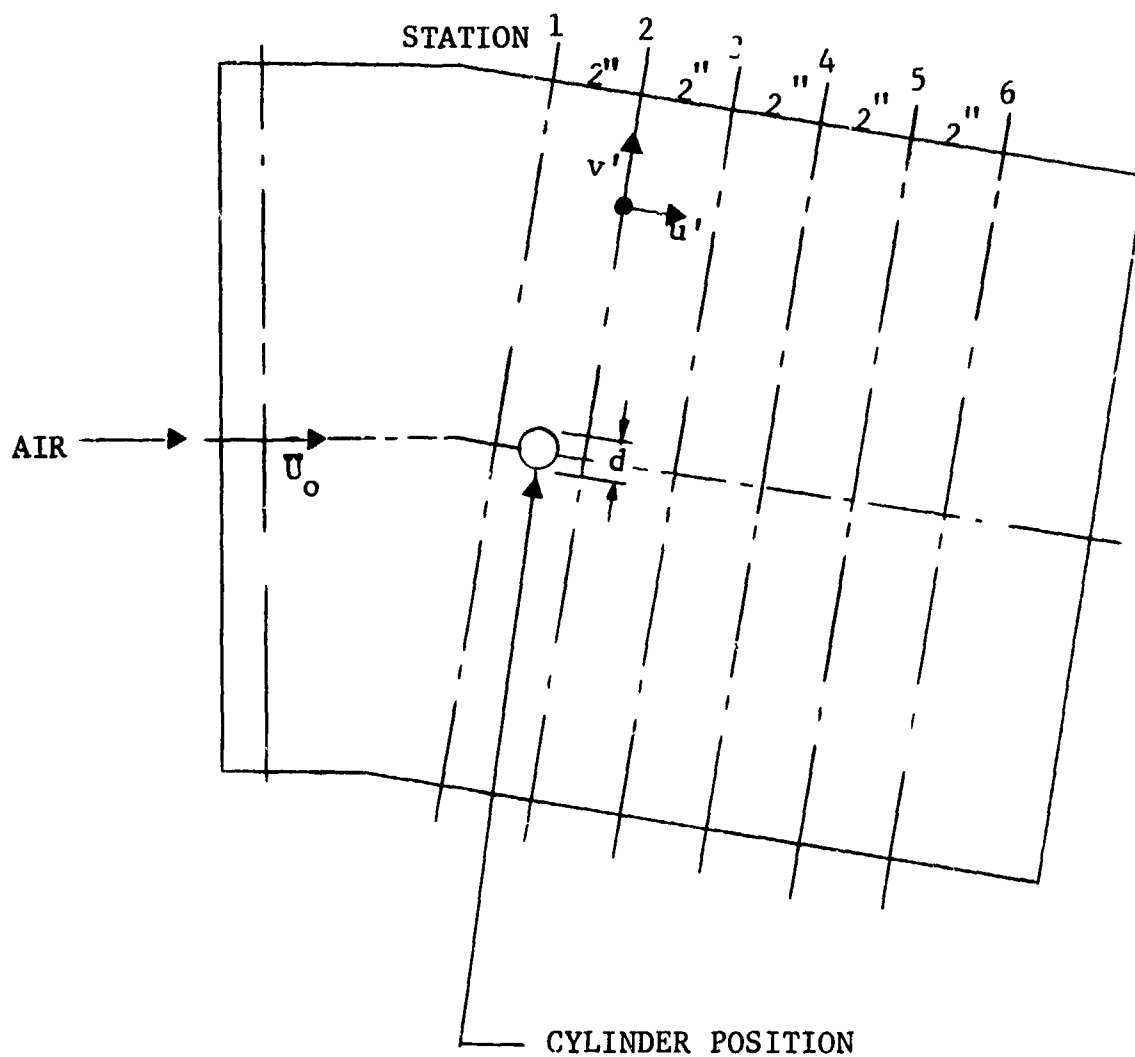


FIGURE II-C12. TEST SECTION WITH UPSTREAM AND DOWNSTREAM MEASURING STATIONS.

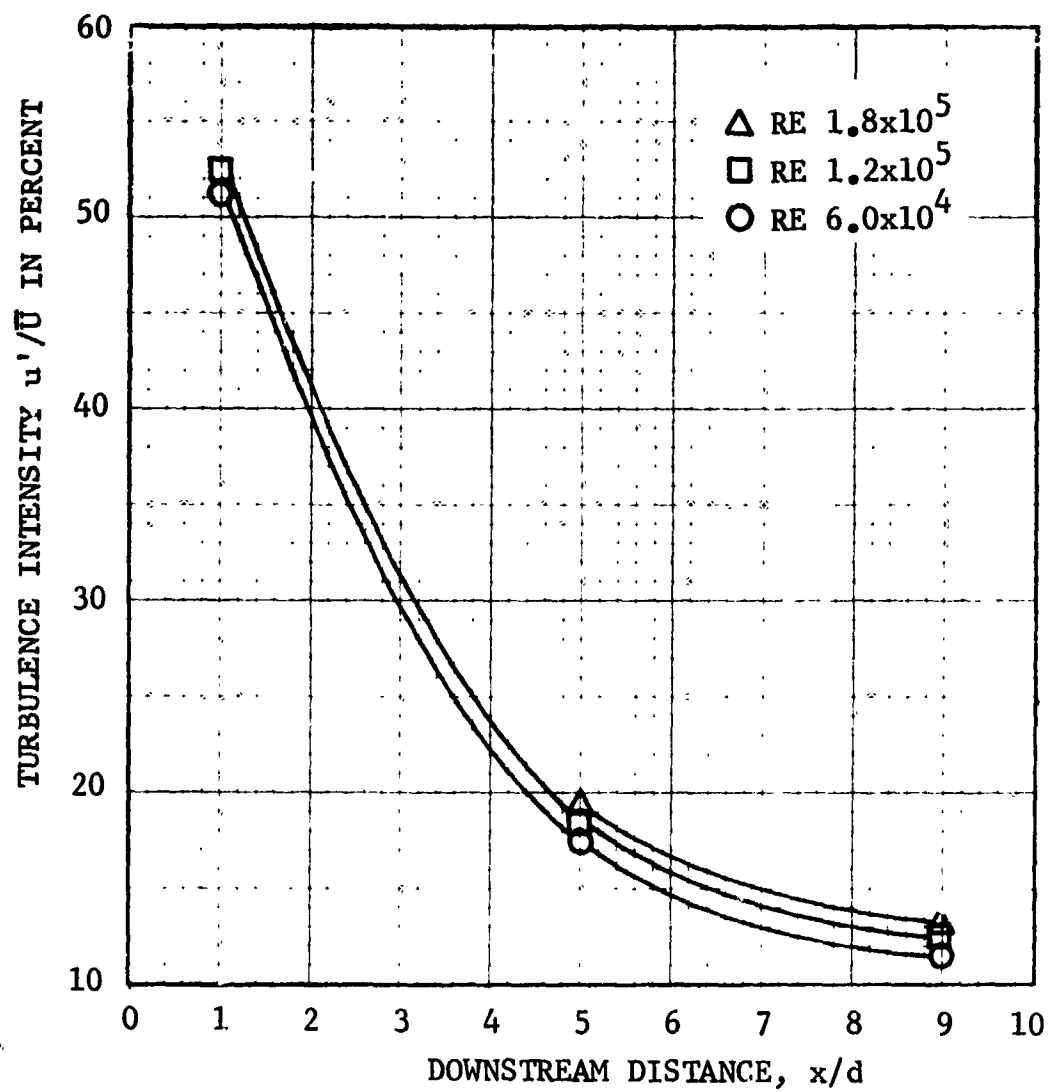


FIGURE II-C13. TURBULENCE INTENSITY, NORMALIZED TO LOCAL MEAN VELOCITY, OF THE WAKE BEHIND A CYLINDER.

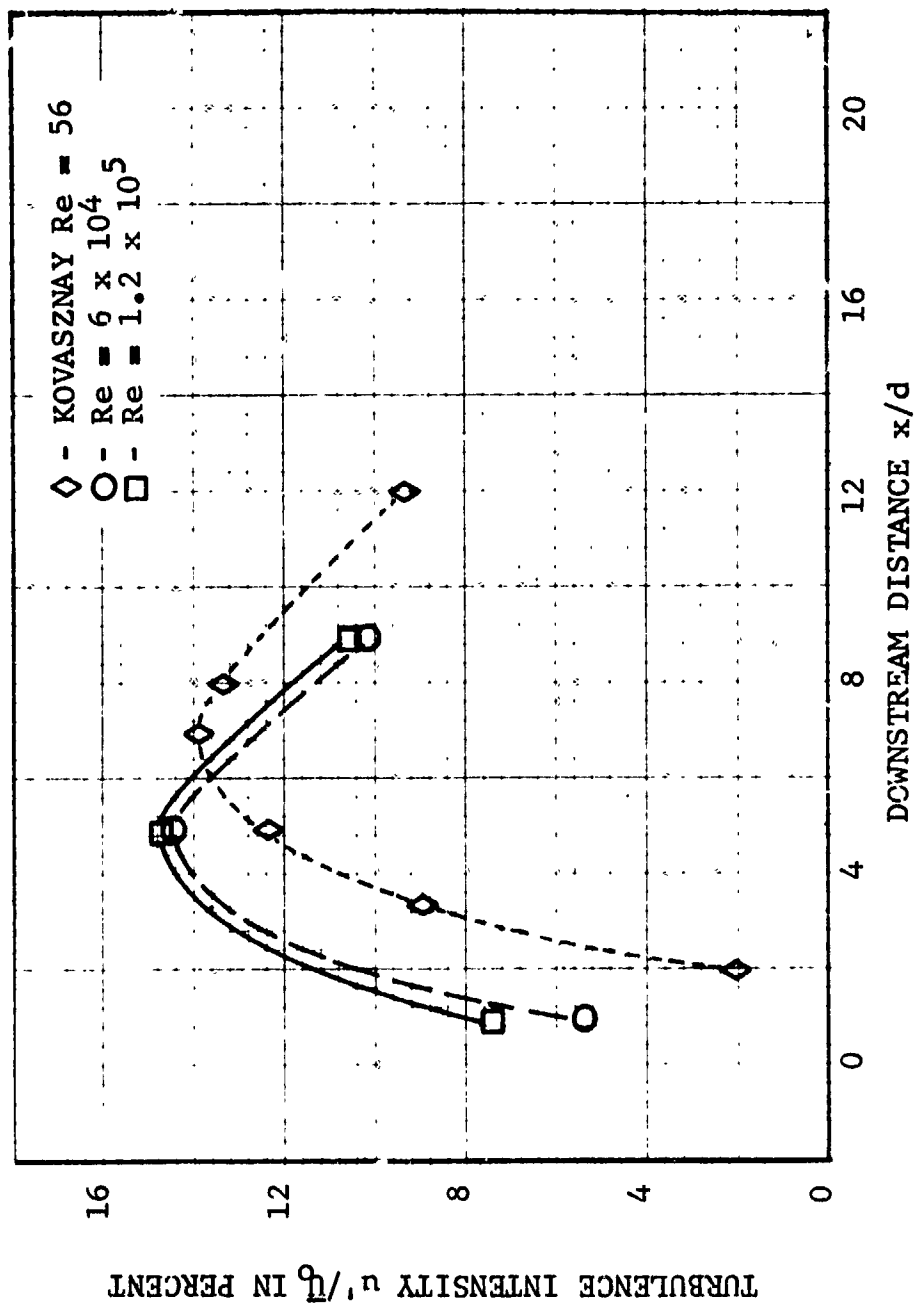


FIGURE II-C14. TURBULENCE INTENSITY, NORMALIZED TO UNDISTURBED (UPSTREAM) MEAN VELOCITY, OF THE WAKE BEHIND A CYLINDER.

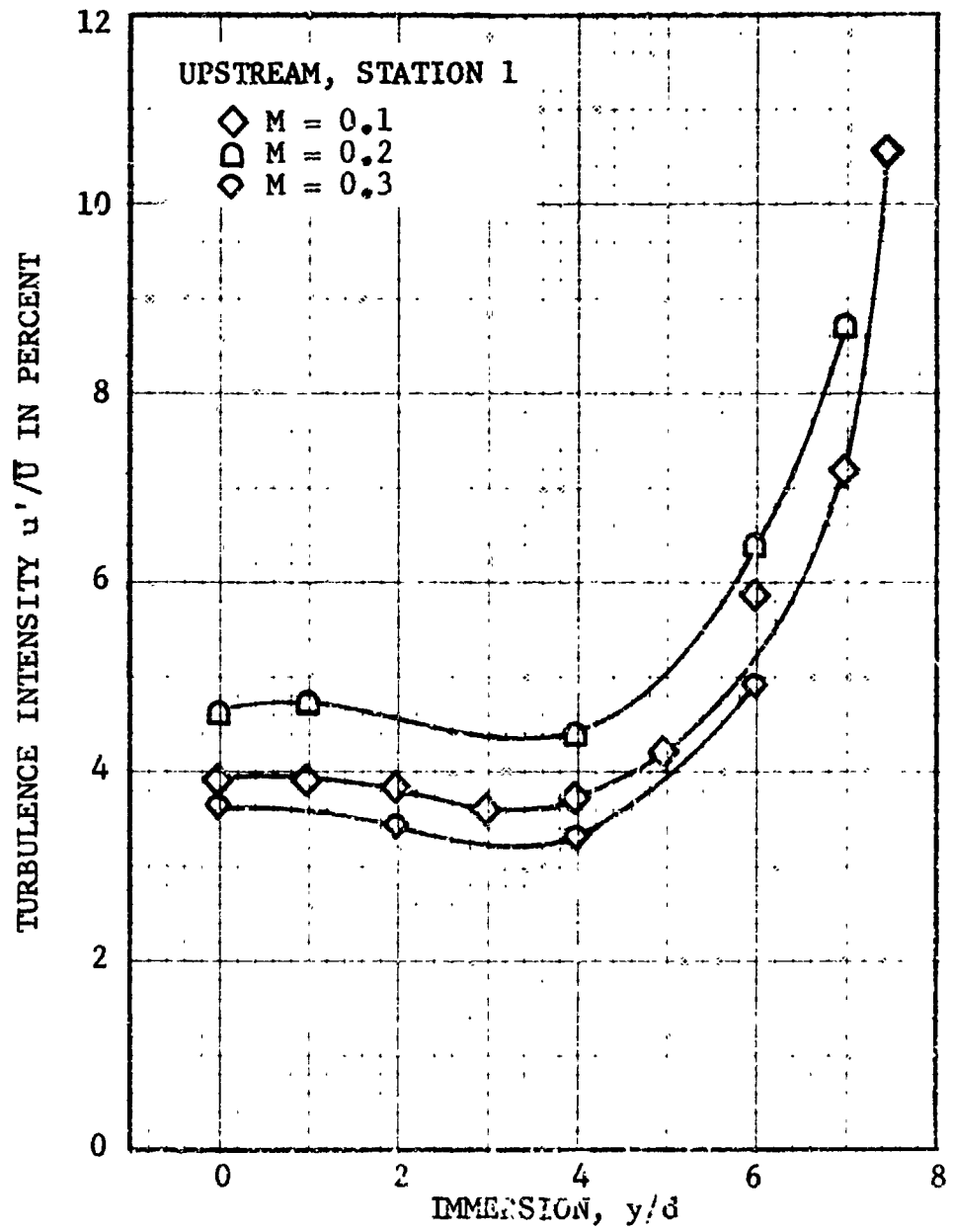


FIGURE II-C15. UPSTREAM TURBULENCE INTENSITY VS. IMMERSION.

In addition to turbulence, noise and vortex shedding frequency determinations were made for a 1/2 inch cylinder for three upstream flow Mach numbers. Figures II-C16, 18 and 19 give the turbulence intensities in the direction of the flow for three downstream stations versus probe position in the duct for three flow Mach numbers. Figure II-C20, 21 and 22 show the turbulence intensities w'/\bar{U} (in the spanwise direction of the cylinder) at three downstream stations for three flow Mach numbers. All these figures show that the turbulence intensities decrease with increasing flow Mach number. This can be explained by considering the hot film probe to be positioned at one point in the wake of the cylinder. If the flow Mach number is increased, the output of the hot film increases, due to the linear response of the hot film with flow. Furthermore; the mean velocity of the flow corresponds to the mean value of the output of the hot film, while the turbulence u' and w' corresponds to small signal fluctuations about this mean level. Hence, when the flow Mach number increases the mean value of the hot film output increases. Since this value appears in the denominator of the turbulence intensity it is evident that the turbulence intensity is decreasing for increasing flow Mach numbers. Figure II-C17 shows the calculated turbulence u' on the wake axis of the cylinder, using the turbulence intensities shown in Figure II-C16. As can be seen the u' turbulence increased with increasing flow Mach number.

Using a single hot film a radial traverse was made of the half inch cylinder wake and the probe stopped at the position of maximum turbulence (position where vortices are shed off the cylinder). This output was fed into a General Radio wave analyzer for spectral analysis. The frequency where the signal was a maximum was noted to be the vortex shedding frequency. Figures II-C23, 24, 25 show the frequency spectra for the half-inch cylinder for flow Mach numbers 0.1, 0.2 and 0.3 respectively. The position for which the turbulence was a maximum was found to be 0.25 inches from the cylinder's axis at two diameters downstream of the cylinder.

(b) Noise Measurements on a Cylinder. The sound radiated by a cylinder immersed in an airstream has been studied by a number of investigators (Reference 2). Etkin (Reference 3) found that the pure tone in the sound spectrum was associated with the shedding of vortices from the cylinder. The frequencies were found to be the same.

In considering the sound intensity spectrum, investigators found that:

- The pure tone associated with the vortex shedding frequency of the cylinder is related to the alternating lift force acting on the cylinder and has the directionality of a line dipole with the axis normal to the flow.
- The tone generated at twice the vortex shedding frequency is related to the fluctuating drag, with the directionality of a line dipole with axis parallel to the stream.
- The acoustic power radiation varies as U_0^n , where n lies between 5 and 6 depending on the ratio of cylinder length to cylinder diameter, i.e., l/d .

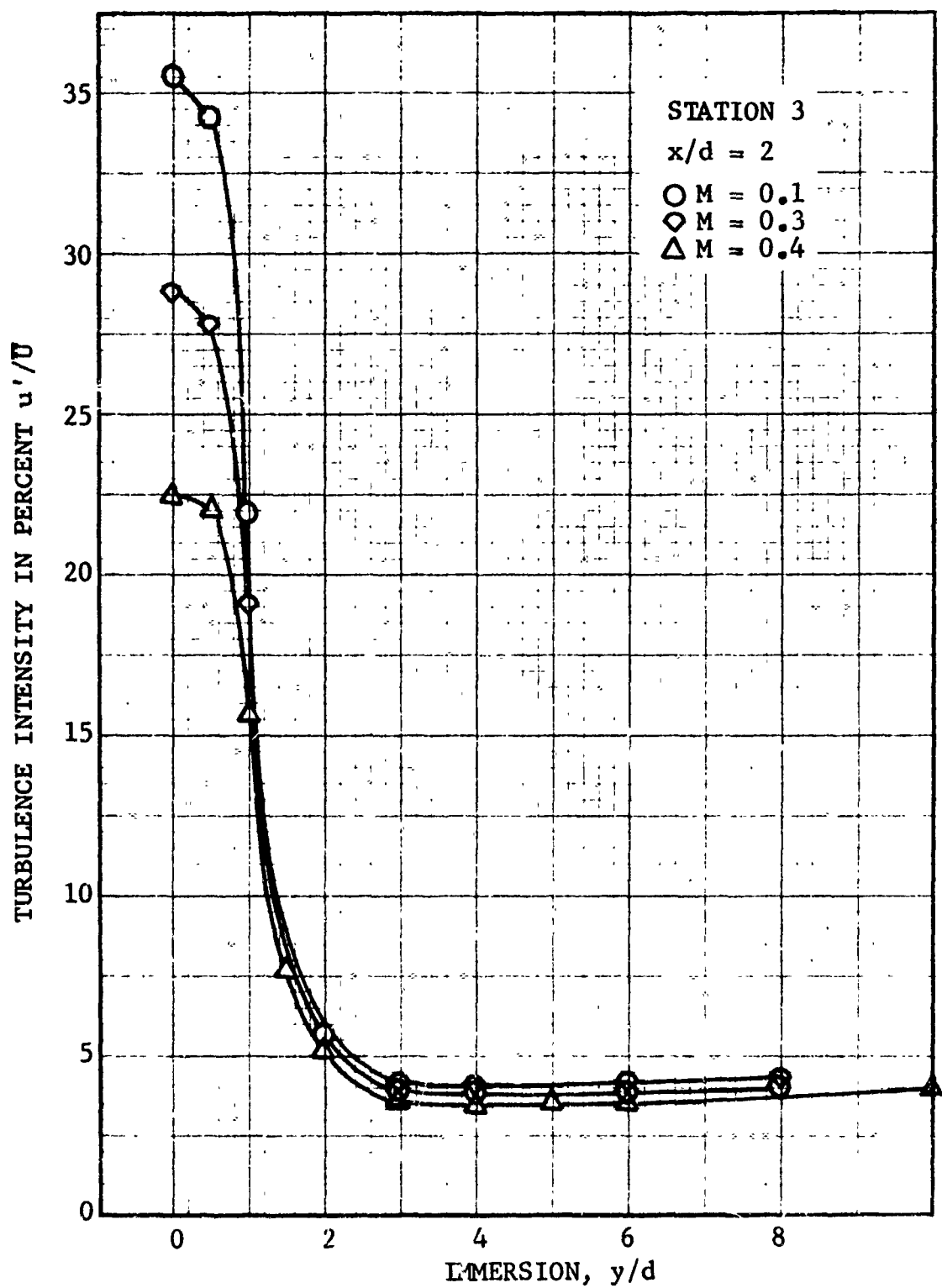


FIGURE II-C16. DOWNSTREAM TURBULENCE INTENSITY VS IMMERSION, TWO DIAMETERS DOWNSTREAM OF A CYLINDER.

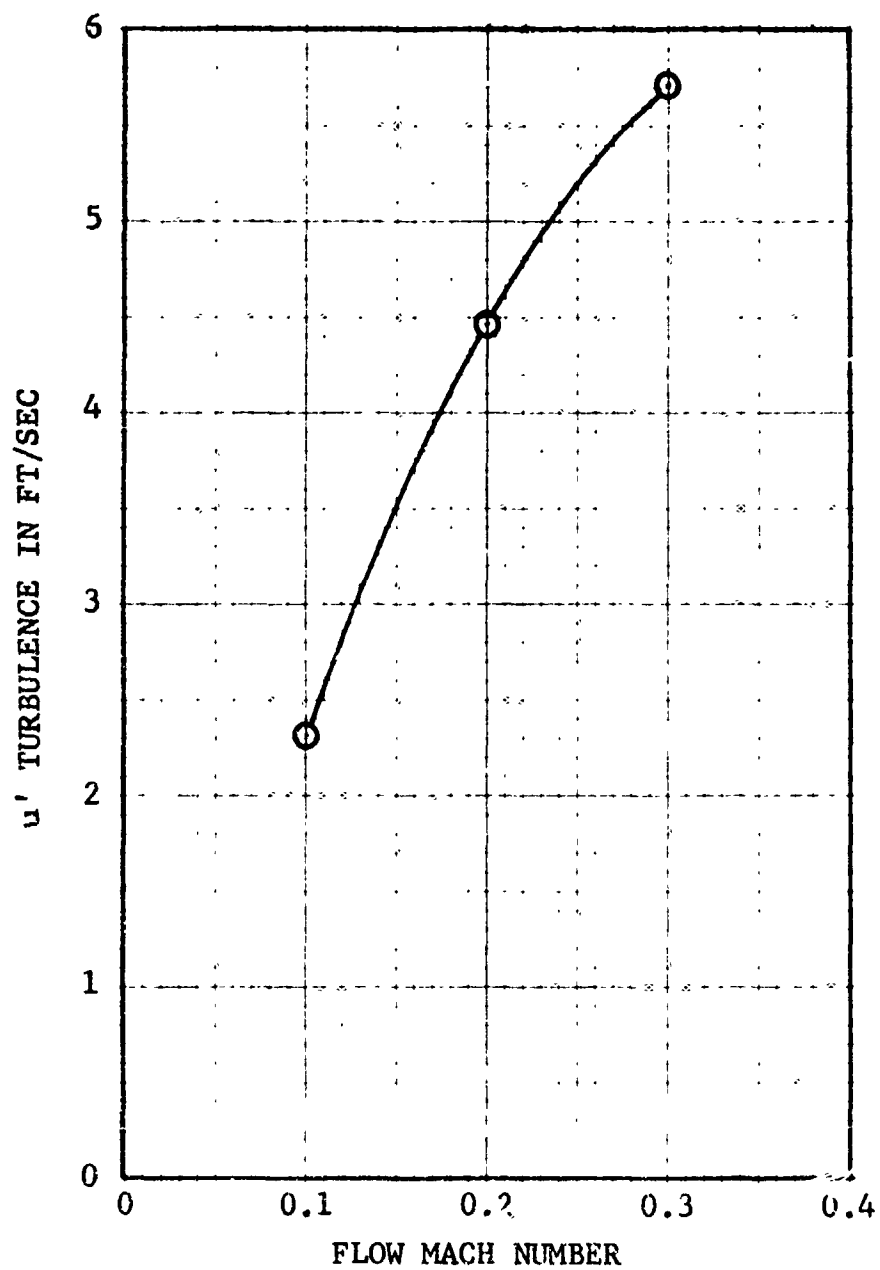


FIGURE II-C17. TURBULENCE ON THE WAKE AXIS, TWO DIAMETERS DOWNSTREAM OF A CYLINDER

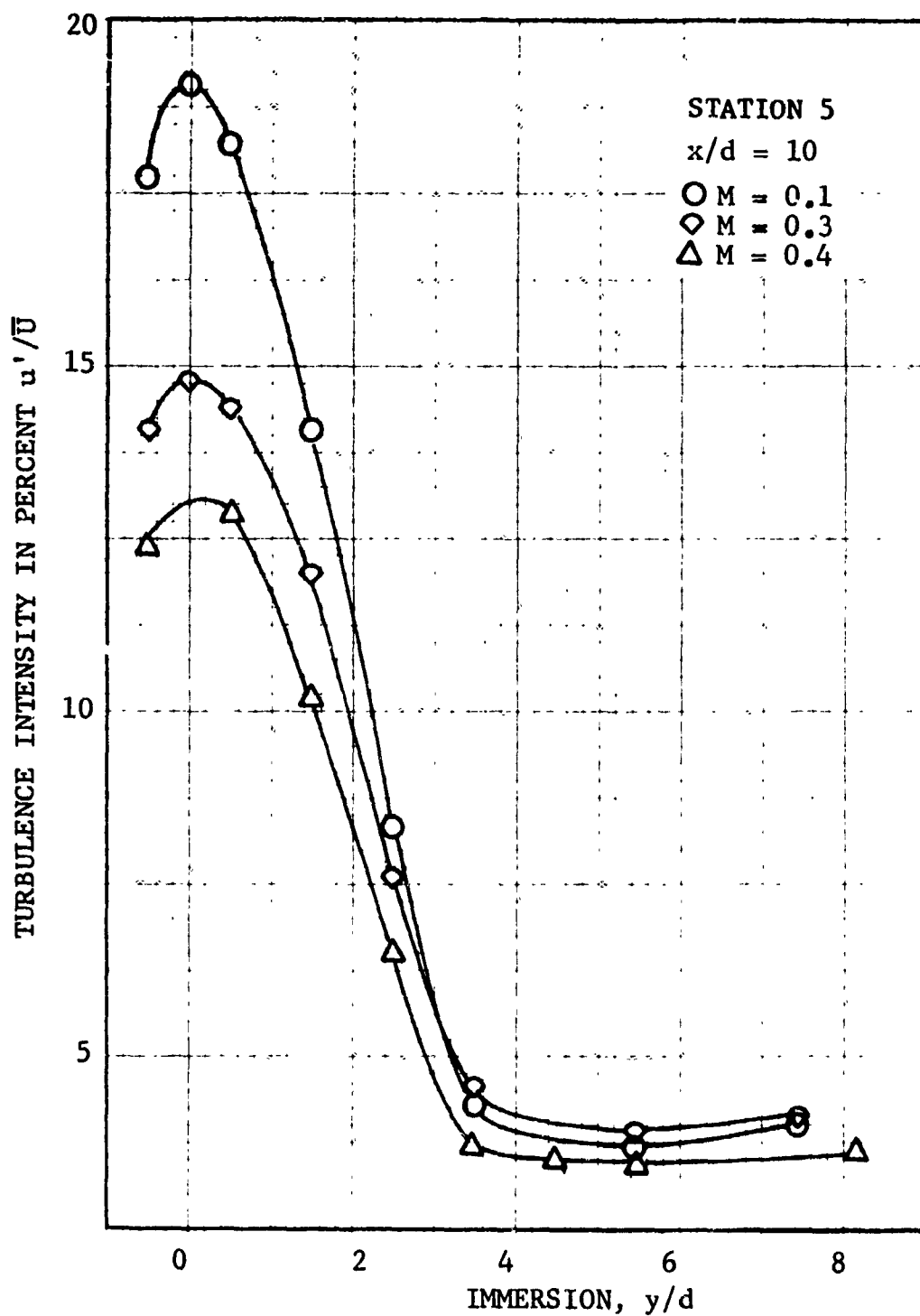


FIGURE II-C18. TURBULENCE INTENSITY VS IMMERSION, TEN DIAMETERS DOWNSTREAM OF A CYLINDER.

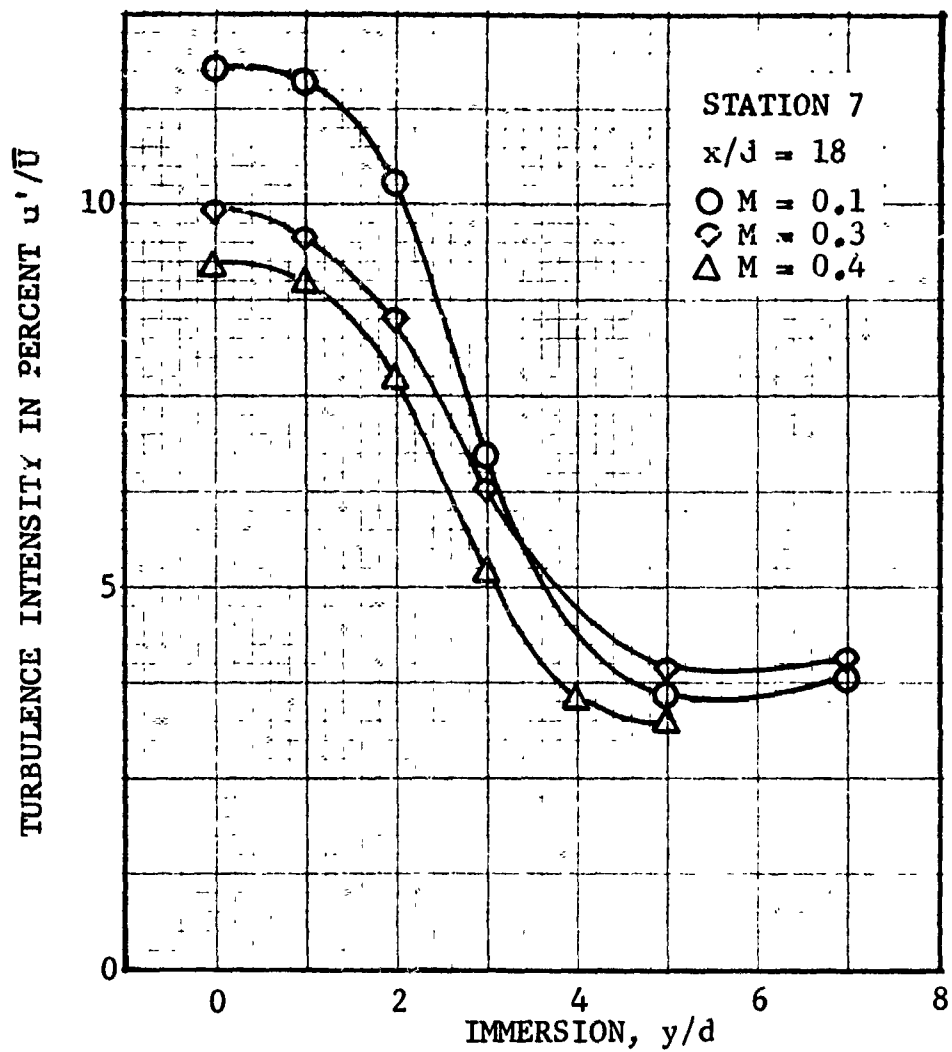


FIGURE II-C19. TURBULENCE INTENSITY VS IMMERSION, EIGHTEEN DIAMETERS DOWNSTREAM OF A CYLINDER.

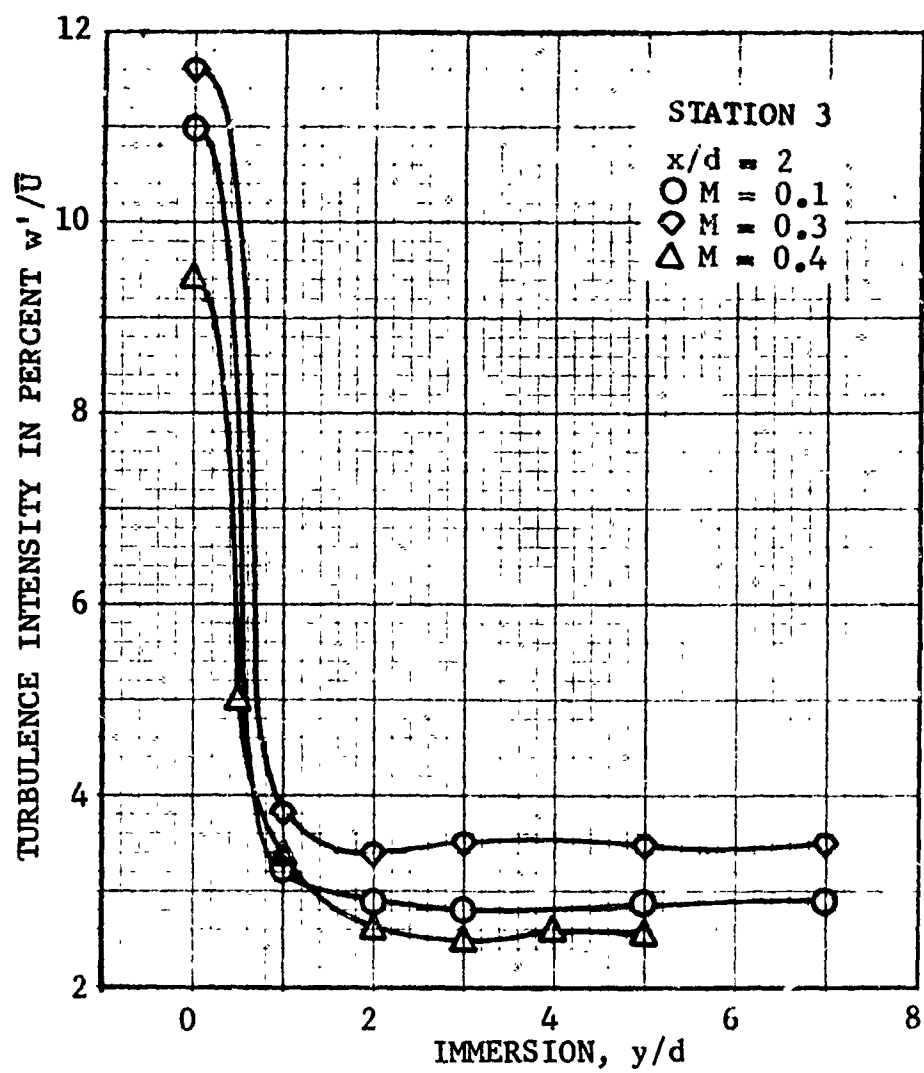


FIGURE II-C20. TURBULENCE INTENSITY VS IMMERSION,
 TWO DIAMETERS DOWNSTREAM OF A CYLINDER

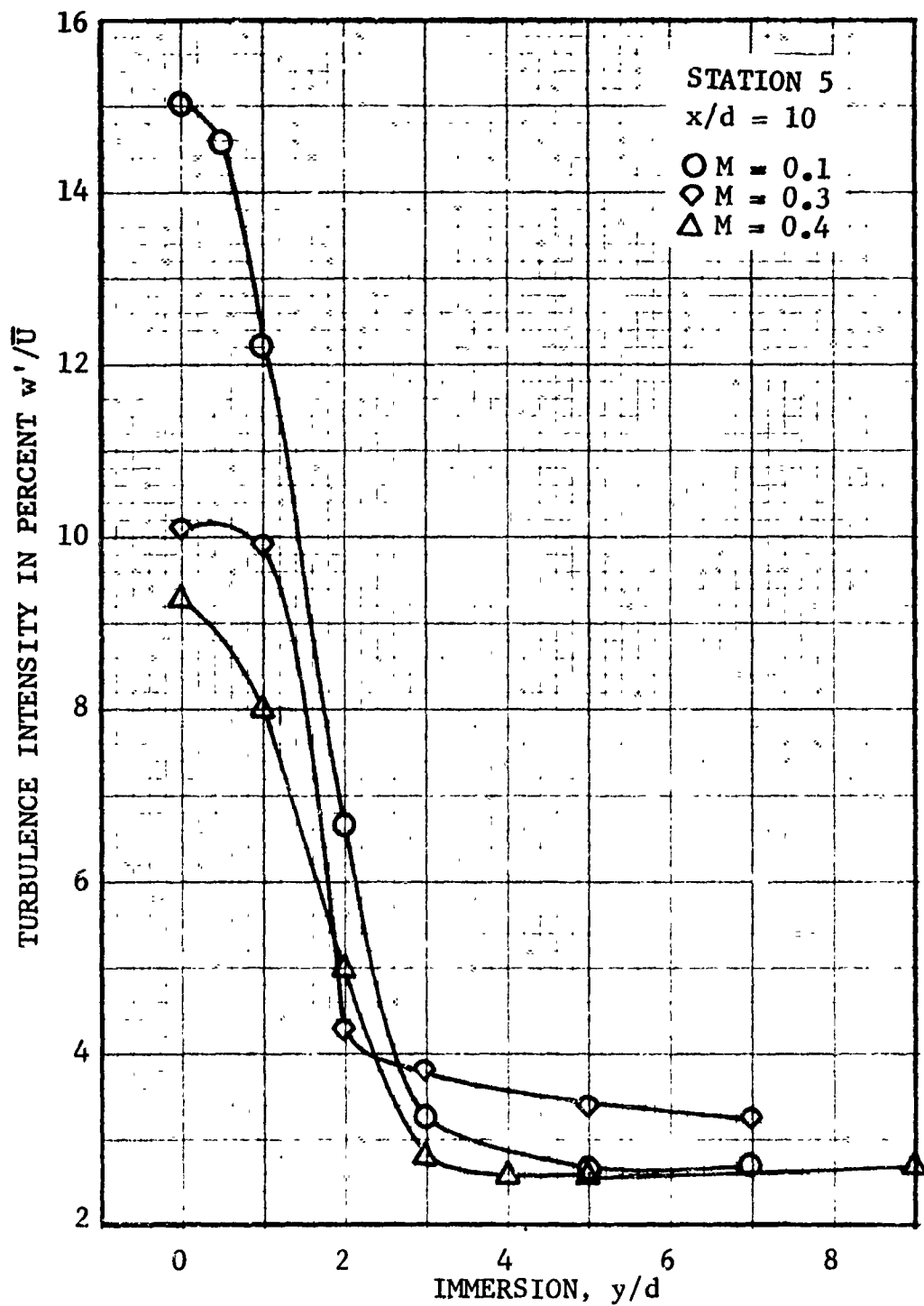


FIGURE II-C21. TURBULENCE INTENSITY VS IMMERSION, TEN DIAMETERS DOWNSTREAM OF A CYLINDER.

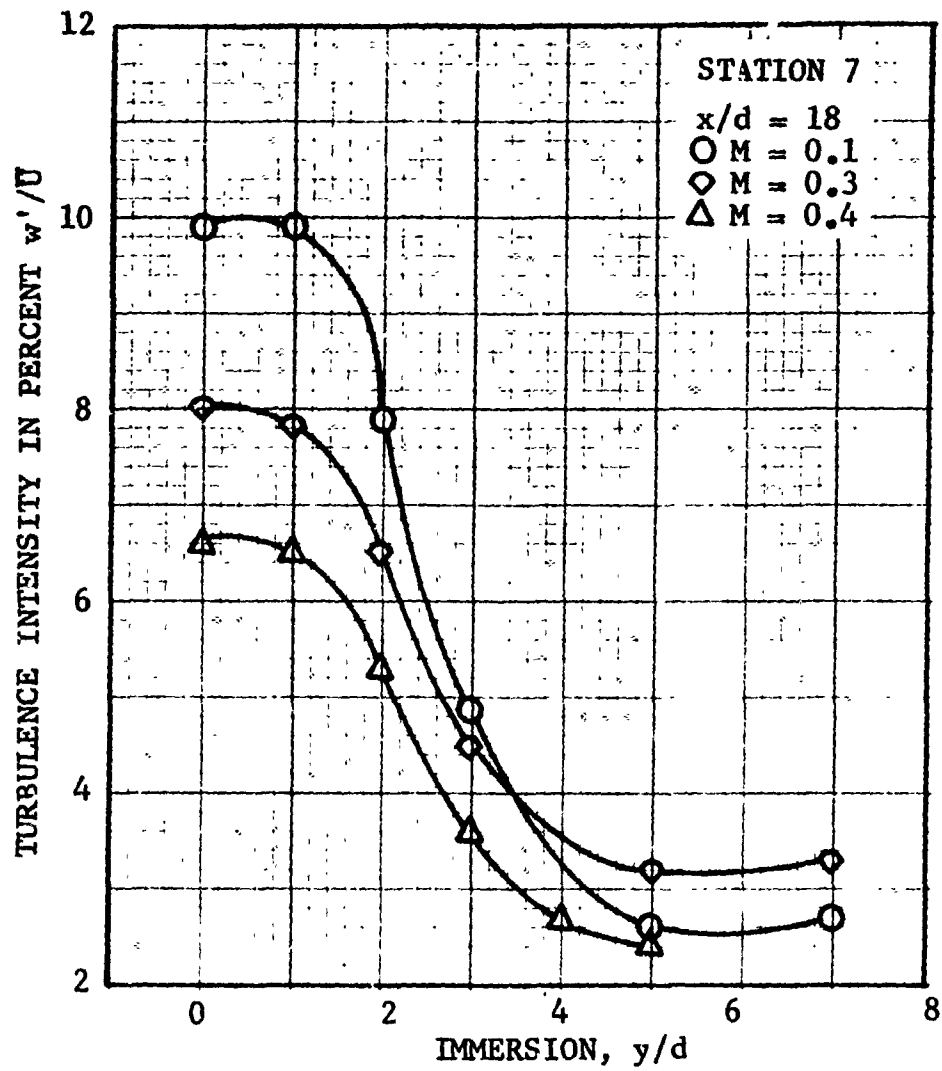


FIGURE II-C22. TURBULENCE INTENSITY VS IMMERSION, EIGHTEEN DIAMETERS DOWNSTREAM OF A CYLINDER.

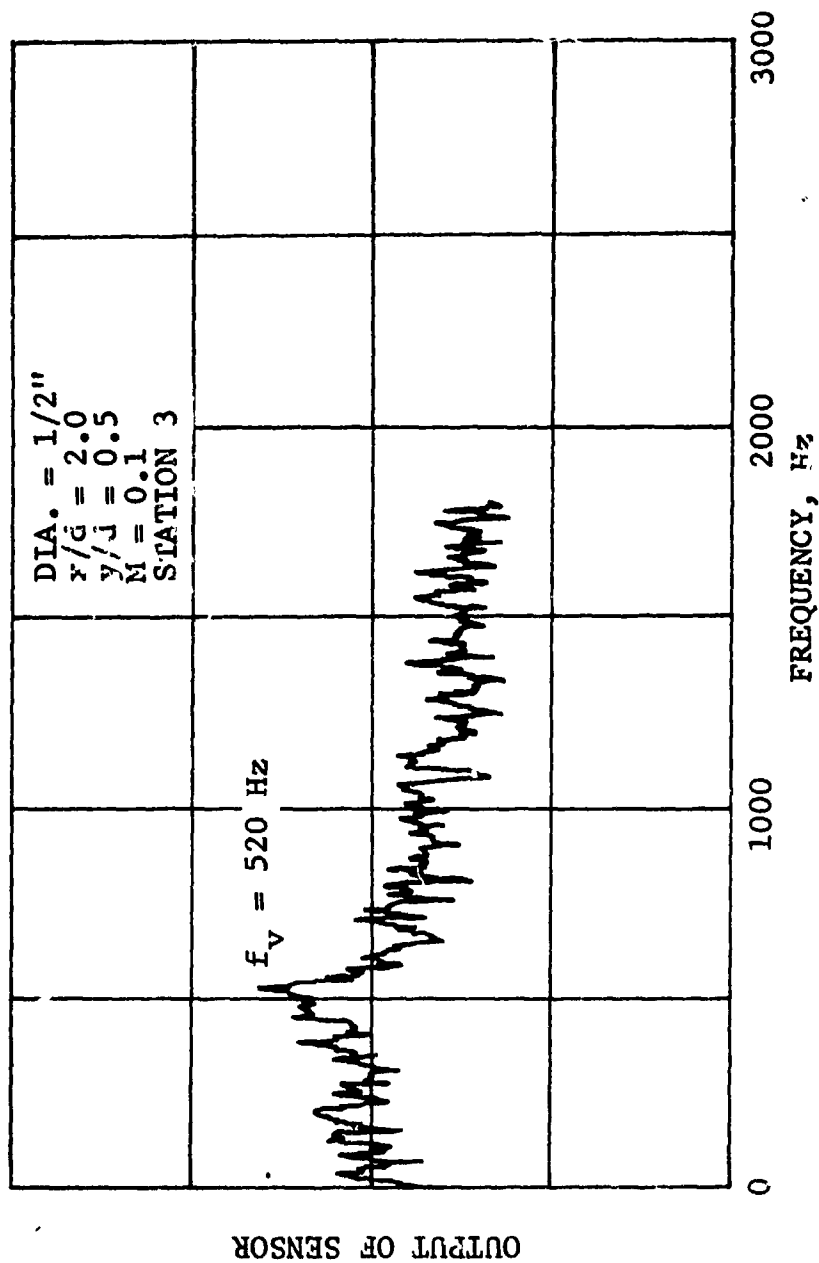


FIGURE II-C23. VORTEX SHEDDING FREQUENCY FOR 1/2" CYLINDER, TWO DIAMETERS DOWNSTREAM.

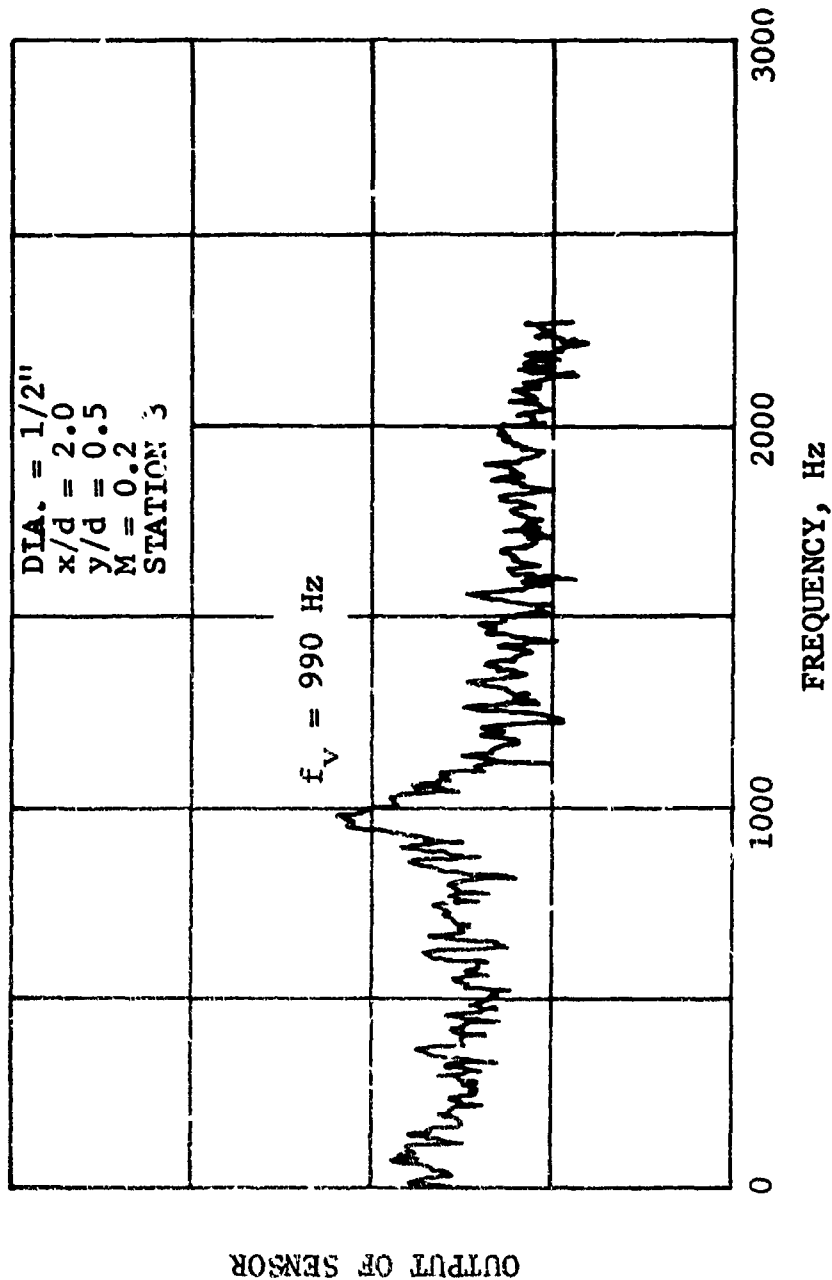


FIGURE II-C24. VORTEX SHEDDING FREQUENCY FOR 1/2" CYLINDER, TWO DIAMETERS DOWNSTREAM.

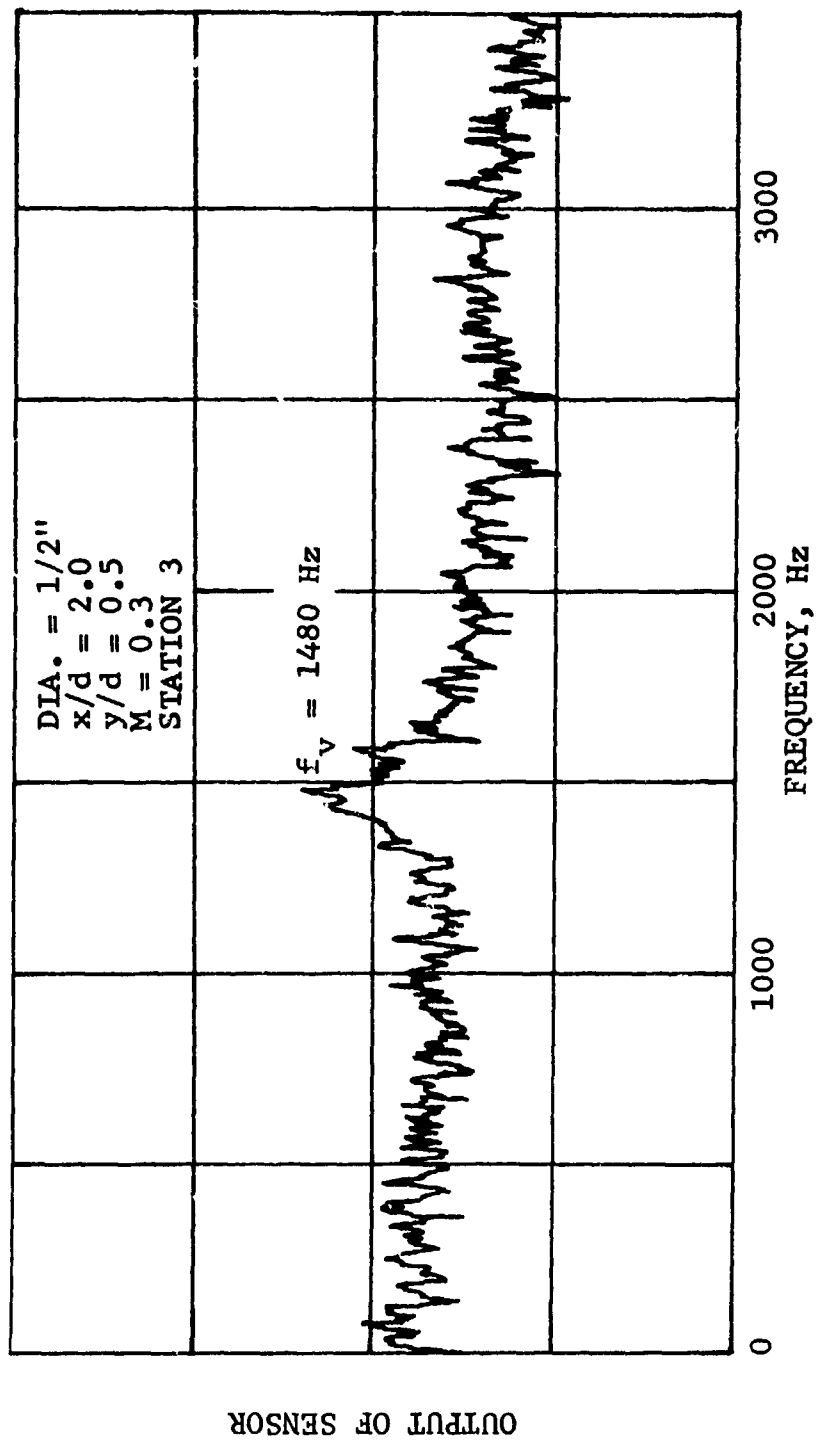


FIGURE II-C25. VORTEX SHEDDING FREQUENCY FOR 1/2" CYLINDER, TWO DIAMETERS DOWNSTREAM.

The main limitations of the theory are that one must know the forces acting on the cylinder and the mechanism for converting aerodynamic to acoustic energy.

An acoustic probe system was placed inside the wind tunnel at the end of the test section, i.e., downstream of the cylinder in a plane that bisects the cylinder span. The system was calibrated and the probe system losses determined in each frequency band. The microphone signal was fed directly into the B&K analyzer.

In addition two microphones were employed: a 1/2 inch microphone 16" downstream of the cylinder and another microphone (1/4 inch) 8" vertically below the cylinder. These two microphones were flush mounted with the wind tunnel walls, i.e., only the microphone diaphragms were exposed to the air stream.

Figures II-C26 through II-C37 show the sound spectra (SPL versus frequency, "f") at various flow Mach numbers, of the noise with and without the cylinder at the two microphone locations. The SPL differences between the background noise (noise without the cylinder) and noise with the cylinder in place are given in Figure II-C28, 31, 34 and 37. In these figures the frequency of the maximum difference between noise with and without the cylinder is clearly visible and indicated by f_t .

Table II-C1 shows the measured vortex shedding frequency f_v , as determined with the hot film probe in the wake of 1/2 inch cylinder, and the tone frequency f_t determined from the noise spectra measured by the microphones for the three Mach numbers. The Strouhal number (Sh) was calculated from the data according to the relation:

$$Sh = f_v d / \bar{U}_0$$

It can be seen that the vortex shedding frequency as measured by the hot film and the noise peak as measured by the microphones are nearly the same. Thus, the maximum turbulence is related to the maximum noise.

Figure II-C38 shows the OASPL versus flow Mach number for a half inch cylinder. The OASPL was read on the General Radio Sound Level Meter. The data represented by the short dashed curve was obtained from the microphone located underneath the cylinder while the solid curve was obtained from the microphone downstream of the cylinder. The slope of these curves was equal to 2.5 for the microphone below the cylinder and 3.0 for the microphone downstream of the cylinder. Figure II-C39 shows the SPL at the vortex shedding frequency generated by the cylinder for various flow Mach numbers.

Making use of the following relationships:

$$I = a U^n$$

ONE-HALF INCH CYLINDER			
M	f_v : Hot Film (Hz)	f_t : 1/2" Mike Below Cylinder (Hz)	Sh
0.1	520	500	0.19
0.2	990	1000	0.18
0.3	1480	1250	0.18
0.4	X	2000	X

X = Not Available

TABLE II-C1

Comparison Between Hot Film and Microphone Vortex Shedding Frequencies

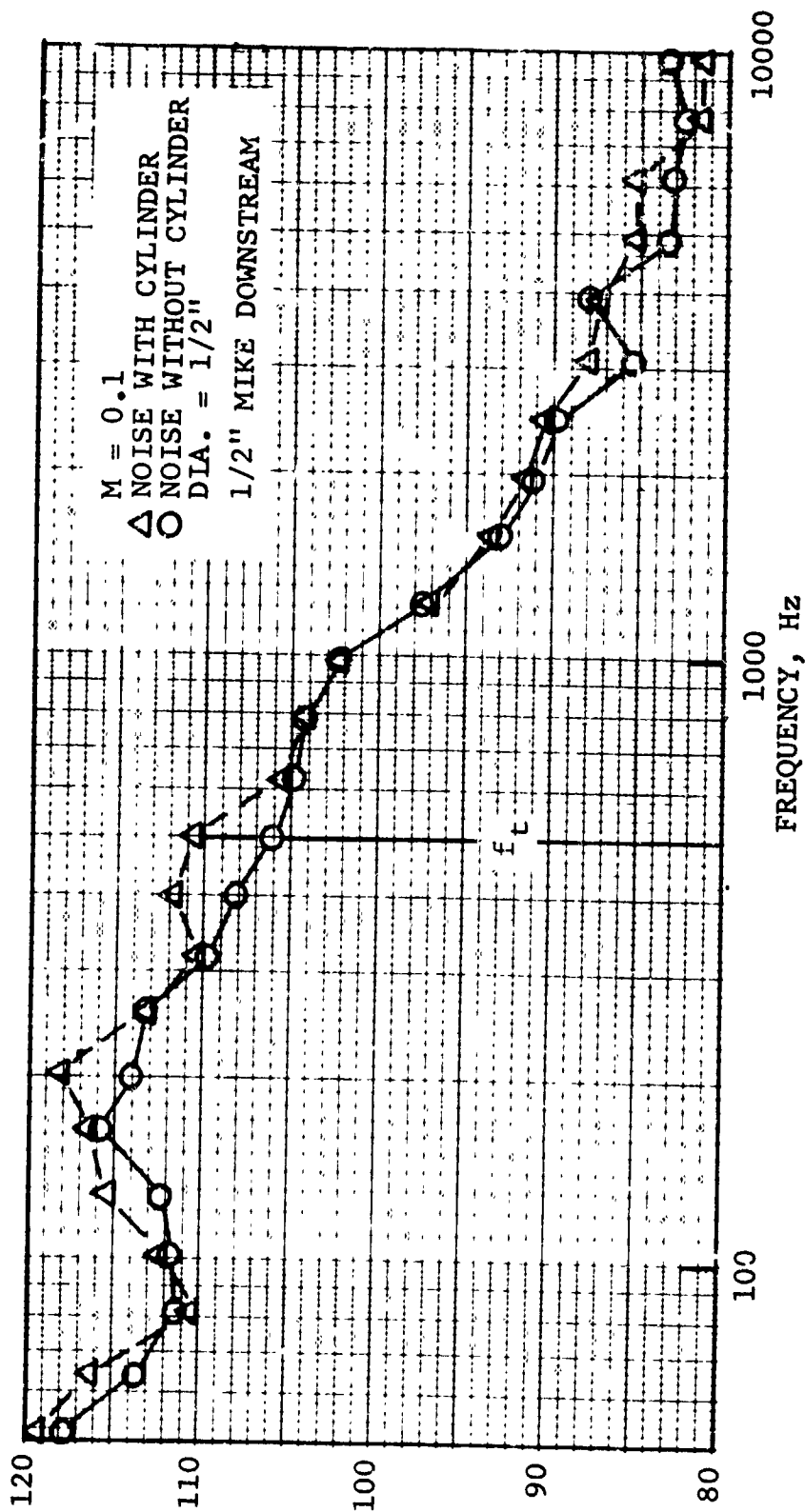


FIGURE II-C26. 1/3 OCTAVE SOUND SPECTRUM OF A 1/2" CYLINDER IMMERSED IN AN AIR STREAM.

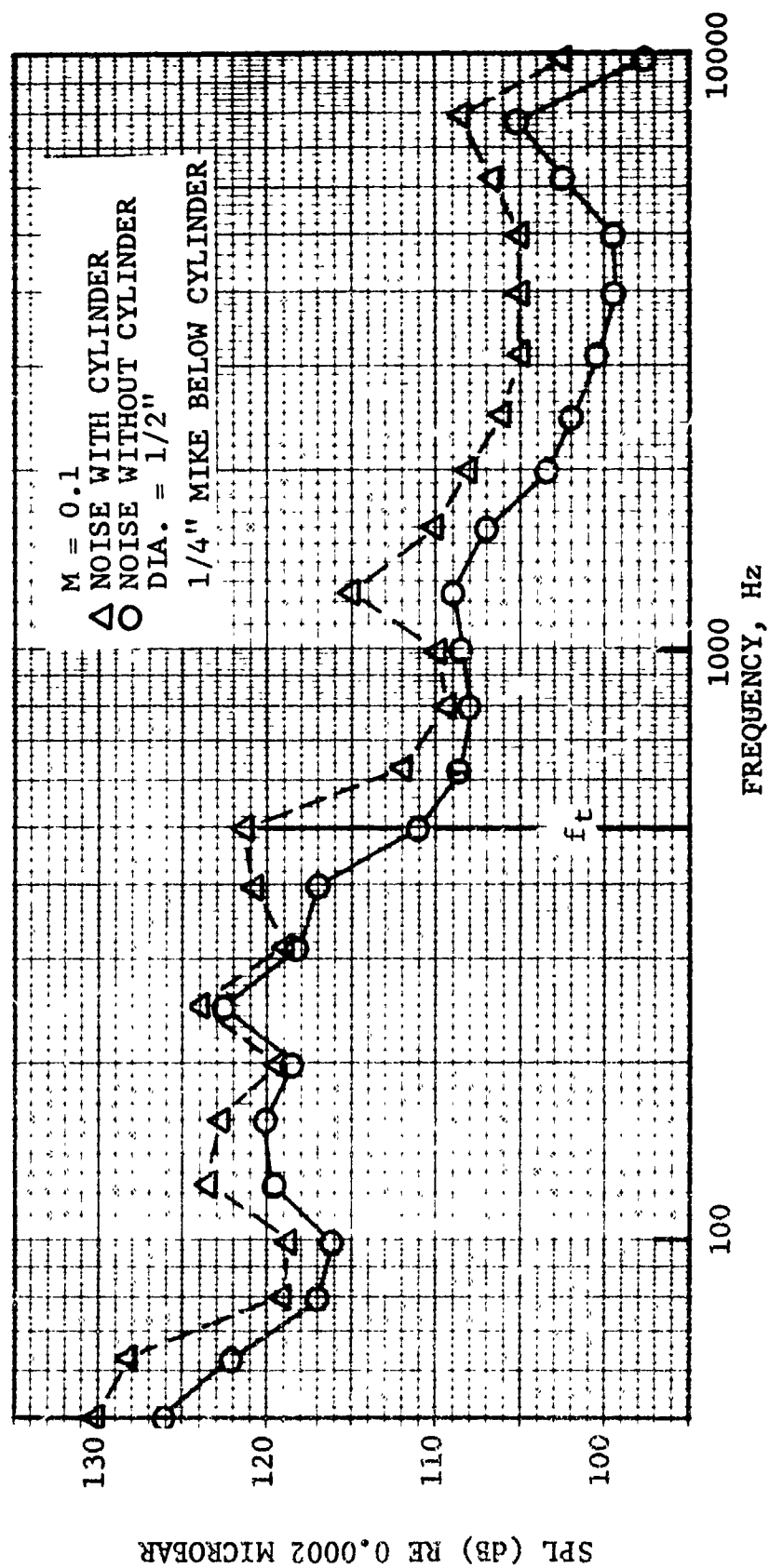


FIGURE 11-C27. $1/3$ OCTAVE SOUND SPECTRUM OF A $1/2''$ CYLINDER IMMERSED IN AN AIR STREAM.

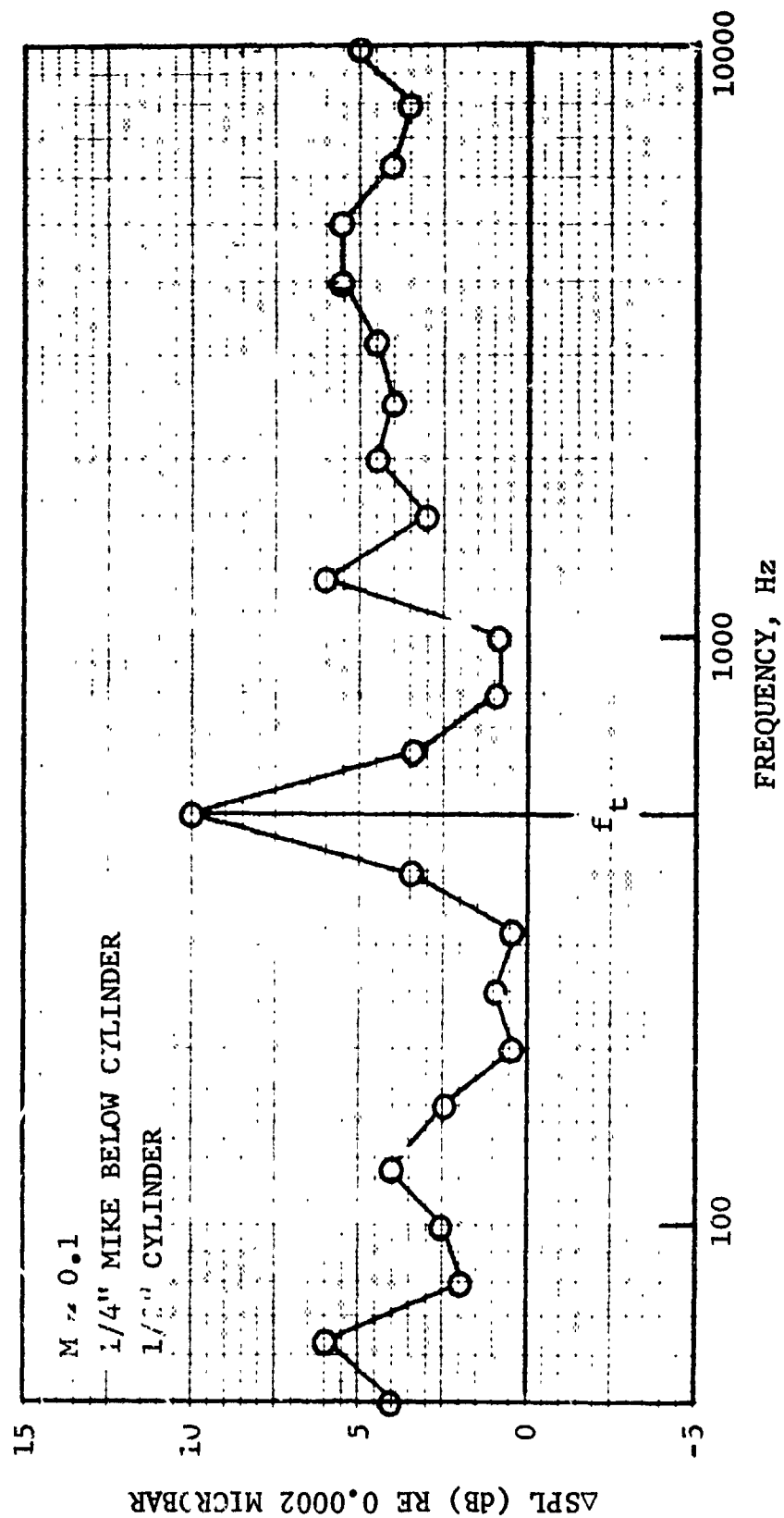


FIGURE II-C28. 1/3 OCTAVE SOUND SPECTRUM OF A 1/2" CYLINDER IMMERSED IN AN AIR STREAM.

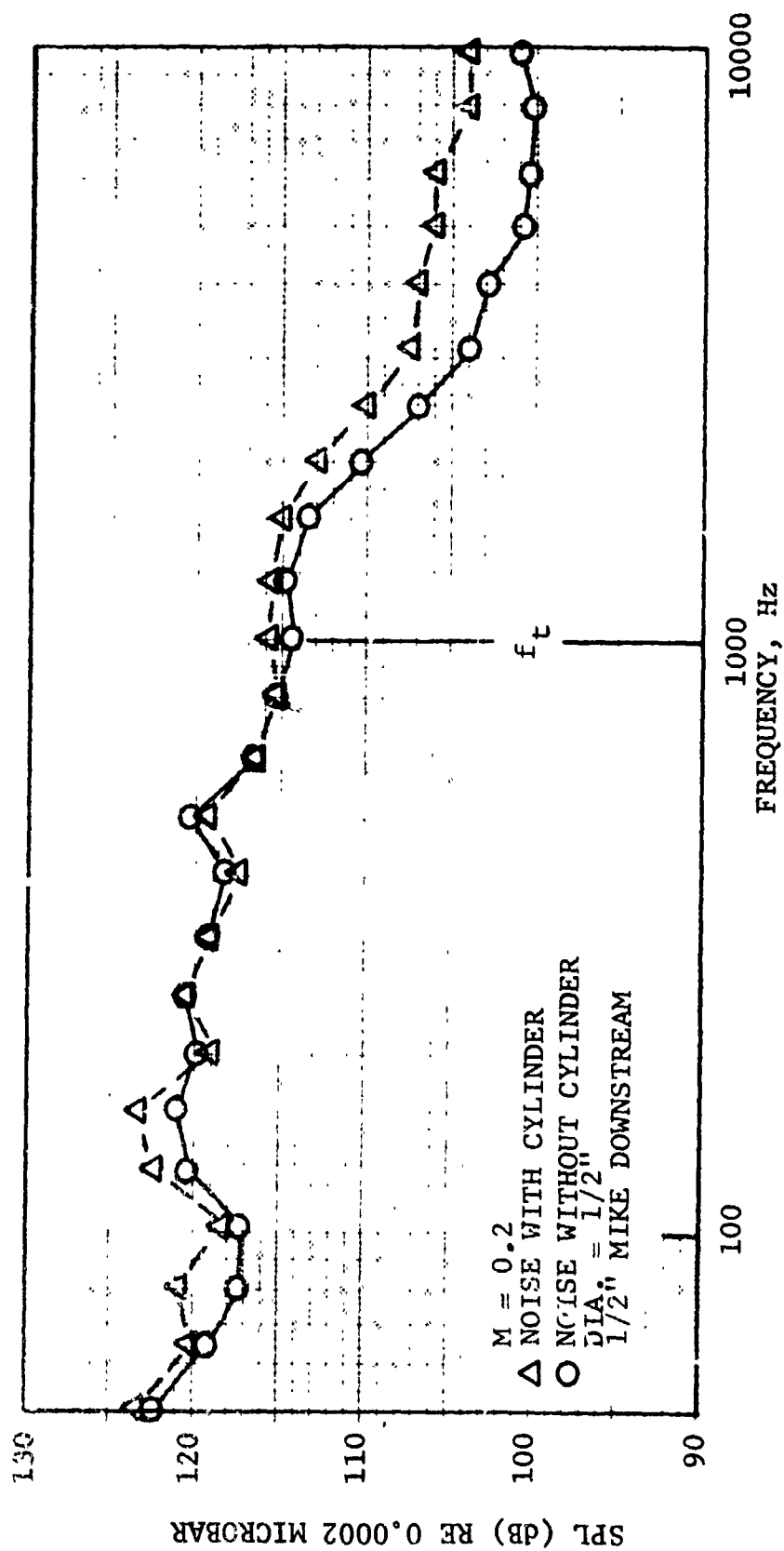


FIGURE II-C29. 1/3 OCTAVE SOUND SPECTRUM OF A 1/2" CYLINDER IMMERSED IN AN AIR STREAM.

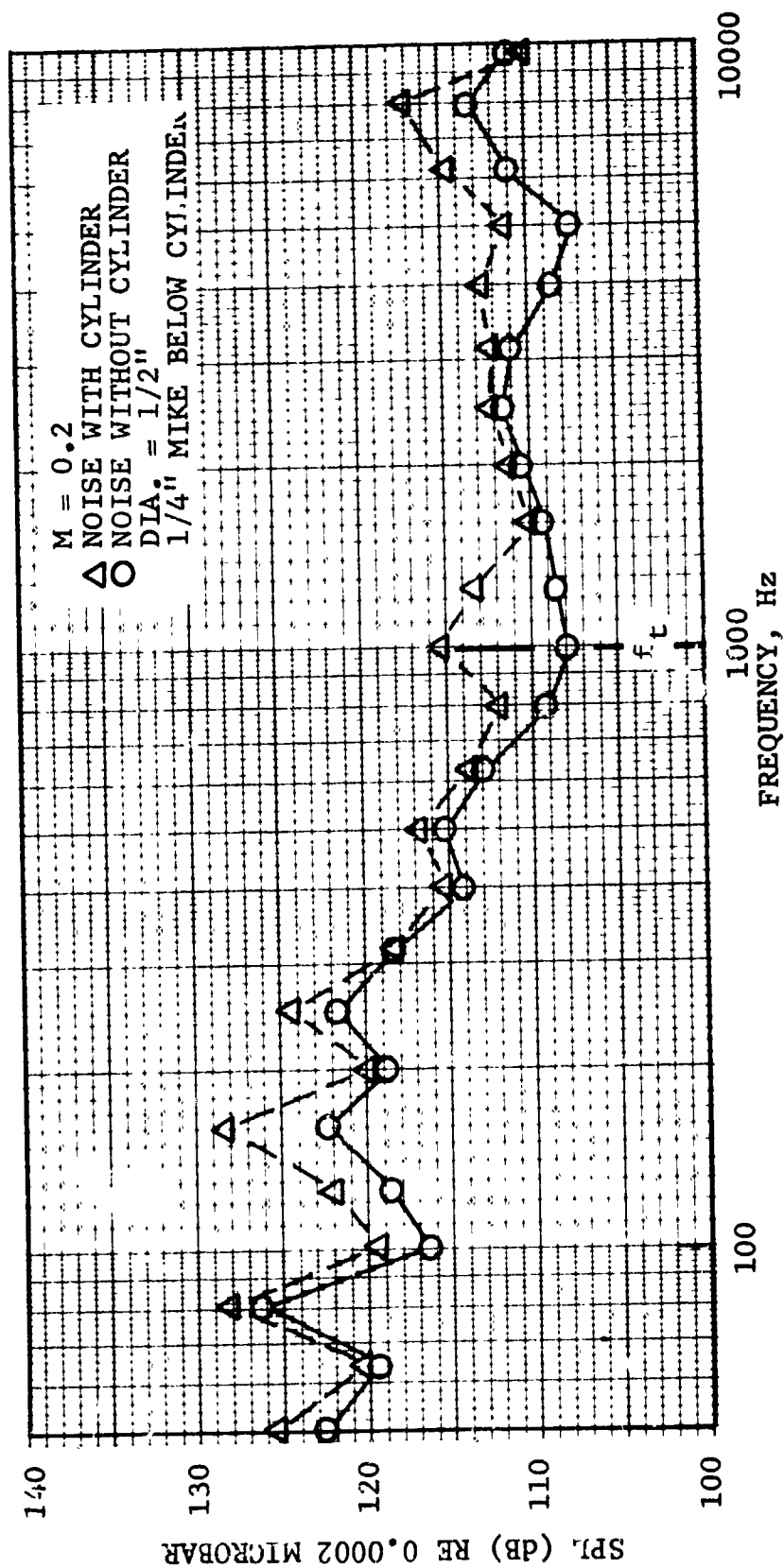


FIGURE II-C30. 1/3 OCTAVE SOUND SPECTRUM OF A 1/2" CYLINDER IMMersed IN AN AIR STREAM.



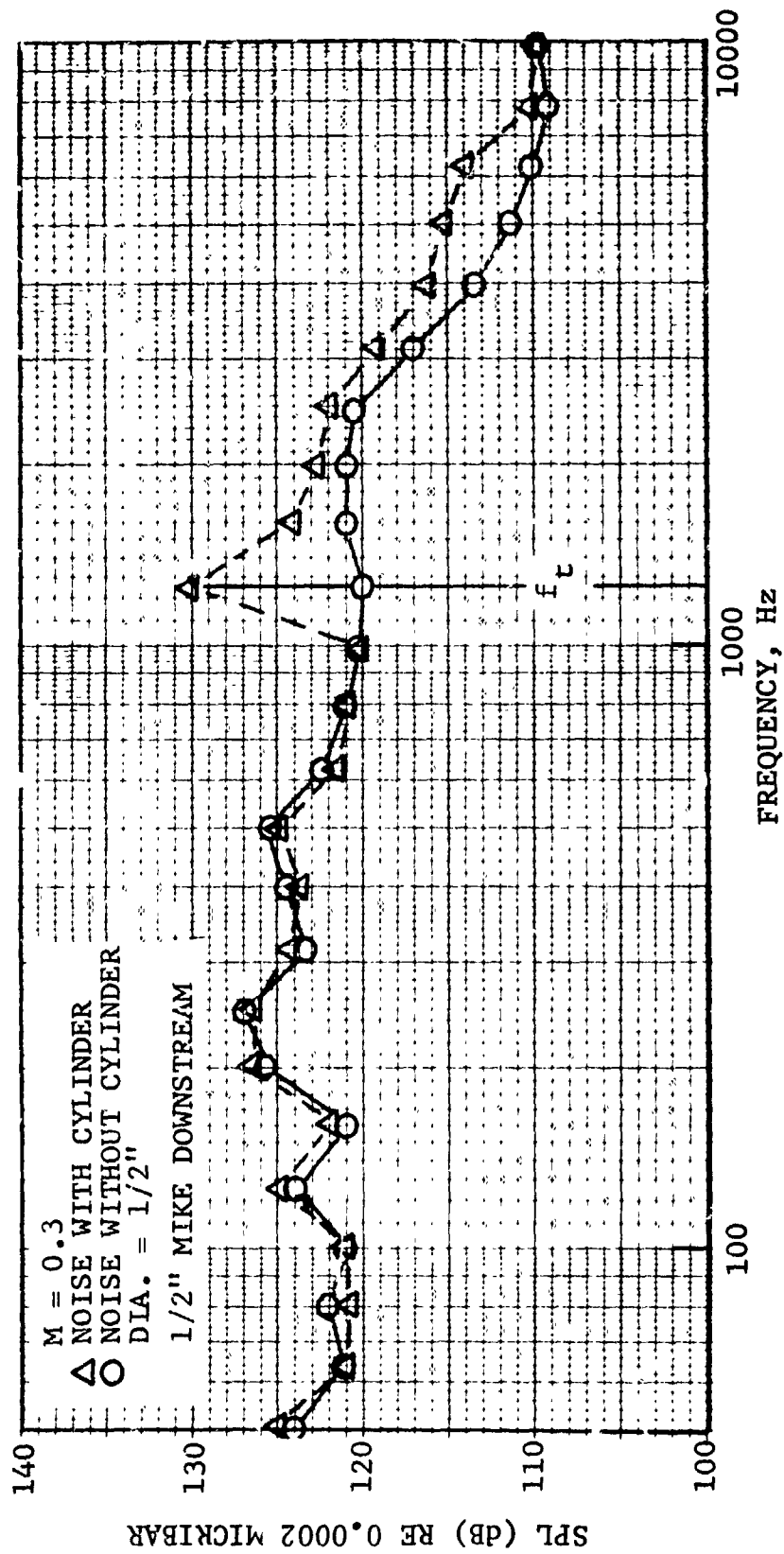


FIGURE II-C32. 1/3 OCTAVE SOUND SPECTRUM OF A 1/2" CYLINDER IMMERSED IN AN AIR STREAM.

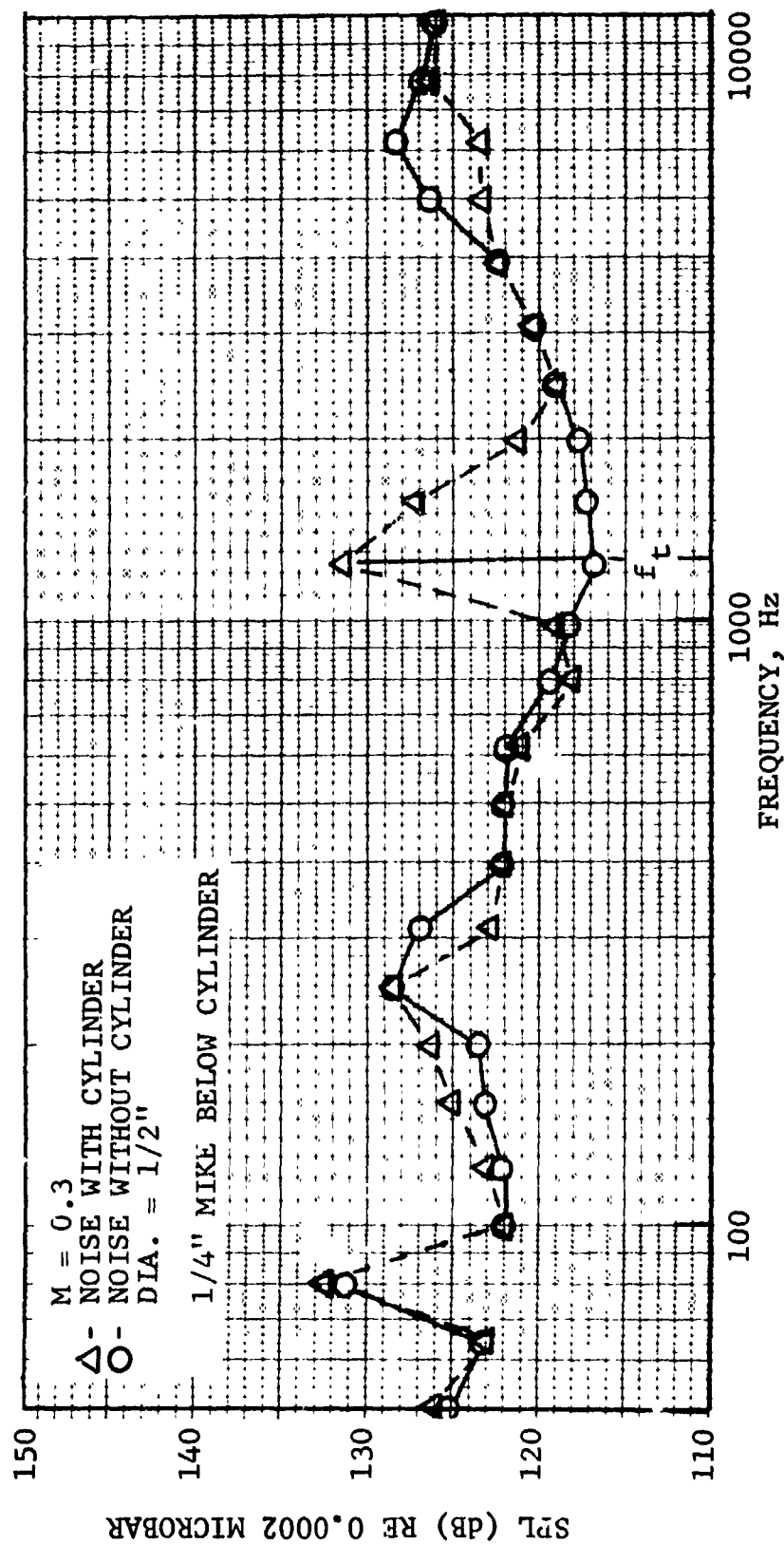


FIGURE II-C33. 1/3 OCTAVE SOUND SPECTRUM OF A 1/2" CYLINDER IMMERSED IN AN AIR STREAM.

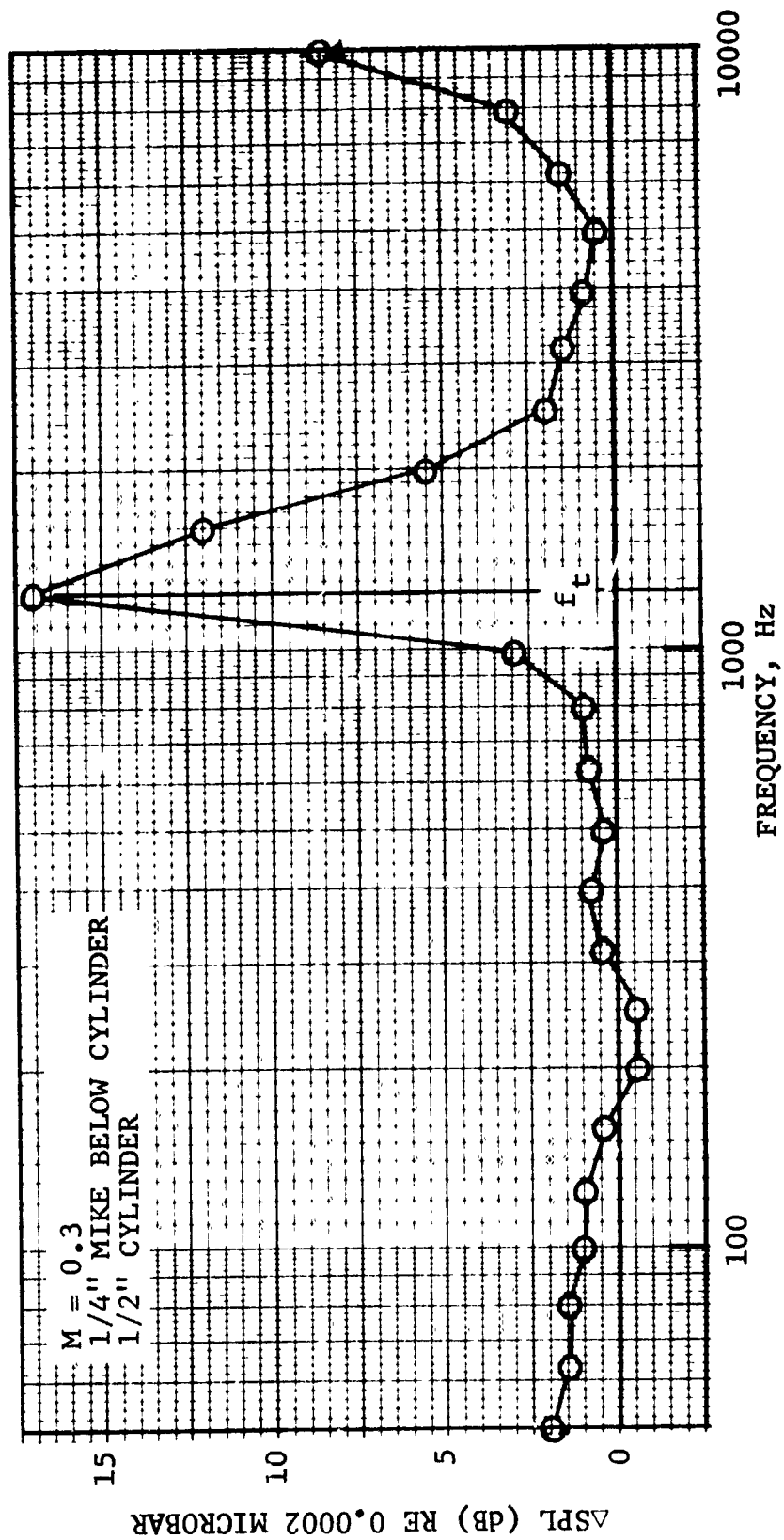


FIGURE II-C34. 1/3 OCTAVE SOUND SPECTRUM OF A 1/2" CYLINDER IMMERSED IN AN AIR STREAM.

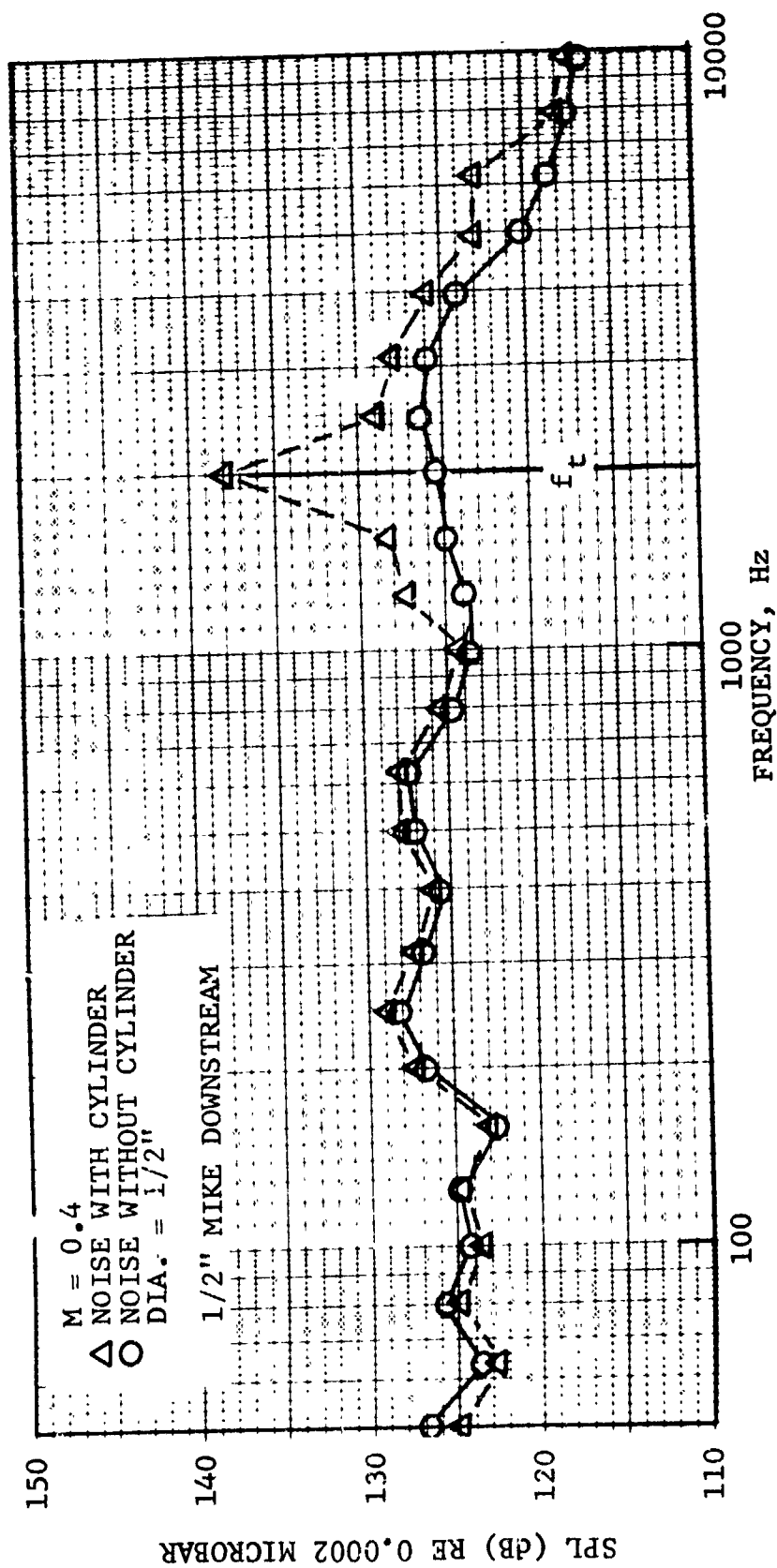


FIGURE II-C35. 1/3 OCTAVE SOUND SPECTRUM OF A 1/2" CYLINDER IMMERSED IN AN AIR STREAM.

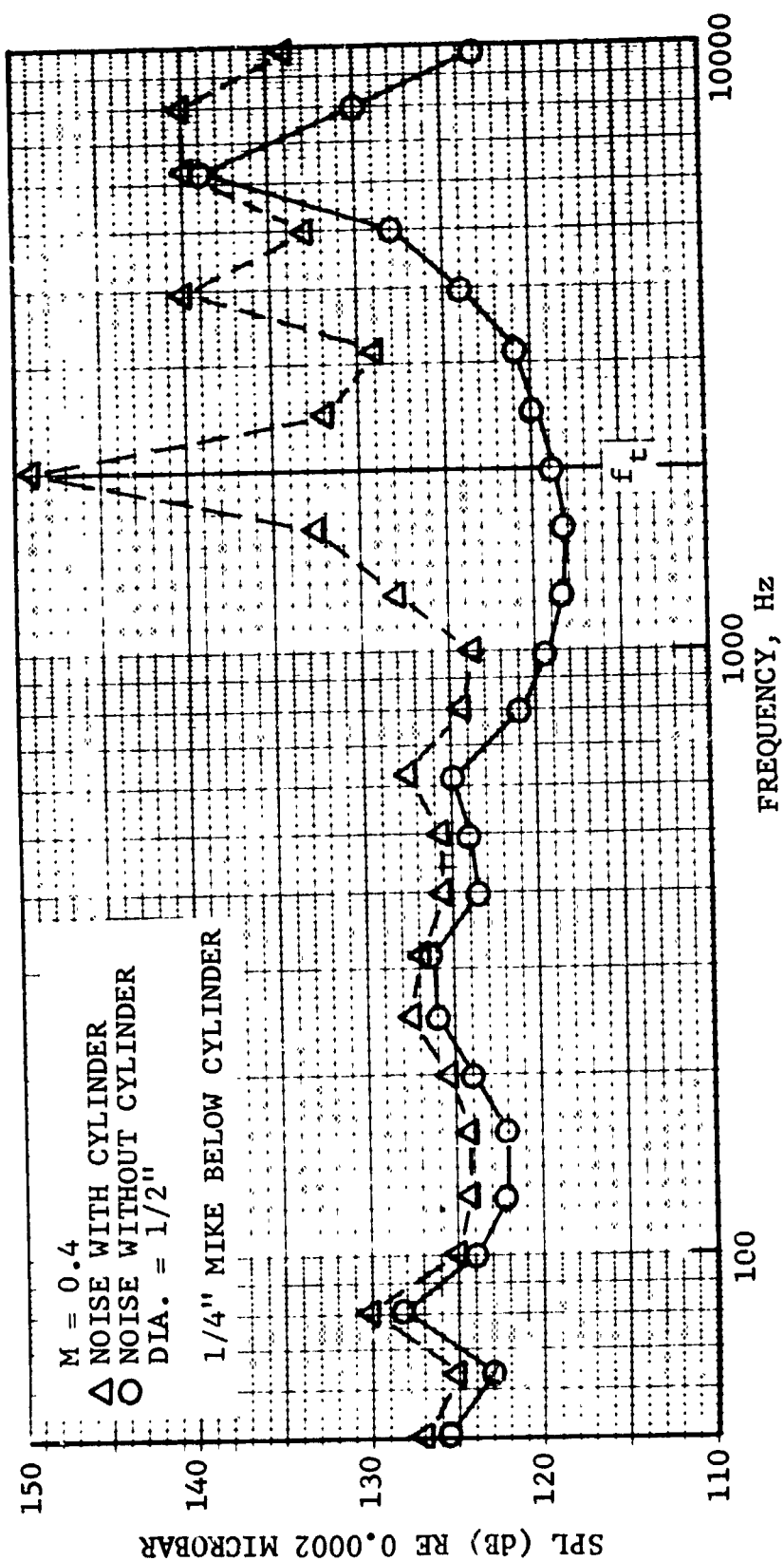


FIGURE II-C36. 1/3 OCTAVE SOUND SPECTRUM OF A 1/2" CYLINDER IMMERSED IN AN AIR STREAM.

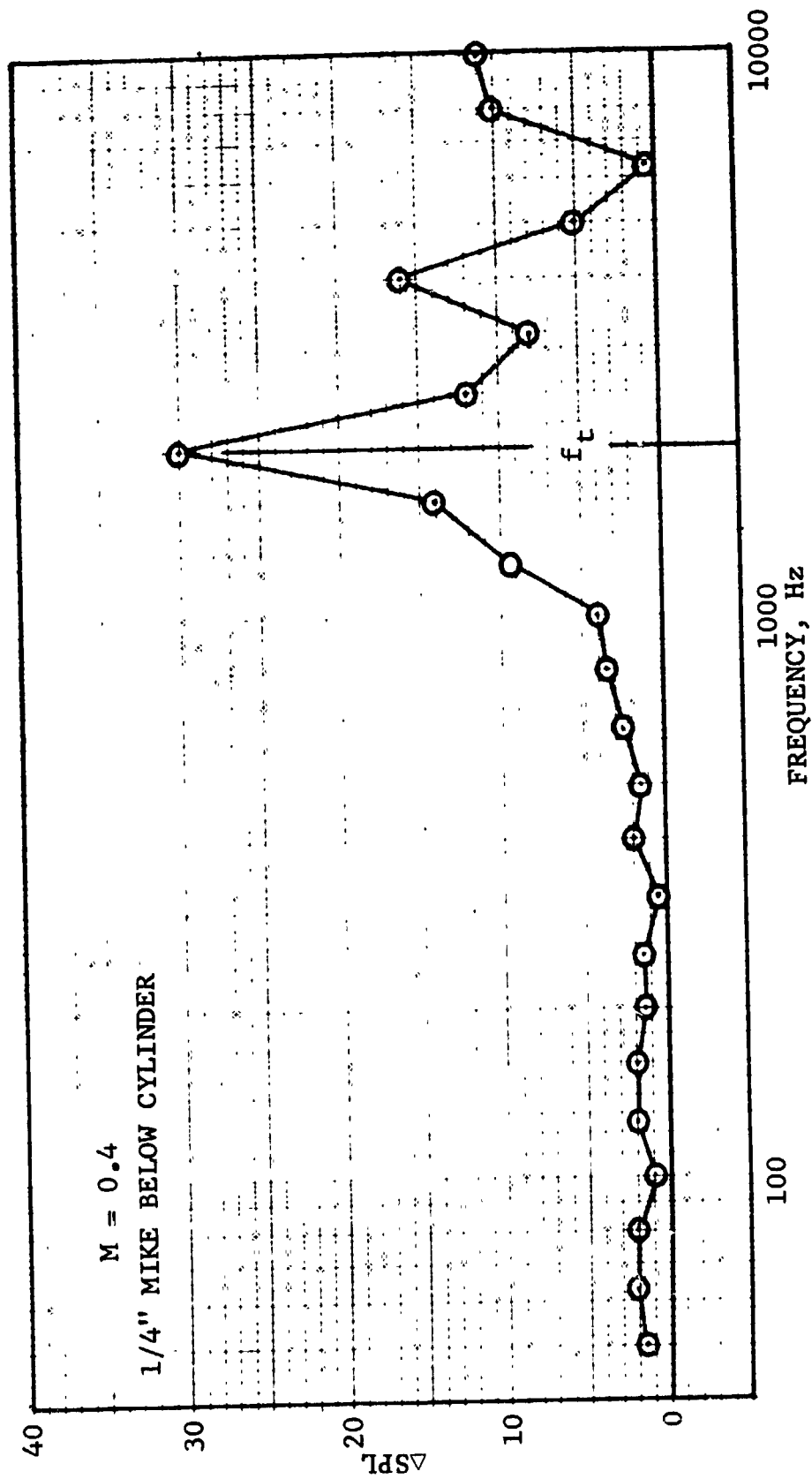


FIGURE II-C37. 1/3 OCTAVE SOUND SPECTRUM OF A 1/2" CYLINDER IMMERSED IN AN AIR STREAM

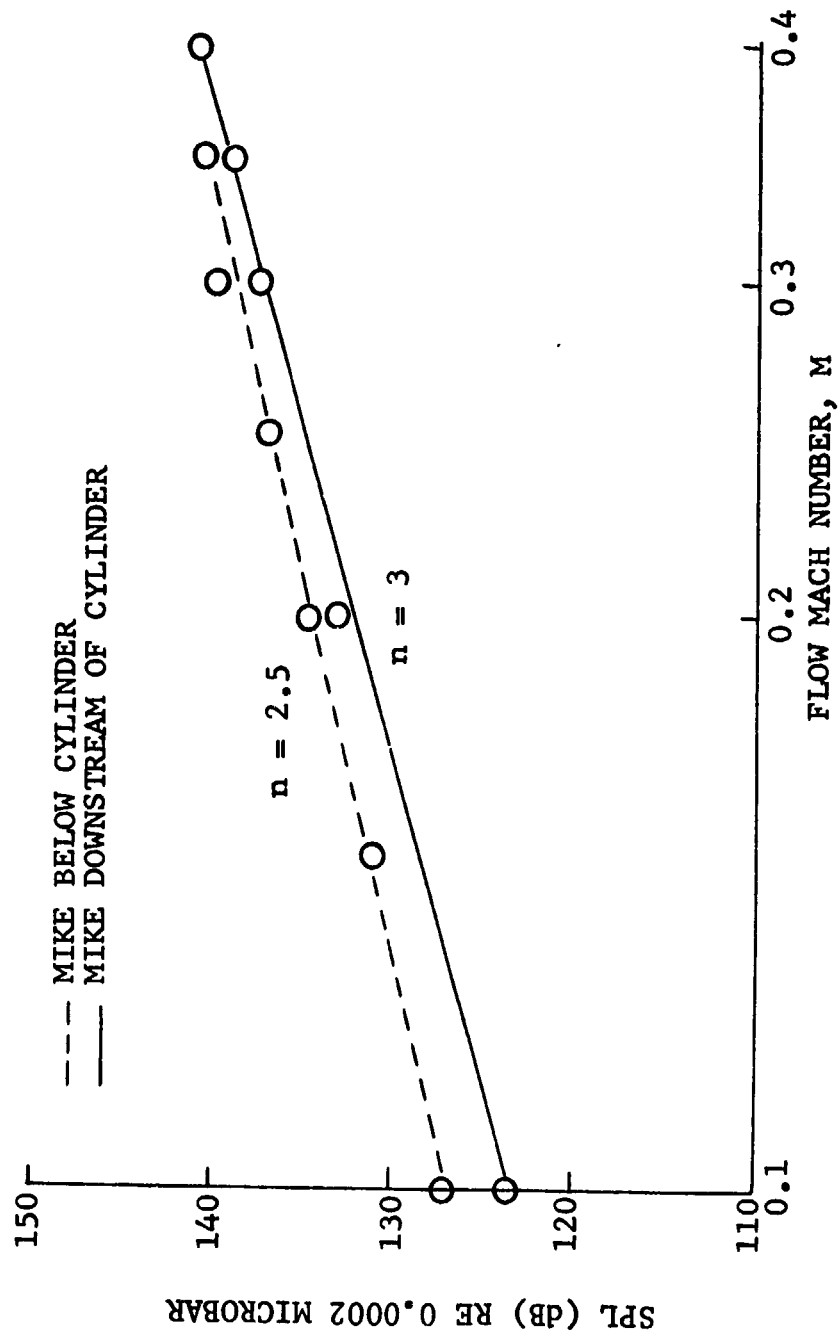


FIGURE II-C38. OASPL OF NOISE WITH AND WITHOUT A 1/2" CYLINDER VS FLOW MACH NUMBER.

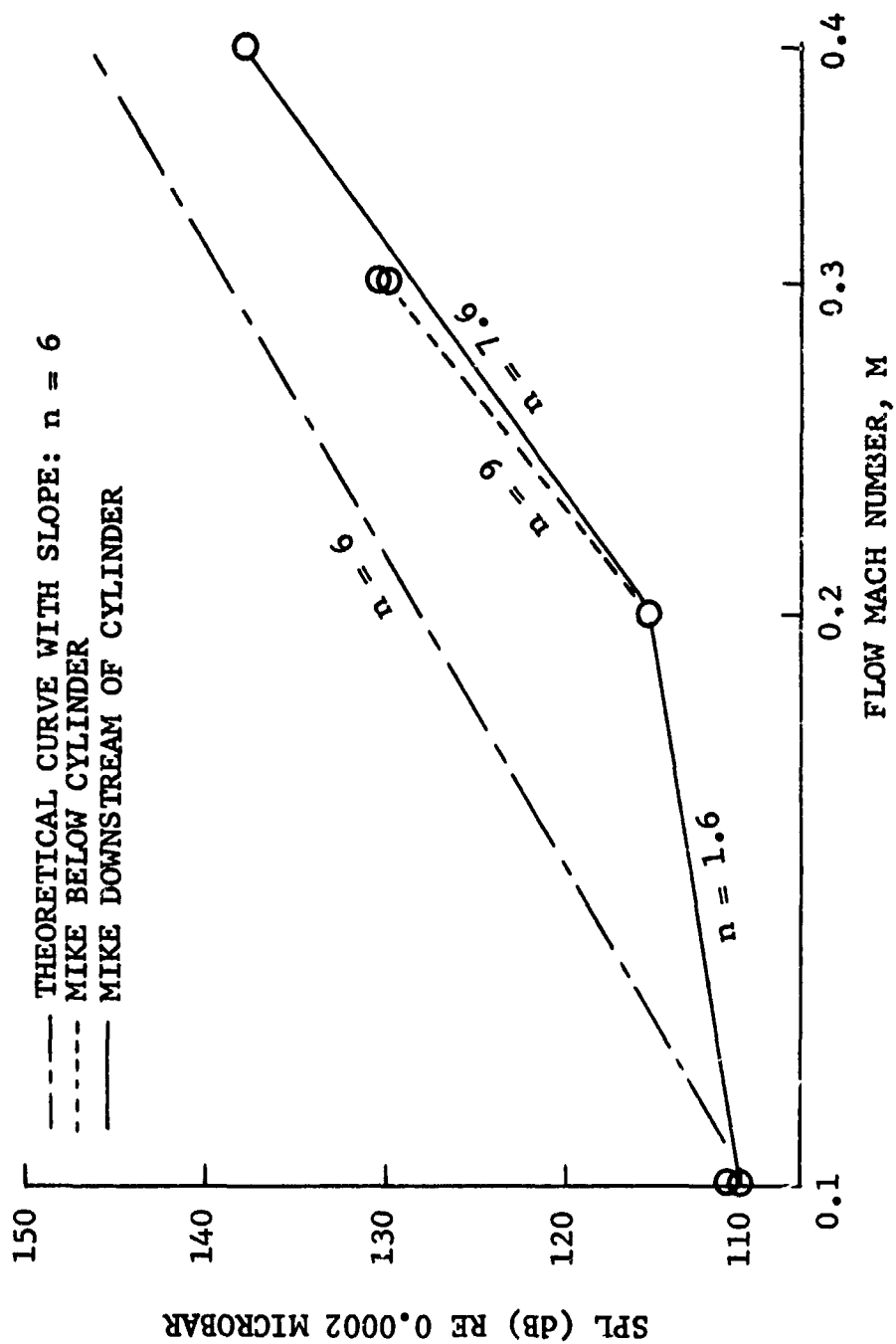


FIGURE II-C39. SOUND PRESSURE LEVEL OF THE FUNDAMENTAL TONE VS. FLOW MACH NUMBER.

and

$$SPL = 10 \log I/I_{ref} + 0.2,$$

it can be shown that the slope of the undisturbed velocity curve can be expressed as:

$$n = \frac{SPL_1 - SPL_2}{10 \log v_1/v_2}$$

where "a" is a constant, "U" the undisturbed velocity of air, and I the intensity of sound. Etkin's (Ref. 3) shows that the value of n is between 5 and 6. In the present experiments the slope of the curves is somewhat greater. Below M=0.2 the slope was equal to 1.6, this is due to the low signal to noise ratio in the subsonic wind tunnel at this low flow Mach numbers.

(c) Symmetric Airfoil Wake Investigation. The wake of a symmetric airfoil (inch chord, 4 inch span, 25% thick) at zero angle of attack was explored at four flow Mach numbers of 0.1, 0.2, 0.3 and 0.4. Velocity and turbulence intensity measurements were made at both upstream and downstream stations. Figure II-C40 depicts the test section in which the airfoil was mounted along with the distances between the various measuring stations. During tests, the turbulence intensity in the axial or X - direction, u'/\bar{U} was measured, together with the turbulence intensity in the spanwise or Z - direction, w'/\bar{U} . In Figure II-C40 the direction of the fluctuating velocity components are drawn at point A. The local mean velocity is denoted by \bar{U} .

Figure II-C41 presents an overall picture of the turbulence intensity u'/\bar{U} on the wake axis as a function of downstream distance, expressed as the dimensionless quantity x/c , (ratio of downstream distance to airfoil chord). Far away from the airfoil turbulence intensities comparable to the inlet turbulence intensities are reached. As can be seen, the turbulence intensities decrease for increasing Mach number; however, the u' turbulence values are increasing. The u' value was obtained by averaging the output of the sensor for 3 seconds. In Figure II-C42 the u' turbulence on the wake axis two chord lengths downstream of the airfoil versus four flow Mach numbers is plotted and is seen to be increasing.

Figure II-C43 and 44 are plots of the turbulence intensity u'/\bar{U} , at two downstream stations, for four flow Mach numbers (as a function of immersion y/c). As may be noted, the intensities decrease rapidly beyond a distance of 3 airfoil chords. Approximately 11 inches downstream, the effect of the airfoil on turbulence is hardly evident. Thus, the axial extent of the wake of this airfoil is, for all practical purposes, 3 airfoil chords. This information is important in establishing the correlation volume in the analysis of broadband noise generation (See Section II-B2).

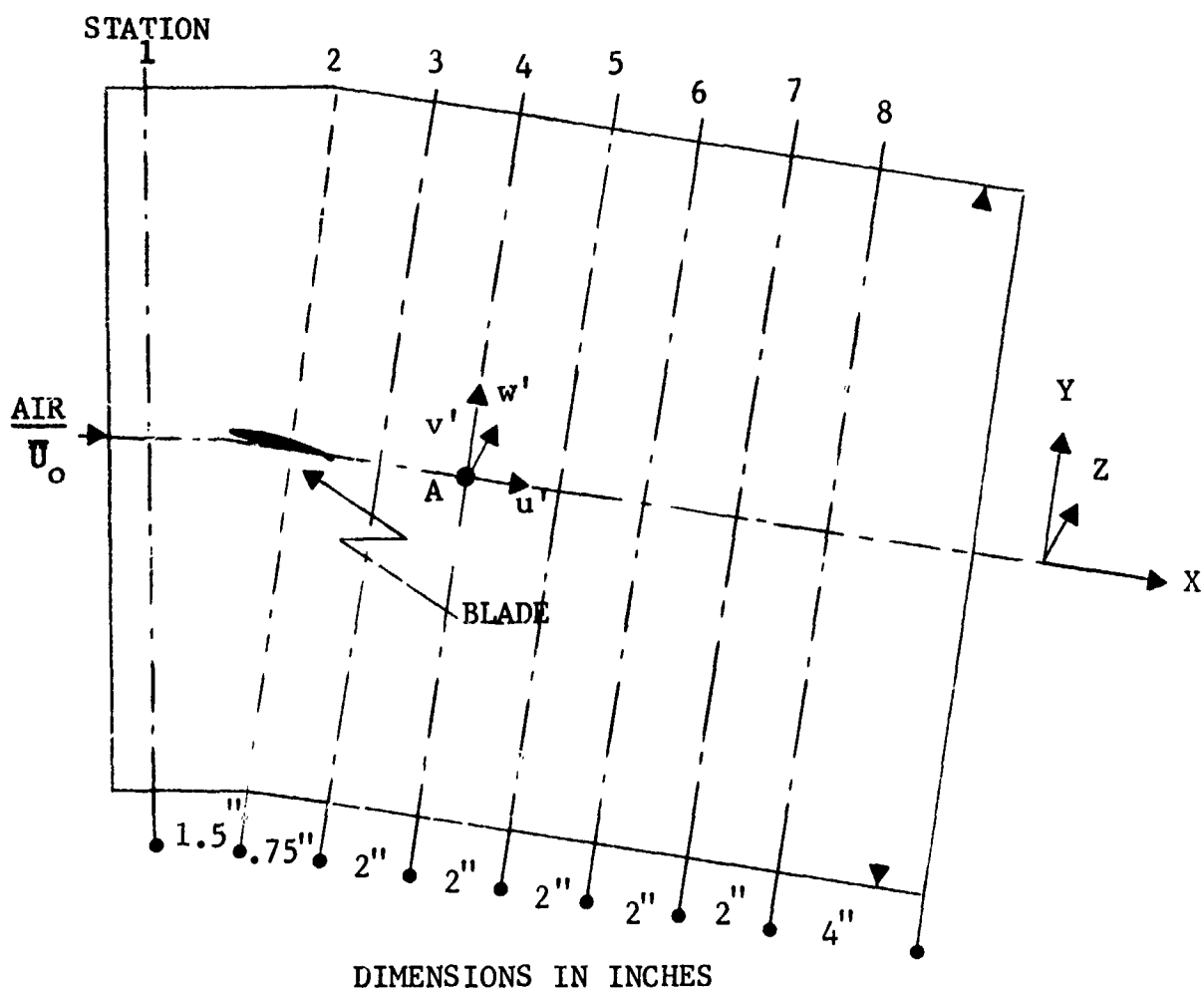


FIGURE II-C40. TEST SECTION WITH UPSTREAM AND DOWNSTREAM MEASURING STATIONS.

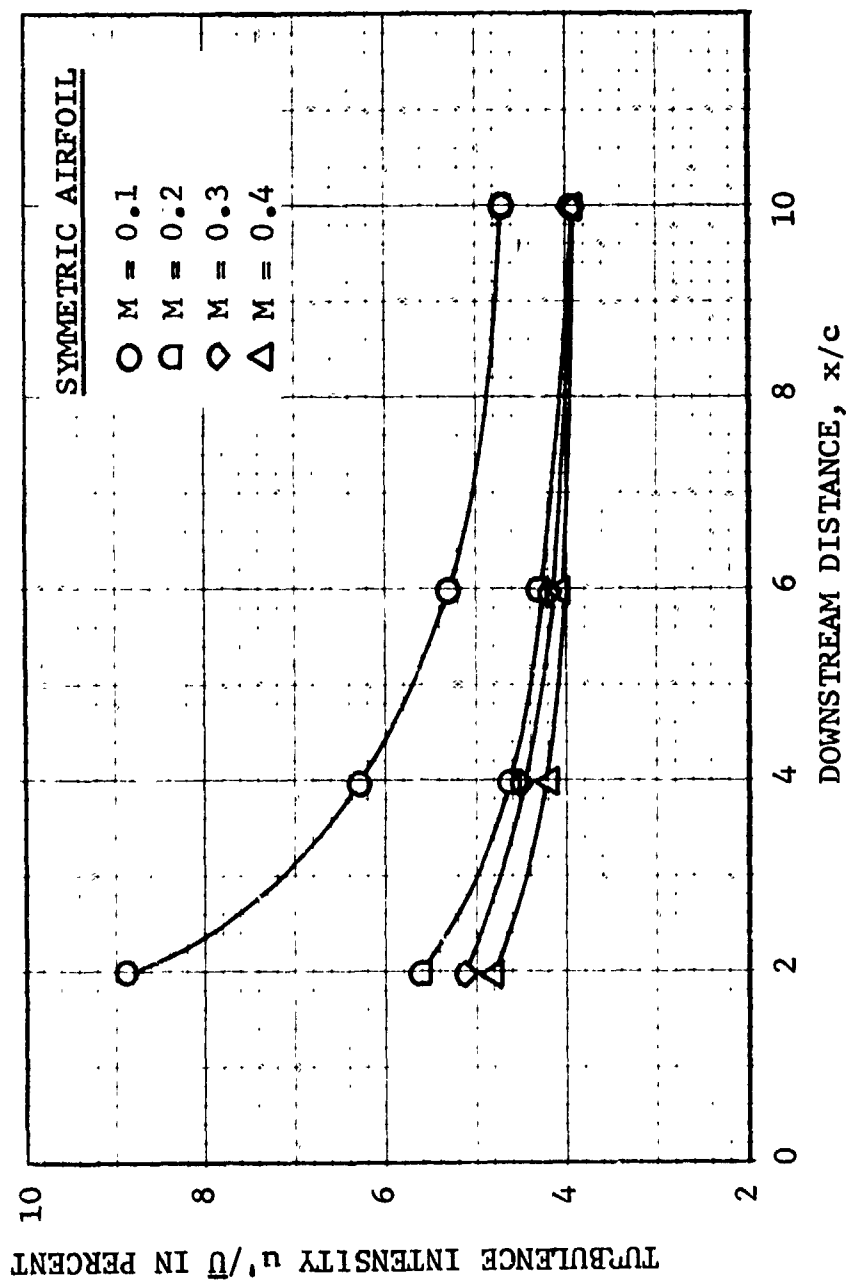


FIGURE II-C41. TURBULENCE INTENSITY ON THE WAKE AXIS OF A SYMMETRIC AIRFOIL VS. DOWNSTREAM DISTANCE.

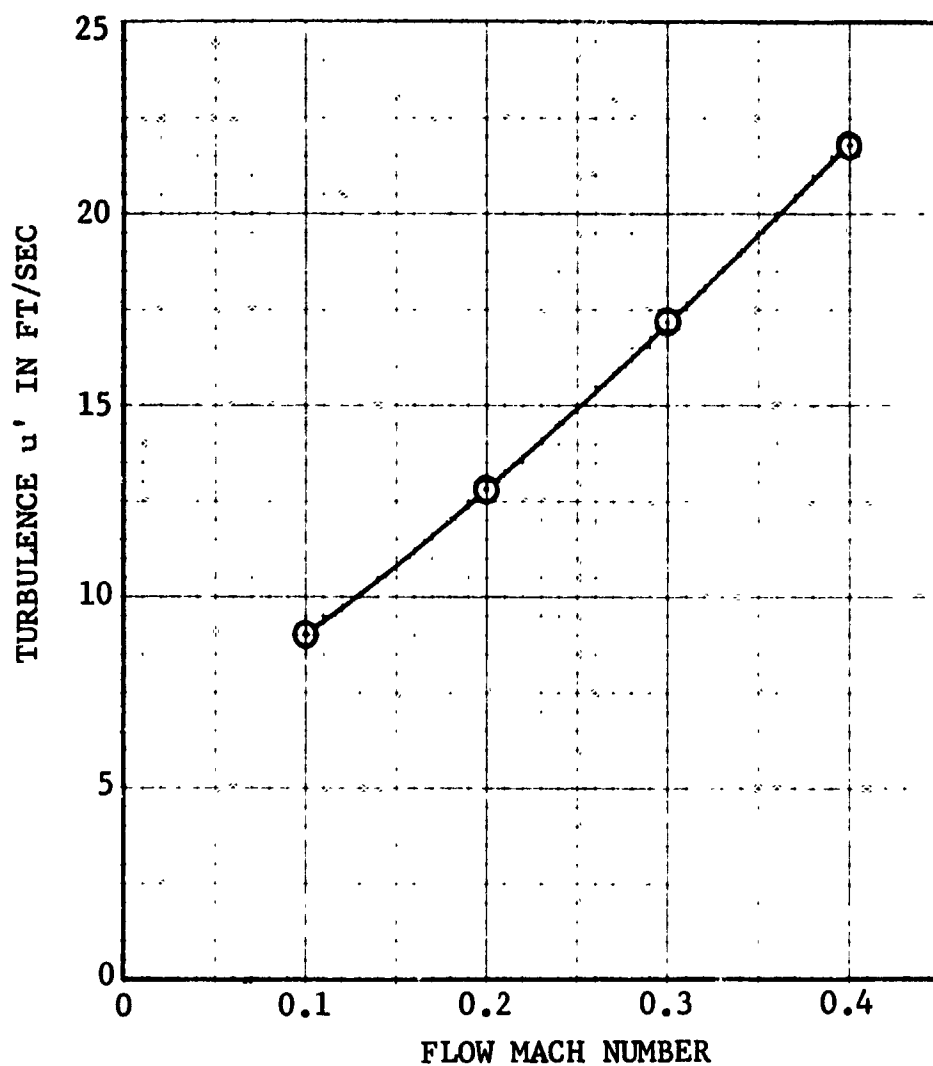


FIGURE II-C42. TURBULENCE ON THE WAKE AXIS, TWO CHORD LENGTHS DOWNSTREAM OF A SYMMETRIC AIRFOIL

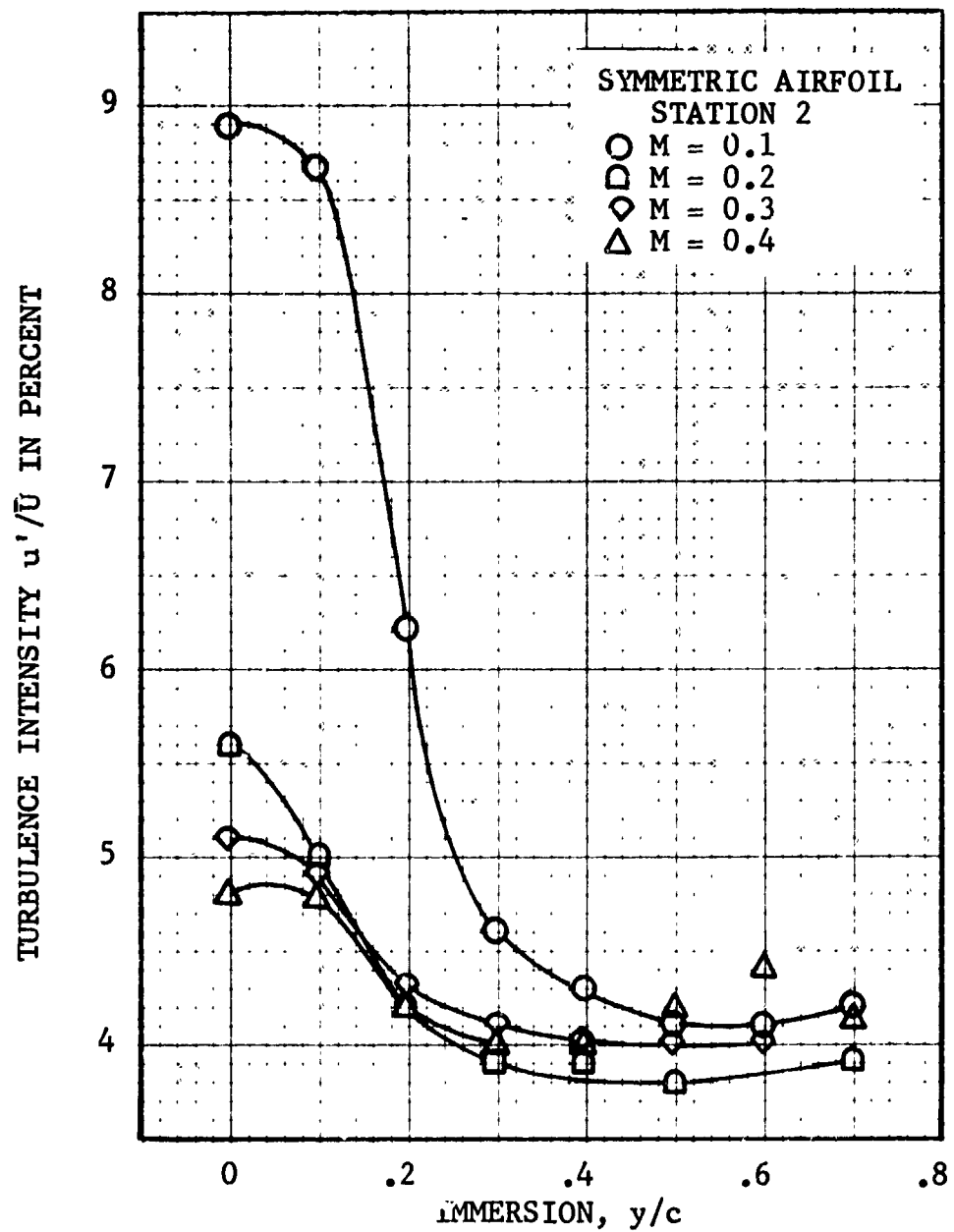


FIGURE II-C43. TURBULENCE INTENSITY OF A SYMMETRIC AIRFOIL VS IMMERSION

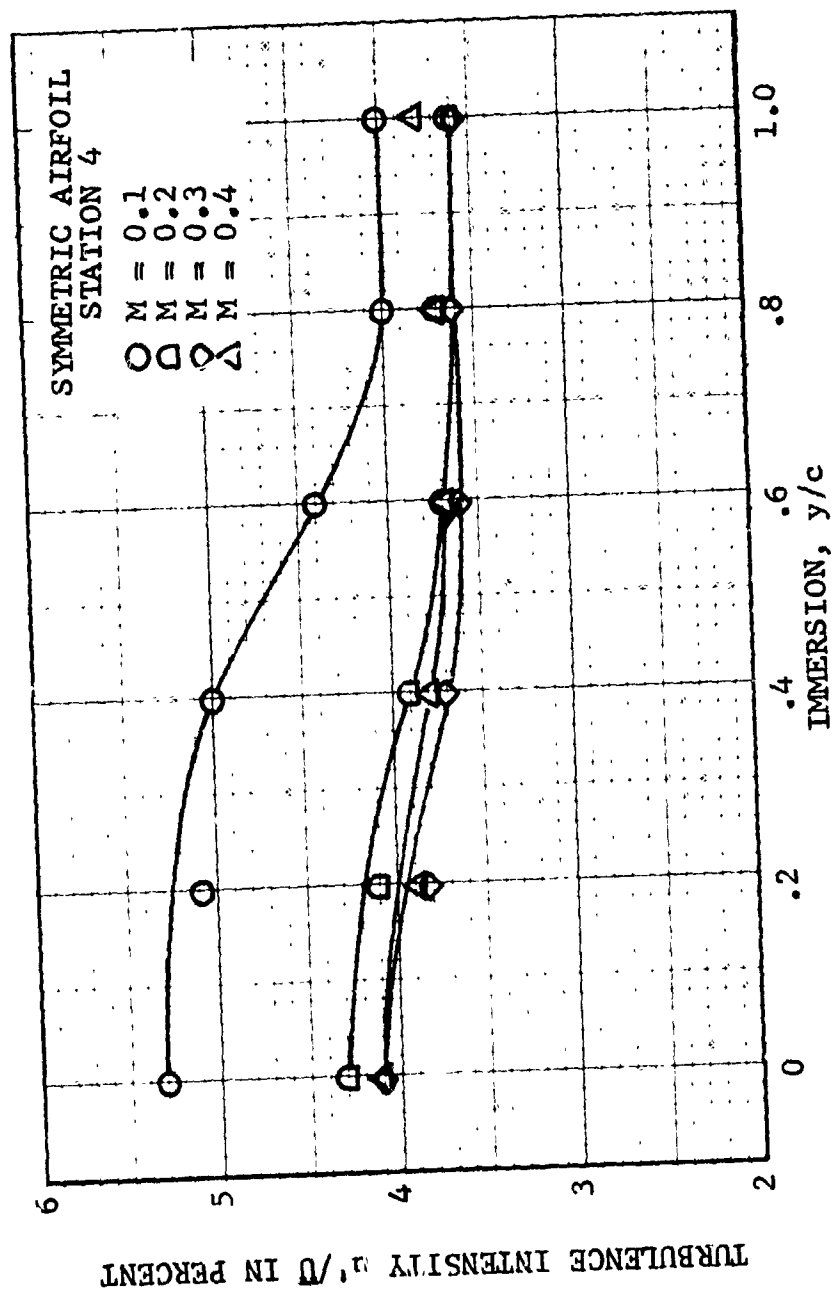


FIGURE II-C44. TURBULENCE INTENSITY OF A SYMMETRIC AIRFOIL VS. IMMERSION.

In Figures II-C45 and 46 the turbulence intensity w'/\bar{U} is plotted as a function of immersion y/c . Comparing u'/\bar{U} at the same station, for example, Figures II-C43 and 46 it is evident that w' is smaller than u' .

An overall picture of w'/\bar{U} versus downstream distance is given in Figure III-C47.

Thus, in the two dimensional case being examined the u' turbulence is the dominant turbulence component. And, as in the case of the cylinder the wake turbulence intensity increases with Mach number relative to the airfoil.

(4) Transonic Wind Tunnel Tests of Thin Airfoils. Tests were carried out with a cascade of thin airfoils (chord length: 2.7 inches, t/c : 2.2%) in a transonic wind tunnel facility. A sketch of this tunnel with its assembled blade package is shown in Figure II-C3.

The incoming air velocity was varied from 452 ft/sec to 891 ft/sec while the turbulence intensities were measured one chord length downstream of the cascade. Turbulence measurements in both the mean flow direction, u'/\bar{U} and in the direction perpendicular to the span of the airfoils v'/\bar{U} were recorded. As in the previous subsonic isolated airfoil tests, hot film sensors were utilized. In addition sound measurements were made during testing in the cascade using a 1/2 inch Bruel and Kjaer condenser microphone. The microphone was located 6 feet from the exit measuring station in the cascade tunnel.

Before examining the wake of the airfoils the magnitude of the inlet turbulence intensities i.e., the intensities one chord length upstream of the cascade were determined. The inlet turbulence intensities were recorded in the center of the four inch wide rectangular cascade duct while varying the inlet Mach number (M). At $M = 0.4, 0.5, 0.7$ the corresponding u'/\bar{U} 's were 1.3, 1.1, 0.7 percent and v'/\bar{U} 's 1.2, 1.1, 0.7 percent respectively. These values are small enough so that the turbulence intensities in the wakes of the airfoils can be distinguished from the tunnel turbulence levels. A total pressure profile measurement was also taken across the width of the duct, upstream of the cascade at $M = 0.7$, using a Pitot tube. Results are plotted as the ratio of the total plenum pressure to the inlet total pressure in Figure II-C48. The pressure profile is flat, away from the walls.

The cascade consisted of 11 airfoils capable of being placed at various angles of attack, corresponding to various incidence angles. The incidence angle being defined as the angle between the tangent to the airfoil's mean camber line at the leading edge, and the inlet air direction. Characteristics of this cascade are shown in Figure II-C49.

Figure II-C50, 51, and 52 show the mean axial velocity distribution behind the cascade for, respectively, free stream Mach numbers of .4, .5, and .7. As would be expected the velocity defects increase with increasing Mach numbers. Or what is more important from the acoustic point of view, the wake volume increases (see Section II-B2).

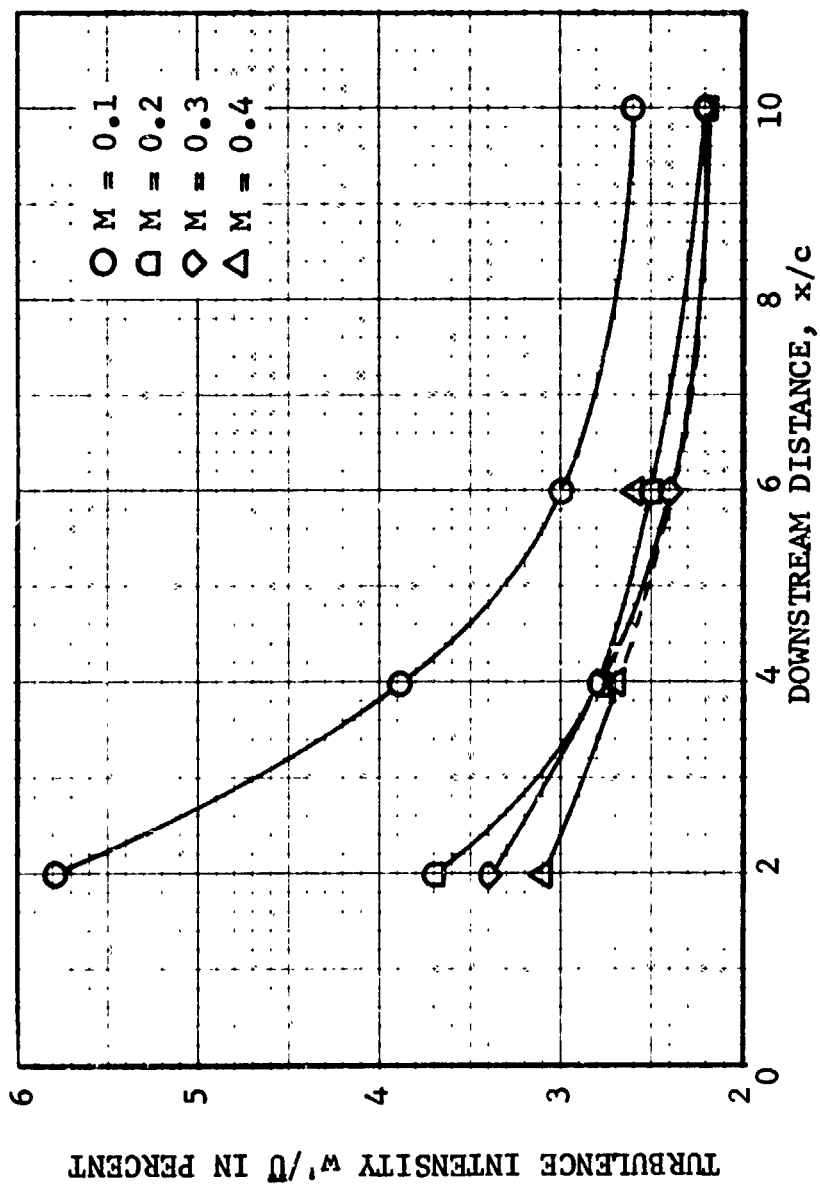


FIGURE II-C45. TURBULENCE INTENSITY ON THE WAKE AXIS OF A SYMMETRIC AIRFOIL VS. DOWNSTREAM DISTANCE

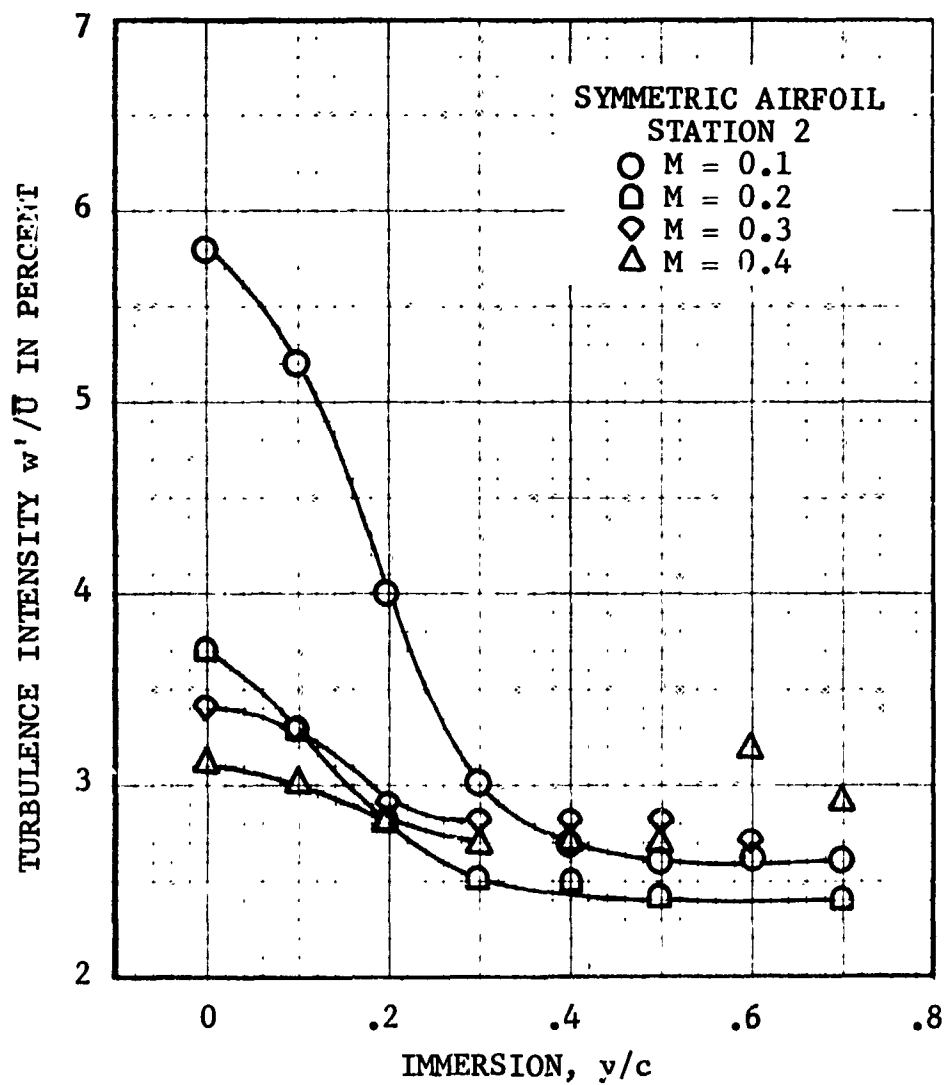


FIGURE II-C46. TURBULENCE INTENSITY OF A SYMMETRIC AIRFOIL VS. IMMERSION

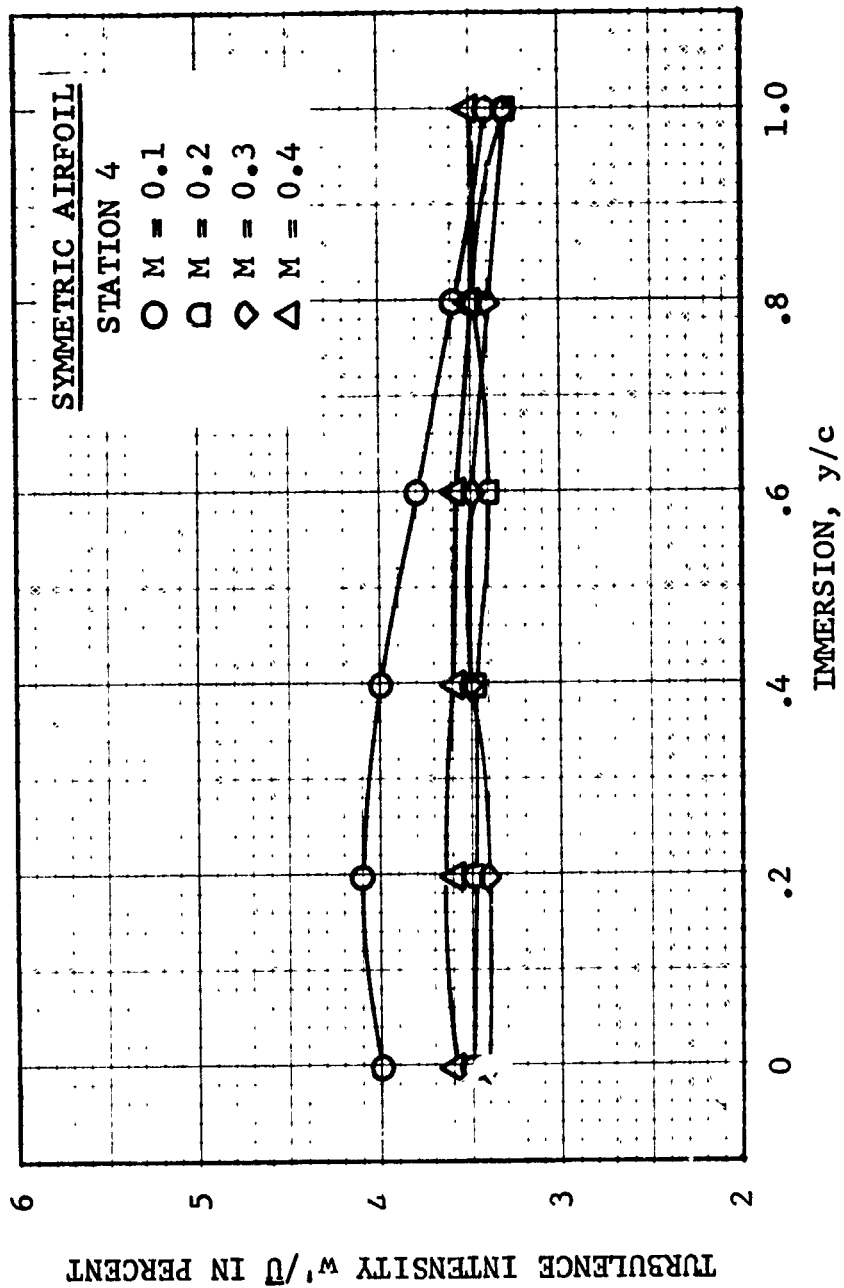


FIGURE II-C47. TURBULENCE INTENSITY OF A SYMMETRIC AIRFOIL VS. IMMERSION.

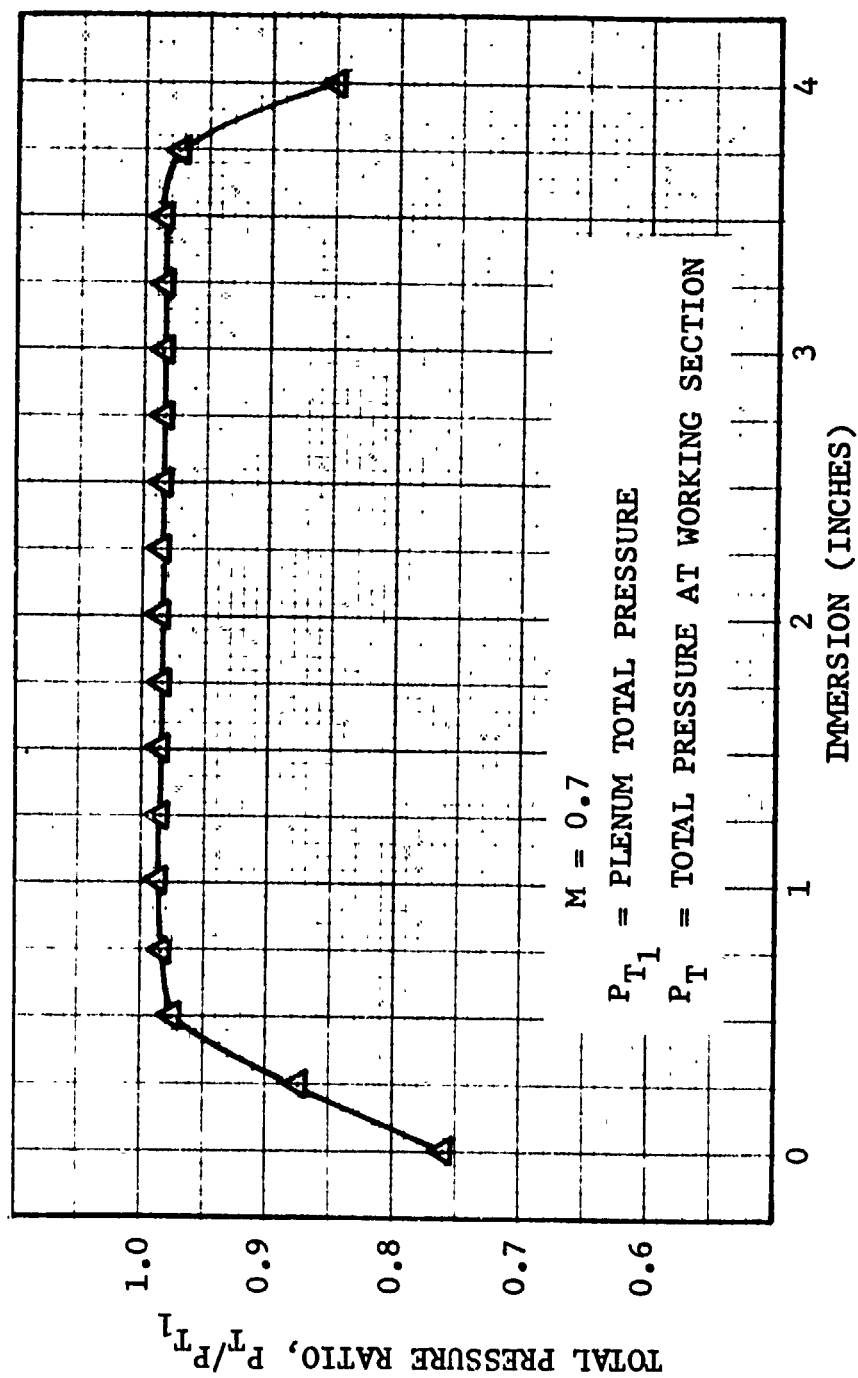
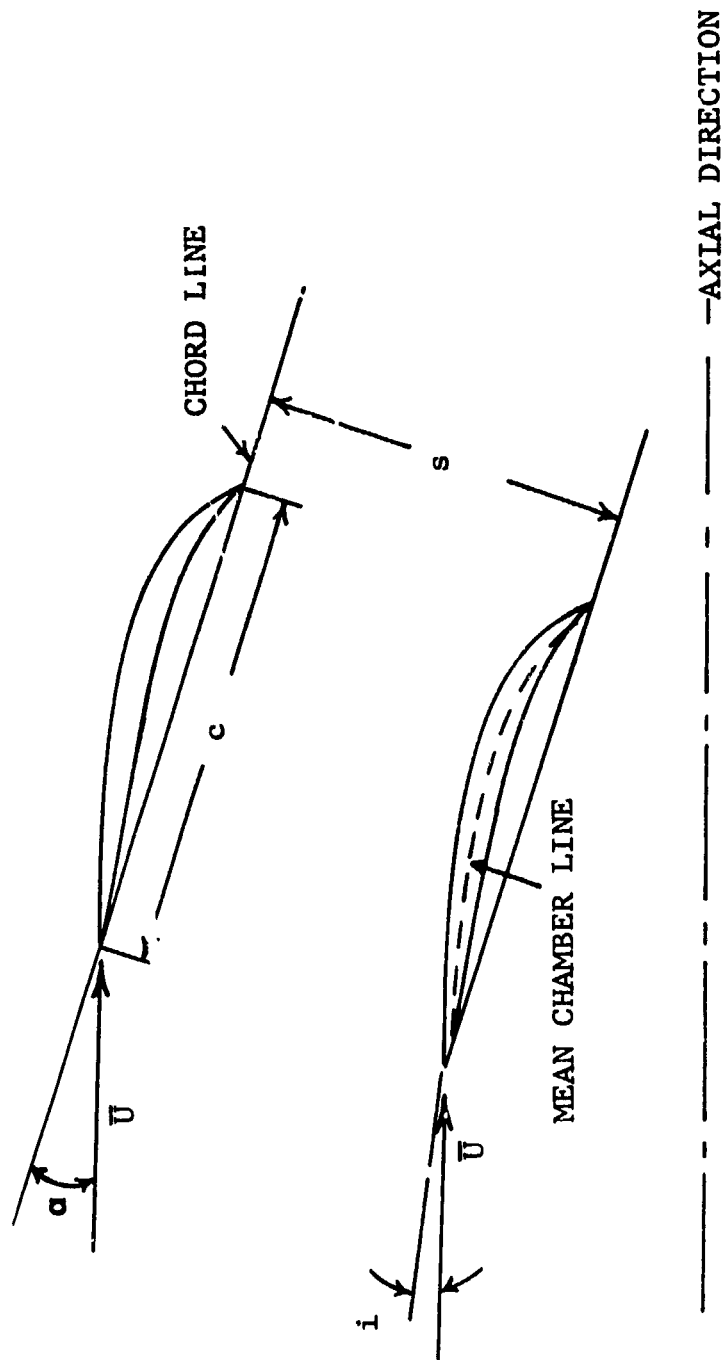


FIGURE II-C48. TOTAL PRESSURE PROFILE ACROSS THE DUCT.



SOLIDITY $(c/s) = 1.3$
 SPACING $s = 2.09$

FIGURE II-C49. CASCADE CHARACTERISTICS

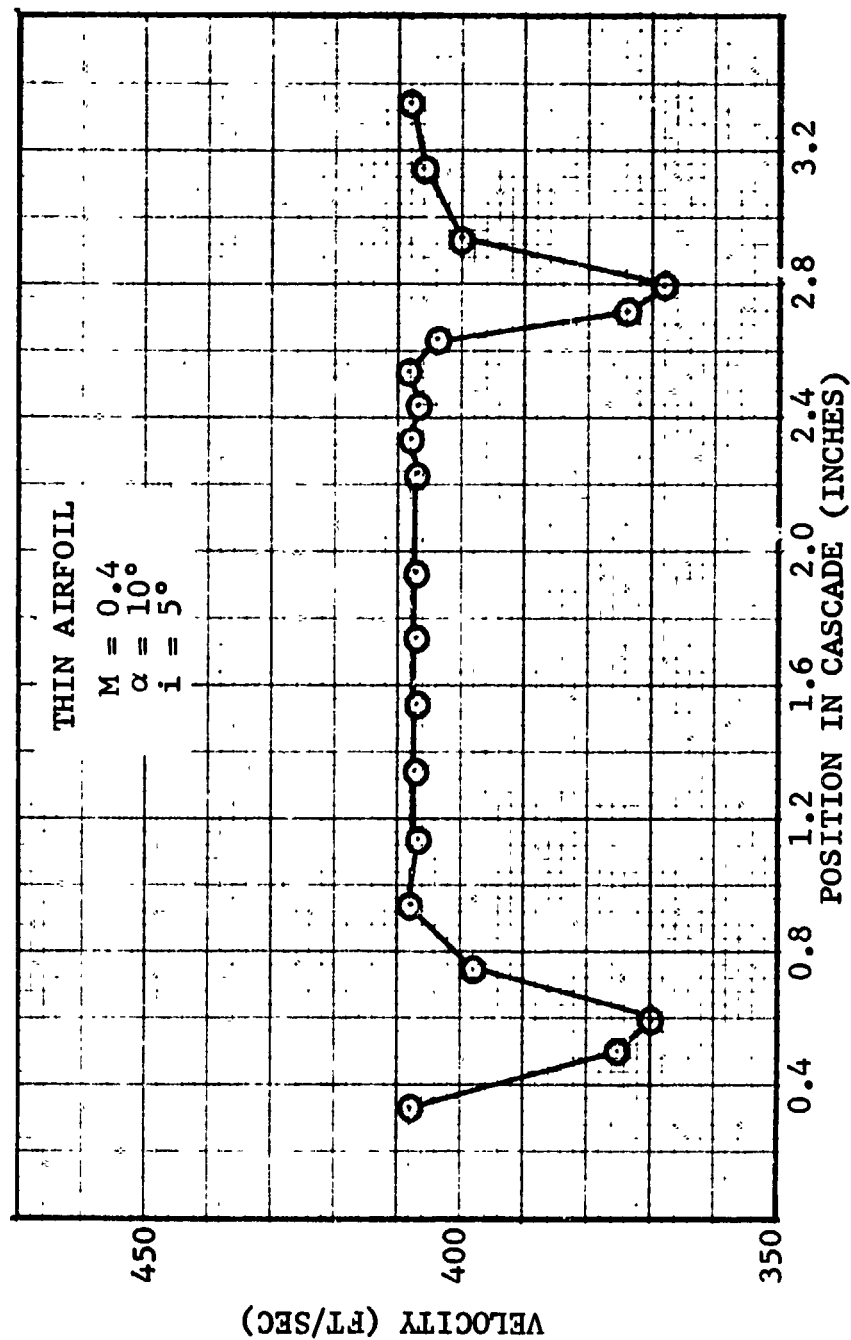


FIGURE II-C50. MEAN VELOCITY PROFILE, ONE CHORD DOWNSTREAM OF CASCADE.

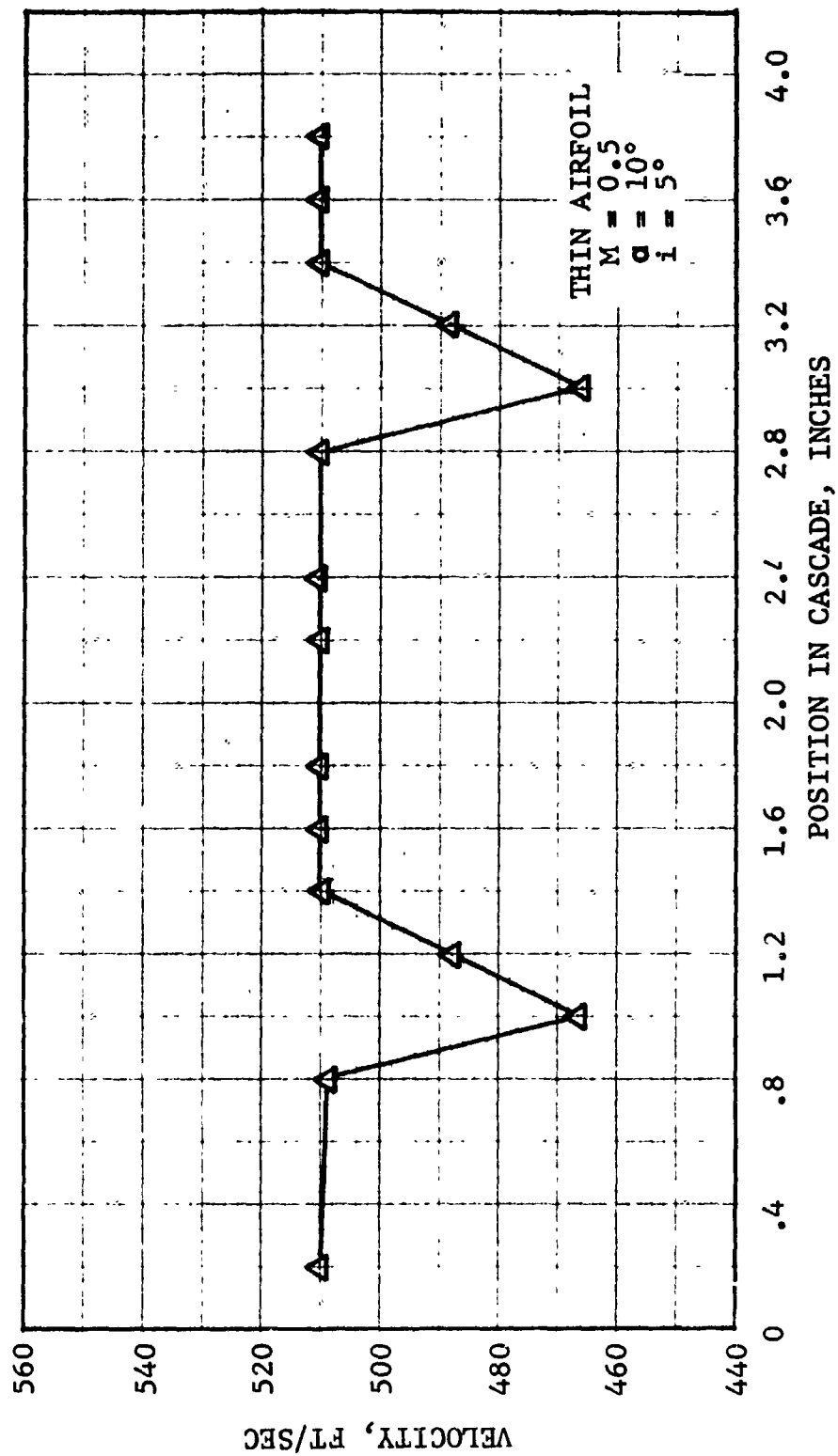


FIGURE II-C51. MEAN VELOCITY PROFILE, ONE CHORD DOWNSTREAM OF CASCADE.

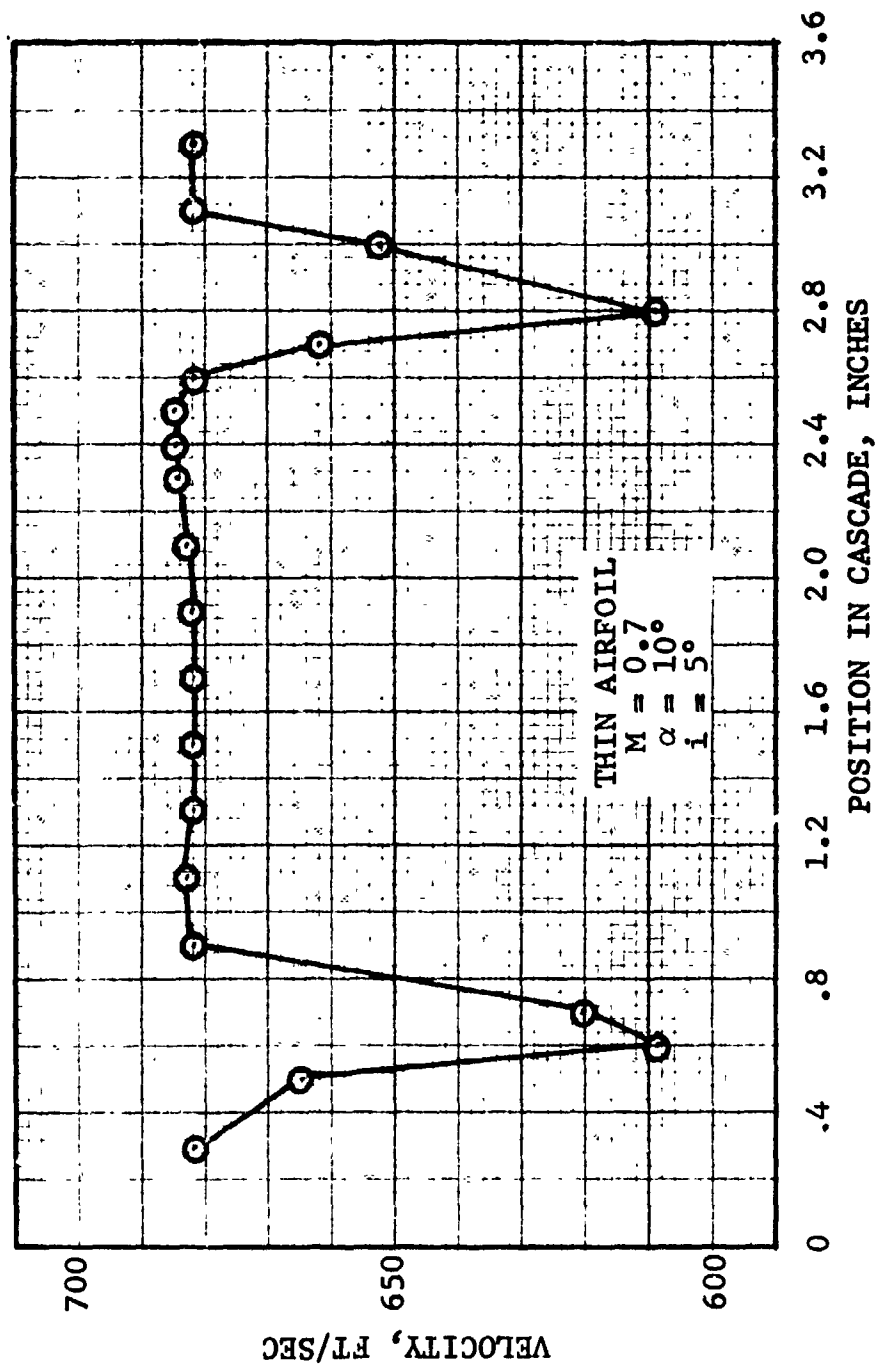


FIGURE II-C52. MEAN VELOCITY PROFILE, ONE CHORD DOWNSTREAM OF CASCADE.

The next 6 figures show the velocity turbulences. As has been noted previously, the turbulence intensity decreases with increasing Mach number; however, the absolute turbulence level increases. Figures II-C59 through 62 show the turbulence levels at .4 and .7 Mach numbers. The increase in u' and v' turbulences with Mach number is clearly seen.

Figure II-C63 is an overlay of the noise data at .4 and .7 Mach number. The broadband noise has increased over most of the audible frequency range at the higher Mach number. Figures II-C64 and 65 contain the corresponding turbulence components u' and v' at both Mach numbers. The increase in both turbulence components with Mach number can be seen.

It is interesting to note that at 12 KHz, there is a peak in both the turbulence (Figures II-C64 and 65) and noise (Figure II-C63) spectra. This peak is believed to be associated with the fluctuation of the airfoil's lift vector.

Another parameter which is important to broadband noise generation is incidence angle. Figure II-C66 shows the mean axial velocity distribution at a Mach number of .7 at two different incidence angles. It is obvious that the increased incidence angle has deepened the wake velocity defect. Figures II-C67 and 68 show the turbulence spectra at 3 incidence angles. In general, the turbulence has increased all across the spectrum with increasing incidence angle.

Figure II-C69 is an overlay of the tunnel noise (no cascade), noise at an incidence angle of 5° , and noise at an incidence angle of 7.5° . The background noise due to the facility is at least 10 dB below the noise with the cascade package in place. The 7.5° incidence angle noise is generally above the 5° incidence angle data; this is particularly true at 12 KHz. Looking back to the turbulence data of Figures II-C67 and 68, it can be seen that a large turbulence increase also occurred at 12 KHz. This is due to the increased lift being generated at the higher incidence angle which, in turn, results in higher noise and turbulence at the characteristic lift fluctuation frequency.

(5) Summary of Wind Tunnel Results. In both subsonic isolated element tests and in cascade tests, the increased generation of broadband noise with increasing relative Mach number was clearly demonstrated. In addition, the content of the noise spectra and the wake turbulence spectra were shown to be related in so far as peaks in the turbulence spectra occurred at the same frequency as peaks in the noise spectra.

Utilizing a cascade of airfoils, it was shown that the noise and turbulence levels increased with increasing incidence angle.

These results suggest that two ways of reducing broadband noise are to reduce relative Mach numbers and/or bring incidence angles closer to optimum (minimum wake turbulence) angles.

(6) Rotating Wake Measurements. In order to better understand the viscous wake properties which affect noise generation on both rotating and non-rotating blades, the hot film instrumentation previously used in the cascade was mounted on a General Electric high bypass ratio single stage fan development vehicle. Traverses were made behind the rotor about one rotor chord downstream and behind the OGV's. The immersion positions are shown in Table II-C2.

Position Number	Radial Immersion Depth, Inches
1	.53
2	1.64
3	2.83
4	4.12
5	5.56

TABLE II-C2
Probe Positions and Immersion Depths

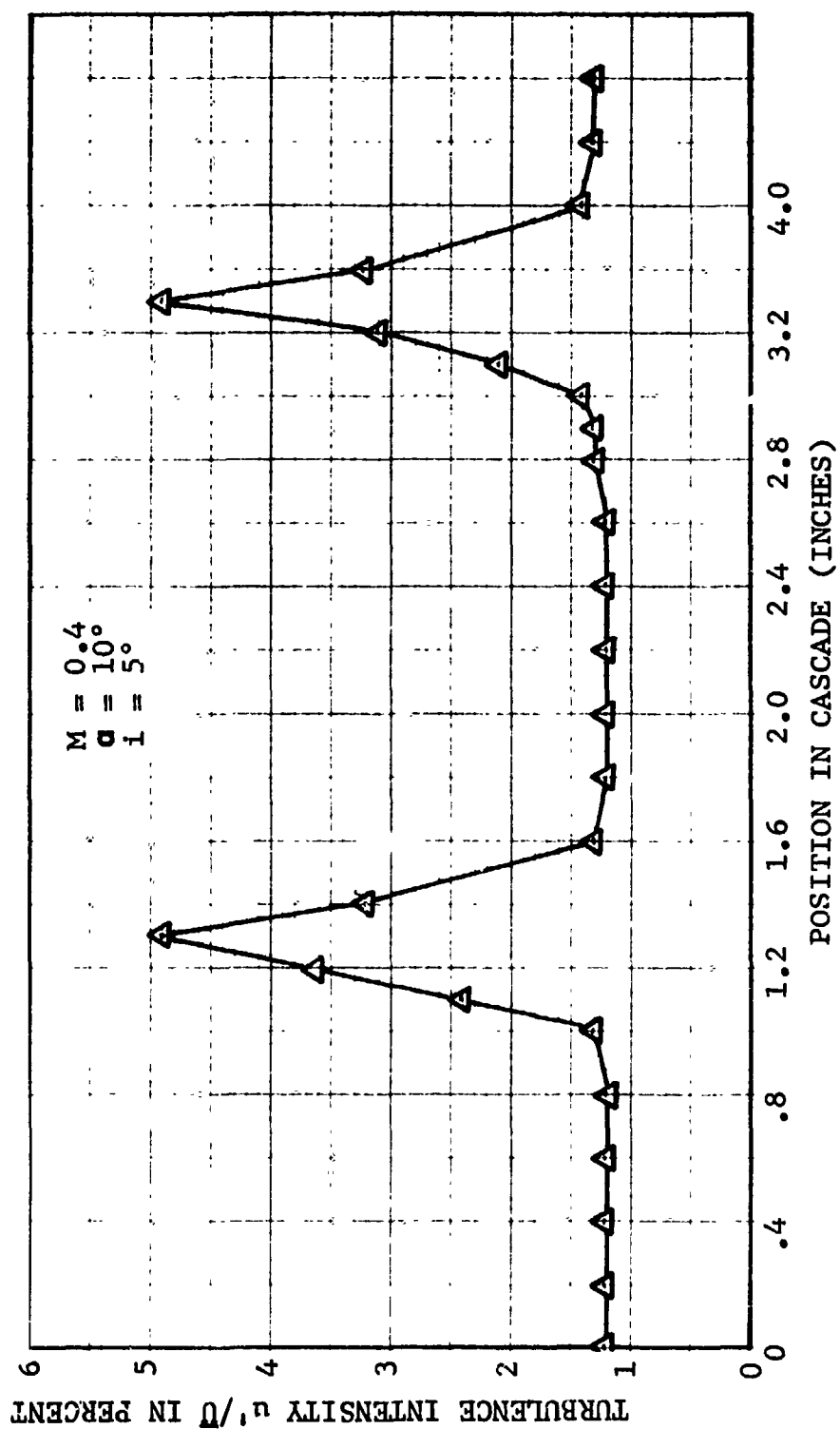


FIGURE II-C53. TURBULENCE INTENSITY VS POSITION IN CASCADE TRANSONIC TUNNEL
FOR A TIP SECTION AIRFOIL ON D/V #4

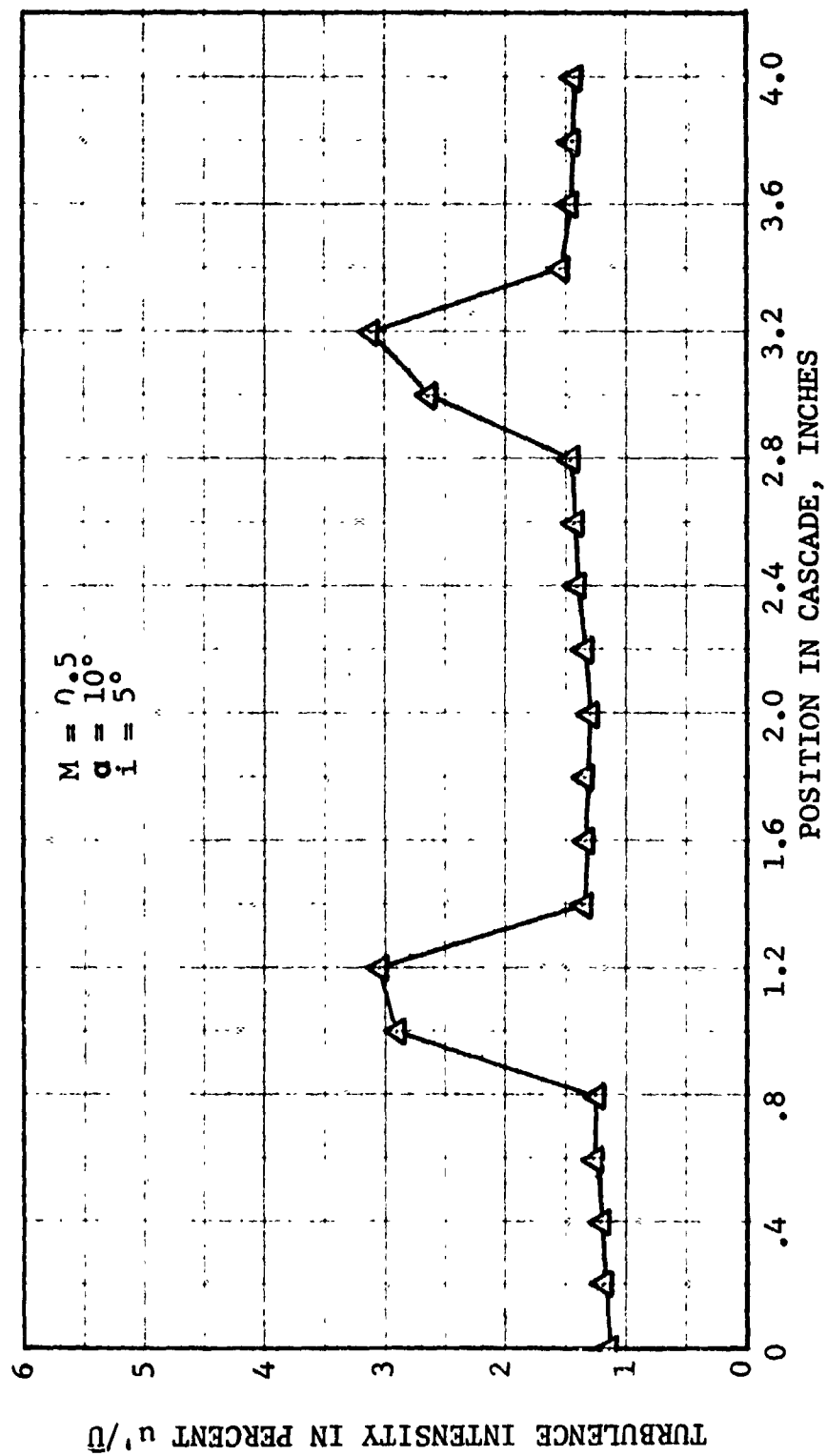


FIGURE II-C54. TURBULENCE INTENSITY VS POSITION IN CASCADE TRANSONIC TUNNEL FOR A TIP SECTION AIRFOIL ON D/V #4

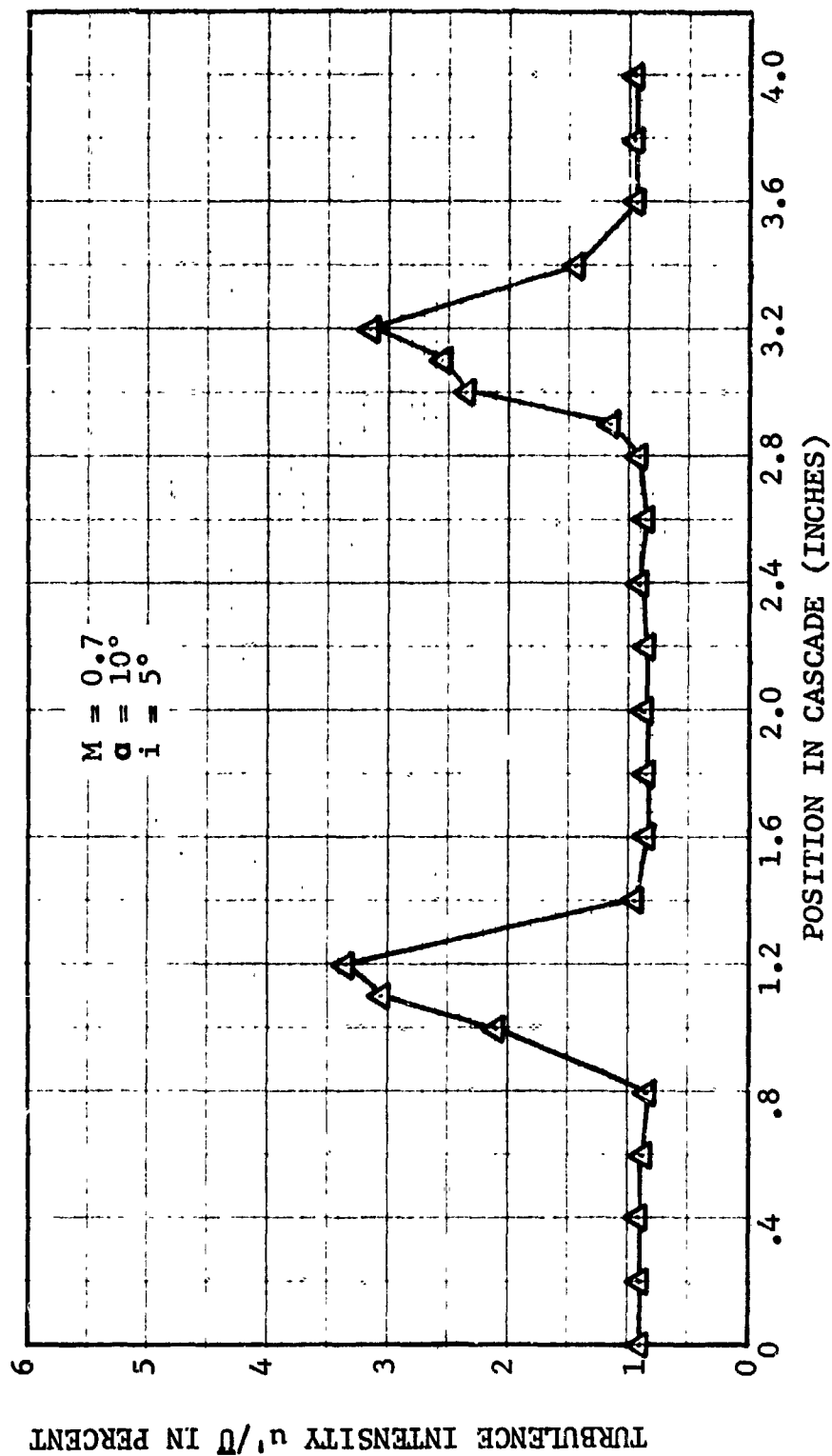


FIGURE II-C55. TURBULENCE INTENSITY VS POSITION IN CASCADE TRANSONIC TUNNEL
FOR A TIP SECTION AIRFOIL ON D/V #4

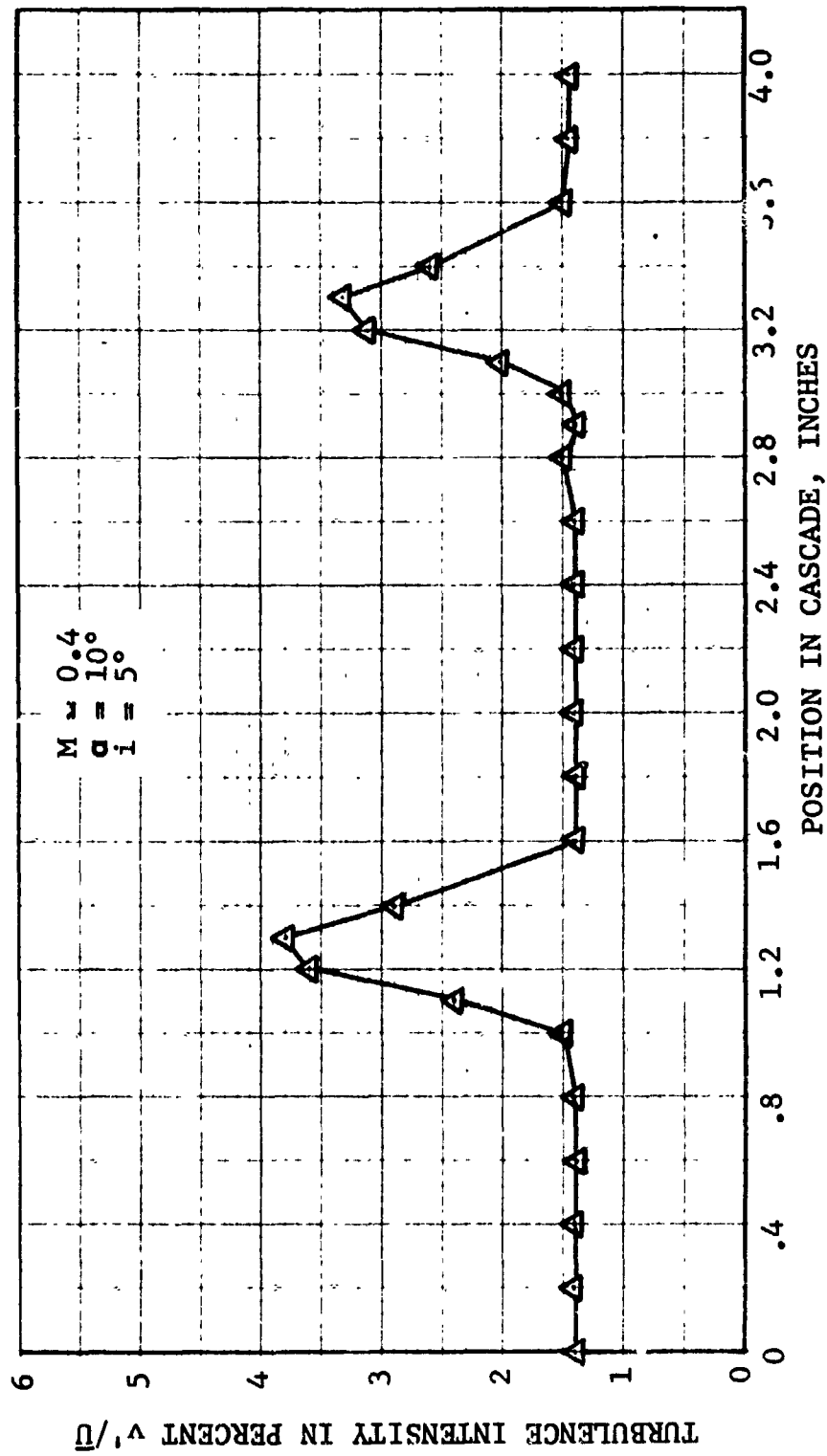


FIGURE II-C56. TURBULENCE INTENSITY VS POSITION IN CASCADE TRANSONIC TUNNEL FOR A TIP SECTION AIRFOIL ON D/V #4

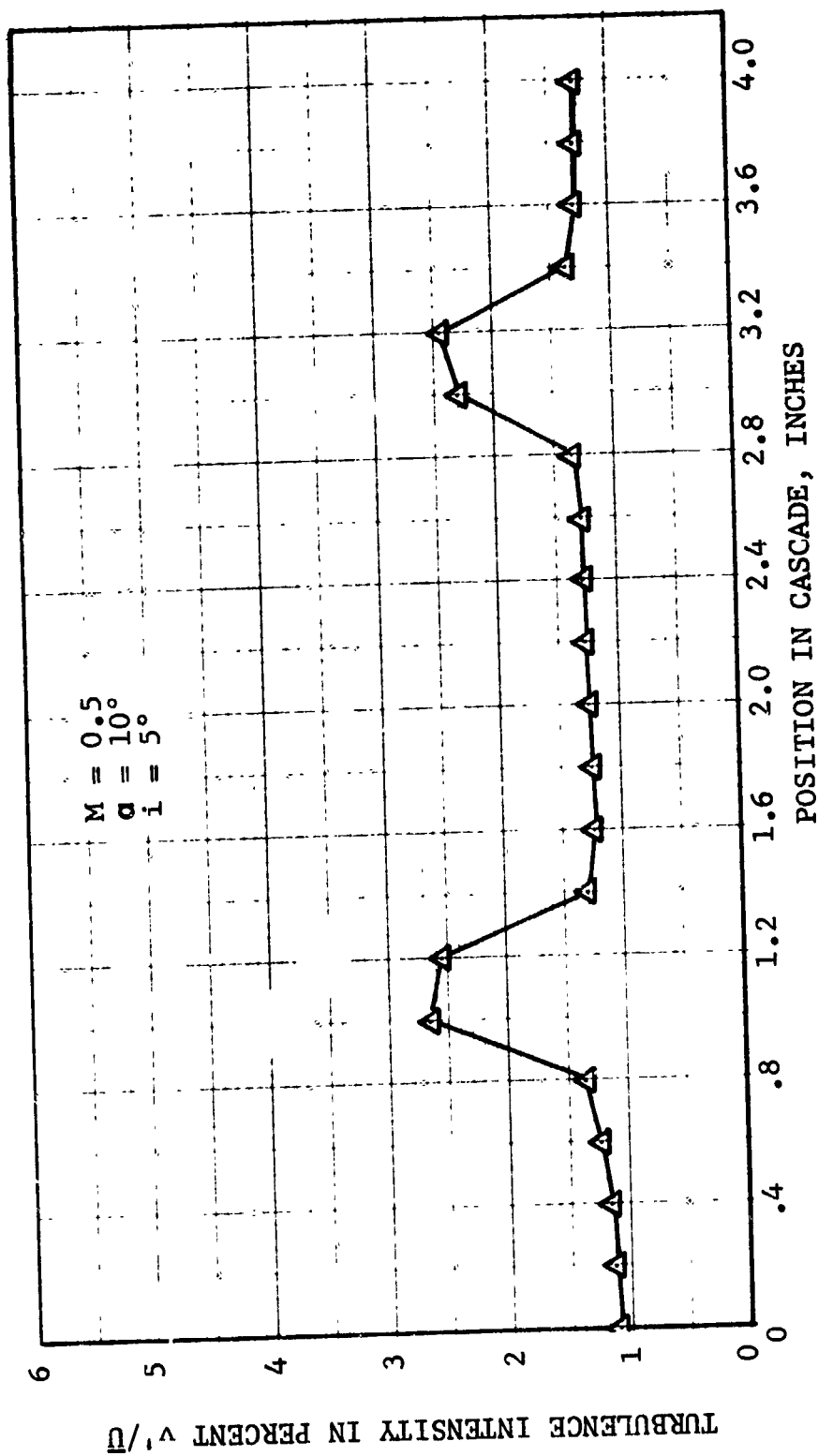


FIGURE II-C57. TURBULENCE INTENSITY VS POSITION IN CASCADE TRANSONIC TUNNEL FOR A TIP SECTION AIRFOIL ON D/V #4

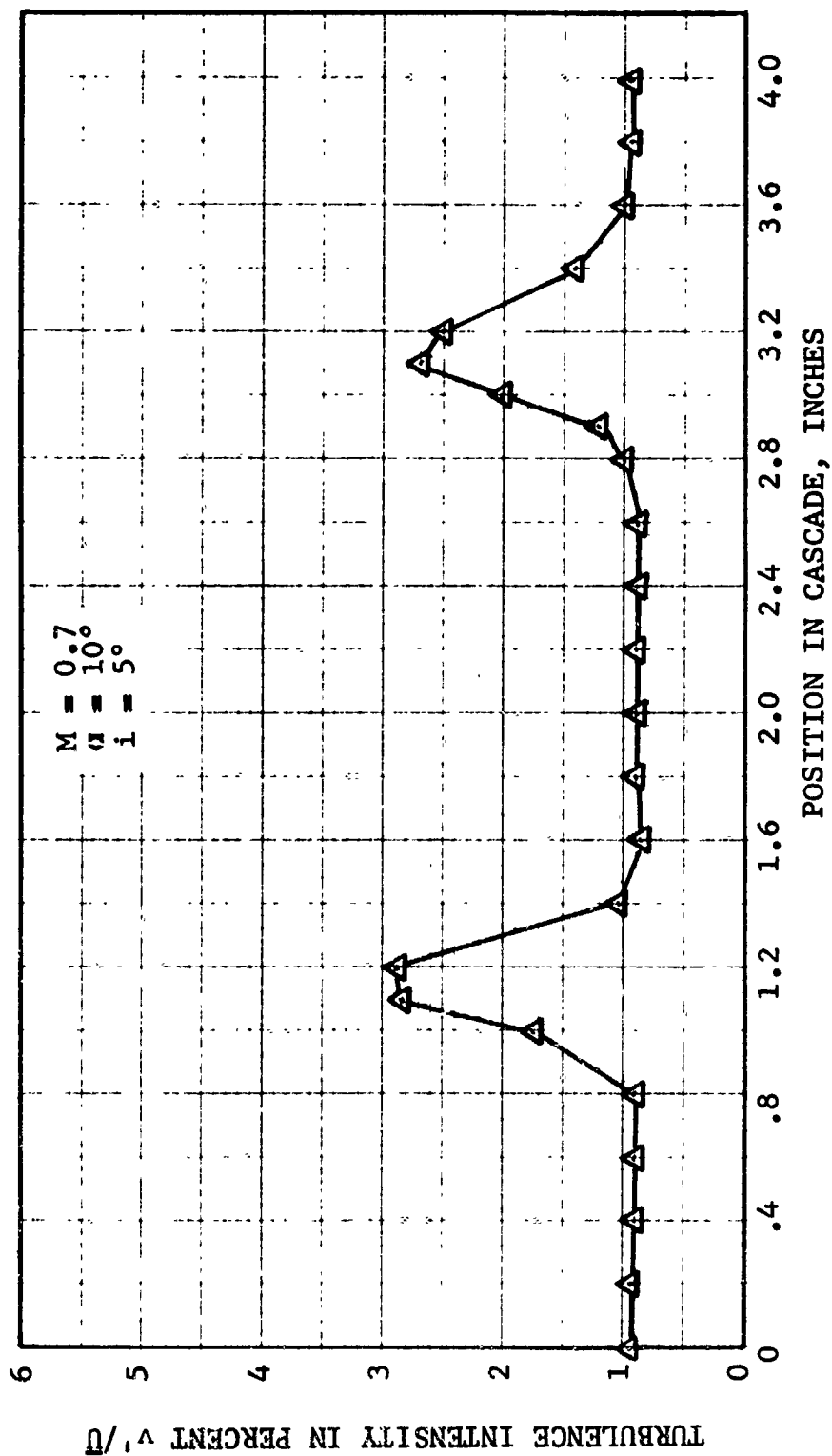


FIGURE II-C58. TURBULENCE INTENSITY VS POSITION IN CASCADE TRANSONIC TUNNEL
FOR A TIP SECTION AIRFOIL ON D/V #4

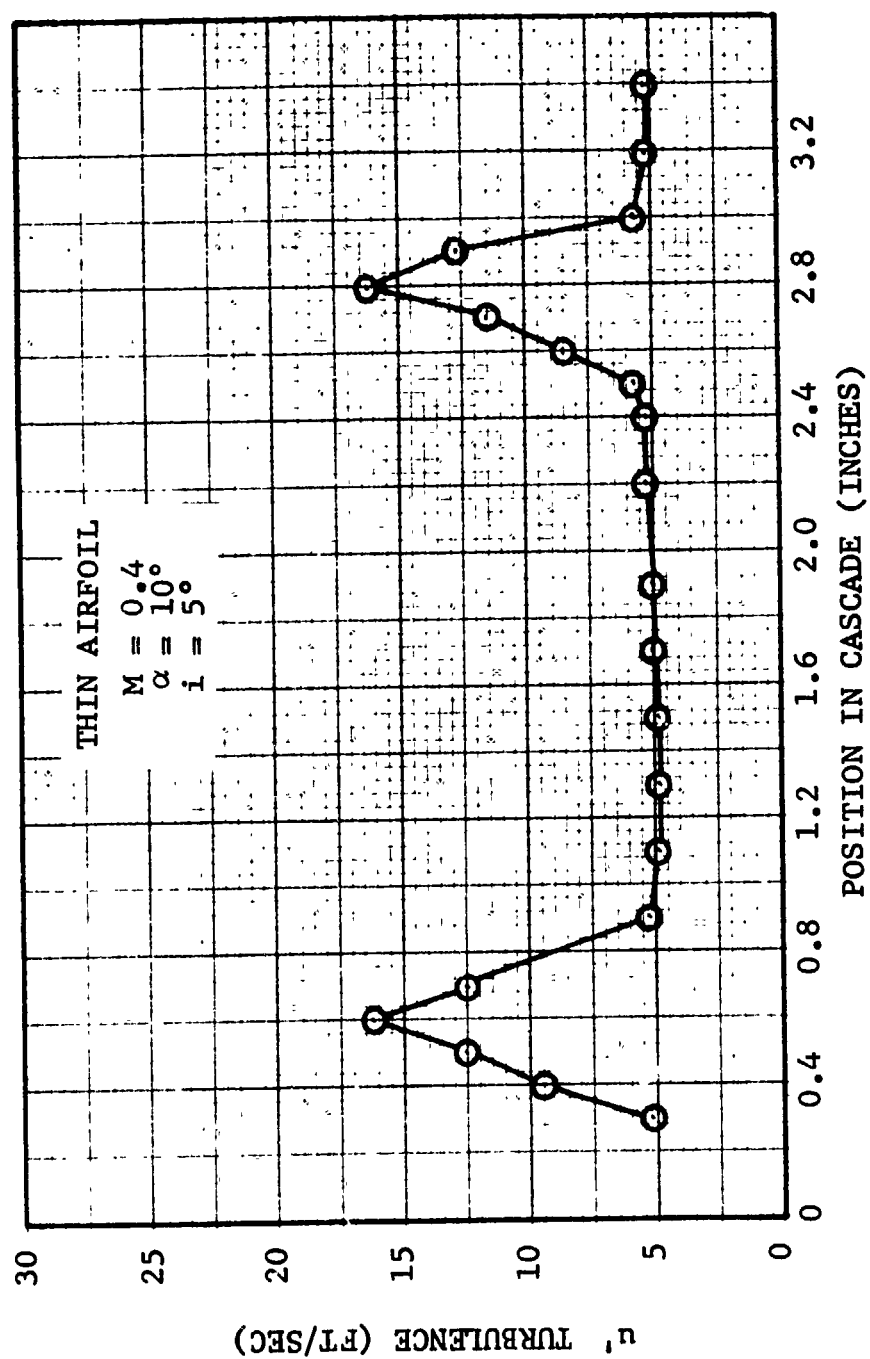


FIGURE 11-C59. u' TURBULENCE INTENSITY DOWNSTREAM OF CASCADE FOR A TIP SECTION AIRFOIL ON D/V #4

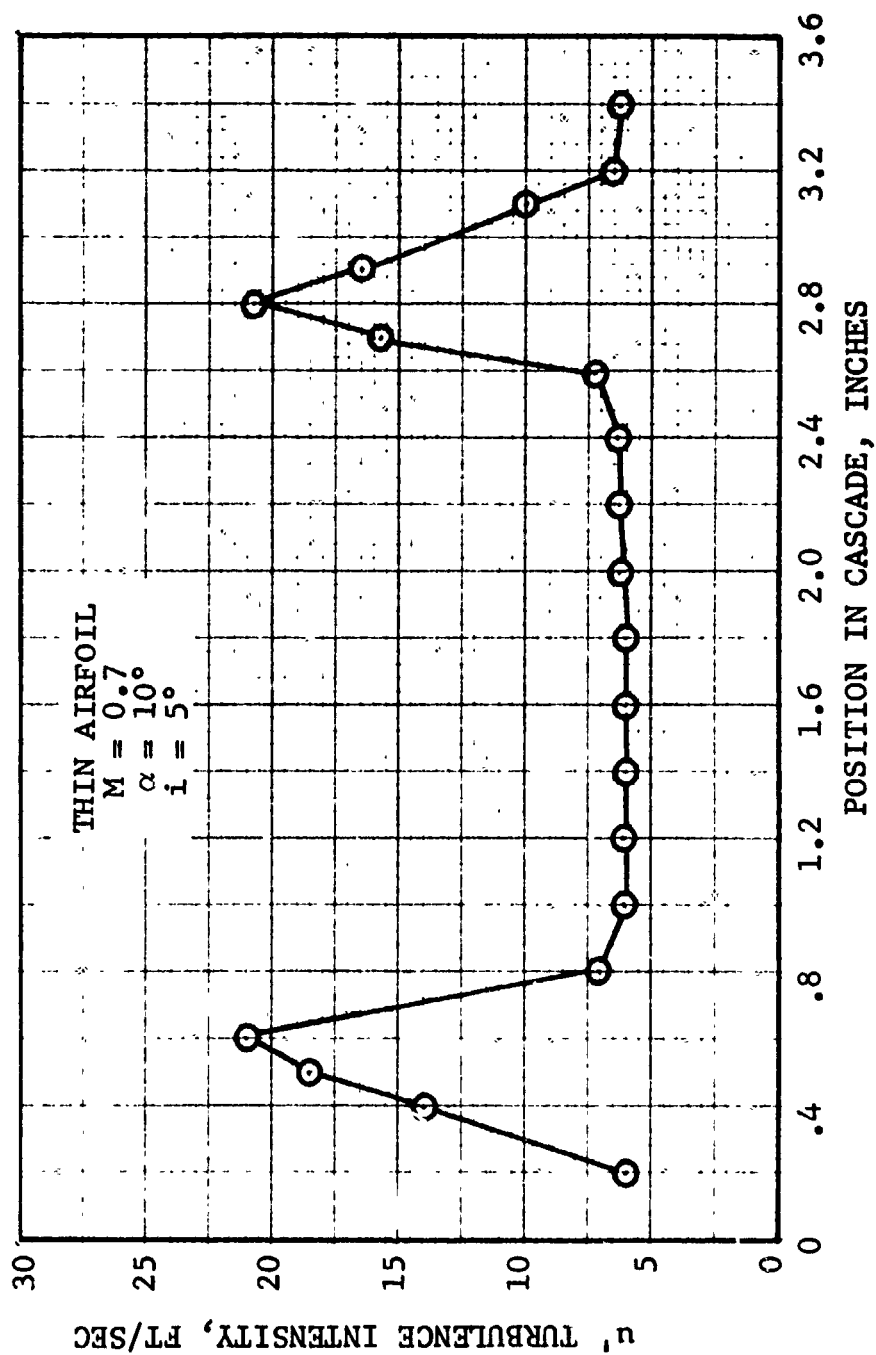


FIGURE II-C60. u' TURBULENCE INTENSITY DOWNSTREAM OF CASCADE .
 FOR A TIP SECTION AIRFOIL ON D/V #4

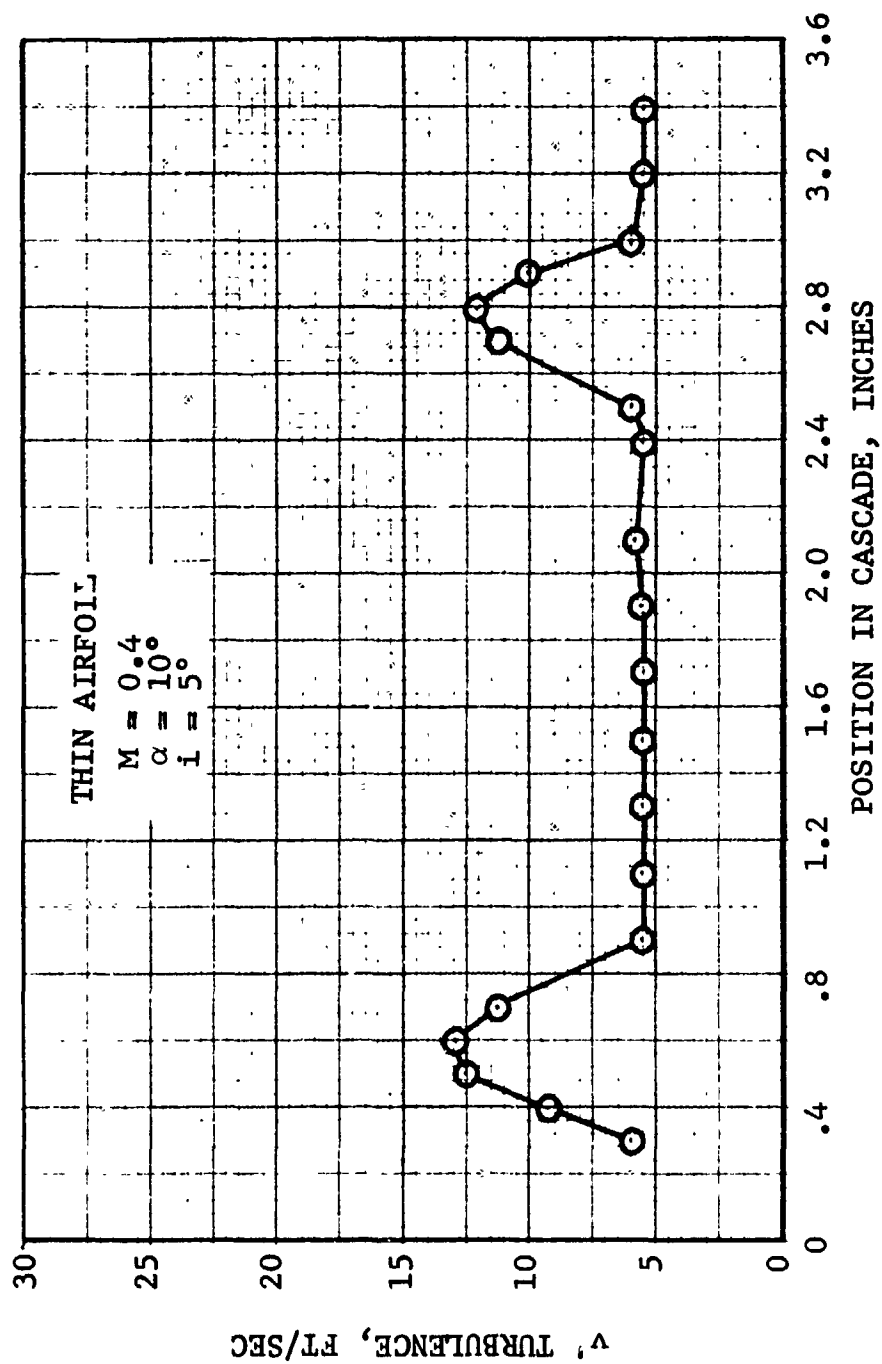


FIGURE II-C61. v' TURBULENCE INTENSITY DOWNSTREAM OF CASCADE
 FOR A TIP SECTION AIRFOIL ON D/V #4

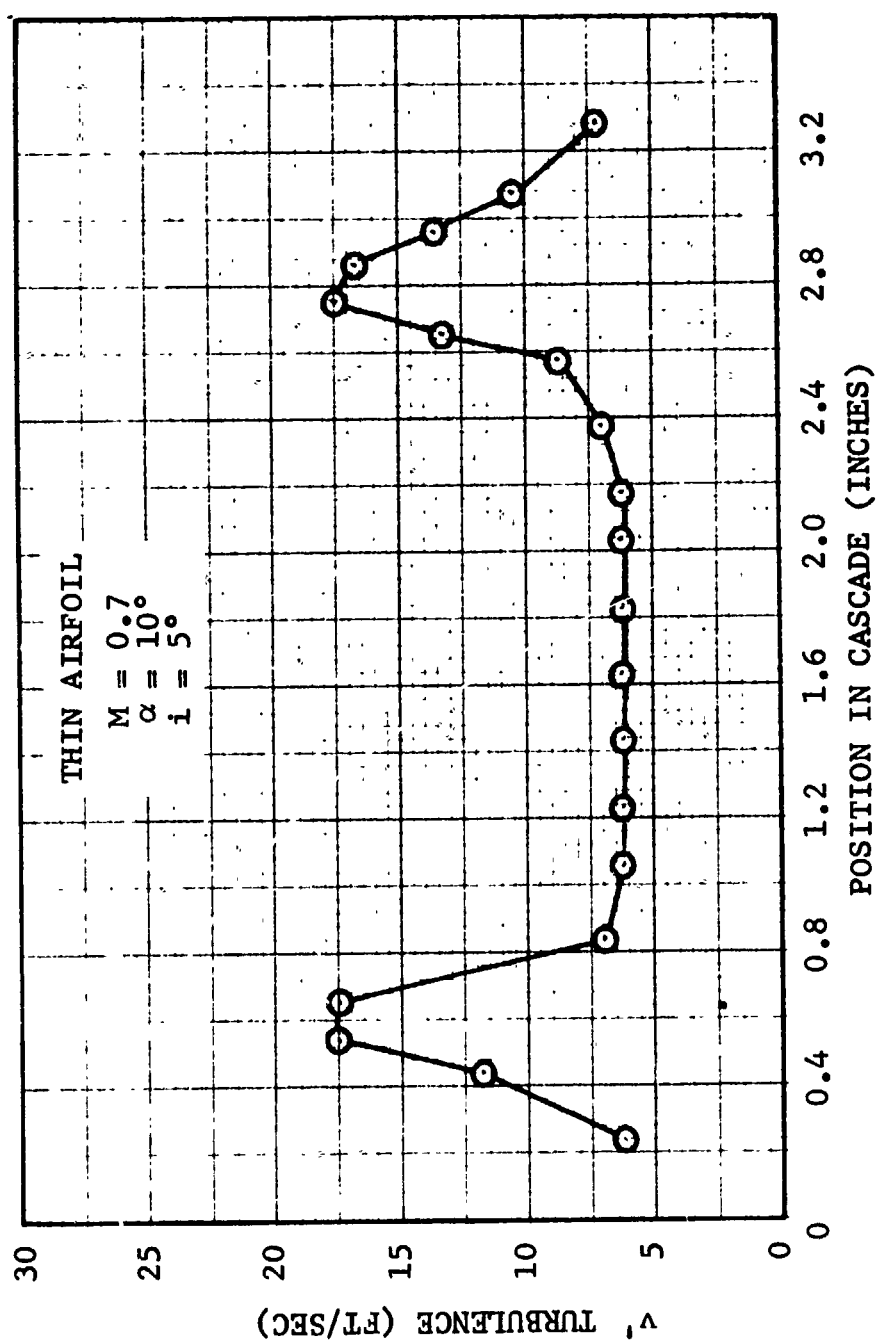


FIGURE II-C62. v' TURBULENCE INTENSITY DOWNSTREAM OF CASCADE FOR A TIP SECTION AIRFOIL ON D/V #4

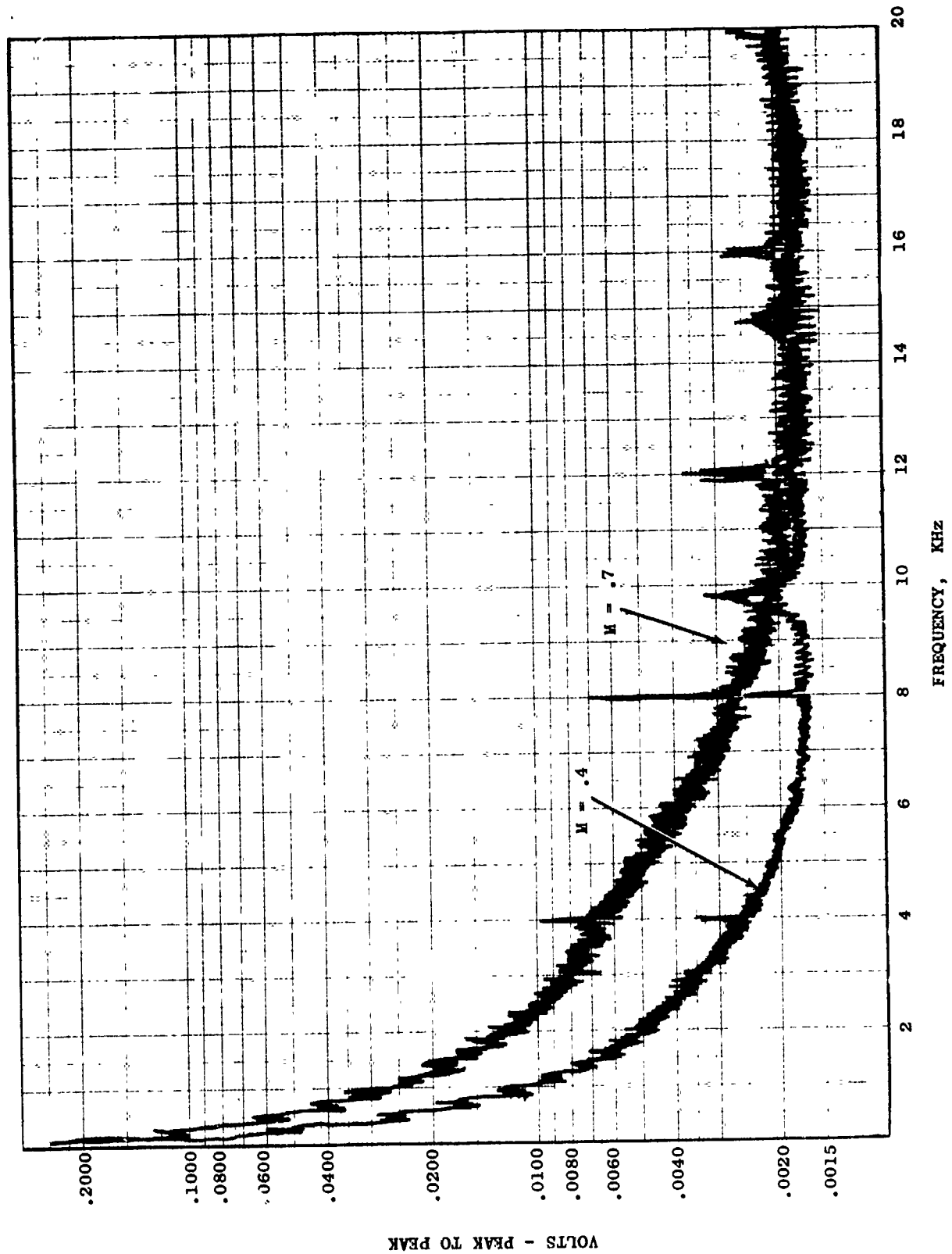


FIGURE 11-663 NOISE FOR A TIP SECTION AIRFOIL OF D/V #4 AT $M = .4$ & $.7$

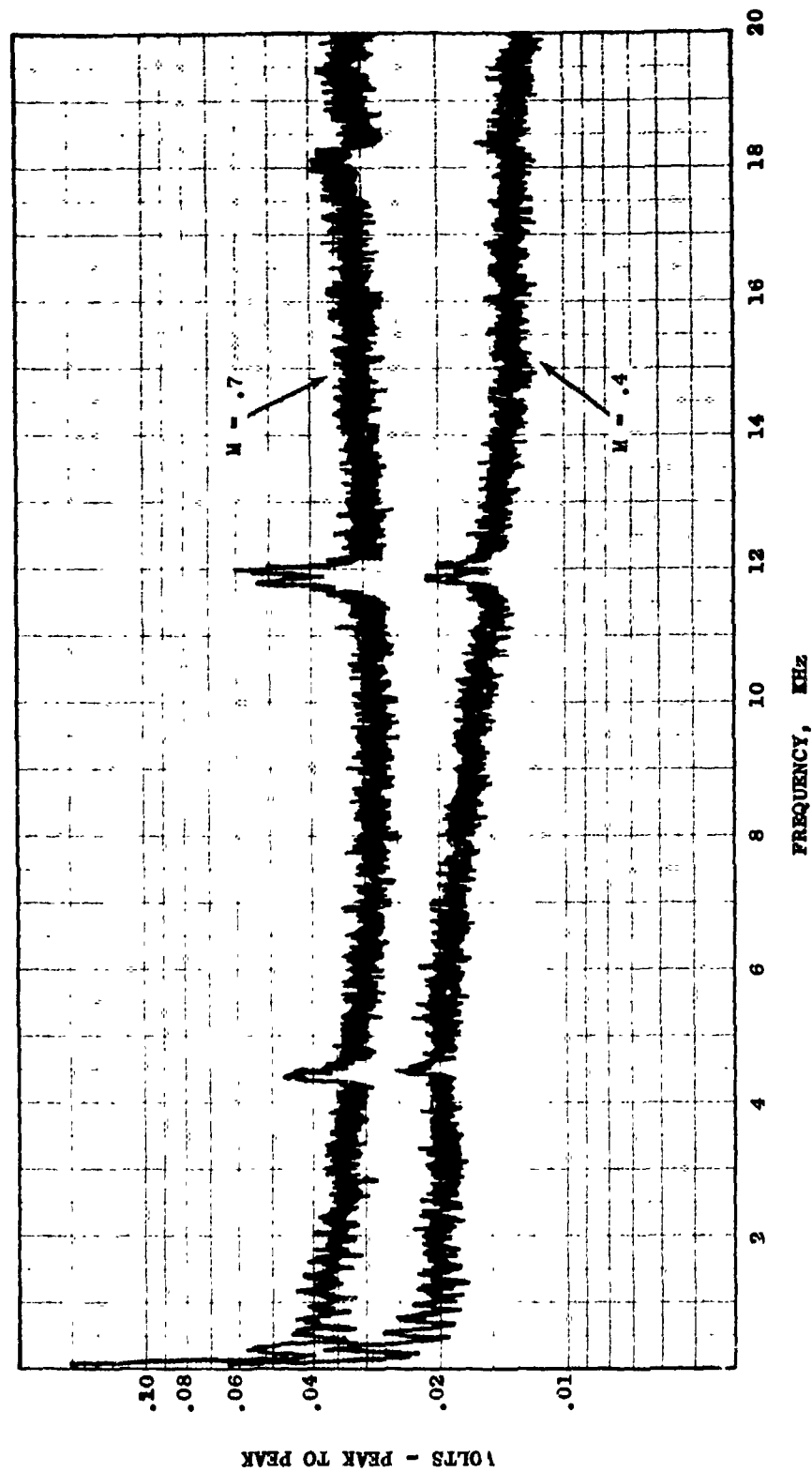


FIGURE II-C64. u' TURBULENCE SPECTRA FOR A TIP SECTION AIRFOIL OF D/V #4 M = .4 & .7

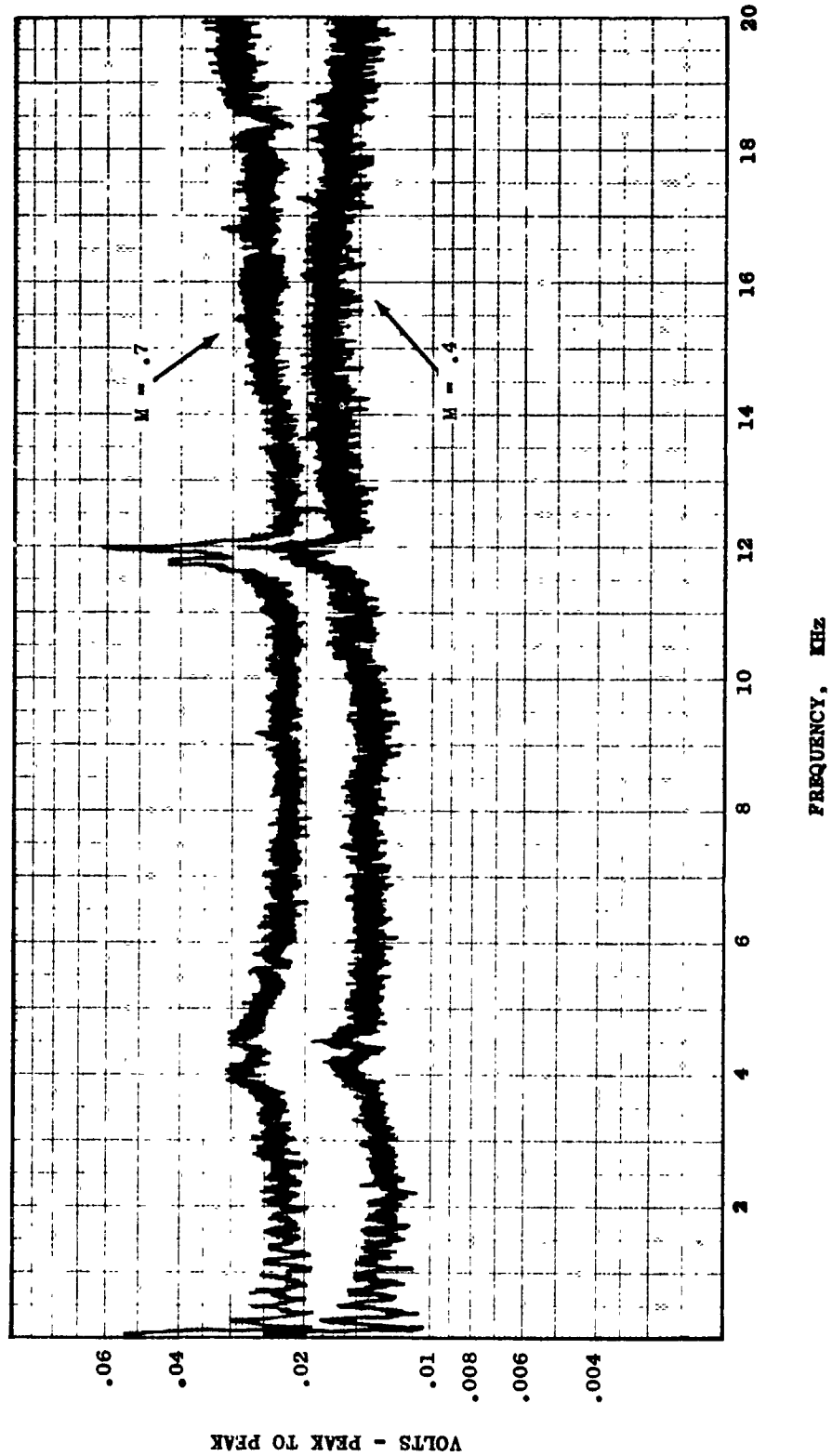


FIGURE II-C65. v' TURBULENCE SPECTRA FOR A TIP SECTION AIRFOIL OF D/V #4 $M = .4$ & $.7$

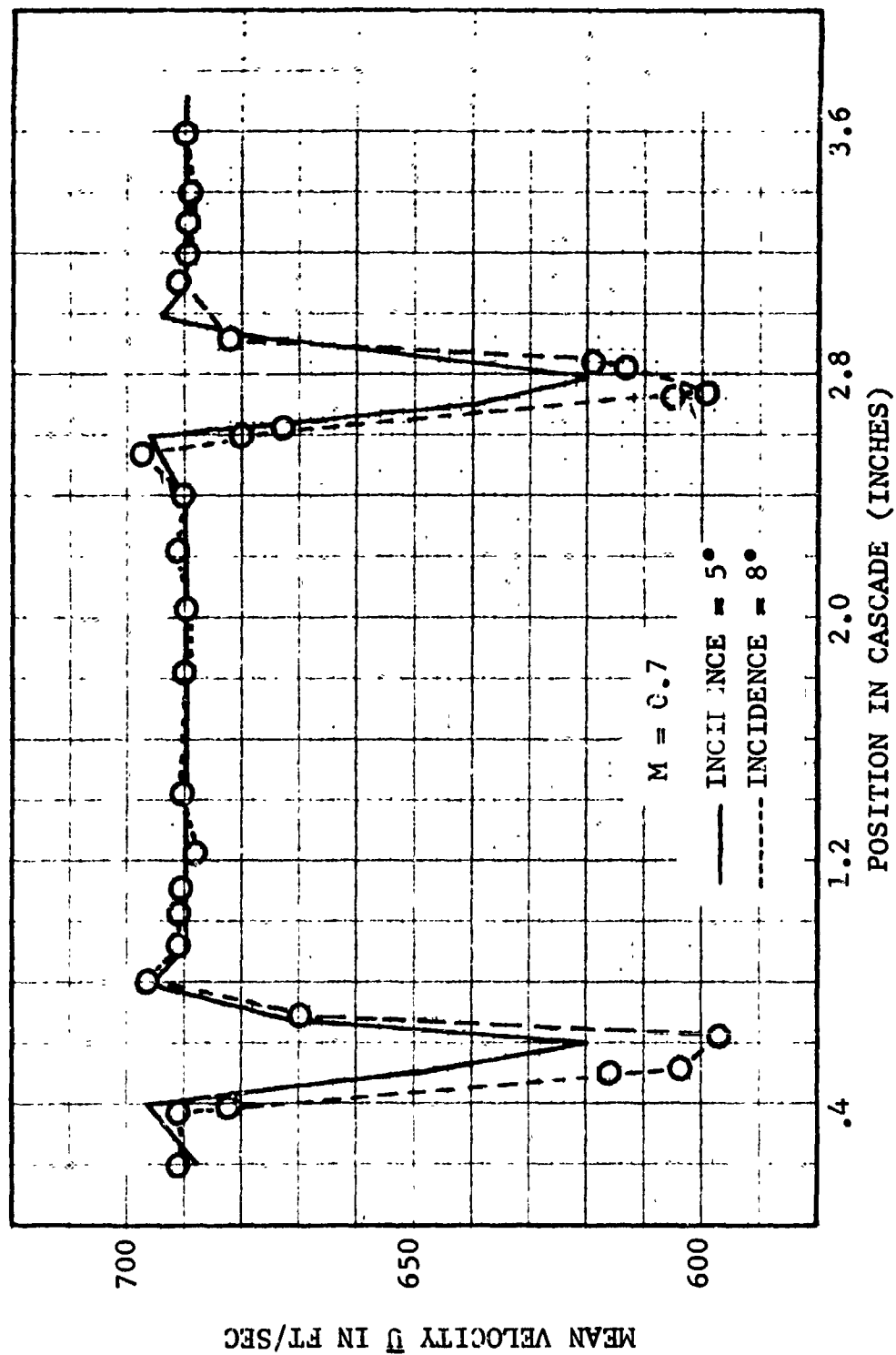


FIGURE II-C66. MEAN VELOCITY PROFILE DECREMENT FOR TWO INCIDENCE ANGLES FOR A TIP SECTION AIRFOIL ON D/V #4

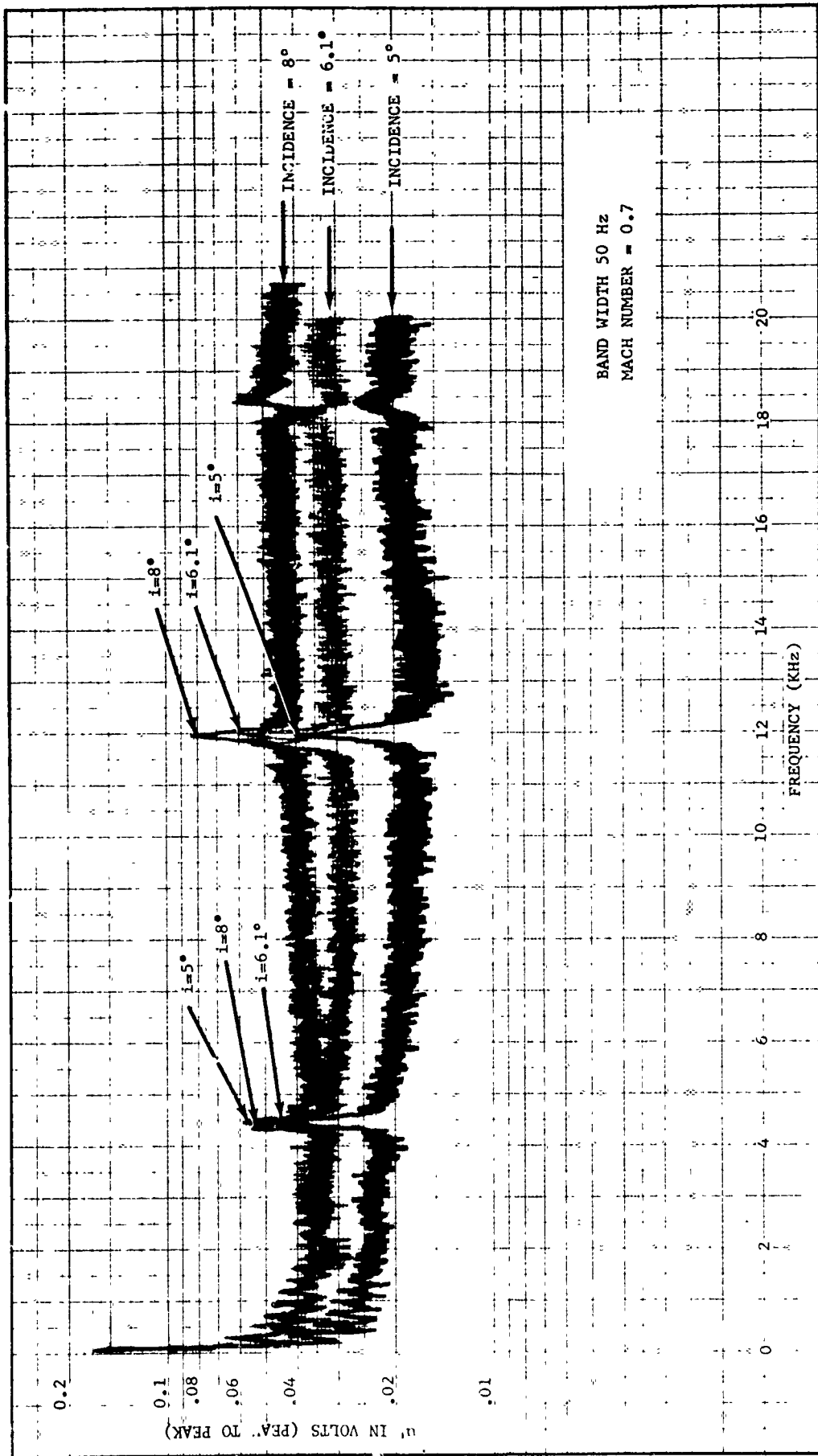


FIGURE II-C67. NARROWBAND FREQUENCY ANALYSIS OF THE TURBULENCE COMPONENT u' FOR A TIP SECTION AIRFOIL OF D/V #4

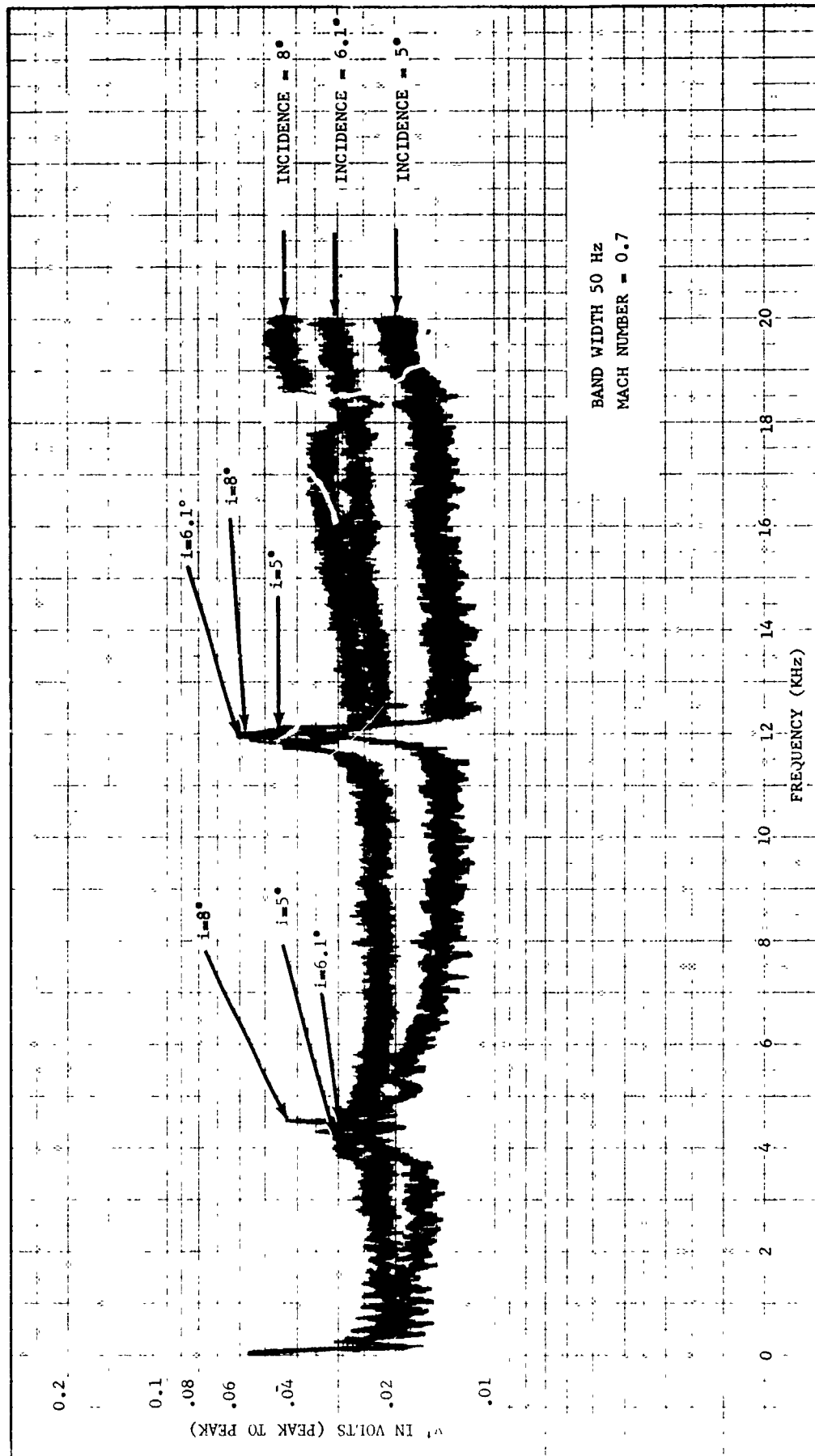


FIGURE II-C68. NARROWBAND FREQUENCY ANALYSIS OF THE TURBULENCE COMPONENT v' FOR A TIP SECTION AIRFOIL OF D/V #4

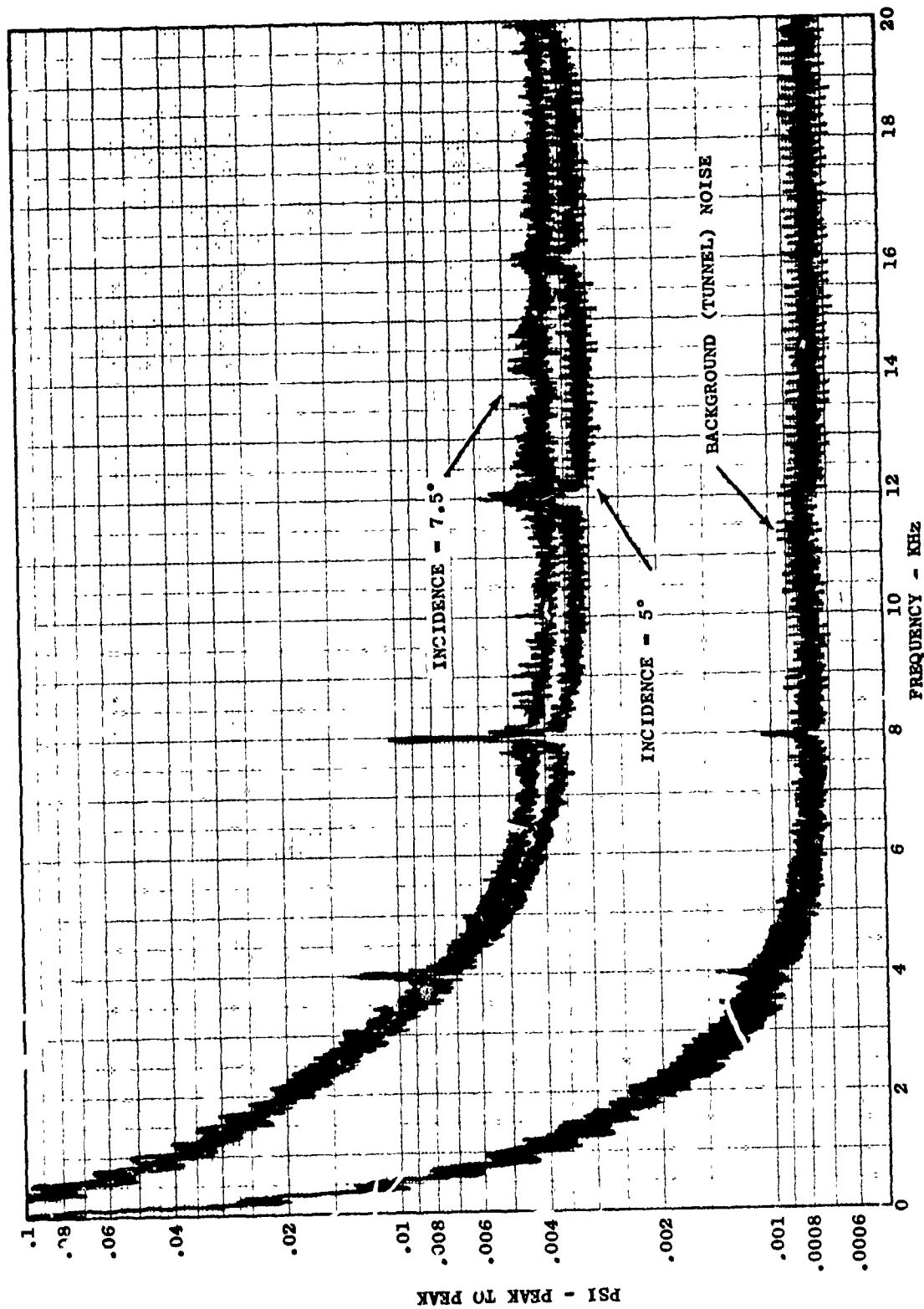


FIGURE II-C69. NOISE FOR A TIP SECTION AIRFOIL OF D/V #4 AT INCIDENCE ANGLES 5° AND 7.5° WITH TUNNEL BACKGROUND NOISE

Data reduction concentrated on narrowband (50 Hz bandwidth) analysis of axial, u' , and tangential, v' , turbulent velocity components. The data behind the rotor, Figures II-C70 - 79, has two striking features.

- Sharp discrete tones at multiples of 2970 Hz. This frequency is the blade passing frequency and thus the tones represent the passage of the rotor blade's pressure field and wake and are not associated with the turbulent velocity components.
- The broader peaks at approximately 4, 10, 13, and 16.5 KHz are the turbulent velocity peaks.

The "cleanest" spectra occur at the tip with an increasing amount of "haystacking" developing as the hub wall is approached. In general the peaks are higher at the tip but the overall level of turbulence appears higher near the hub.

The two prominent peaks are most likely due to the vortices being shed from the pressure and suction surfaces of the blades. There appears to be a decrease in the amplitude of these two peaks as the immersion depth increases. This would be expected since the blade relative Mach number is decreasing. It was shown in Section II-B3 that the lower relative Mach numbers produced lower u' and v' turbulence levels.

As far as the increase in the number of "haystacks" at the deeper immersion depths is concerned it appears that the higher aerodynamic loading in the hub region is playing an important part in this phenomenon. Table II-C3 shows the design $\Delta P/q$ distribution for the D/V #4 fan. It is evident that the wide band turbulence (immersion #5) and the high loading region correspond. Since these data are derived from rms narrowband results, the peaks in the turbulent spectra represent the "average" of occurrences on each blade. Thus, it can be assumed that the "averaged" turbulence spectra are characteristic of each blade. It then appears that if noise and u' , v' turbulence are related, as reported in Section II-B3, that the hub region of the rotor blade is as important in generating broadband noise as the tip region.

Figures II-C80 through 85 show the v' , u' turbulence spectra behind the OGV. For these traverses the hot film probe was positioned about 2 chords downstream and in between two OGV wakes. At this distance from the rotor fewer and weaker harmonics of the blade passing frequency can be observed. The two turbulent peaks at 4 and 10 KHz are still strong. In addition the u' spectra show a high turbulence level at the low frequency (less than 2 KHz) near the outer wall. This is due to the tip wall boundary layer which is thicker behind the OGV than behind the rotor.

Figures II-C86 and 87 show the v' and u' turbulence spectra for a tip relative Mach number of .729 as measured behind the rotor at immersion #1. The two peaks at about 4 and 10 KHz can still be observed although they are lower in amplitude than those at the higher Mach number (Figures II-C70 and 75).

Radius, in.	$\Delta P/q$
16.71	.252
16.15	.295
15.55	.337
14.91	.376
14.28	.412
13.51	.447

TABLE II-C3

Radial Design Point $\Delta P/q$ Distribution For D/V #4

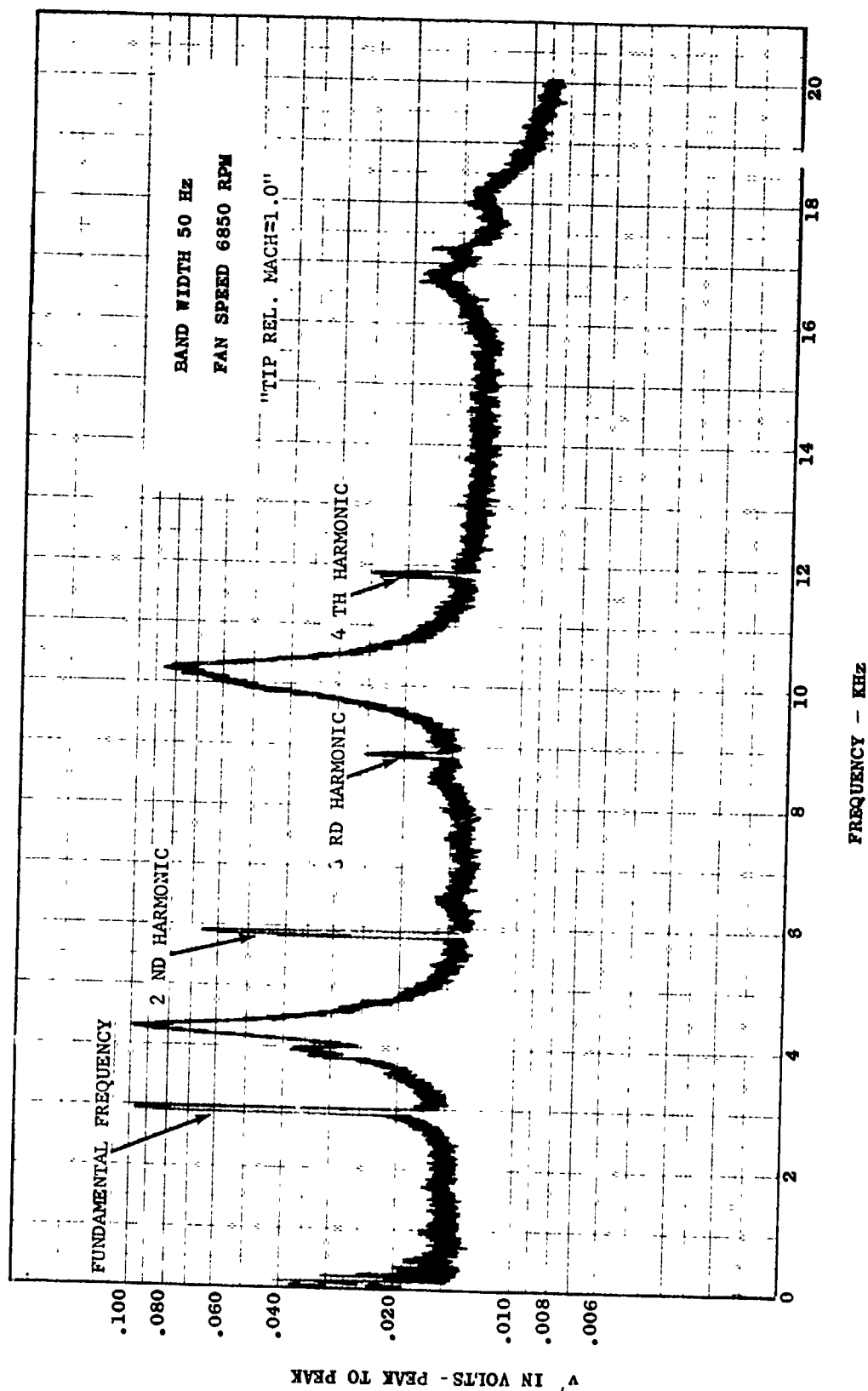


FIGURE II-C70. 3-D ROTOR WAKE NARROWBAND ANALYSIS OF TURBULENT COMPONENT v' AT IMMERSION #1 - D/V #4

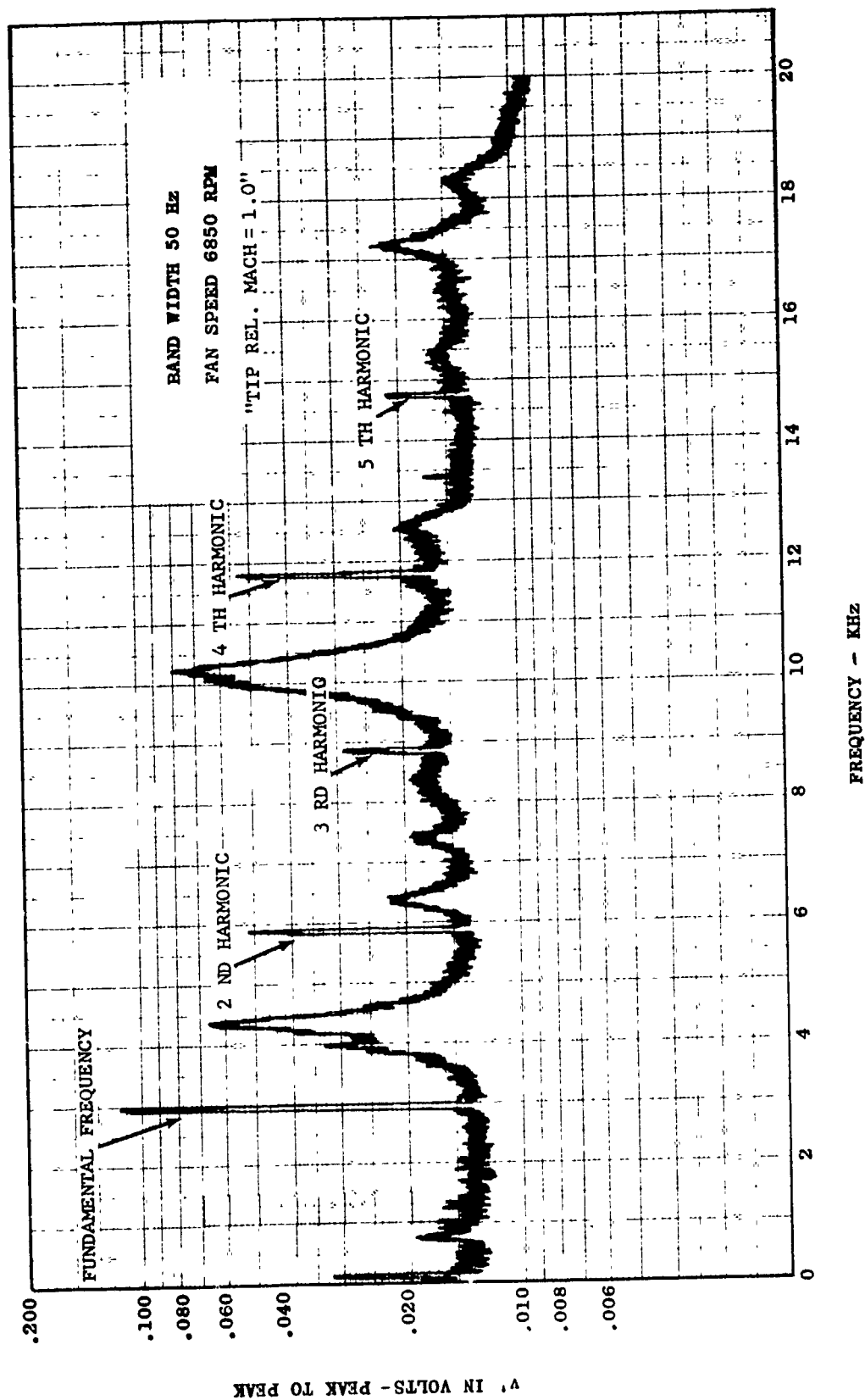


FIGURE II-C71. 3-D ROTOR WAKE NARROWBAND ANALYSIS OF TURBULENT COMPONENT v' AT IMMERSION #2 - D/V #4

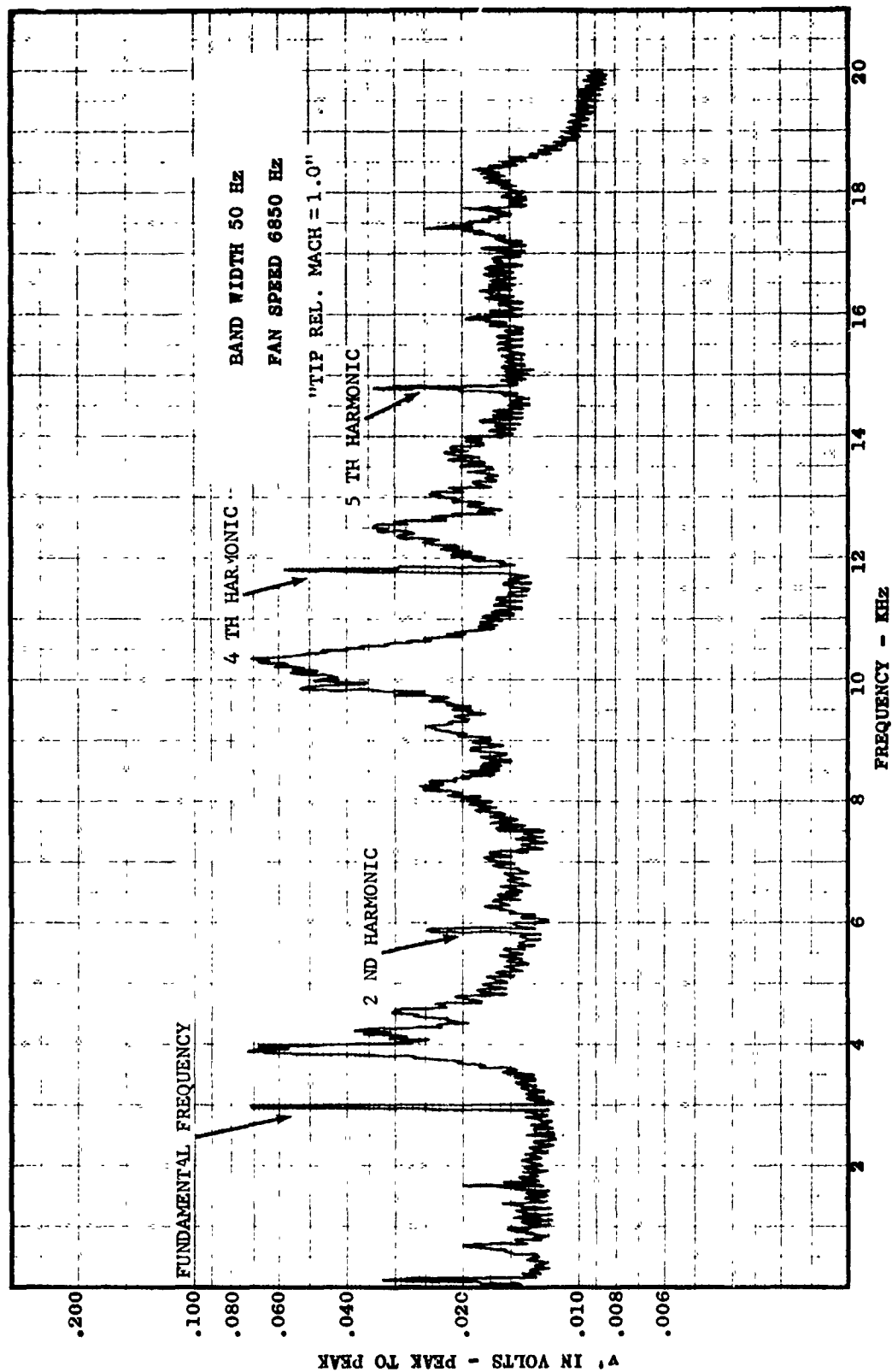


FIGURE II-C72. 3-D ROTOR WAKE NARROWBAND ANALYSIS OF TURBULENT COMPONENT v' AT IMMERSION #3 - D/V #4

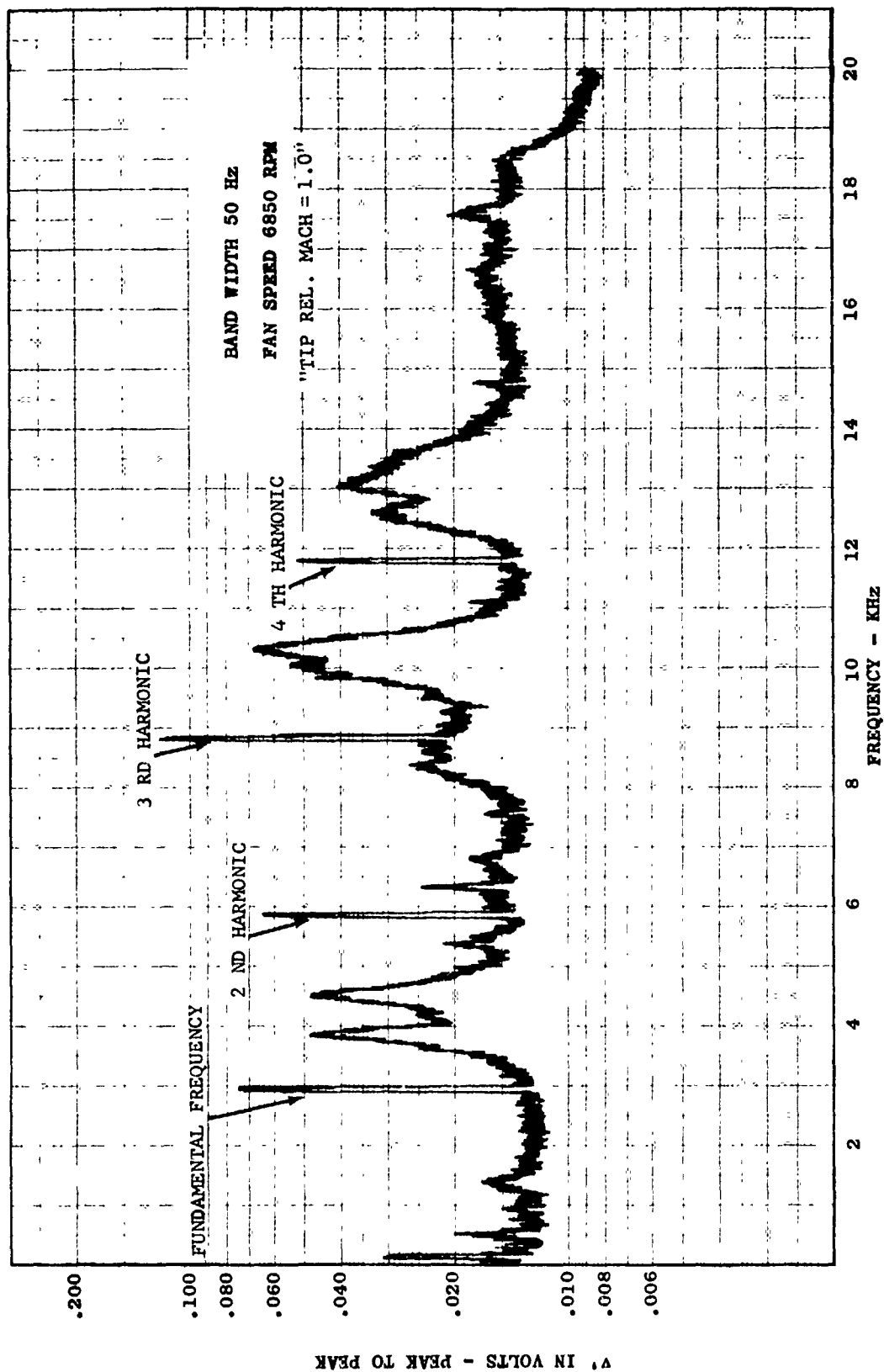


FIGURE 11-C73. 3-D ROTOR WAKE NARROWBAND ANALYSIS OF TURBULENT COMPONENT v' AT IMMERSION #4 - D/V #4

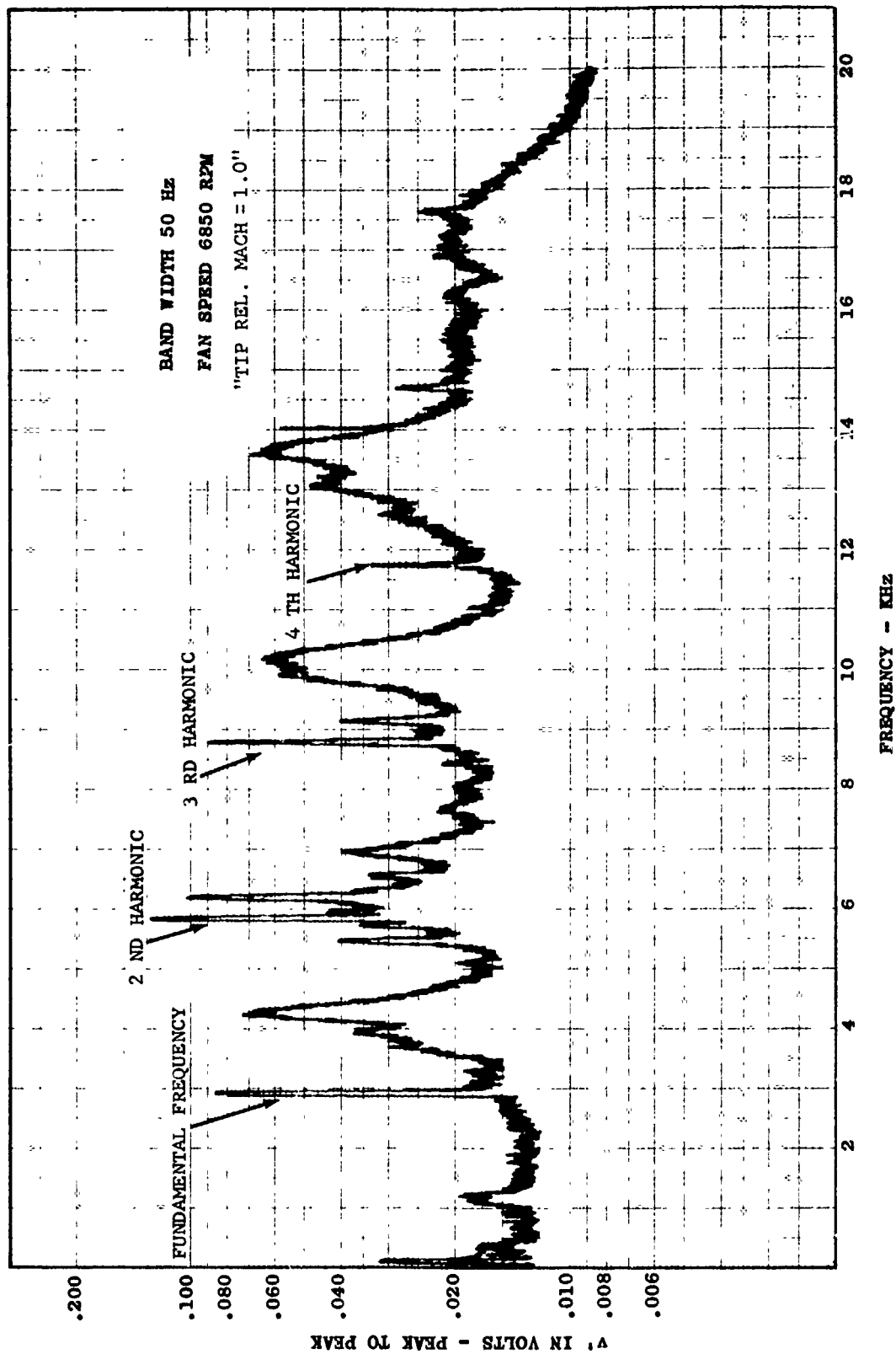


FIGURE II-C74. 3-D ROTOR WAKE NARROWBAND ANALYSIS OF TURBULENT COMPONENT v' AT IMMERSION #5 - D/V #4

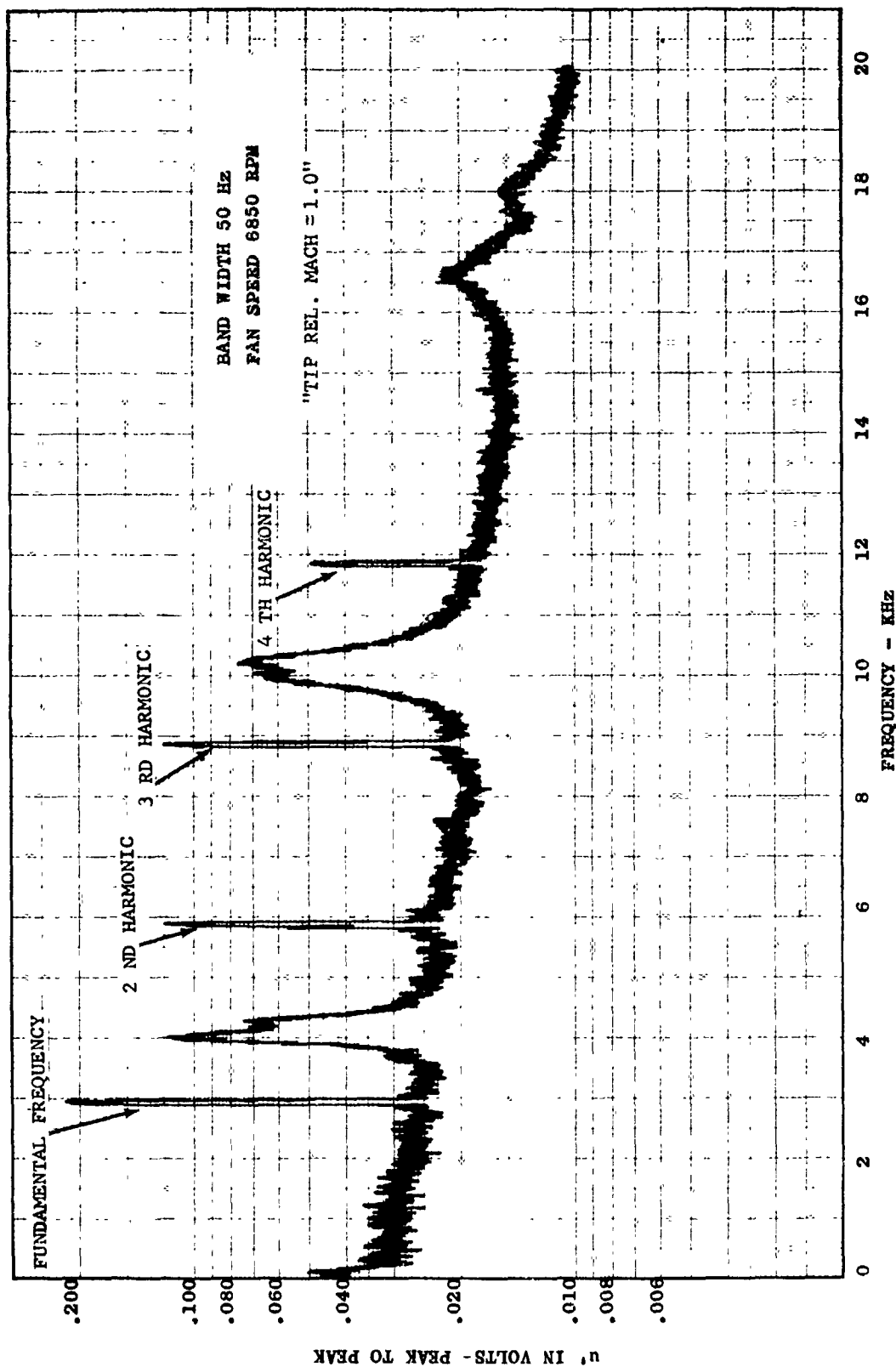


FIGURE II-C75. 3-D ROTOR WAKE NARROWBAND ANALYSIS OF TURBULENT COMPONENT u' AT IMMERSION #1 - D/V #4

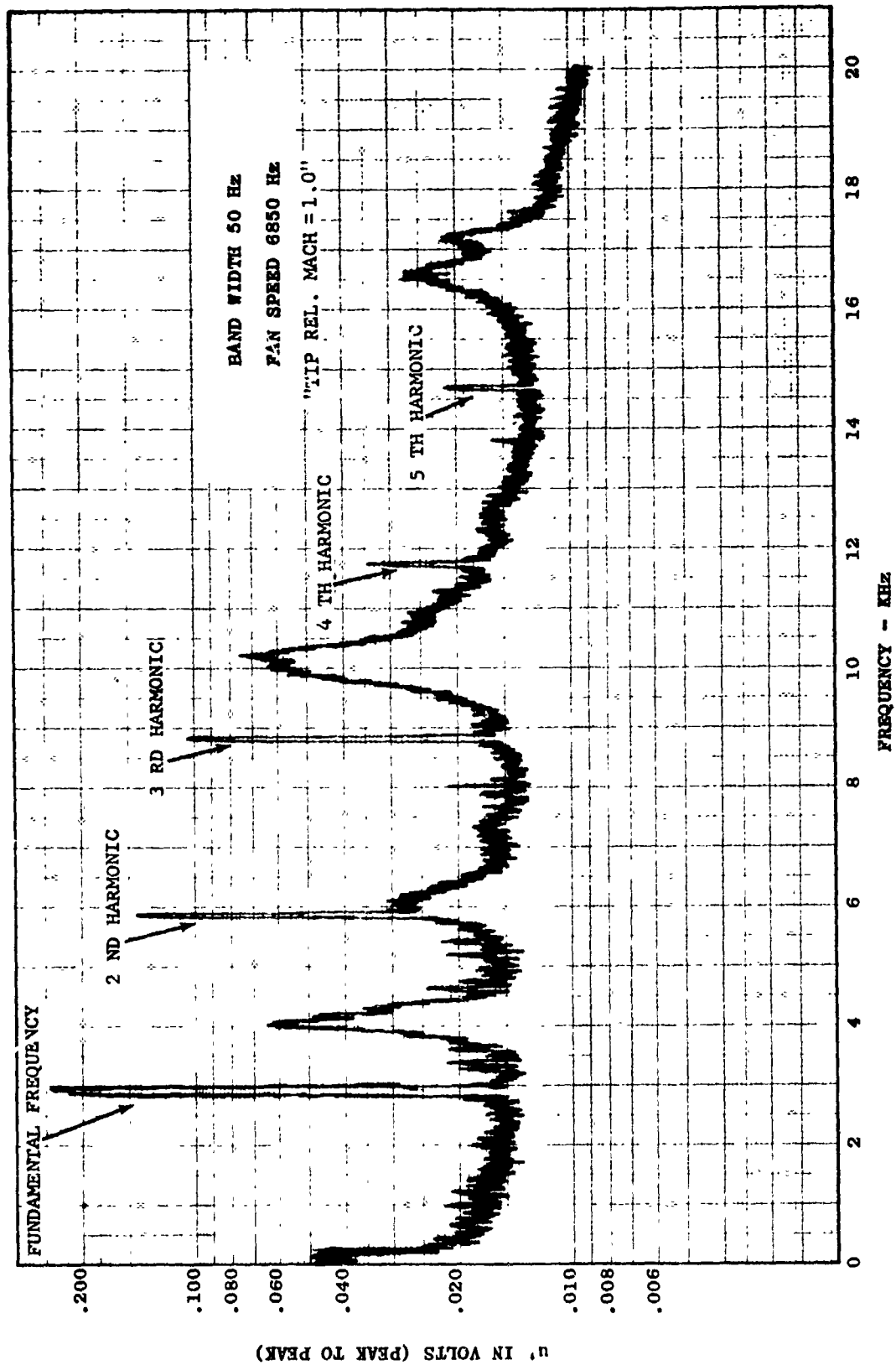


FIGURE 11-C76. 3-D ROTOR WAKE NARROWBAND ANALYSIS OF TURBULENT COMPONENT u' AT IMMERSION #2 - D/V #4

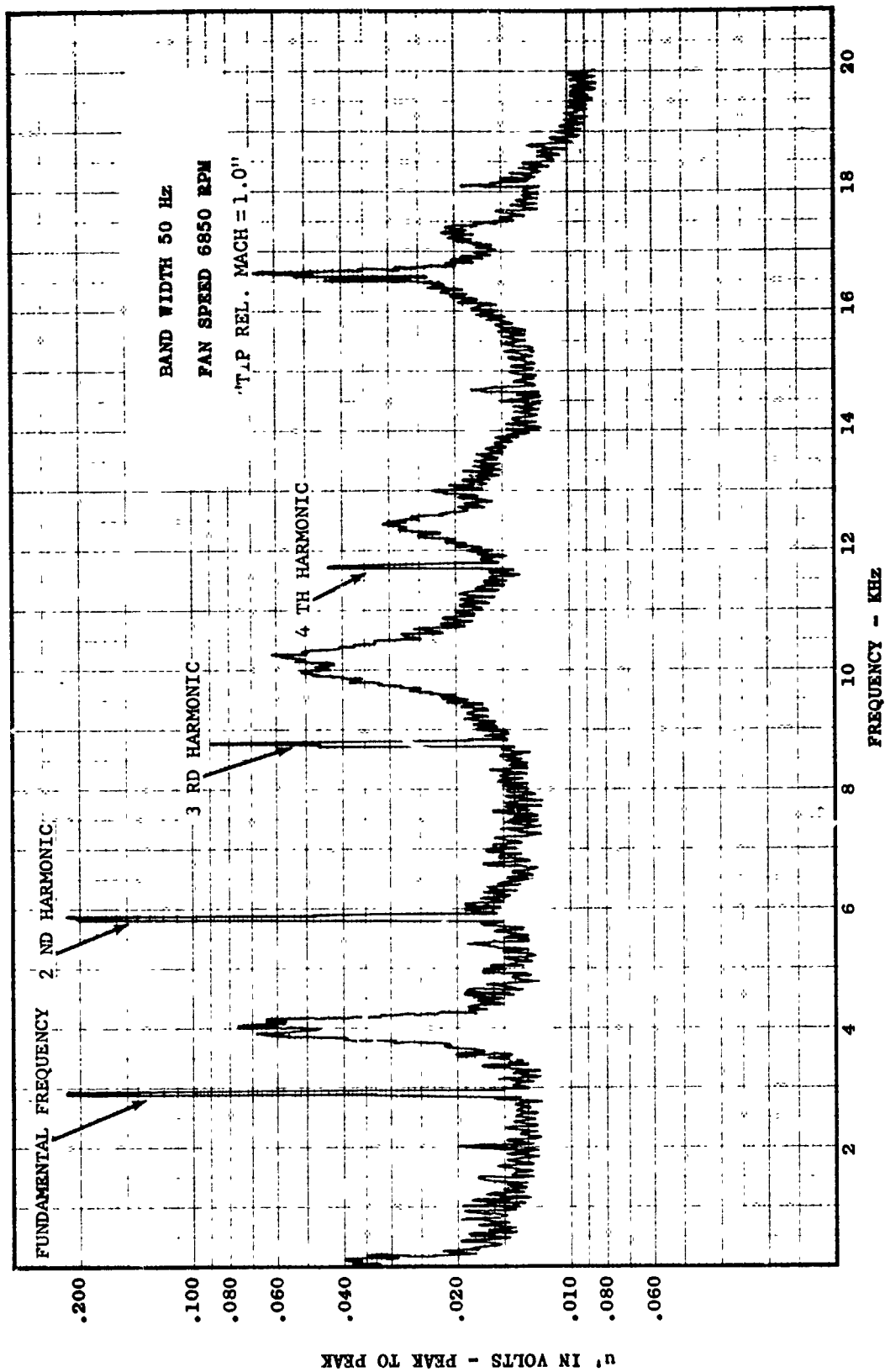


FIGURE II-C77. 3-D ROTOR WAKE NARROWBAND ANALYSIS OF TURBULENT COMPONENT u' AT IMMERSION #3 - D/V #4

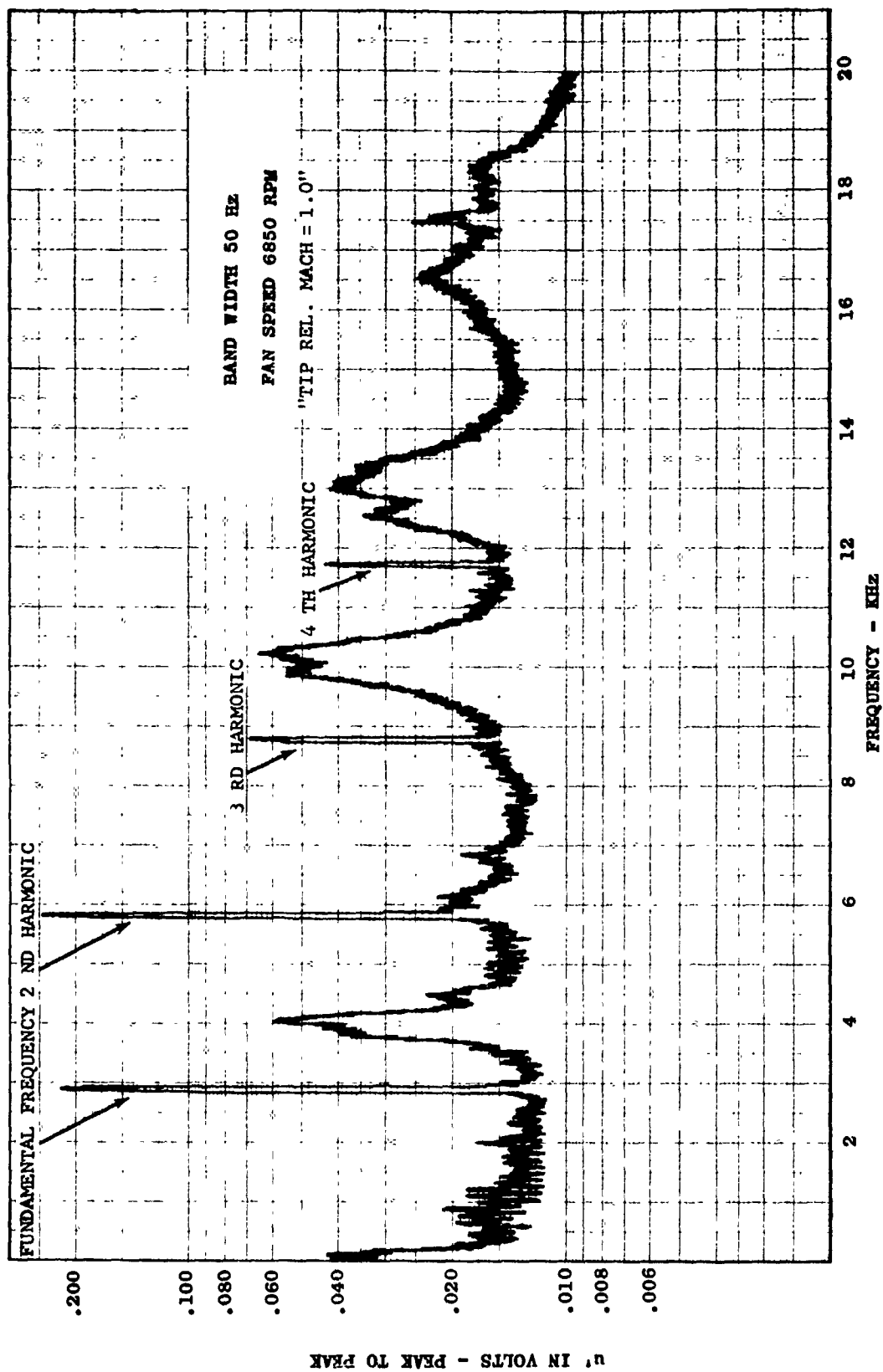


FIGURE II-C78. 3-B ROTOR WAKE NARROWBAND ANALYSIS OF TURBULENT COMPONENT u' AT IMMERSION #4 @ D/V #4

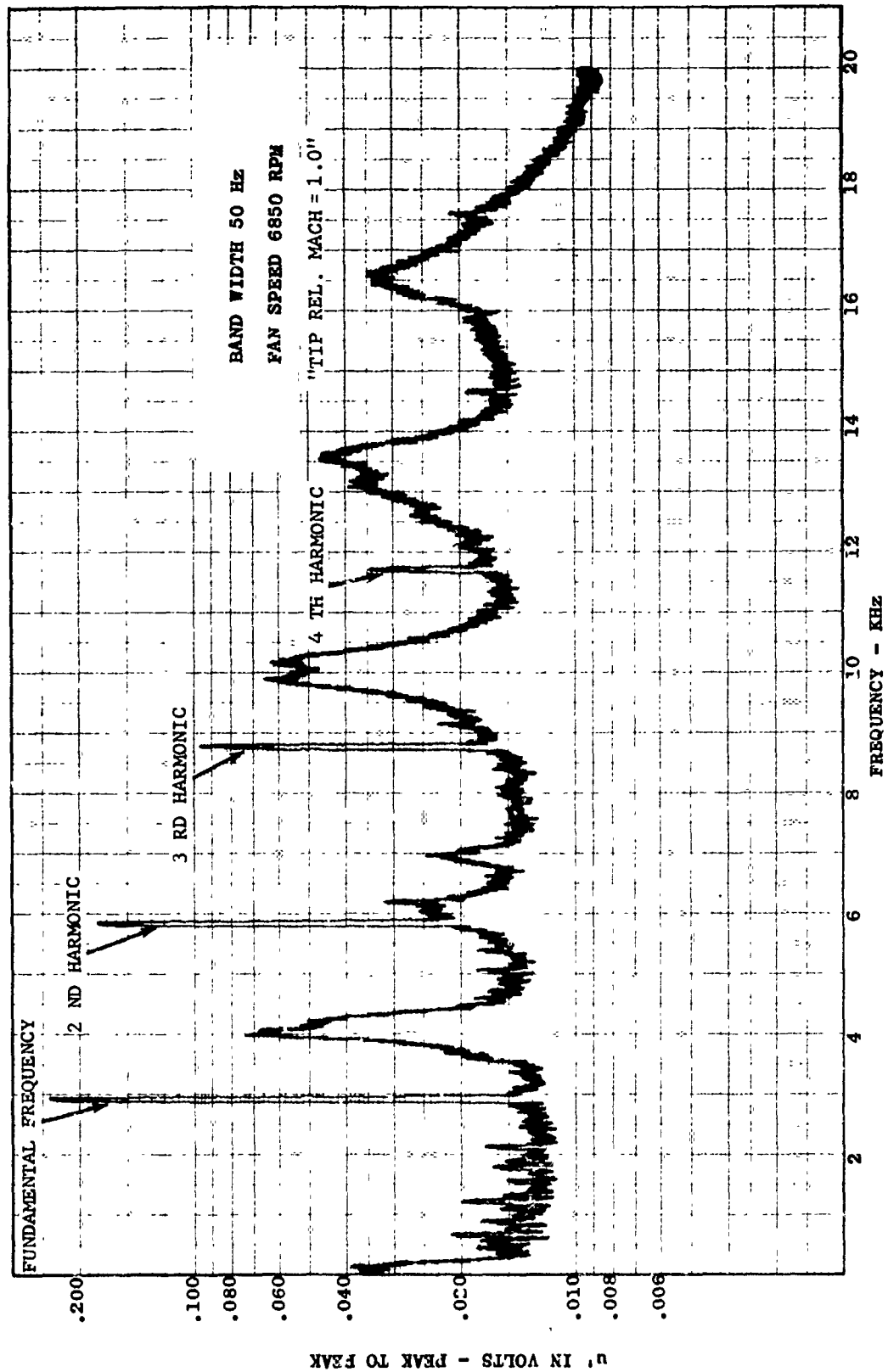


FIGURE II-C79. 3-D ROTOR WAKE NARROWBAND ANALYSIS OF TURBULENT COMPONENT u' AT INVERSION #3 - D/V #4

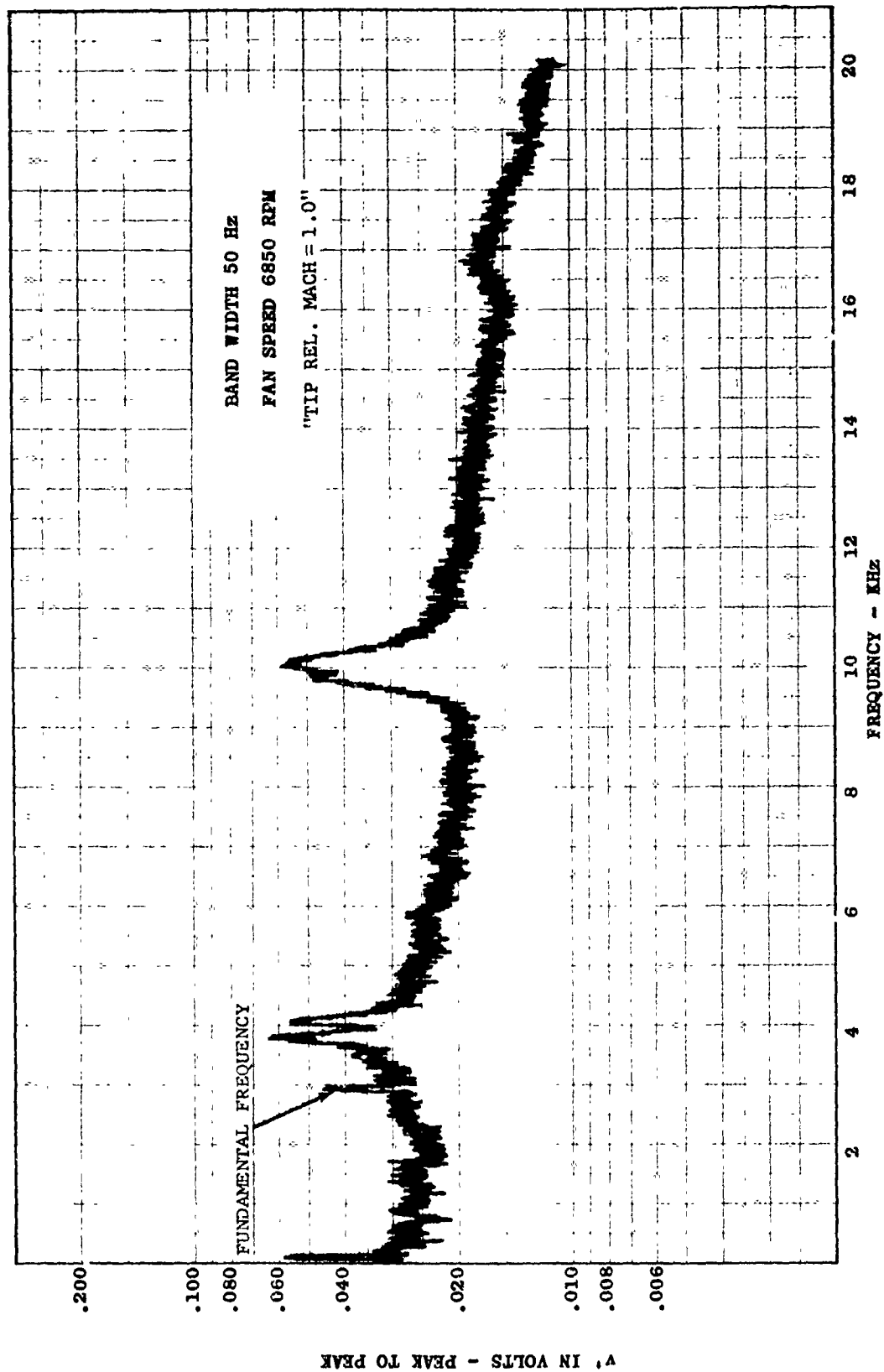


FIGURE II-C80. 3-D OGV WAKE NARROWBAND ANALYSIS OF TURBULENT COMPONENT v' AT IMMERSION #1 - D/V #4

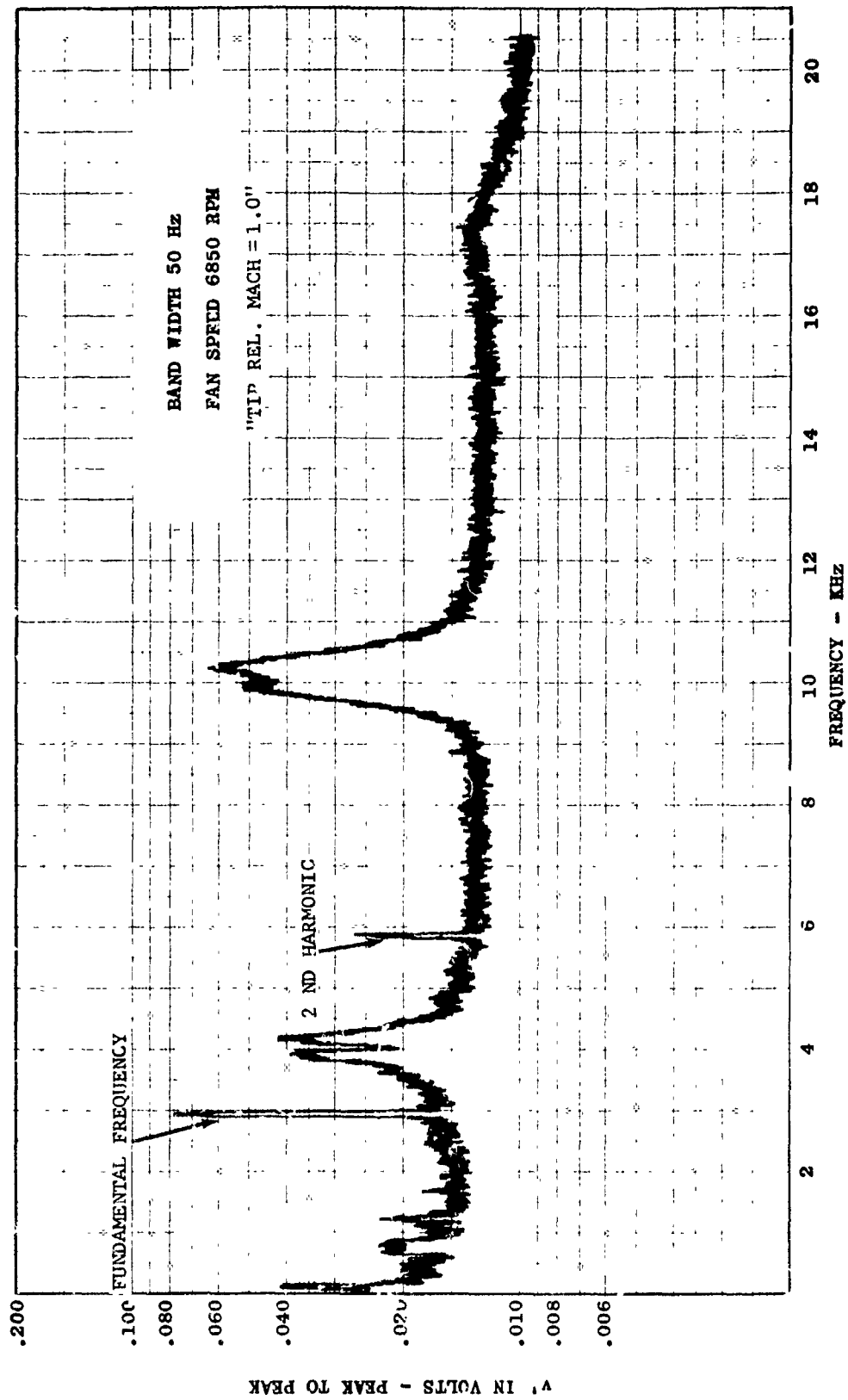


FIGURE II-C81. 3-D QCV WAKE NARROWBAND ANALYSIS OF TURBULENT COMPONENT v' AT IMMERSION #3 - D/V #4

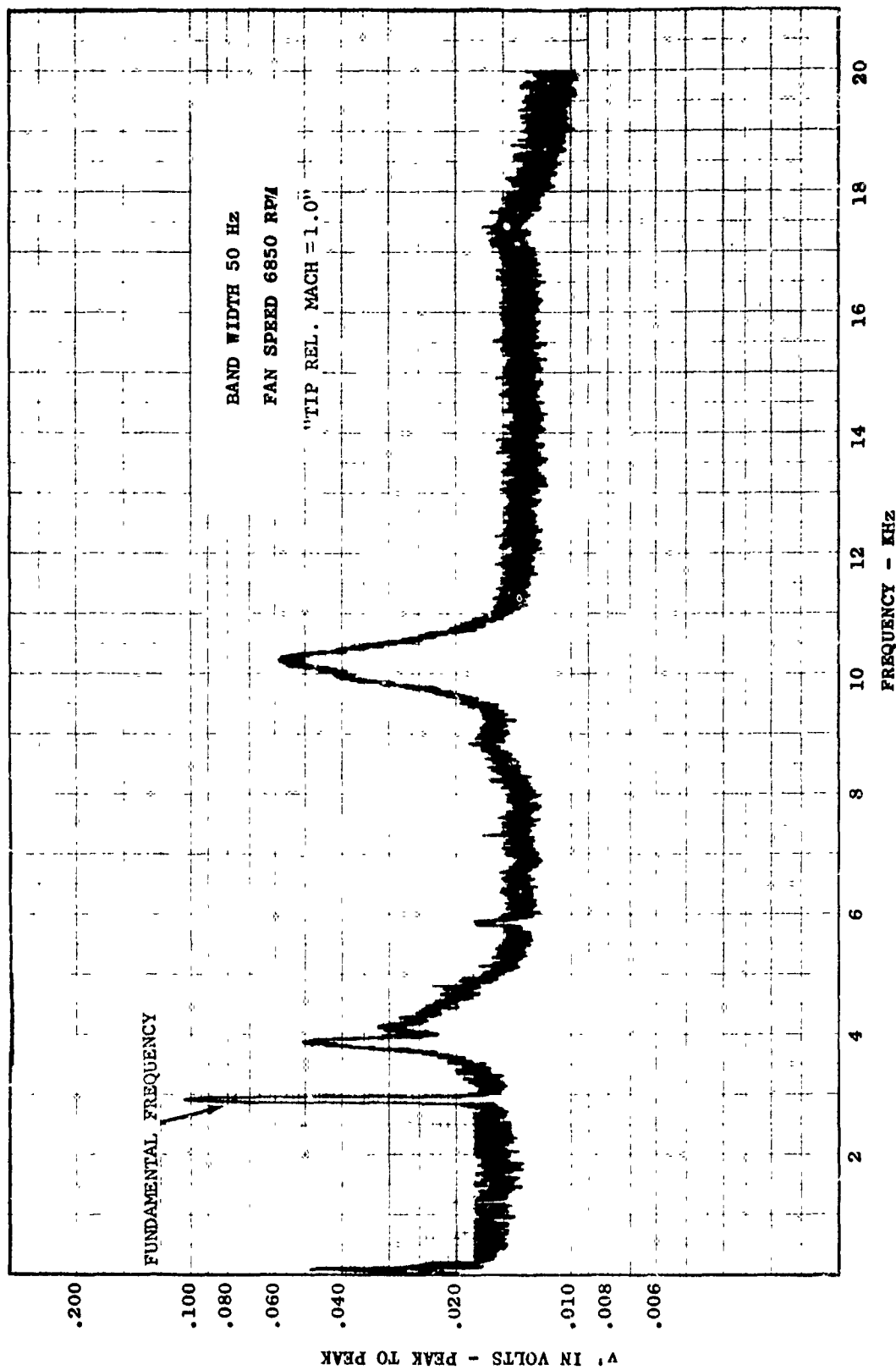


FIGURE 11-C82. 3-D OGV WAKE NARROWBAND ANALYSIS OF TURBULENT COMPONENT v' AT IMMERSION #4 - D/V #4

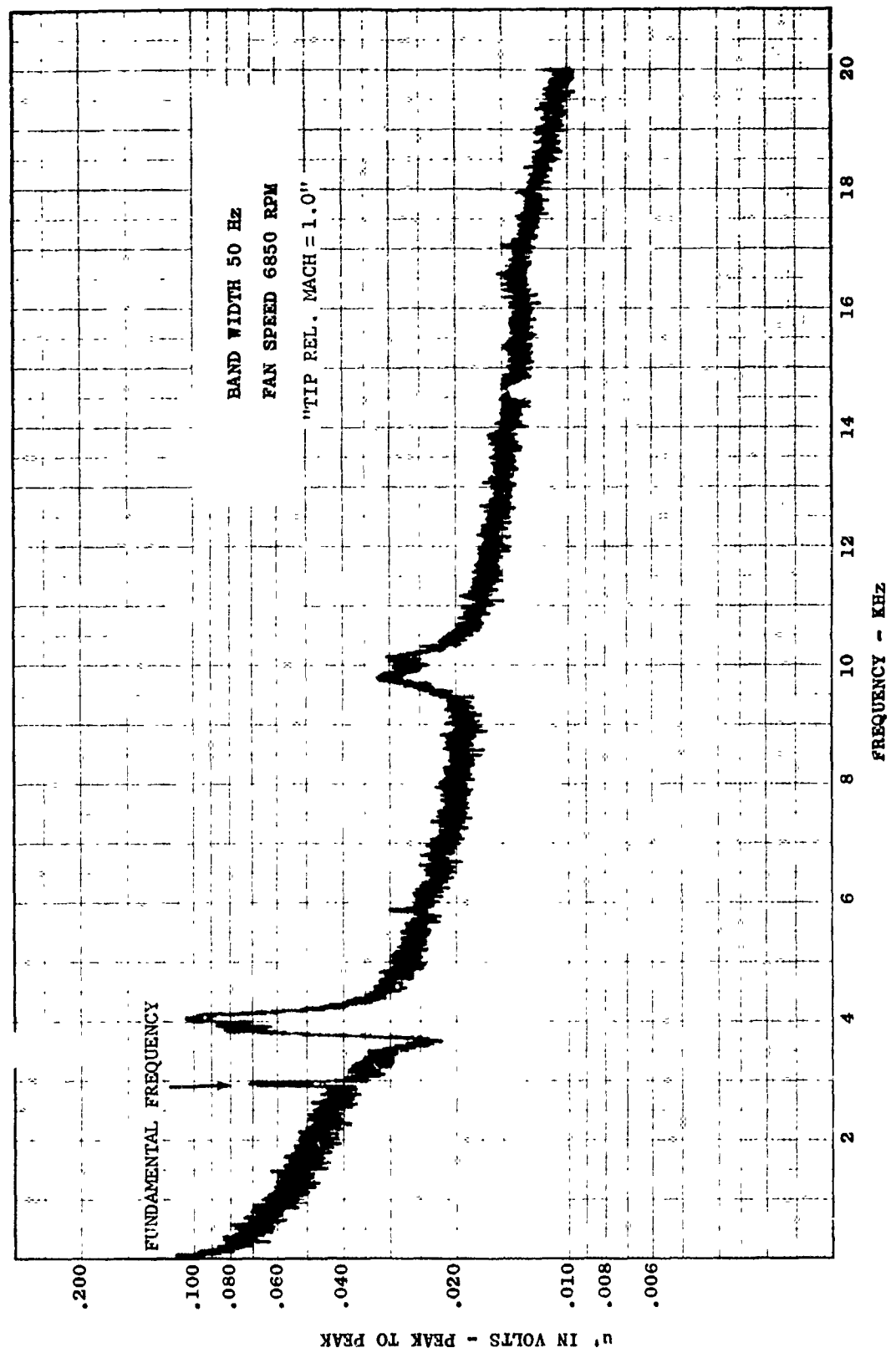


FIGURE II-C83. 3-D OGV WAKE NARROWBAND ANALYSIS OF TURBULENT COMPONENT u' AT IMMERSION #1 - D/V #4

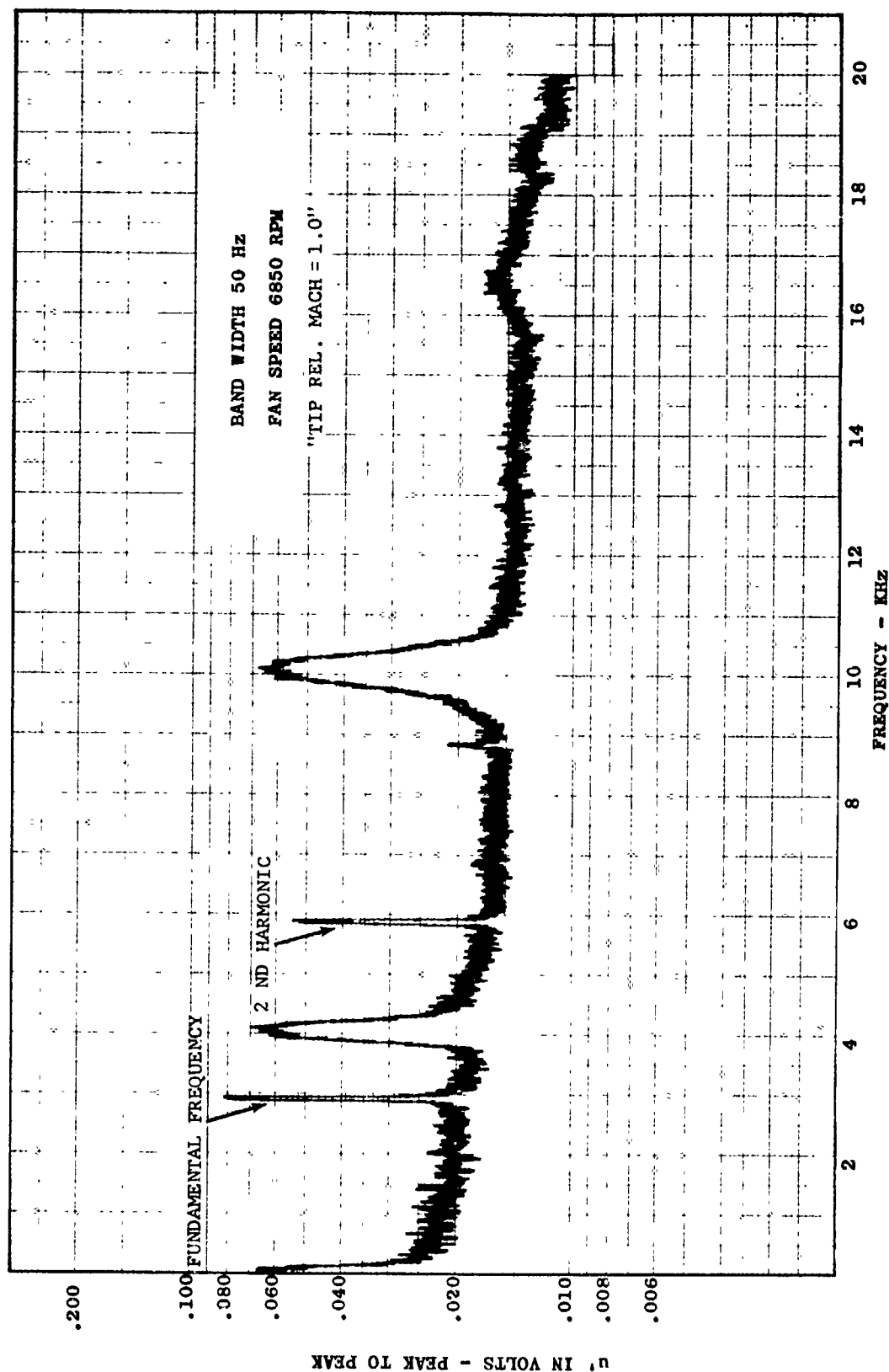


FIGURE II-C84. 3-D OGV WAKE NARROWBAND ANALYSIS OF TURBULENT COMPONENT u' AT IMMERSION #3 - D/V #4

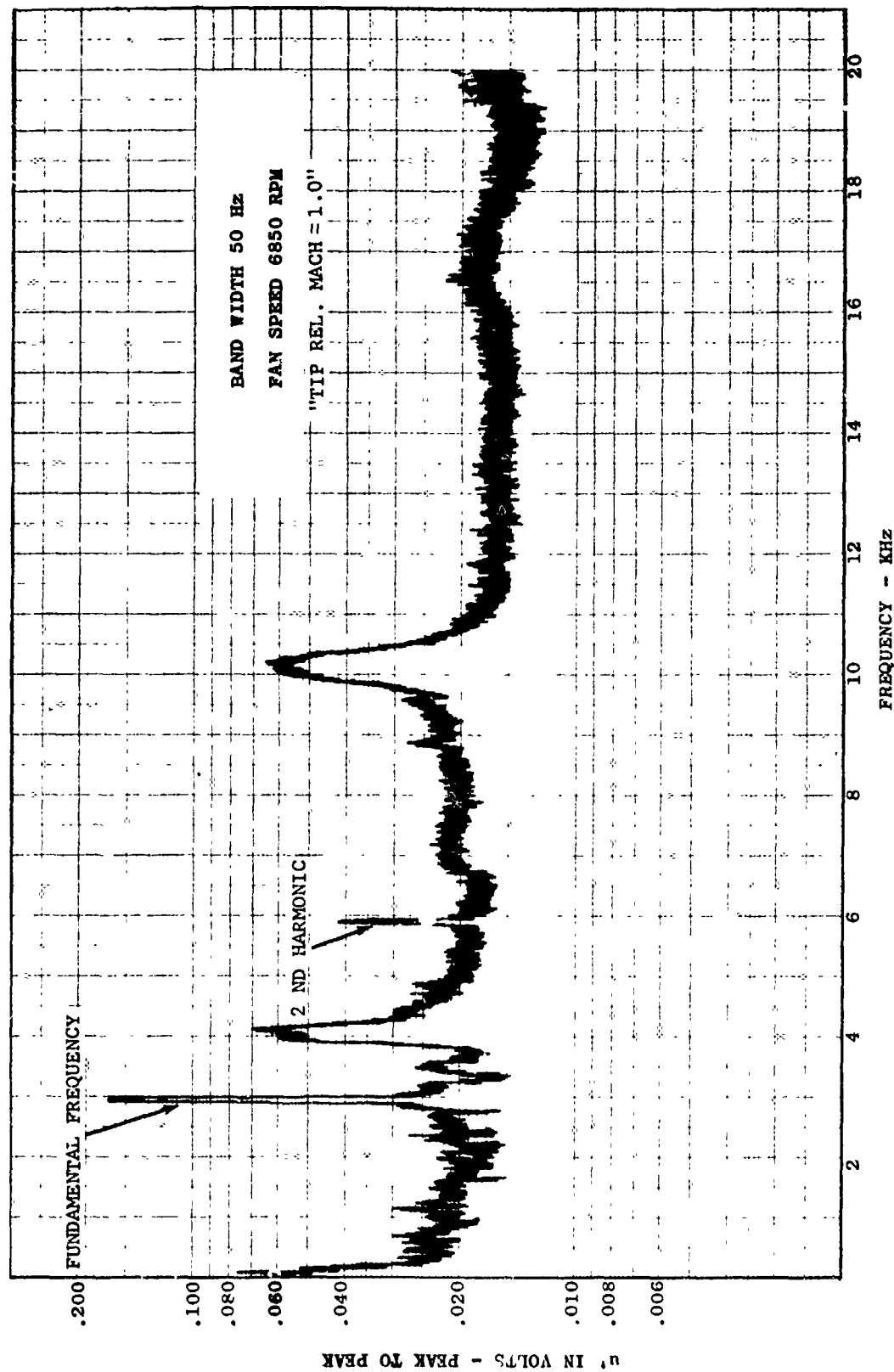


FIGURE II-C85. 3-D OGV WAKE NARROWBAND ANALYSIS OF TURBULENT COMPONENT u' AT IMMERISON #4 - D/V #4

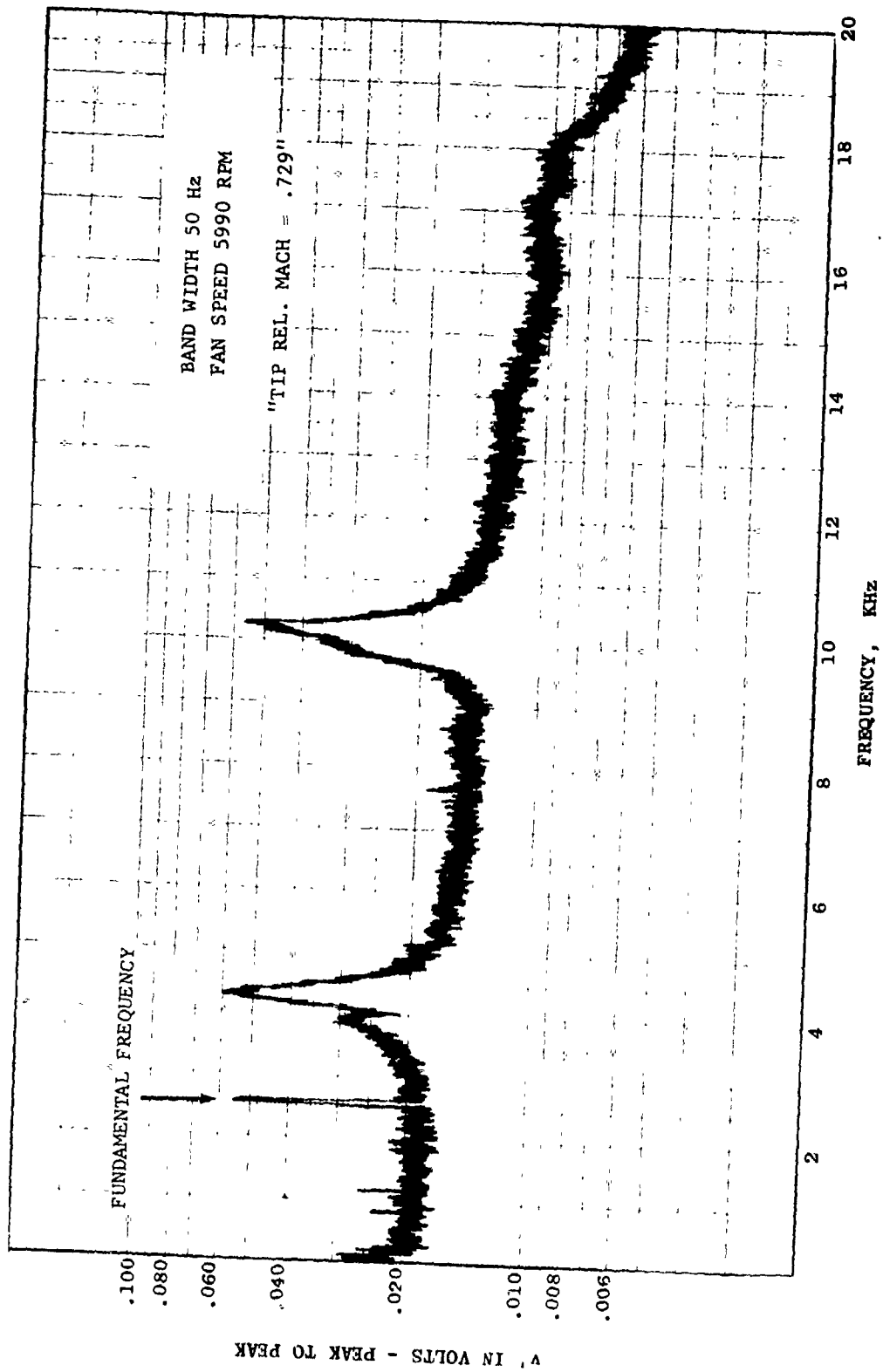


FIGURE II-C86 3-D OGV WAKE NARROWBAND ANALYSIS OF TURBULENT COMPONENT v' AT IMMERSION #1 - D/V #4

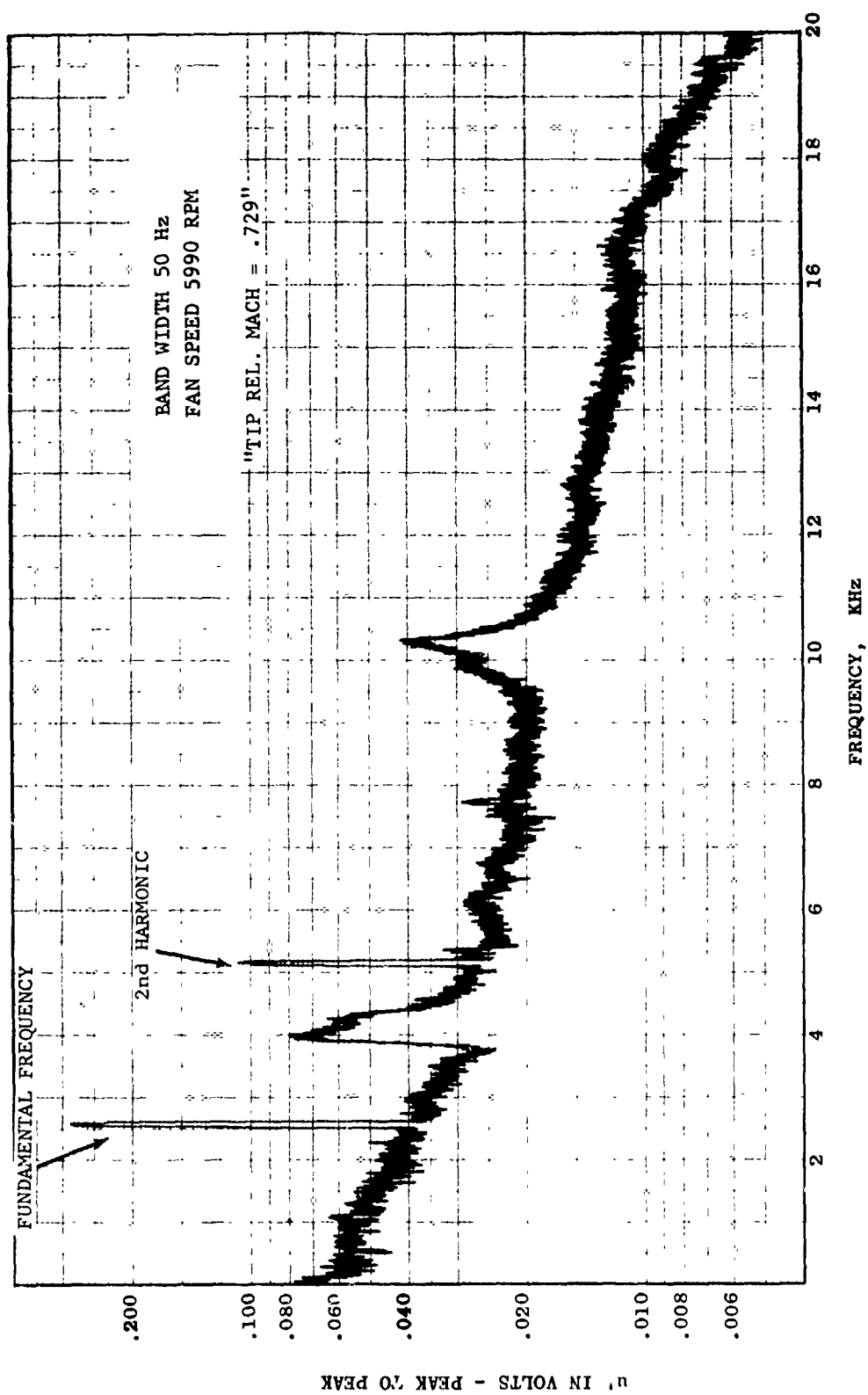


FIGURE II-CS7 3-D OGV WAKE NARROWBAND ANALYSIS OF TURBULENT COMPONENT u' AT IMMERSION #1 - D/V #4

A comparison of Figures II-C67 and II-C68 in the two dimensional cascade II-C86 and 87 shows a correspondance at 4 KHz; however the higher frequency peak occurs at 12 KHz in the cascade. Table II-C4 contains a comparison of the levels of the high and low frequency peaks. In general the level agreement is within reason.

Further research will be required to make a direct connection between far-field noise and the hot film turbulence measurements. The cascade results reported in Section II-C4; however, do indicate a direct connection between turbulence and noise. More two dimensional and rotating wake data will be needed as input to the broadband noise theoretical models outlined in Section II-B. This type of investigation should be pursued in the future.

<u>Frequency</u>	<u>Cascade*</u>		<u>D/V #4**</u>	
	u'	v'	u'	v'
4 KHz	.058	.030	.080	.060
10 or 12 KHz	.040	.046	.042	.056

- * Incidence angle 8°
Tip Relative Mach Number .7
- ** Tip Relative Mach Number .729
- + Measured in Volts

TABLE II-C4

Comparison of Peak Turbulence Level Amplitudes for the Cascade and D/V #4

NOMENCLATURE - SECTION II-C

d	Diameter of cylinder
f_v	Observed vortex shedding frequency
l	length of cylinder
M	Upstream flow Mach number
Re	Reynolds number
Sh	Strouhal number
u'	Fluctuating velocity in the flow direction
u'/\bar{U}	Turbulence intensity in the flow direction
\bar{U}	Local mean velocity in the flow direction
\bar{U}_o	Undisturbed (upstream) mean velocity
v'	Traverse fluctuating velocity
w'	Spanwise fluctuating velocity
w'/\bar{U}	Turbulence intensity perpendicular to the flow direction
x	Downstream coordinate in the flow direction
y, z	Coordinate perpendicular to the flow direction
c/s	Solidity
c	Airfoil Chord
s	Spacing between airfoils
c	Airfoil maximum thickness
i	Incidence angle
α	Air inlet angle

REFERENCE SECTION II-C

1. Kovasnay, LSG, "Hot Wire Investigation of the Wake Behind Cylinders at Low Reynolds Numbers", Proc. Roy. Soc. (London) series A, Volume 198, Number 1053, August 15, 1949, pp. 174 - 190.
2. Roshko, A., "On the Development of Turbulent Wakes From Vortex Streets", NACA Report 1191.
3. Etkin, B., Korbacher, G.K., Keefe, R. T., Journal of the Acoustical Society of America, Volume 29, 1, 1957.

(D) Multiple Pure Tones - Blade Passing Frequency Sub-Harmonics

(1) General Description of the Phenomena. One of the most "intriguing" aspects of noise generated by transonic rotors is the phenomena of multiple pure tones (MPT's). These strong pure tones have been observed to be of greater amplitude than the blade passing frequency (Figure II-D1) at high engine speeds and are, therefore, significant in terms of overall fan/compressor noise.

Several very distinct phenomena which characterize MPT's are listed below:

- . Detected only in the inlet duct
- . Generated only when the rotor tip Mach number is greater than one
- . Strongest MPT's exist at frequencies below rotor blade passing frequency and occur at integral multiples of engine revolutions
- . Amplitude varies with engine speed
- . Lower frequency MPT's appear as engine speed increases

The first point is exemplified by the probe narrowband data shown in Figures II-D2 and II-D3. The exhaust probe (Figure II-D2) shows only the blade passing frequency tone. The inlet probe at the same fan speed (Figure II-D3) shows multiple pure tones not only below the blade passing frequency, but at higher frequencies as well.

The second characteristic has some far reaching effects. Figure II-D4 shows the occurrence of multiple pure tones (MPT's) in the Development Vehicle with and without IGV's (see Section V). It is clear from this presentation that the MPT's began to propagate when the tip Mach number of the rotor became sonic; and not when the tip relative Mach number exceeds one. Since propagation of MPT's begins before tip relative Mach numbers become sonic, the occurrence of bow shock waves must be incidental to MPT propagation.

The third characteristic is clearly seen in Figures II-D1 and II-D3.

The fourth phenomenon can be seen in the fan acceleration tracking filter plot shown in Figure II-D5. The level of the 10th per rev tone (Figure II-D3) is shown during a slow accel. The rise in level is clearly shown with the tone at a high plateau above 8,000 rpm.

Finally, there is a fifth point. Both Figures II-D4 and II-D6 show that the lower number MPT's appear as fan speed increases. Thus, it appears that the propagation and generation of the MPT's is closely related to the engine speed.

(2) Some Theoretical Considerations. A theory which examines MPT's will have to conform to the five phenomena mentioned above.

Consider the following:

In Section II-A an equation was derived for the acoustic pressure in an annular duct,

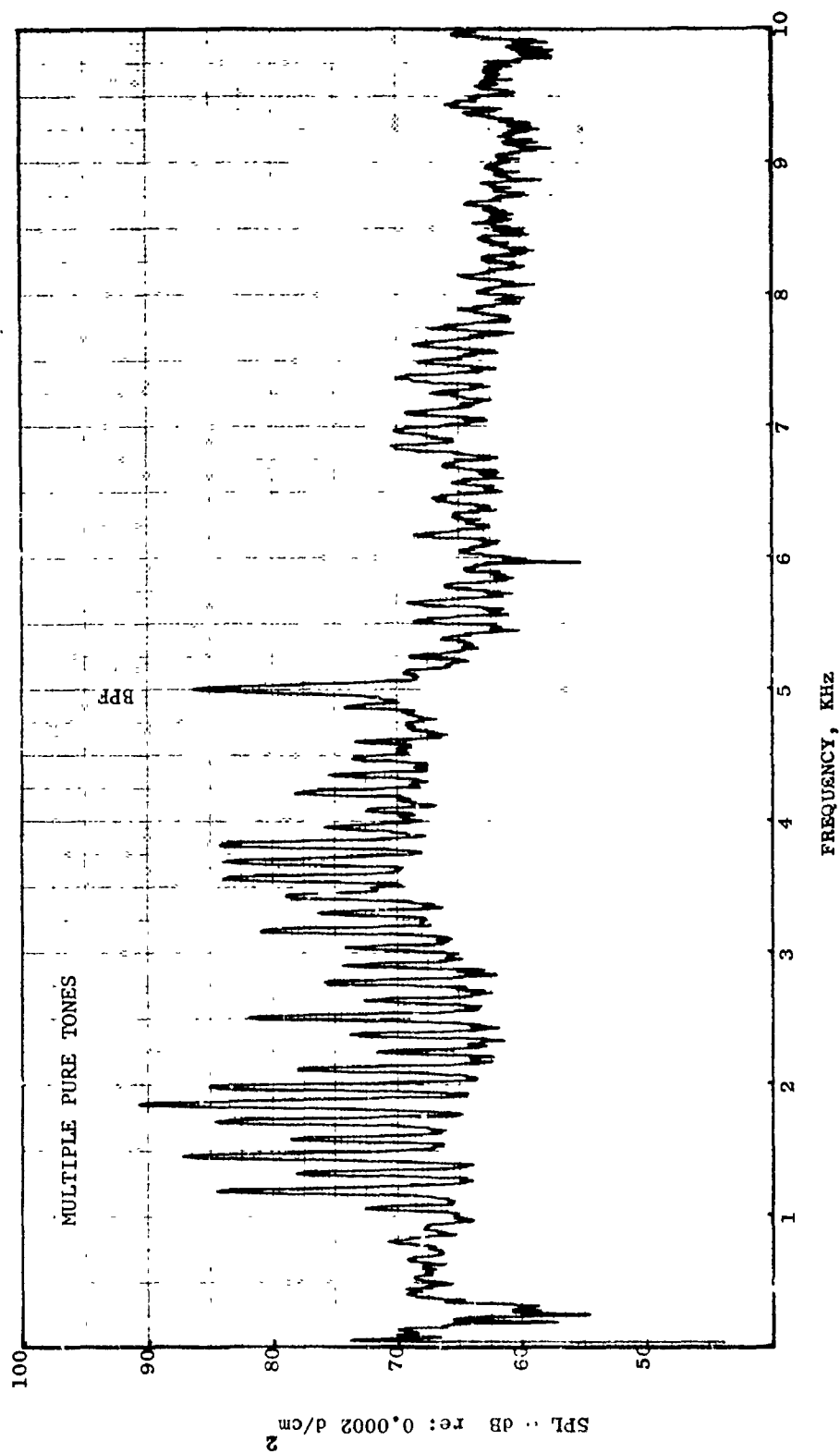


FIGURE II-D1 TYPICAL SPECTRUM CONTAINING MULTIPLE PURE TONES - FARFIELD DATA

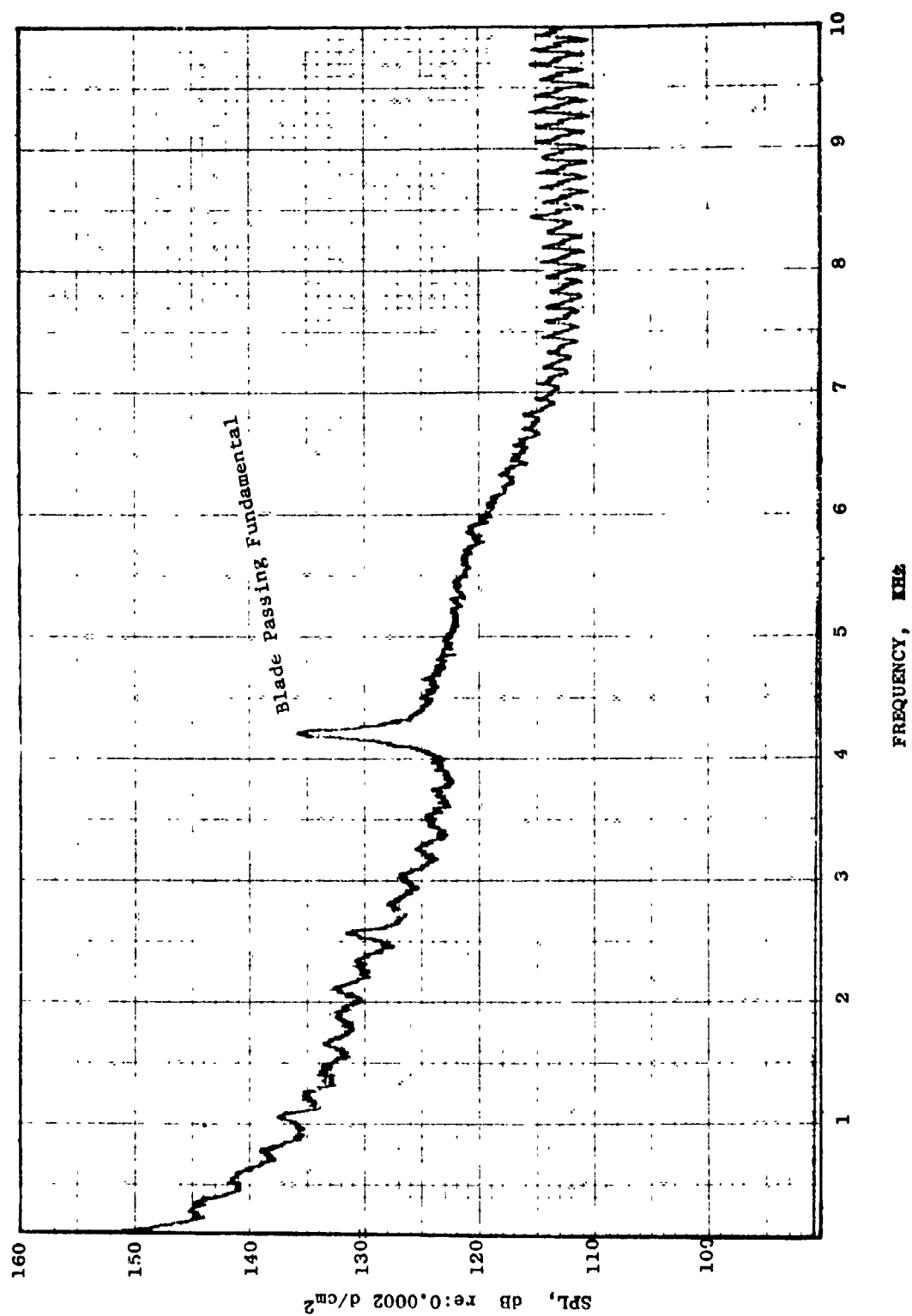


FIGURE 11-D2 EXHAUST PROBE NARROWBAND SPECTRAL ANALYSIS INDICATING THE ABSENCE OF MPT'S

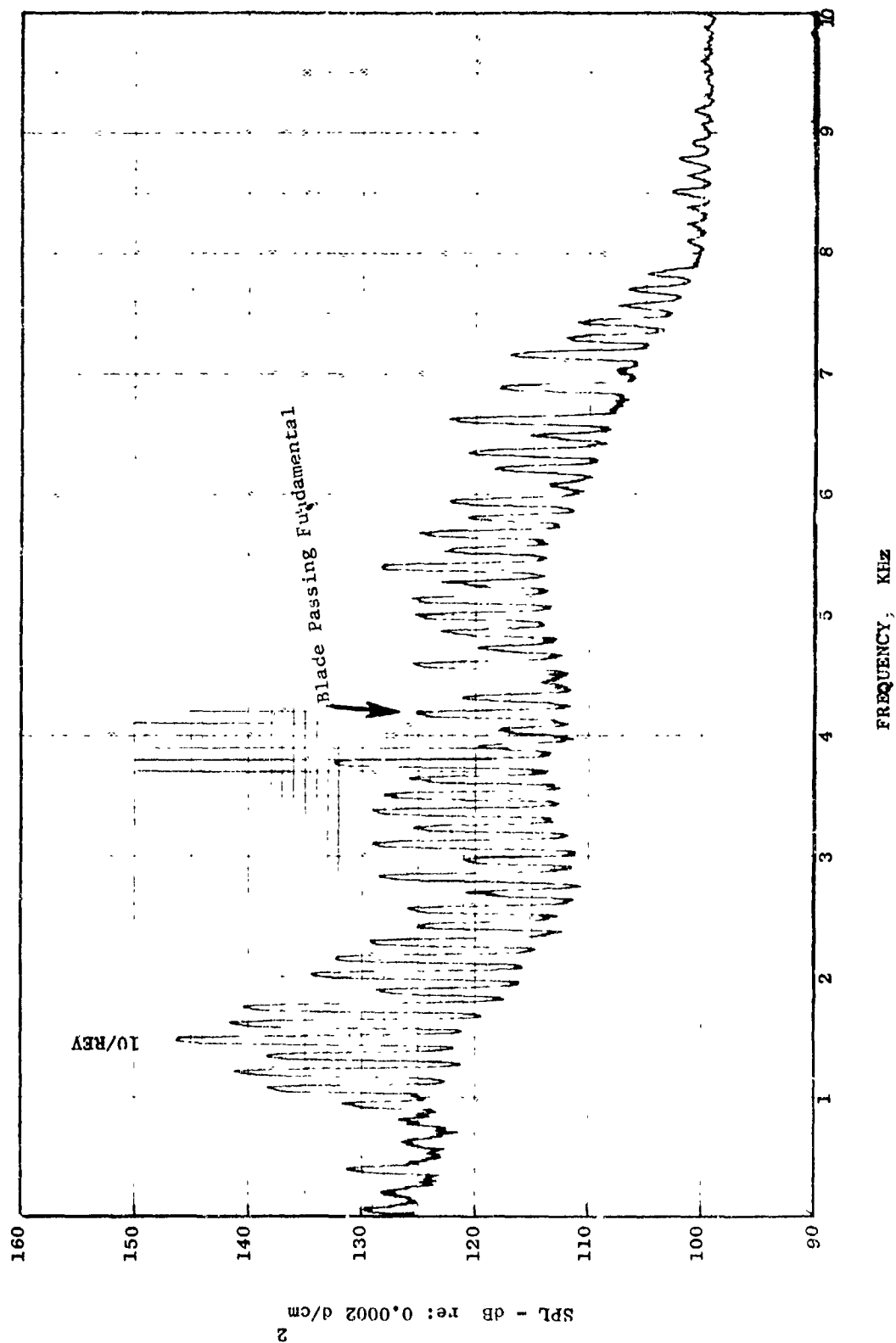


FIGURE 11-D3 INLET PROBE NARROWBAND SPECTRAL ANALYSIS SHOWING MULTIPLE PURE TONES
8989 RPM - 50 Hz B.W.

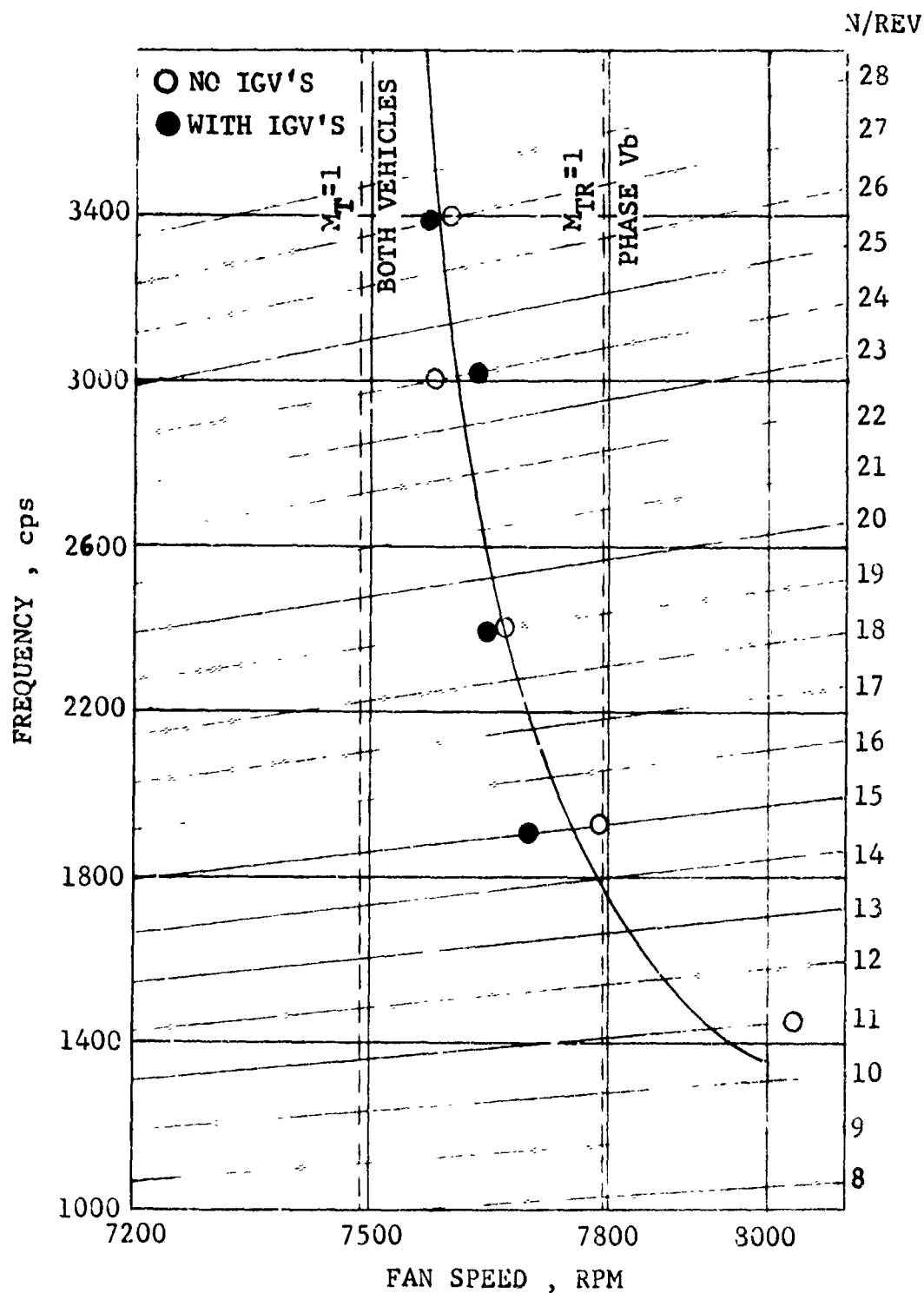


FIGURE II-D4 CAMPBELL DIAGRAM OF MPT'S IGV AND NO IGV

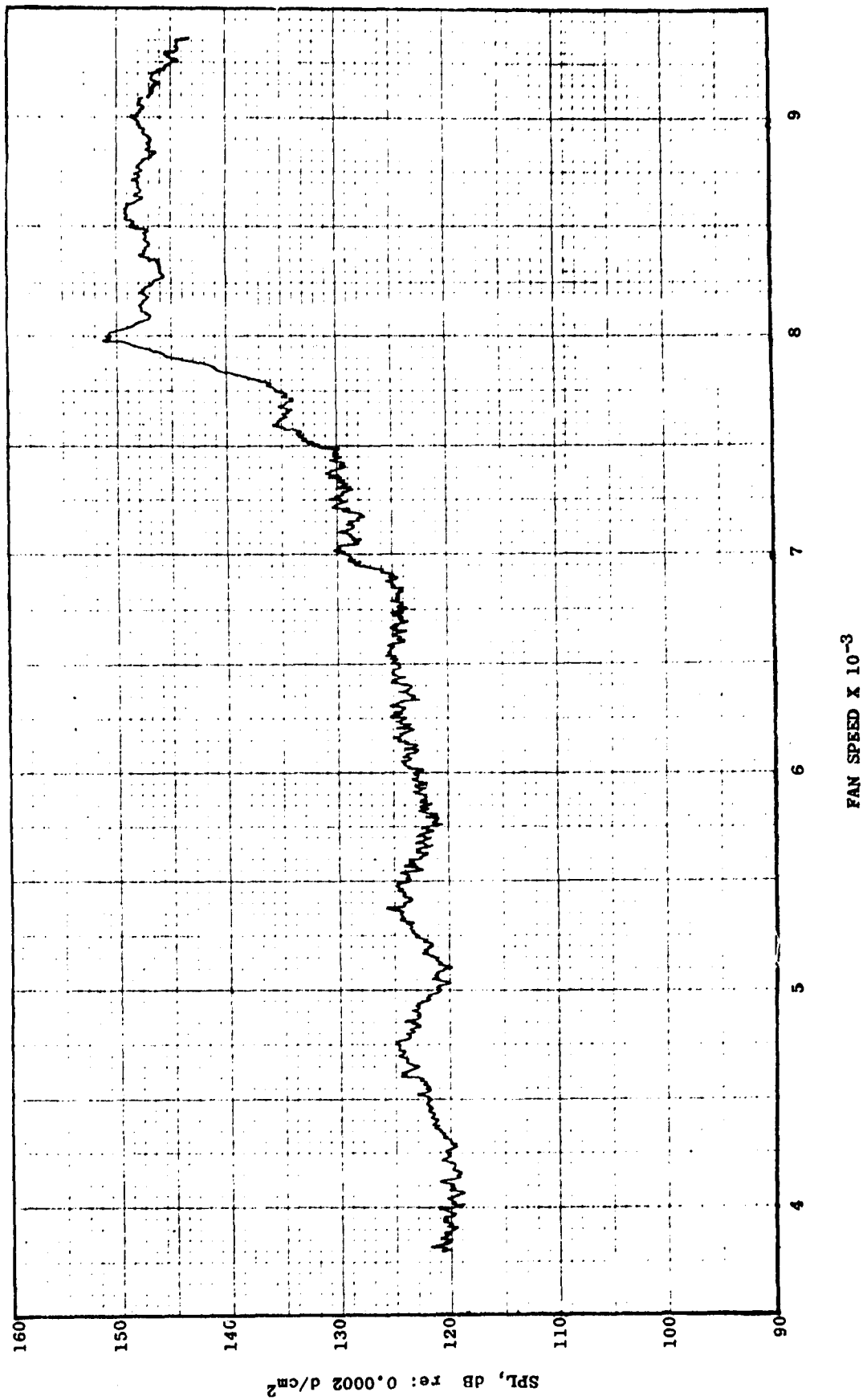


FIGURE II-D5 TRACKING FILTER NARROWBAND SPECTRUM OF 10/REV SPL vs. FAN SPEED

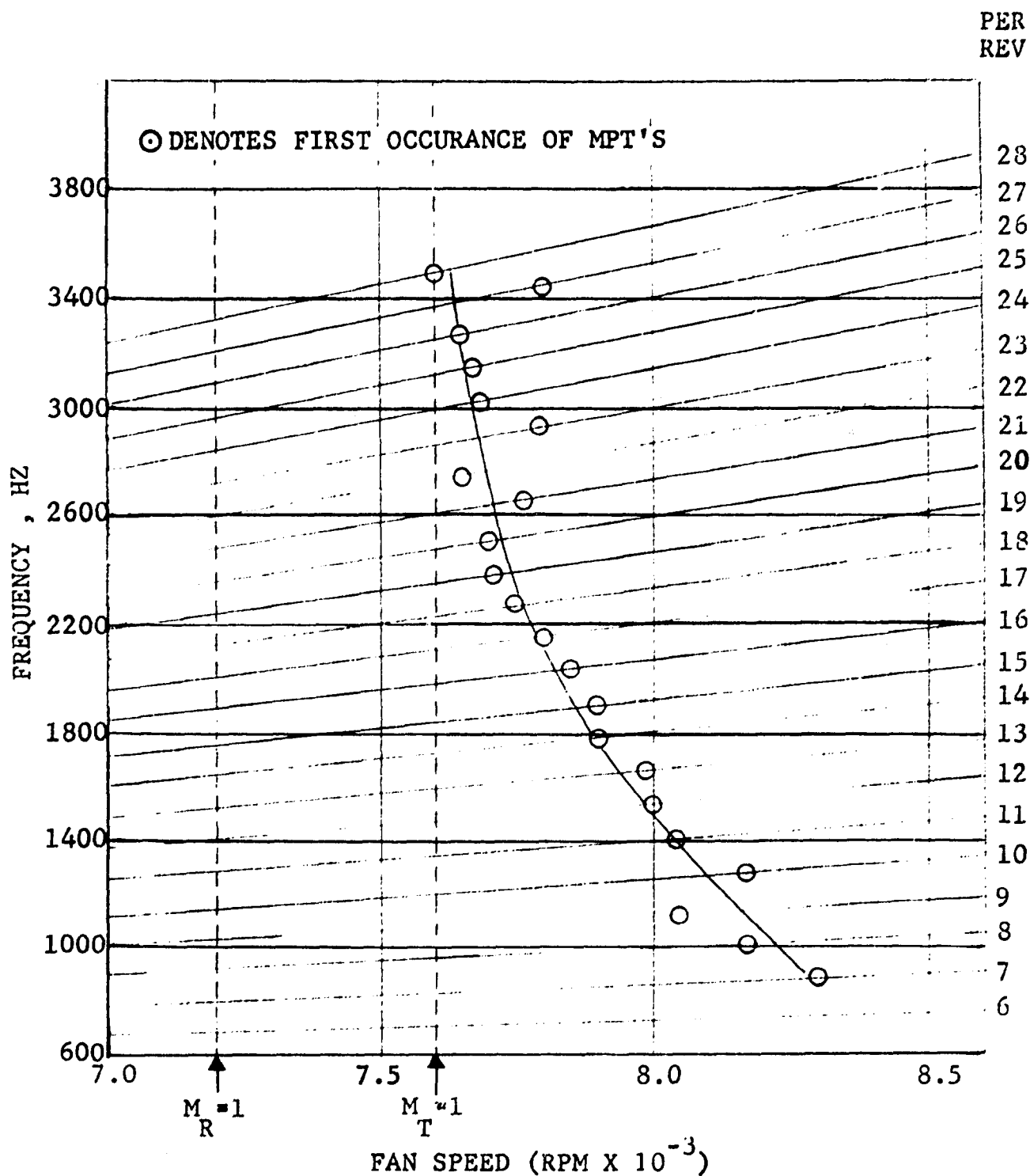


FIGURE II-D6 MULTIPLE PURE TONE OCCURANCE

$$P_{nm} = A_{nm} \rho c^2 n \omega e^{in(\theta - \omega t)} R_n(\lambda_{nm} r) e^{i\alpha z} e^{i\beta z} \quad (II-D1)$$

where

$$\beta = \frac{\sqrt{n^2 (\omega - \bar{M}_\theta)^2 - \lambda_{nm}^2 (1 - M_z^2)}}{1 - M_z^2}$$

In equation (II-D1) the expression for β defines the well known cutoff speed. That is,

$$N_{c.o.} = \left[\frac{\lambda_{nm}}{n} \sqrt{1 - M_z^2} + \bar{M}_\theta \right] \frac{30 \text{ nc}}{n B \pi R_o} \quad (II-D2)$$

where $N_{c.o.}$ is the cutoff speed of the fan in rounds per minute. For the simple case of zero flow ($M_z = \bar{M}_\theta = 0$) equation (II-D2) becomes

$$N_{c.o.} = \frac{\lambda_{nm} 30c}{n B \pi R_o} \quad (II-D3)$$

Equation (II-D3) can be rewritten in terms of fan tip Mach number

$$(M_T)_{c.o.} = \frac{\lambda_{nm}}{n B} \quad (II-D4)$$

It has previously been shown (Section II-A1) that the eigenvalue, λ_{nm} is a function of the radius ratio h , spinning mode number n , the radial mode number m .

For the case of a source with no stator the spinning lobe number is given by

$$n = \bar{n} b \quad (II-D5)$$

Then equation (II-D4) becomes

$$(M_T)_{c.o.} = \frac{\lambda_{nm}}{n} \quad (II-D6)$$

In the case of the MPT source it may be hypothesized that there exists in the inlet a single wave form composed of many harmonics. Figure II-D7 illustrates this condition. Each of the harmonics would then occur at a frequency equal to a multiple of the fan rotational frequency. Or in other words at the per revs shown in Figures II-D1 and II-D2.

In reference 1 the value of $(M_T)_{c.o.}$ for various modes and radius ratios was presented. Figure II-D8 is a reproduction of Figure 1 of reference 1. It is clear that for the case being considered that the fan tip Mach number must exceed unity in order for unattenuated propagation of the type represented by equation (II-D1) to take place.

This characteristic of the analysis satisfies the second point made earlier. Figure II-D8 further supports the observations made in Figures II-D4 and II-D6. That is, that the lower per revs (lower values of spinning lobe number) propagate unattenuated at higher tip Mach numbers.

Then equation (II-D1) can be used to predict the occurrence of MPT's with respect to the fan speed at which they occur and their frequency. The amplitude prediction can only be accomplished if the amplitude constant A_{nm} can be determined.

Thus far evidence has shown that MPT propagation occurs when tip Mach number exceeds one. It appears that the source of MPT's is the rotor's pressure field. That is, the pressure pattern exhibited by the rotor blades as they rotate.

Therefore, let it be assumed that at a given radial location the circumferential circulation distribution is made up of arbitrary rectangular segments as shown in Figure II-D7.

Each segment constitutes the circulation of an individual blade. Thus there are B such rectangular segments around the circumference.

There are three pertinent variables associated with the segments form:

- . amplitude
- . duration
- . interval

The amplitude is the magnitude of the circulation about each blade. In general, there is a slight variation from blade to blade and therefore the amplitude varies circumferentially. The duration is the width of the rectangular segment while the interval is the distance between segments. Both of these quantities will vary with blade geometry and blade loading level.

The circulation distribution of Figure II-D7 represents a generalization of the analysis of Section II-A1. If the duration of each wave is shrunk to zero and the intervals are all set equal to $2\pi/B$ the case of the impulse input results.

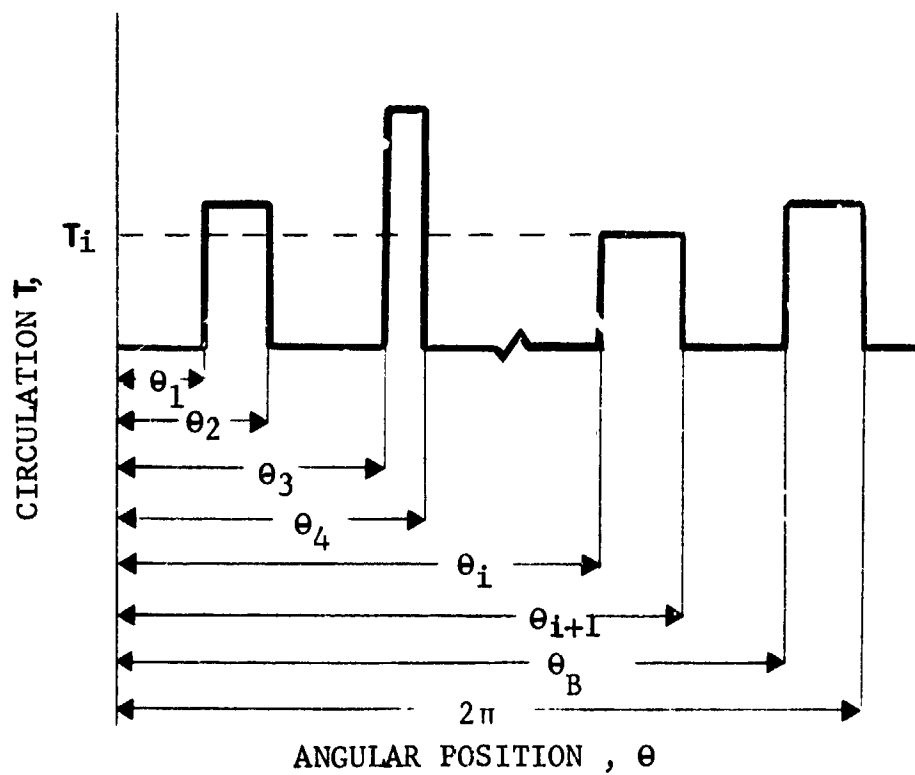


FIGURE II-D7 ARBITRARY BLADE LOADING DISTRIBUTION

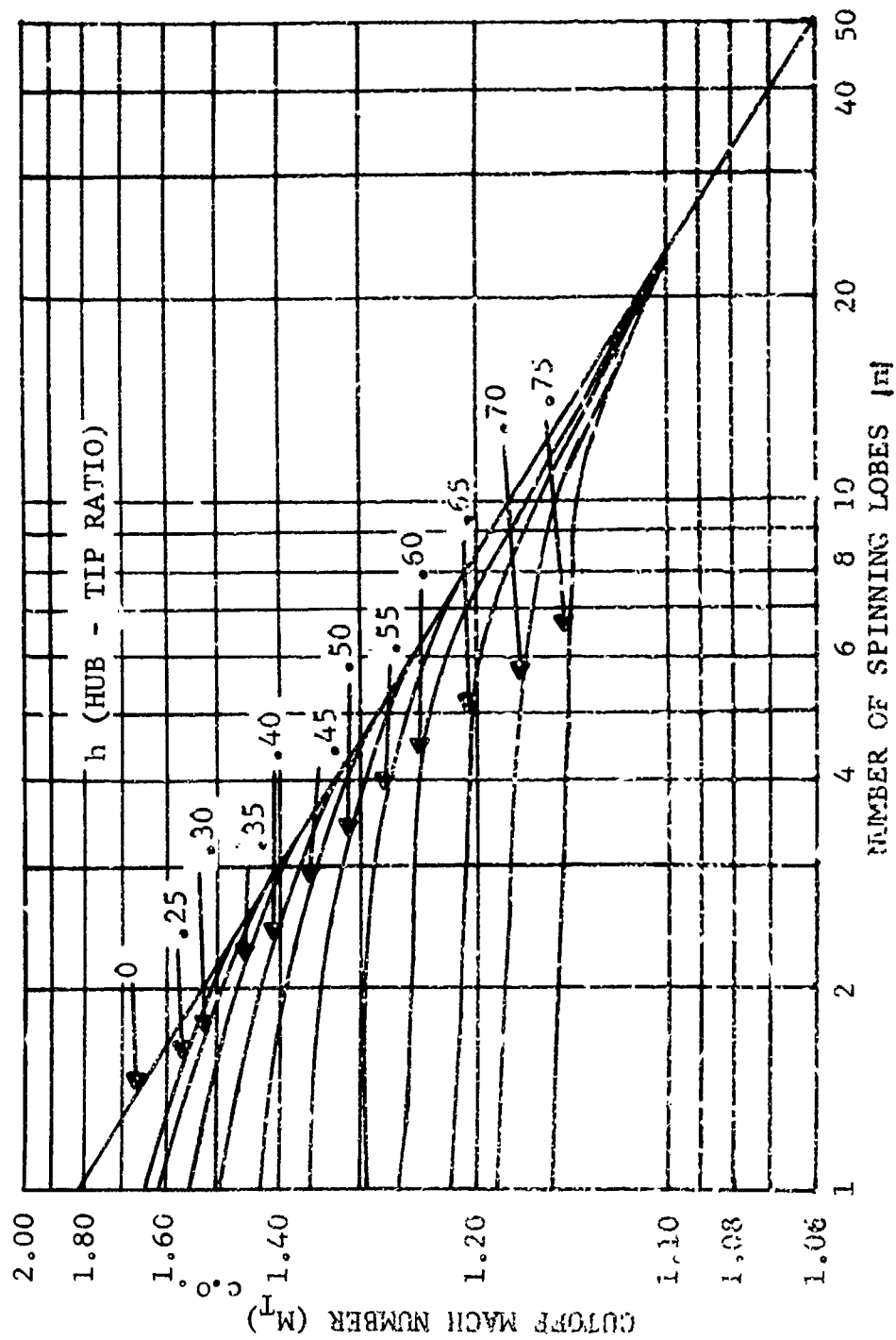


FIGURE 11-D8 CUTOFF MACH NUMBER FOR SPINNING MODES

The wave form of Figure II-D7 may be expressed in a reference frame relative to the rotor in a complex Fourier series,

$$\Gamma(r, \theta) = \sum_{n=-\infty}^{+\infty} C_n(r) e^{in\theta} \quad (\text{II-D7})$$

where

$$C_n(r) = \frac{1}{2\pi} \int_0^{2\pi} \Gamma(r, \theta) e^{-in\theta} d\theta \quad (\text{II-D8})$$

If the wave form of Figure II-D7 is available at three radial locations, then the coefficient $C_n(r)$ may be expressed as a second order polynomial.

$$C_n(r) = a_n + a_n r + a_n r^2 \quad (\text{II-D9})$$

The series equation (II-D7) is expressed relative to the rotor. In order to transfer it to the absolute reference frame it must rotate with the wheel speed. Thus,

$$\Gamma(r, \theta, t) = \sum_{n=-\infty}^{+\infty} C_n(r) e^{in(\theta - \omega t)} \quad (\text{II-D10})$$

From Figure II-D7 it is seen that the circulation is piecewise constant. Therefore, equation (II-D8) can be expressed as

$$C_n = \frac{1}{2\pi} \sum_i^B \int_{\theta_i}^{\theta_{i+1}} \Gamma_i e^{-in\theta} d\theta \quad (\text{II-D11})$$

Integrating

$$C_n = \frac{1}{2\pi n} \sum_i^B \Gamma_i \left[e^{-in\theta_{i+1}} - e^{-in\theta_i} \right] \quad (\text{II-D12})$$

Thus, equations (II-D10) and (II-D12) are equivalent expressions for the wave form of Figure II-D7 in terms of n harmonics.

The circulation can be expressed as

$$\Gamma(r) = \int_0^{2\pi} V_r \, d\theta \quad (\text{II-D13})$$

where V is the net tangential velocity in the plane of the rotor. Therefore

$$\frac{d\Gamma}{d\ell} = V_r \quad (\text{II-D14})$$

Using equation (II-D10)

$$V_r = i \sum_{-\infty}^{+\infty} n C_n(r) e^{in(\theta-\omega t)} \quad (\text{II-D15})$$

Equation (II-D15) constitutes a boundary condition for the acoustic wave problem for which equation (II-D1) is the solution.

Equation (I-1) for the acoustic pressure may be recast for the tangential velocity perturbation as

$$V_{nm} r = A_{nm} \frac{2}{n} e^{in(\theta-\omega t)} R_n(\lambda_{nm} r) e^{i\alpha z} e^{i\beta z} \quad (\text{II-D16})$$

Since only positive values of n will exist, equation (II-D15) can be expressed as

$$V_r = i \sum n C_n(r) e^{in(\theta-\omega t)} \quad (\text{II-D17})$$

for the n^{th} harmonic. Equation (II-D17) can now be equated to equation (II-D16) for the n, m mode

$$C_n(\cdot) = 2 R_0 c A_{nm} K_n(\lambda_{nm} r) \quad (\text{II-D18})$$

Proceeding as in Section II-A1

$$A_{nm} = -\frac{1}{\eta_{nm}^{1/2} 2 R_o c} \int_h^1 C_n(r) r R_n(\lambda_{nm} r) dr \quad (II-D19)$$

Combining equations (II-D1) and (II-D19), the pressure is

$$P_{nm} = \frac{\rho c n \omega}{\eta_{nm}^{1/2} 2 R_o} e^{i\beta z} R_n(\lambda_{nm} r) e^{in(\theta - \omega t)} e^{i\alpha z} \int_h^1 C_n(r) r R_n(\lambda_{nm} r) dr \quad (II-D20)$$

where

$$n\omega = \frac{N\pi R_o B}{30 c} \quad (II-D21)$$

From equation (II-D21) the radial distribution of MPT amplitude may be calculated for each n per rev if $C_n(r)$ can be determined. The term $C_n(r)$ is dependent on the distribution of Figure II-D7. Unfortunately, there does not exist an analytical method of determining this pattern. Further work is needed in this area.

(3) Some Conclusions on MPT Generation. Relevant test data and the theory contained in Section II-D2 indicate that MPT's are generated and propagate when the tip Mach number of the rotor exceeds unity. It is therefore, possible to avoid MPT's by simply holding M_T below one. This, however, exerts a severe penalty on turbofan and compressor designs.

The distribution of Figure II-D7 implies that the noise source strength associated with the rotor steady loading is distributed over what amounts to sub-harmonics of the blade passing frequency. If the pattern of Figure II-D7 is more uniform (the most uniform condition being defined as equal amplitude rectangular segments of constant width and spaced at a $2\pi/B$ angular positions) than more energy will be fed into the BPF. Conversely, a more random pattern produces more MPT content and less BPF generation. It must be kept in mind,

however, that this source of BPF noise is not the only source; e.g., viscous wake interactions, and therefore changes in BPF amplitude may not be detectable.

Figure II-D8 shows that MPT propagation may be delayed by decreasing radius ratio. This is true only for lobe numbers below about 25.

Additional noise reduction procedures will have to await a more precise definition of Figure II-D7.

**THIS
PAGE
IS
MISSING
IN
ORIGINAL
DOCUMENT**

REFERENCES SECTION II-D

1. Sperry, W.C. and Benzakein, M.J. "Experimental Results of Vane/Blade Number Effects on Compressor Noise", ASME 13th Annual International Gas Turbine Conference, Washington, D.C., March 17-21, 1968.

III. FAN COMPRESSOR NOISE TRANSMISSION AND RADIATION MECHANISMS

(A) Sound Transmission in a Turbomachinery Duct. The idea that sound can be transported along a duct by plane waves has been known for some time. The higher order modes of transmission were at one time regarded as a high frequency phenomena of secondary importance. Tyler and Sofrin, however, illustrated the importance of these modes in the analysis of transmission and radiation of sound in an axial compressor.

Compressors and fan ducts of modern turbofan engines are potent sources of discrete frequency noise. Tyler and Sofrin had shown that the radiated discrete frequency sound is strongly influenced by the walls of the air intake duct, and that this effect is due to the transmission of higher order modes in the duct. This type of sound wave was called "spinning modes". A property which is not found in plane waves, but was found for "spinning modes" was the cut-off property: each higher mode in a uniform duct fails to propagate if the frequency falls below a critical value, the cut-off frequency.

The effect of flow on higher order modes propagation were problems not considered by the early investigators of compressor/fan transmission and radiation. For instance, for a sound wave emitted from a point and traveling through a moving fluid the sound wave is known to experience changes in its wave length (Doppler effect). The moving fluid also produces an asymmetric pressure distribution about the source. In the limiting case of a Mach number equal to one normal to the direction of propagation the wave ceases to propagate and a zone of silence results upstream of the source.

In the case of the spinning modes generated in fan and compressor operation, the effect is somewhat similar. That is, the perturbation pressure is distorted by the axial and swirl velocities in the engine. In addition to pressure changes, it can be expected that the cut-off speed and decay rate below cut-off will be altered by the moving medium.

Further, directivity measurements of the noise radiated from a duct or annulus to the far field shows a pattern which is a result of reinforcement and cancellation of sound pressure as well.

In an effort to better understand compressor/fan acoustic wave transmission and radiation mechanisms a number of studies were instituted. In the sub-sections which follow analytical and experimental investigations will be discussed which enable the prediction of fan/compressor noise through ducts and into the radiation field, the sound transmission through blade rows, and the refraction effects on pure tones.

(1) The Three-Dimensional Acoustic Transmission and Radiation Program. The three-dimensional acoustics computer program (References 1 and 2) is a unique and versatile tool to investigate spinning mode discrete frequency sound wave propagation in axially symmetric cylindrical or annular ducts of finite length and radiation into free space. It incorporates a numerical solution of the wave equation in a cylindrical coordinate system subject to boundary conditions at the walls of the duct, e.g., a compressor or fan duct. A brief description of the code follows.

Theory For Axially Symmetric Geometries with Uniform Medium Axial Flow. Assuming small acoustic pressures in a homogeneous medium and ignoring second order effects, (linear theory) the velocity potential in the field is described by the following equation

$$\left[\frac{1}{r} \frac{\partial}{\partial r} \left(r \frac{\partial}{\partial r} \right) + \frac{1}{r^2} \frac{\partial^2}{\partial \theta^2} + (1-M^2) \frac{\partial^2}{\partial z^2} - \frac{2M}{c} \frac{\partial^2}{\partial z \partial t} - \frac{1}{c^2} \frac{\partial^2}{\partial t^2} \right] \phi = 0 \quad (\text{III-A1})$$

where

c	=	acoustic velocity
t	=	time
r, θ, z	=	cylindrical coordinates as shown in Figure III-A1
M	=	V_z/c = steady Mach number of the fluid in the +z - direction
\bar{V}_z	=	steady velocity in the z-direction
ϕ	=	velocity potential
\hat{n}	=	$-\frac{\partial \phi}{\partial n}$ defines the velocity potential and \hat{u} is the velocity normal to the boundary

The sound pressure, p , is related to the velocity potential by means of the expression

$$p = \rho_0 \frac{\partial \phi}{\partial t} + \rho_0 \bar{V}_z \frac{\partial \phi}{\partial z} \quad (\text{III-A2})$$

where ρ_0 is the fluid density. A sinusoidal time variation of the sound pressure, velocity and velocity potential is assumed, i.e.,

$$\begin{aligned} p &= \hat{p} e^{-i\omega t} \\ \phi &= \hat{\phi} e^{-i\omega t} \\ \bar{V}_z &= \hat{u} e^{-i\omega t} \end{aligned} \quad (\text{III-A3})$$

Then the expression for the pressure becomes

$$\hat{p} = -i\omega \rho_0 \hat{\phi} + \rho_0 \bar{V}_z \frac{\partial \hat{\phi}}{\partial z} \quad (\text{III-A4})$$

If one considers an acoustic source located at the origin of the coordinate system, the velocity potential distribution in the field is as follows, (Reference 3):

$$\phi = \frac{\hat{A} e^{-i(\omega t - \nu R_0)}}{R_0^*} = \hat{\phi}'(z, r) e^{-i\omega t} \quad (\text{III-A5})$$

where

$$R_0 = \frac{-Mz + [z^2 + (1-M^2)r^2]^{1/2}}{1-M^2} \quad (\text{III-A6})$$

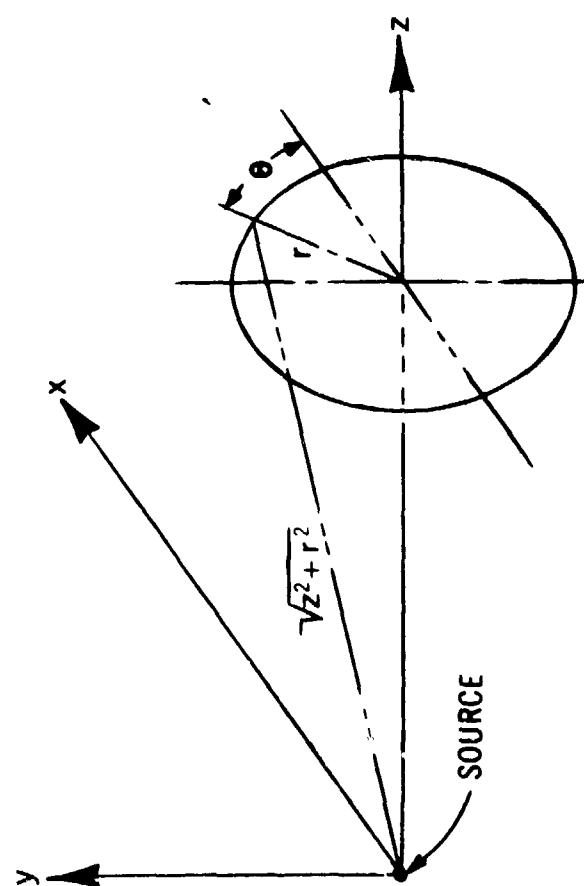


FIGURE III-A1 CYLINDRICAL COORDINATE SYSTEM

$$R_o^* = \left[\frac{z^2}{1 - M^2} + r^2 \right]^{1/2} \quad (\text{III-A7})$$

$$r^2 = x^2 + y^2 \quad (\text{III-A8})$$

$$\hat{\phi}' = \frac{\hat{A}' e^{i\nu R_o}}{R_o^*} \quad (\text{III-A9})$$

$$\nu = \omega/c \quad (\text{III-A10})$$

$$\hat{A}' = \text{source strength}$$

$$\omega = 2\pi f = \text{the frequency}$$

$$i^2 = -1$$

and the symbol $\hat{}$ is used to denote a complex number.

Relation (III-A5) satisfies the differential equation (III-A1). A series of terms of the same form as equation (III-A5) is used to obtain the solution when boundaries are present. Assume a specified geometry, as shown in Figure(III-A2). The continuous boundaries are replaced by discrete source points associated with surface elements, as illustrated in Figure III-A3. Each source radiates in an infinite medium. The pressure in the field is the sum of the contributions due to all sources which must satisfy specified boundary conditions. The distribution of source strengths on the surface is assumed to be continuous and representable by means of a Fourier series.

Considering a point ξ somewhere in the acoustic field, the velocity potential may be expressed as follows:

$$\hat{\phi}'(\xi) = \int_S \int \hat{A}'(s) \frac{e^{i\nu R}}{R^*} ds \quad (\text{III-A11})$$

where S denotes the total surface of sources and $\hat{A}'(s)$ is the source strength per unit area. R and R^* are defined as follows:

$$R = \frac{-(z-z')^2 M + \sqrt{(z-z')^2 + (1-M^2) [(x-x')^2 + (y-y')^2]}}{1-M^2}$$

$$R^* = \sqrt{\frac{(z-z')^2}{1-M^2} + (x-x')^2 + (y-y')^2} \quad (\text{III-A12})$$

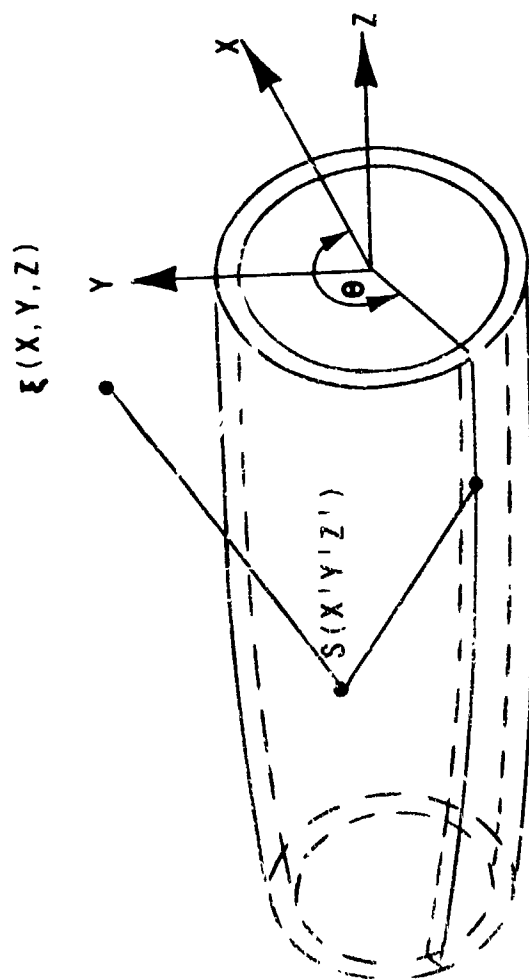


FIGURE III-A2 ACTUAL CONFIGURATION

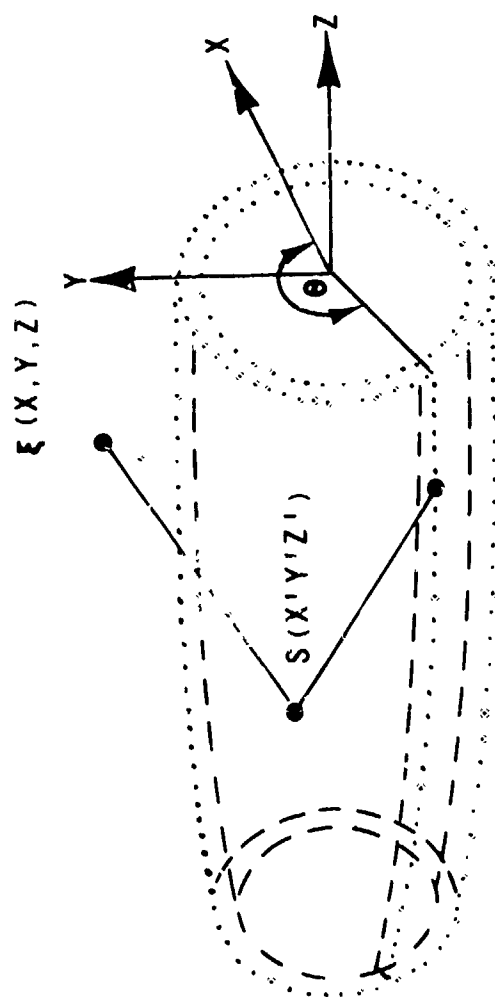


FIGURE III-A3 ANALYTICAL MODEL FOR DUCT SOUND TRANSMISSION

Because the wave equation is linear, it is satisfied by relation (III-A11). The objective is to determine the unknown source strength distribution $A(s)$, such that the boundary conditions are also satisfied.

Boundary conditions must be defined for every point on the boundary S . These conditions may be a statement of normal velocity, pressure, or acoustic impedance. Let one assume that the normal velocity at the boundary S is given by

$$u = \hat{U}(s) e^{i(m\theta - \omega t)} \quad (\text{III-A13})$$

where m is the number of lobes.

Because of the rotating pressure field shown in Figure (III-A4) it is logical to assume a source of the following type:

$$\text{Source strength per unit area} = \hat{A} e^{-i\omega t} = \hat{A} e^{i(m\theta - \omega t)}.$$

According to the definition of the velocity potential, the outward normal derivative of potential can be written as follows:

$$\frac{\partial \phi}{\partial N} = -u \quad (\text{III-A14})$$

where

$$\phi = \hat{\phi} e^{-i\omega t} = \hat{\phi} e^{i(m\theta - \omega t)}$$

Substituting equation (III-A11) into equation (III-A14) and considering point j on the surface S one gets

$$\hat{U}_j = - \int_S \int \hat{A}(s) \frac{\partial}{\partial N_j} \left[\frac{e^{i\omega R}}{R^*} \right] ds \quad (\text{III-A15})$$

where N_j is the unit vector normal to the boundary at point j .

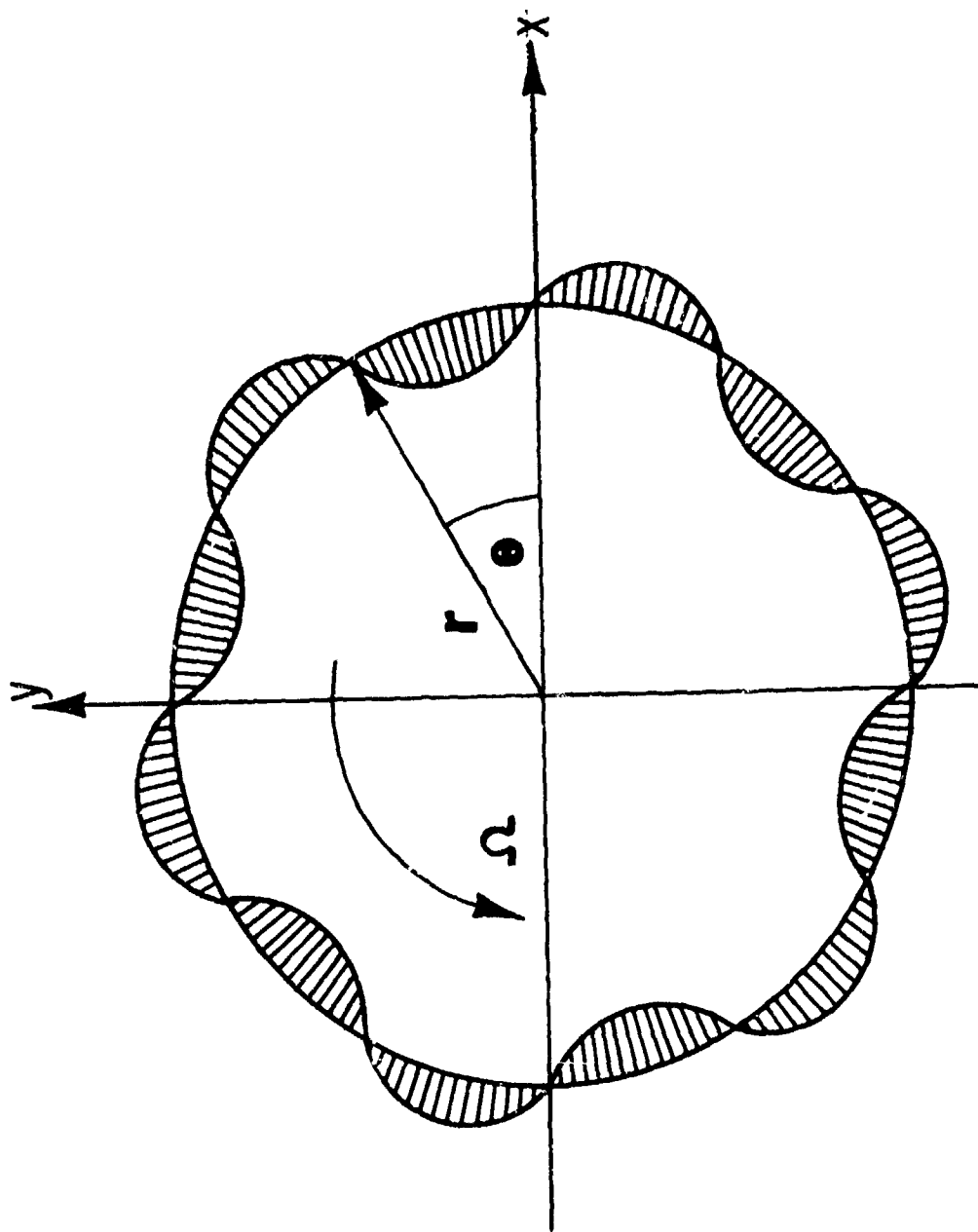


FIGURE III-A4 SIX - LOBE PRESSURE PATTERN ROTATING WITH ANGULAR VELOCITY
RAD./SEC.

The boundary is described by a set of short rings. Each ring is paired with another ring of uniform source strength (with a phase variation of $e^{im\phi}$). The boundary conditions of each ring will be satisfied only at discrete points at the mid-point of the ring. Therefore, j in equation (III-A15) takes on a finite number of values:

$$\hat{U}_j = - \sum_{k=1}^K A_k \frac{\partial}{\partial N_j} \left[\frac{e^{i\nu R_{kj}}}{R_{kj}^*} \right] \Delta s_k \quad (\text{III-A16})$$

In like manner, equation (III-A11) (for a rotating lobed pattern) may be expressed as follows:

$$\hat{\phi}_j = \sum_{k=1}^K \hat{A}_k \left[\frac{e^{i\nu R_{kj}}}{R_{kj}^*} \right] \Delta s_k \quad (\text{III-A17})$$

This can be used with equation (III-A4) to obtain the acoustic pressure at j :

$$\hat{p}_j = \rho_0 \sum_{k=1}^K \hat{A}_k \left[-i\omega + v_z \frac{\partial}{\partial z_j} \right] \frac{e^{i\nu R_{kj}}}{R_{kj}^*} \Delta s_k \quad (\text{III-A18})$$

where $p'_j = \hat{p}_j e^{i(m\theta - \omega t)}$

For the impedance condition at j , one must have

$$Z_j = - \frac{\hat{p}_j}{\hat{U}_j} \quad \hat{p}_j + Z_j \hat{U}_j = 0 \quad (\text{III-A19})$$

The minus sign is introduced here because one is interested in the ratio of pressure to velocity in the fluid, and impedance is usually defined as the ratio for the lining. A positive resistance will then indicate energy absorption at the surface.

By substituting equations (III-A16) and (III-A18) into equation (III-A19) one obtains:

$$\sum_{k=1}^K \hat{A}_k \left[-i\omega\rho_0 + V_{z0} \frac{\partial}{\partial z_j} - z_j \frac{\partial}{\partial N_j} \right] \frac{e^{iVR_{kj}}}{R_{kj}^*} = 0 \quad (\text{III-A20})$$

The \hat{A}_k values represent a set of K unknowns. Equation (III-A16, 18, or 20) or a combination of these equations, then gives the needed matrix which can be solved for \hat{A}_k . Although equation (III-A18) was written to describe the pressure at point j on the boundary, it may also be used to calculate the pressure at any other position in the acoustic field.

The equations described here were programmed for the General Electric 635 computer. The program permits the calculation of acoustic pressures at any point inside or outside the duct once the boundary conditions are properly defined. The input to the computer program consists, normally, of the prescription of the blade passing frequency, the number of spinning lobes and the detailed description of the geometry. The boundary conditions are used in the following manner:

- The pressure or the acoustic particle velocity is usually defined as a function of location in the generation plane. Their values are an input to the transmission problem and are to be obtained from the noise generation analysis (reference 4).
- If one deals with a hard wall duct (no acoustic treatment), the particle velocity normal to the wall is prescribed equal to zero.

The program is flexible. The boundary conditions can be varied and could reflect, for example, a gradient in generation pressures from hub to tip.

(2) Experimental Verification. In order to validate the analysis, theory-experiment comparisons were made for the test configuration of a phased speaker array and for a 26-inch diameter single-stage research compressor.

(a) Phased Speaker Array. In order to validate the analysis experimentally, a test configuration was run in a phased speaker array. This device consists of a wooden pipe with 24 sound sources located on the outer periphery of a 35" diameter cylinder axis of the device. The sources can be phased in such a way as to produce rotating lobed patterns similar to those produced in an actual jet engine. The phased speaker model is shown in Figure III-A5.

Figure III-A6 to 9 show a comparison between the calculated and measured pressure distributions inside the duct of a four-lobed pattern at a frequency of 700 Hz. The results show a pronounced standing-wave pattern because the frequency of 700 Hz is only slightly higher than the cutoff frequency (630 Hz). The calculations agree quite well with the experimental results. Small differences near the mouth of the duct may be caused by room reflections because the model was not tested in an anechoic chamber.

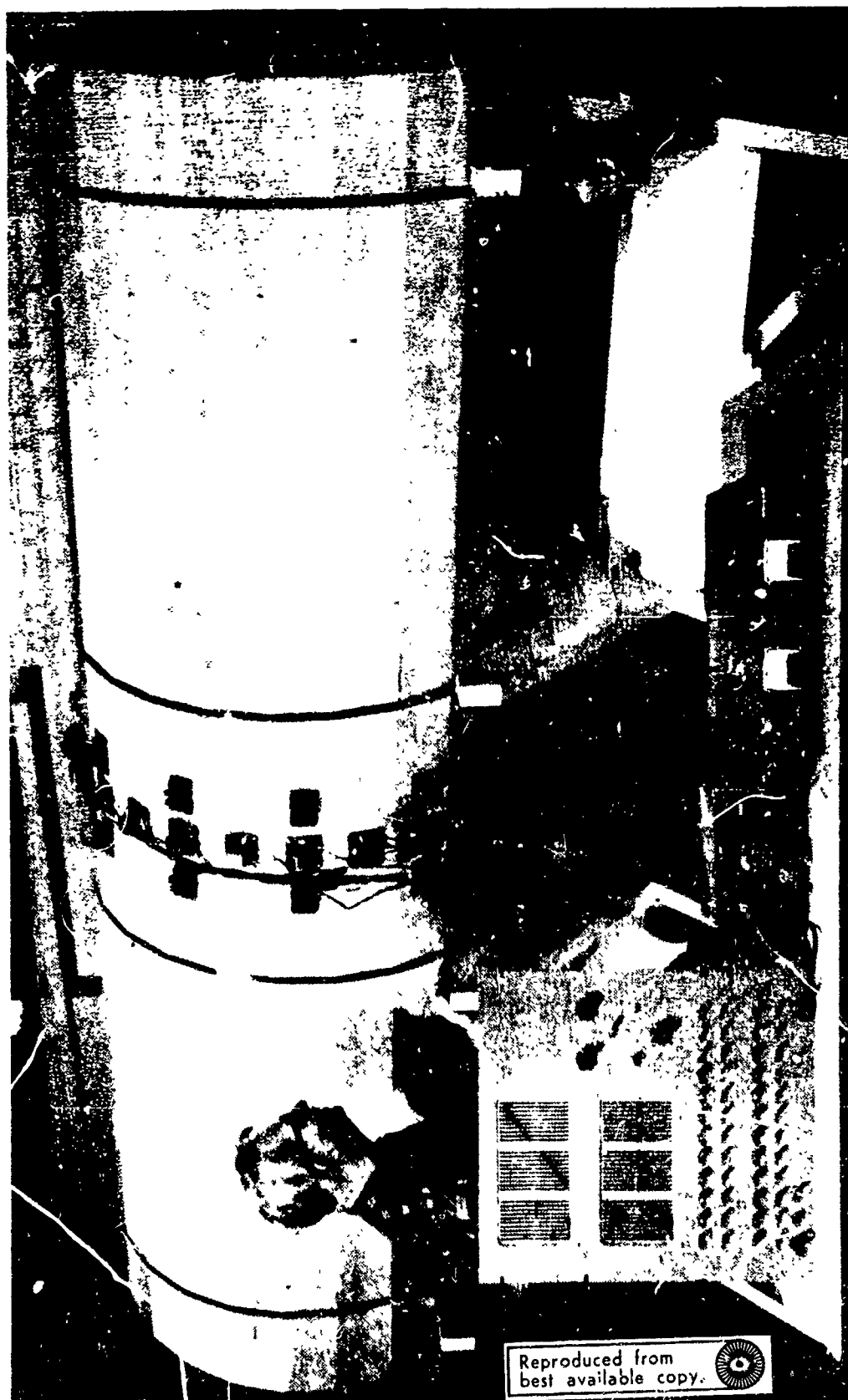


FIGURE III-A5 PHASED SPEAKER MODEL

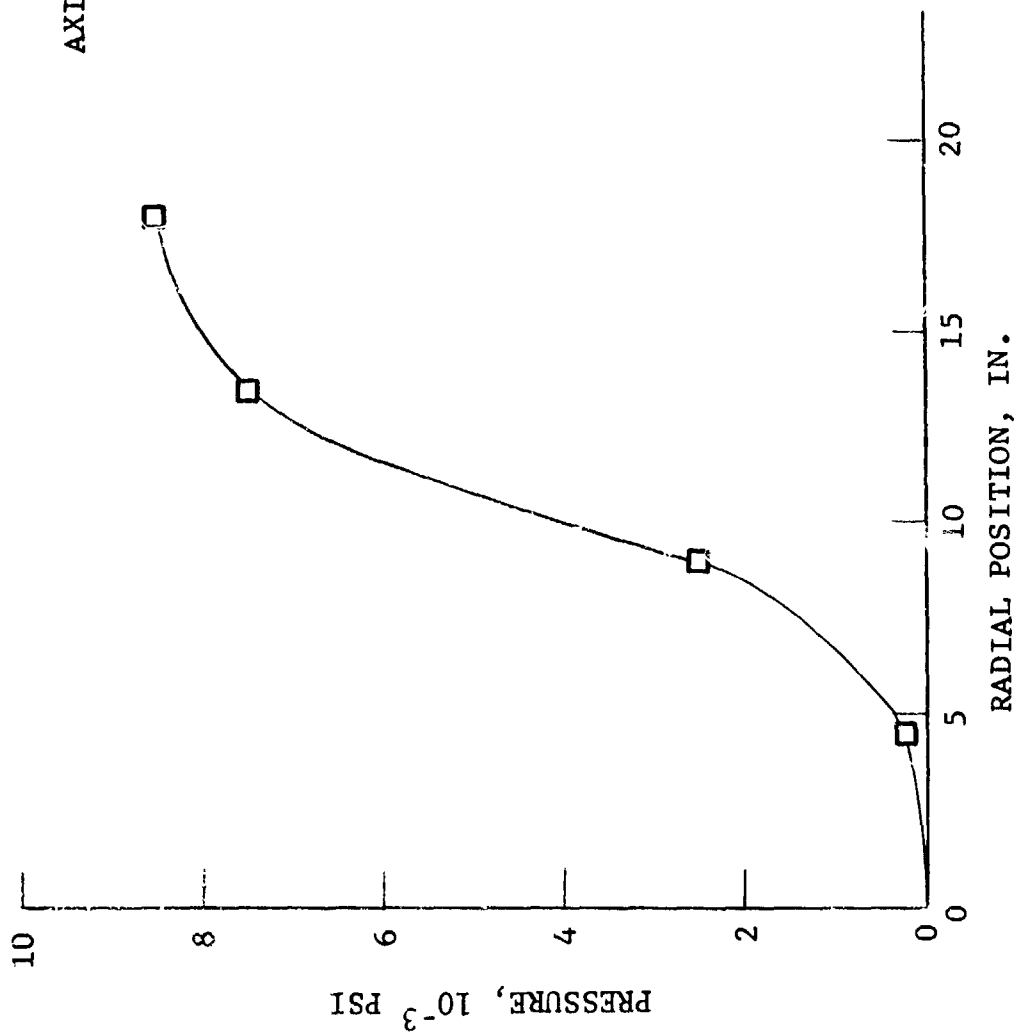


FIGURE III-A6 PHASED SPEAKER MODEL RESULTS. FOUR LOBES, 700 Hz (ABOVE CUTOFF), NO ACOUSTIC LINING (RIGID WALLS). RADIAL PRESSURE DISTRIBUTION AT AXIAL LOCATION 0 INCH.

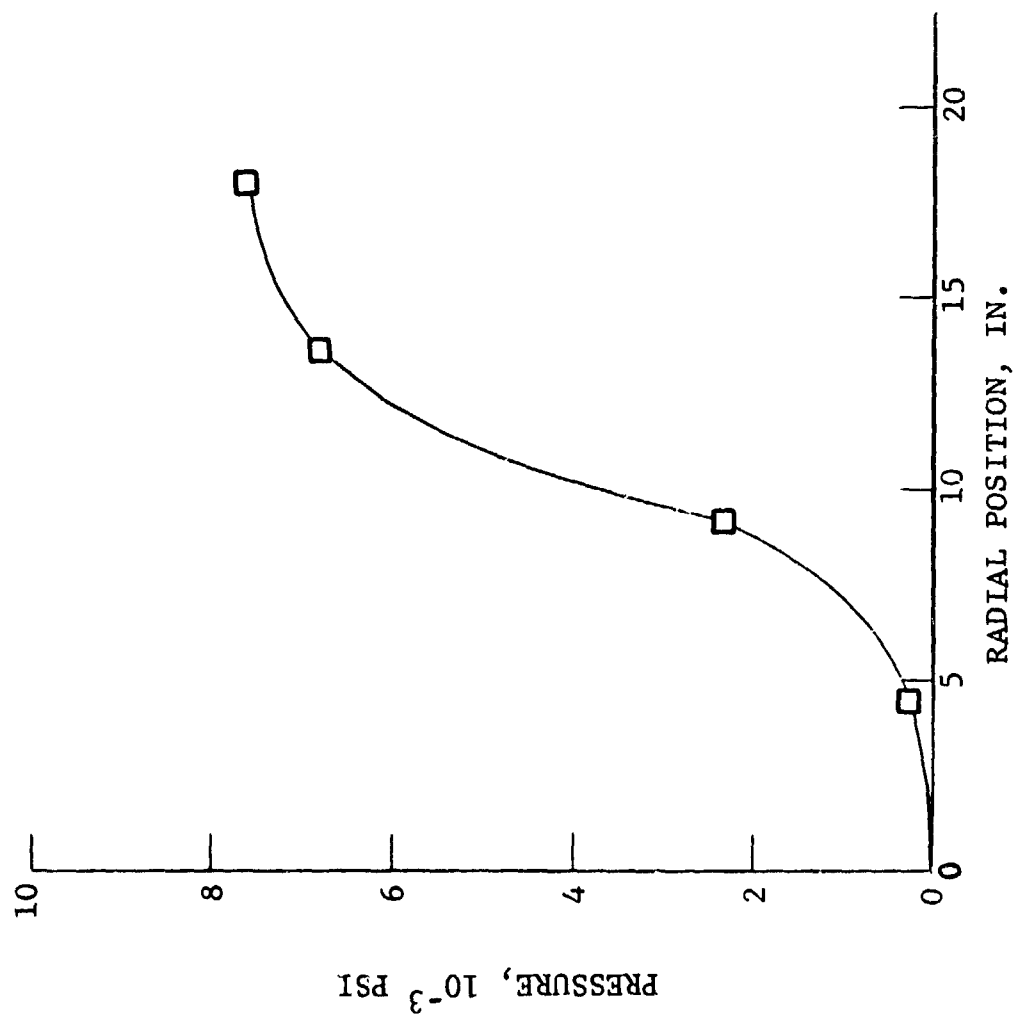


FIGURE III-1-A7 PHASED SPEAKER MODEL RESULTS. FOUR LOBES, 700 Hz (ABOVE CUTOFF), NO ACOUSTIC LINING (RIGID WALLS). RADIAL PRESSURE DISTRIBUTION AT AXIAL LOCATION 30 INCHES.

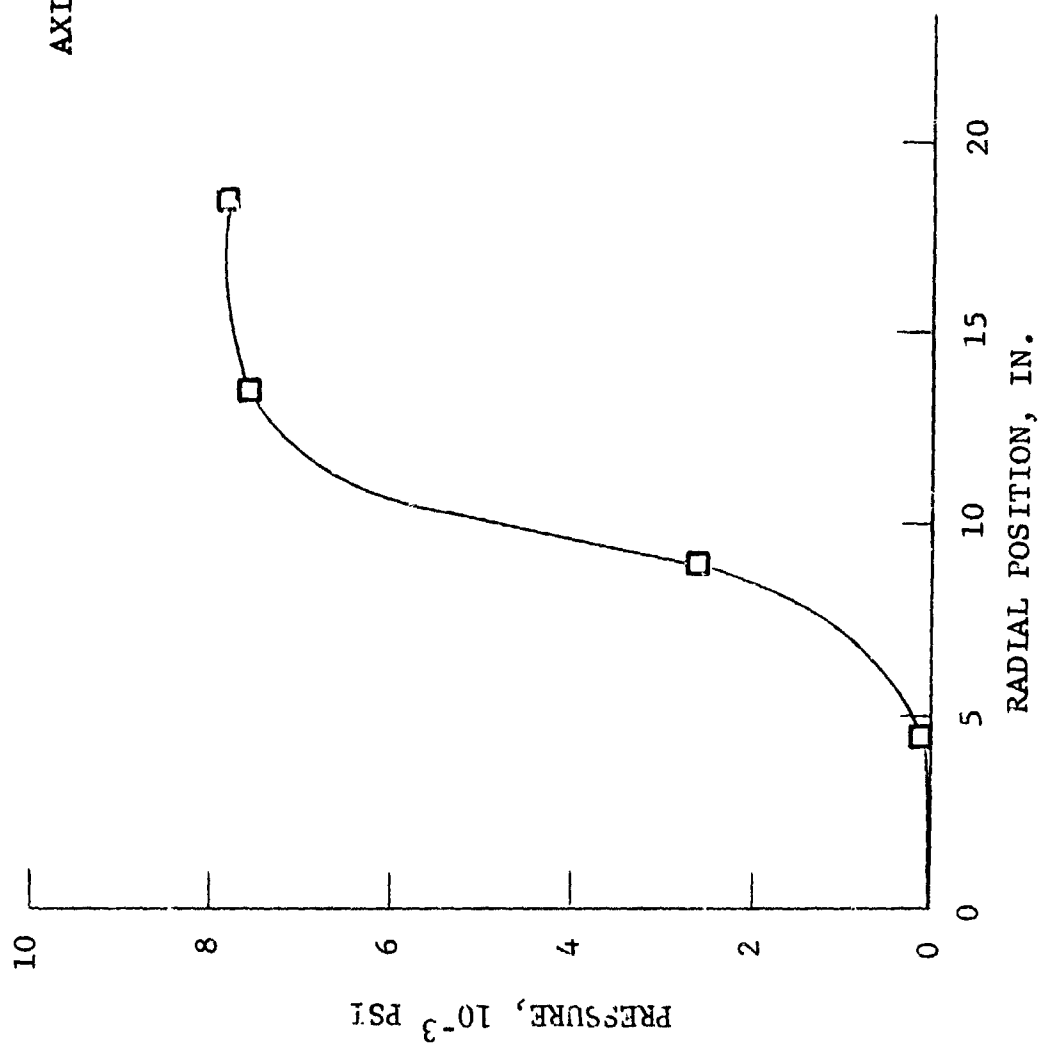


FIGURE III-A8 PHASED SPEAKER MODEL RESULTS. FOUR LOBES, 700 Hz (ABOVE CUTOFF), NO ACOUSTIC LINING (RIGID WALLS). RADIAL PRESSURE DISTRIBUTION AT AXIAL LOCATION 55 INCHES.

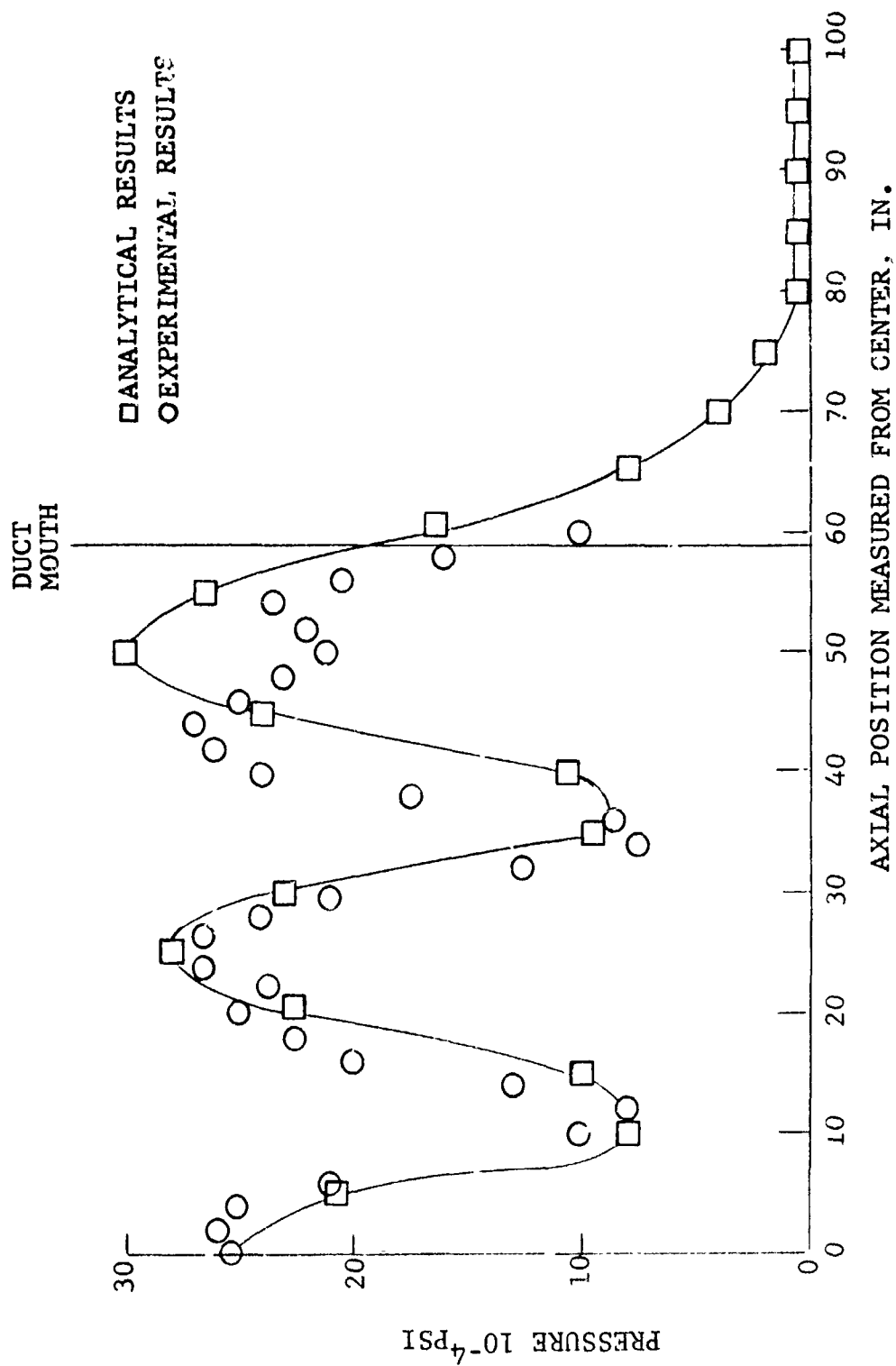


FIGURE III-A9 PHASE SPEAKER MODEL RESULTS. FOUR LOBES, 700 Hz (ABOVE CUTOFF), NO ACOUSTIC LINING (RIGID WALLS). AXIAL PRESSURE DISTRIBUTION AT $R = 8.9$ INCHES.

(b) 26-Inch Diameter Research Compressor. Various treated and untreated duct configurations were experimentally investigated on a 26" outside diameter, low speed single stage research compressor having a 0.85 radius ratio (reference 5).

The research compressor with a 24-inch long duct extension is shown in Figure III-A10. The compressor has 56 blades and 48 outlet guide vanes. This yields an 8-lobed spinning sound wave for the lowest possible circumferential mode. Four rotational speeds are possible through the electric motor drive and high speed gear arrangement shown in Figure III-A10. A schematic representation of the compressor model used in the calculations and the dimensions are shown in Figure III-A11.

Sound pressure level measurements were taken in the compressor duct and in the far field ($0^\circ \leq \theta < 90^\circ$). Figure AIII-12 depicts a comparison of calculated and measured sound pressure level directivities at 2585 Hz.

As one can see, the analysis predicts the data fairly well for angles exceeding 25° . It does predict, however, zero acoustic pressure along the engine centerline for any spinning lobe pattern and, therefore, deviates from the experimental data. Crigler and Copeland (reference 6) experienced similar difficulties when they tried to compare results based on Tyler and Soifrin's analysis (reference 7) with experimental data. They, too, predicted a zero pressure along the engine axis. The Morfey-Dawson analysis (reference 8) gives the same results. It seems that failure to predict finite acoustic pressure on the engine axis results from the fact that these different analyses do not take into account the refraction phenomena which arise from inlet and exhaust flow effects. In fact, refraction effects were found to be dominant in establishing some radiated sound directivity. A special experimental investigation was therefore, set up to investigate in detail the refraction phenomena and is reported in Section III-C.

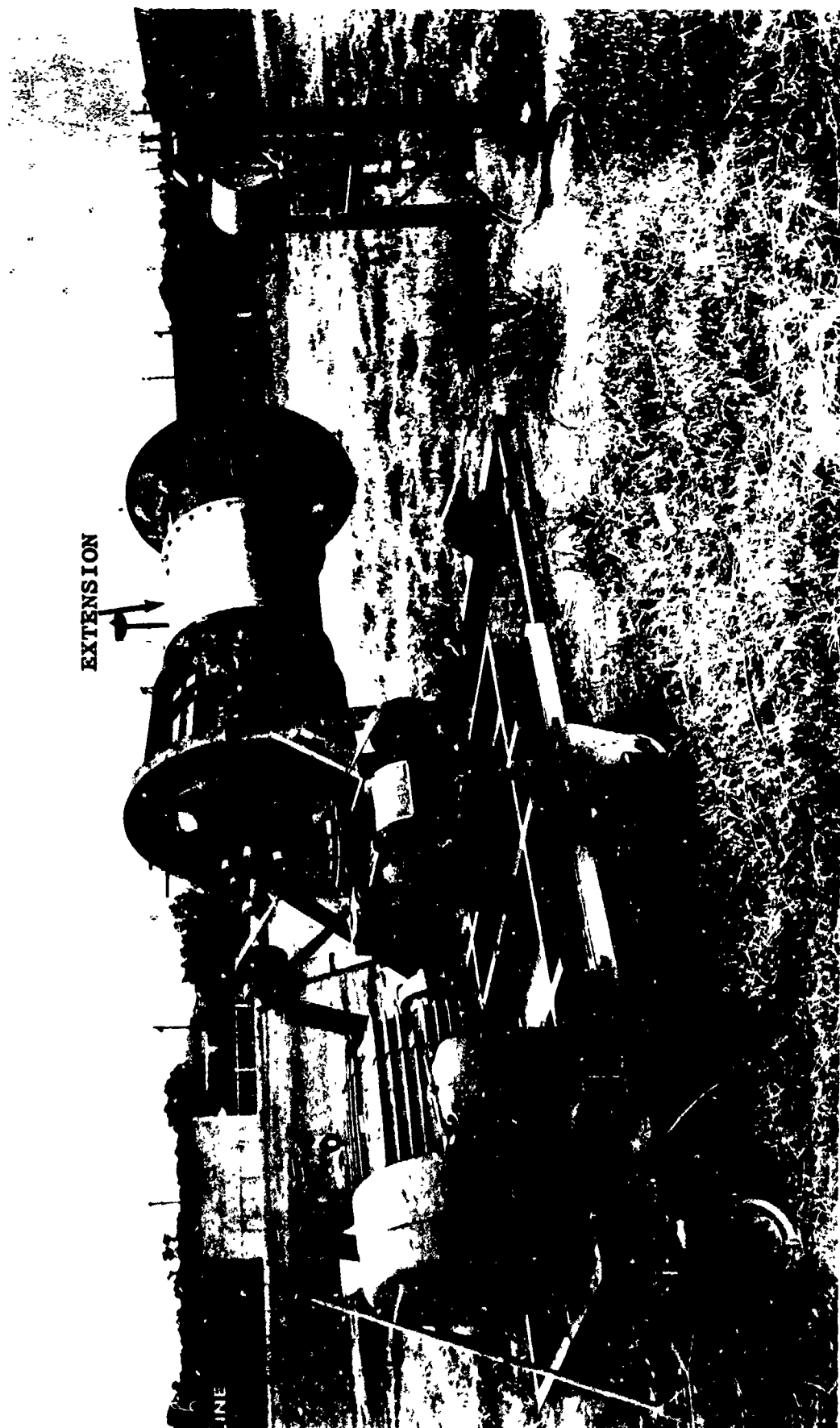


FIGURE III-A10 26" DIAMETER SINGLE STAGE RESEARCH COMPRESSOR
WITH THE ANNULAR DUCT EXTENSION

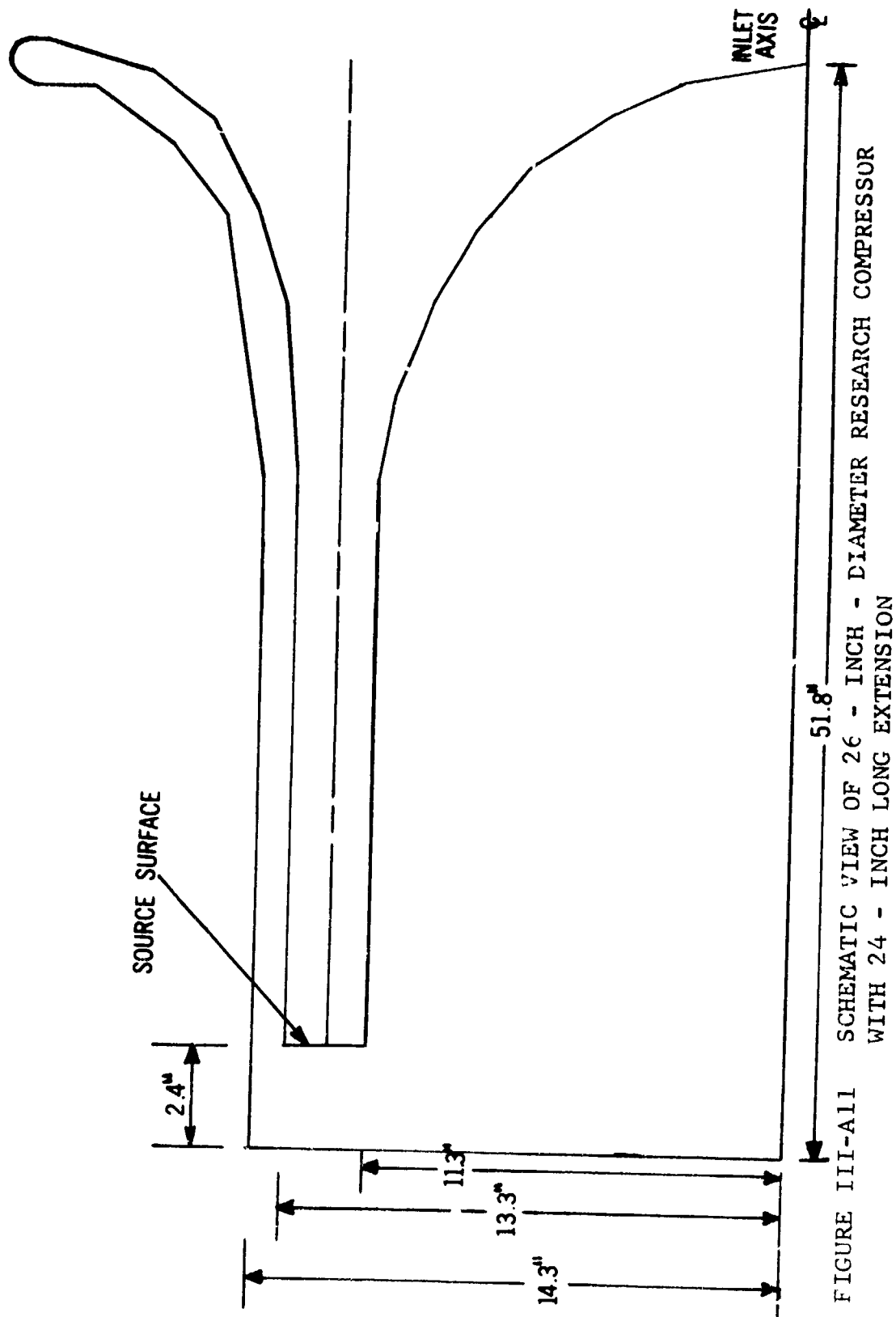


FIGURE I11-A11 SCHEMATIC VIEW OF 26 - INCH - DIAMETER RESEARCH COMPRESSOR WITH 24 - INCH LONG EXTENSION

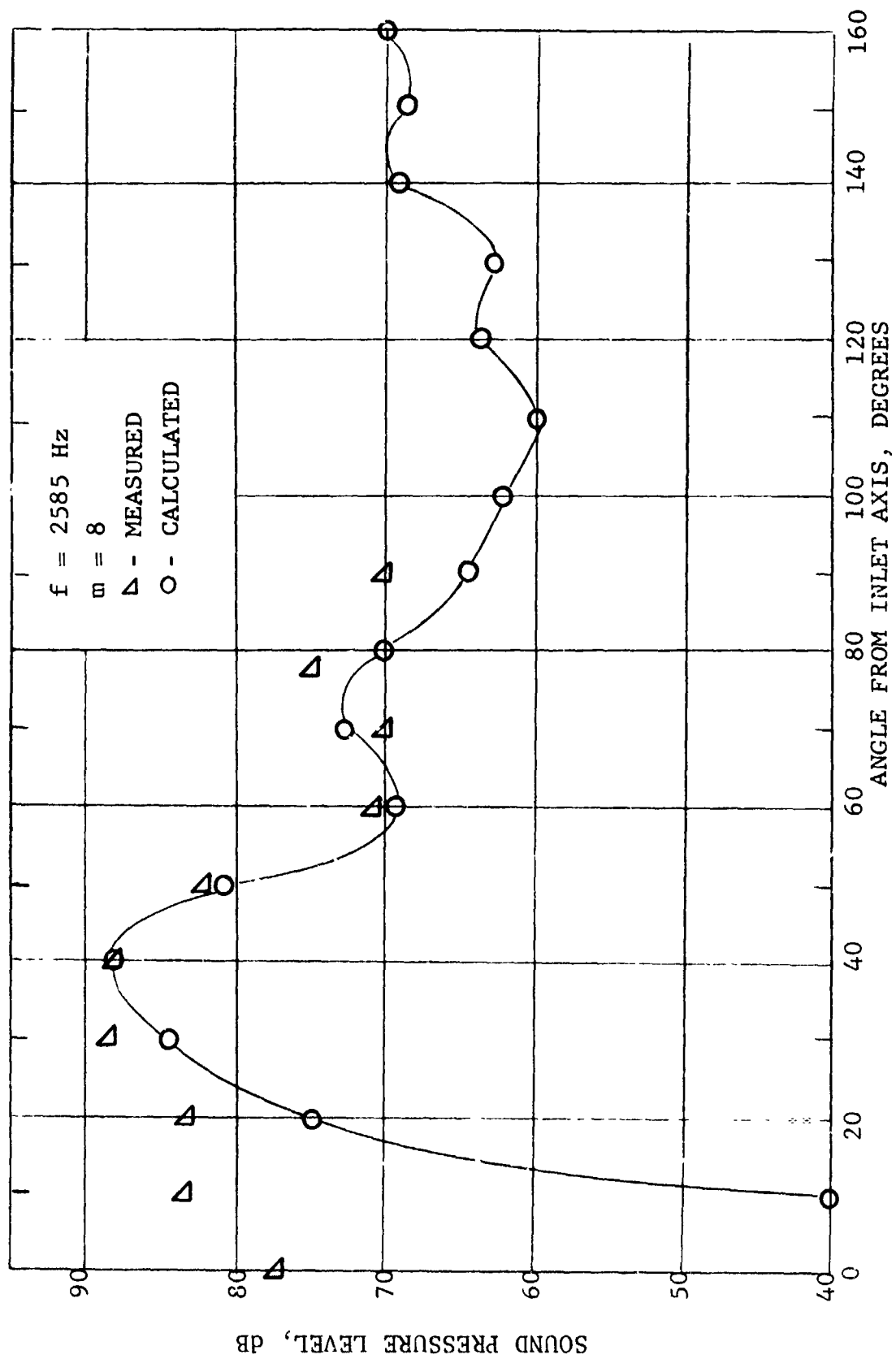


FIGURE III-A12
COMPARISON BETWEEN CALCULATED AND MEASURED FARFIELD SOUND PRESSURE
LEVEL FOR A 2" DIAMETER RESEARCH COMPRESSOR

NOMENCLATURE SECTION III-A

\hat{A}, \hat{A}'	Acoustic source strength
c	Acoustic velocity
e	Base of natural logarithms
f	Sound frequency
i	$\sqrt{-1}$
m	Number of circumferential lobes
M	Axial flow Mach number
P	Acoustic pressure
p	Instantaneous acoustic pressure
r	Radial distance in cylindrical coordinates
r	Polar radius in the cylindrical coordinates
R_o, R_o^*	Modified distance from source to observer (Equ. III-A6 and III-A7)
s	Midpoint of a surface element
S	Duct surface
t	Time
\hat{u}	Time-independent, Particle velocity (Equ. III-A3)
$u, U(s)$	Normal particle velocity (Equ. III-A13)
\vec{v}	Time-independent, Particle velocity (Equ. III-A3)
V_z	Steady medium flow velocity in the z-direction
x, y, z	Rectangular coordinates
z	axial distance in cylindrical coordinates
Z	Acoustic impedance

θ Axial angle in cylindrical coordinates

ν Wave number

ξ Point in the field

ρ_0 Medium density

ϕ Velocity potential

$\hat{\phi}, \hat{\phi}'$ Instantaneous velocity potential

ω Angular frequency

Ω Angular velocity

Subscripts

f

j Integer subscripts

k

REFERENCES-SECTION III-A

1. Martenson, A.J., and Liu, H.K., "Propagation of a Rotating Acoustic Field in Axisymmetric Ducts of Arbitrary Shape with Soft Walls, to be published in the Journal of Sound and Vibration.
2. Liu, H.K., and Martenson, A.J., "Optimum Lining Configurations", Proceedings of the Conference on Basic Aerodynamic Noise Research, NASA SP-207 (1969) p. 425.
3. Blokhintsev, D.I., "Acoustics of a Non-homogeneous Moving Medium", NACA TM 1399 (February 1956).
4. Benzakein, M.J., "A Study of Fan/Compressor Noise Generation", Proceedings of the Conference on Basic Aerodynamic Noise Research, NASA SP-207 (1969) p. 257.
5. Smith, E.B., Benzakein, M.J., and Radecki, K., "Study and Tests to Reduce Compressor Sounds of Jet Aircraft", FAA Report DS-68-7 (February 1968).
6. Crigler, J.L. and Coepland, W.L., "Noise Studies of Inlet Guide Vane Rotor Interaction of a Single-Stage Axial Flow Compressor, NASA TN D-2962, (1965).
7. Tyler, J.M. and Sofrin, T.G., "Axial Flow Compressor Noise Studies", SAE Transactions, Vol. 70, 1962 p. 309.
8. Morfey, C. L. and Dawson, H., "Axial Compressor Noise: Some Results from Aero-Engine Research", presented at the ASME 11th Annual Turbine Conference in Zurich, March, 1966.

(B) Sound Transmission Through Blade Rows. Discrete frequency components of rotor noise and rotor/stator interaction noise has been known for many years to propagate along an engine duct as rotating spinning modes. When the traveling waves encounter a blade row, i.e., inlet guide vanes, rotor blades, outlet guide vanes, etc., a part of the incident wave energy is transmitted through the blade row and a part is reflected. An analysis of the sound transmission through a blade row is, therefore, necessary to evaluate which portion of the sound energy generated in a multistage compressor is radiated to the atmosphere. An analysis of the phenomena was undertaken by R. Mani at the General Electric Research and Development Center. The analysis is based on a Wiener Hopf solution of the wave equation for a flowing medium and is described in detail in Reference 1. A program based on Mani's work was written for a high speed computer. It permits the investigation of sound transmissions in both stationary and rotating frames of reference.

Experimental Check. The sound transmission through stationary blade rows was experimentally investigated in a two-dimensional cascade in the Laboratory. A sketch of the experimental set-up is shown in figure III-B1. Air was supplied through the double plenum chambers. A muffler section seventy-two inches long, consisting of one-inch thick Scottfelt on two eighteen-inch walls, was designed to damp out the upstream generated piping and valve noise. A sound source consisting of an Altec Lansing high intensity driver was located downstream of the vanes and mounted on a horn adapter radiating through a perforated plate set flush with the duct wall. A Bruel and Kjaer condenser microphone was positioned upstream of the vanes. A total of two full vanes and two one-half vanes were used in these tests. The one-half vanes were mounted on the upper and lower duct surfaces. The vanes were spaced four inches between mean lines. A more detailed description of the test setup is reported in reference 2. The sound transmission through the vanes was investigated at flow Mach numbers, varying from 0.0 to 0.9 at frequencies ranging from 800 to 6300 Hz. Some of the experimental data are reported in figure III-B2 with the corresponding analytical results. One can see that the agreement between experiment and theory is fairly good.

An analytical investigation was also undertaken to determine what parameters are important in the evaluation of the sound energy transmission through a blade row. A sketch of the analytical model is shown in Figure III-B3 where:

- α_m is the angle between the blade plane and the circumferential direction.
- θ is the angle of incidence which can be calculated from spinning mode theory (see reference 3, for example). The incidence angle is positive when measured in the same sense as the angle of stagger α . It is, therefore, restricted to values $\theta < \frac{\pi}{2}$. Otherwise, the angle of incidence is negative. A positive Mach number $M < 0$ represents the case of upstream sound wave propagation. The Mach number is negative ($M < 0$) for downstream sound wave propagation.

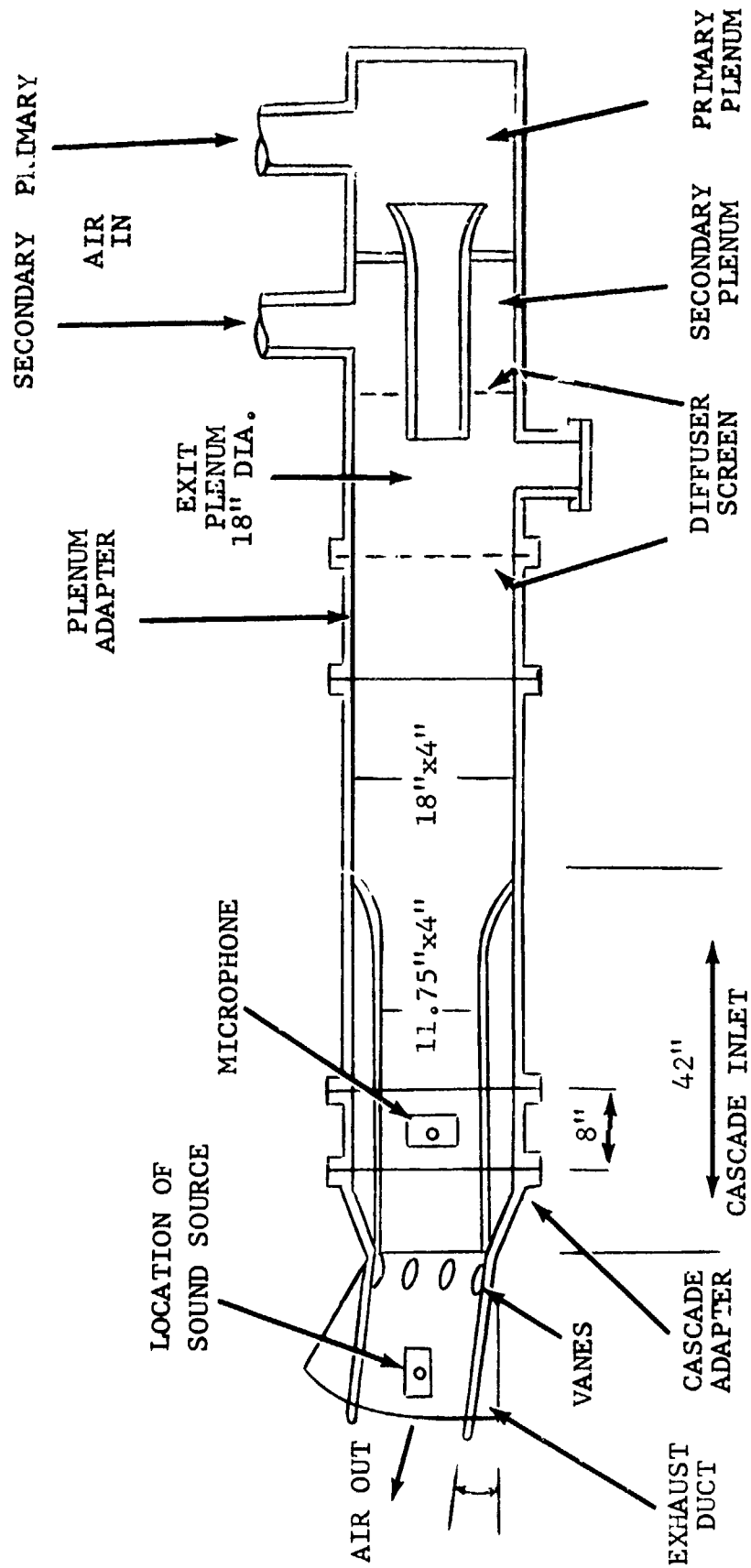


FIGURE III-B1 LABORATORY DUCT AND CASCADE SET-UP

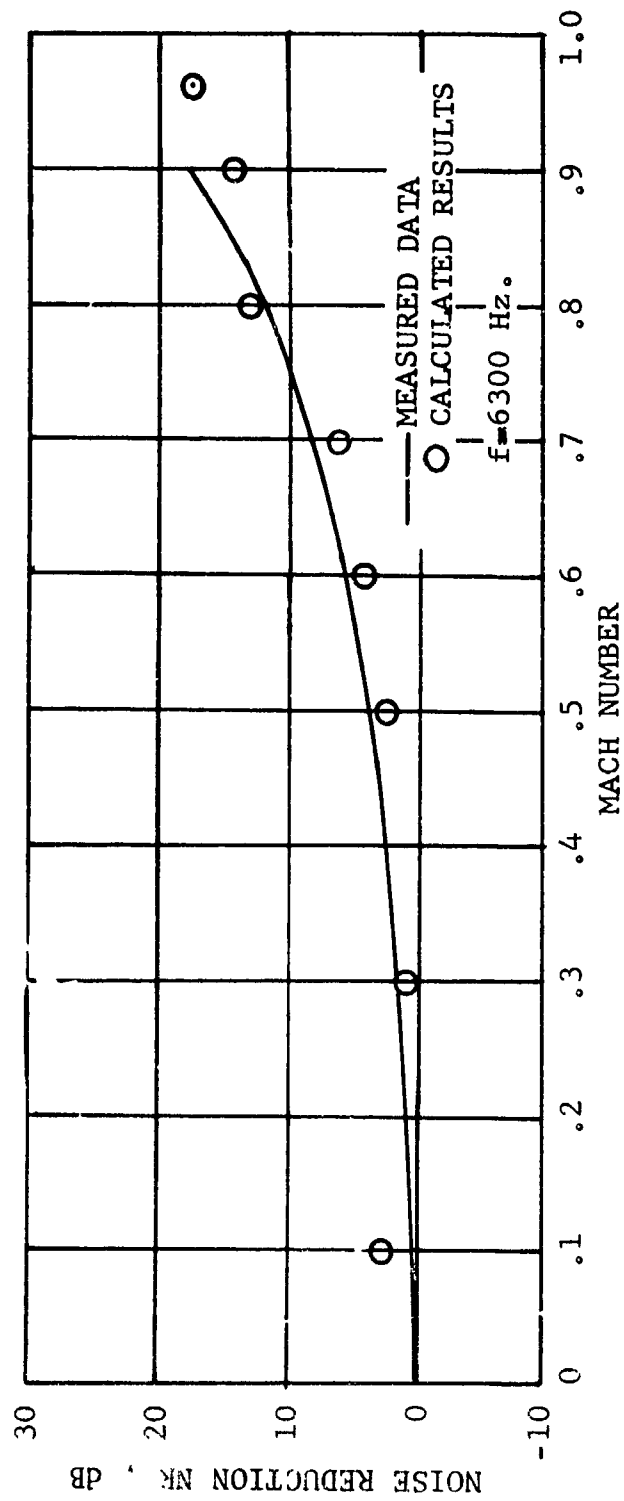


FIGURE III-B2 AIR FLOW NOISE REDUCTION THROUGH CASCADE VANES -
COMPARISON BETWEEN MEASURED AND CALCULATED RESULTS

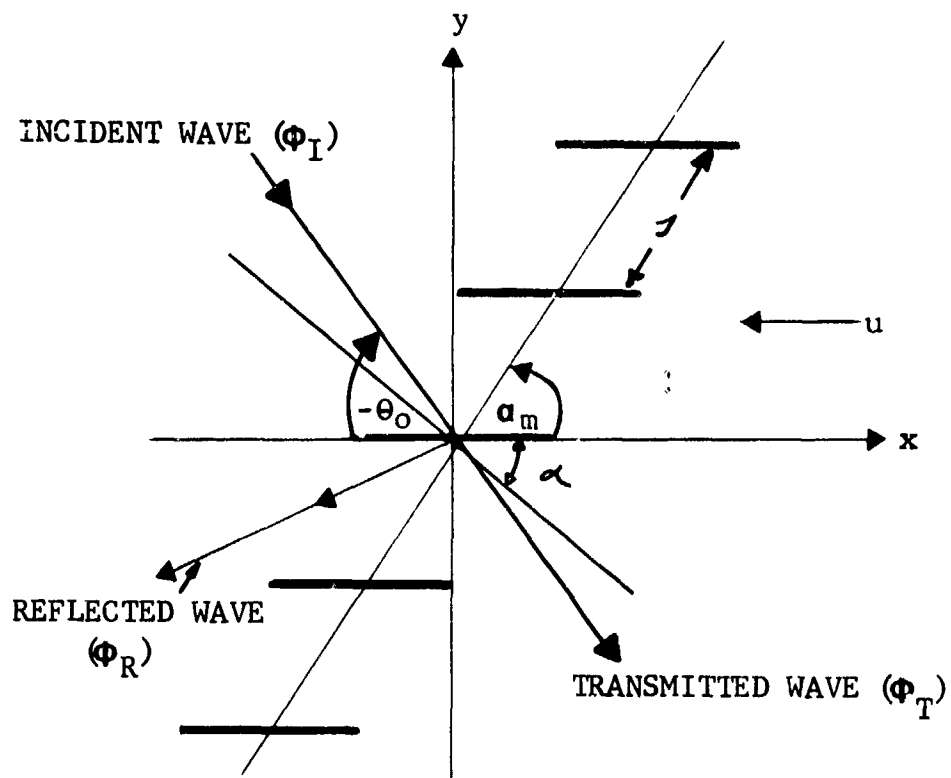


FIGURE III-B3 MODEL FOR SOUND WAVE TRANSMISSION
THROUGH A BLADE ROW

Effect of Cascade Solidity. The solidity, $\sigma = \frac{c}{s}$ = airfoil chord/circumferential spacing was varied from 0.5 to 4.0 for a given airfoil stagger, sound frequency and airflow Mach number. The ratio of energy transmitted through the cascade to the incident energy is plotted in function of incidence angle θ_0 in Figure III-E4. For different cascade solidities, the results indicate that for values of solidity above 1.0 (which is a lower limit from an aerodynamic viewpoint) the solidity has only a minor effect on the transmission of sound.

Effect of Sound Frequency. The results of an investigation of the frequency of sound on its transmission through a stationary blade row are presented in Figure III-B5. It is shown, as one would expect, that the large energy reduction is obtained at low frequencies and high upstream Mach numbers (choking effect).

Effect of Wave Angle of Incidence. The angle of wave incidence to a given cascade is a primary factor in the evaluation of the sound transmission. Figure III-B6 shows some results on the effect of positive and negative incidence angles, respectively, on the energy transmission through a cascade at a given frequency. One can see that the energy reduction increases as the magnitude of the wave angle of incidence is increased, whereas most of the energy is transmitted at zero incidence angle.

Effect of Airfoil Stagger. The effect of airfoil stagger was investigated and some results are shown in Figure III-B7. It is apparent that airfoil stagger can be a primary factor in sound transmission, particularly at high upstream Mach numbers.

Effect of Flow Mach Number. Figures III-B5 to 7 have shown that the amount of sound energy transmitted is a strong function of the relative Mach number to the airfoil. One can see that inlet guide vane choking can be advantageously used in multistage compressors as demonstrated in reference 2.

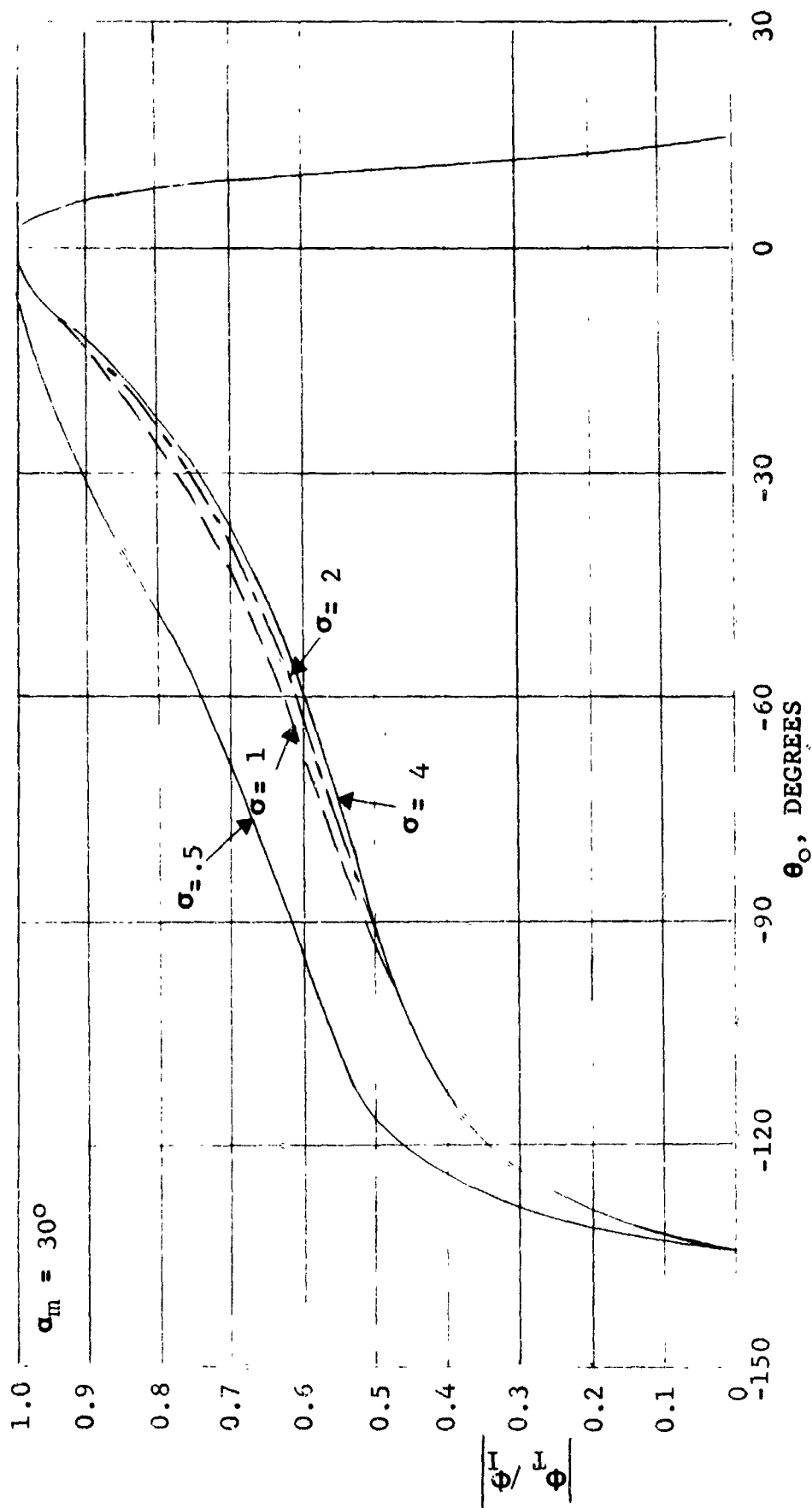


FIGURE III-B4 CALCULATED RATIOS OF TRANSMITTED TO INCIDENT SOUND WAVE AMPLITUDES FOR VARIOUS BLADE SPACINGS AND INCIDENCE ANGLES.

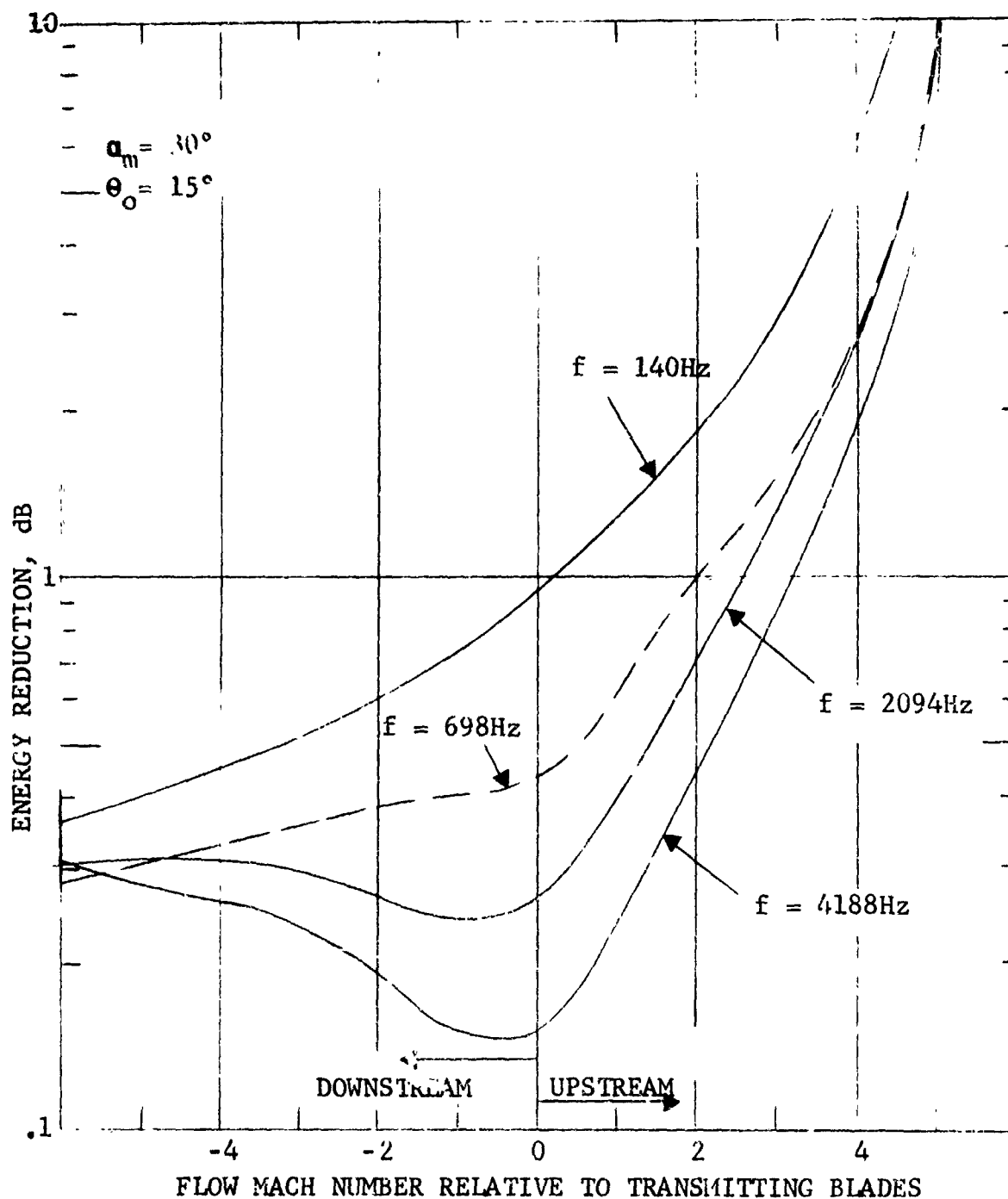


FIGURE III-B5

EFFECT OF INCIDENT SOUND FREQUENCY AND FLOW MACH NUMBER ON SOUND ATTENUATION BY A BLADE ROW.

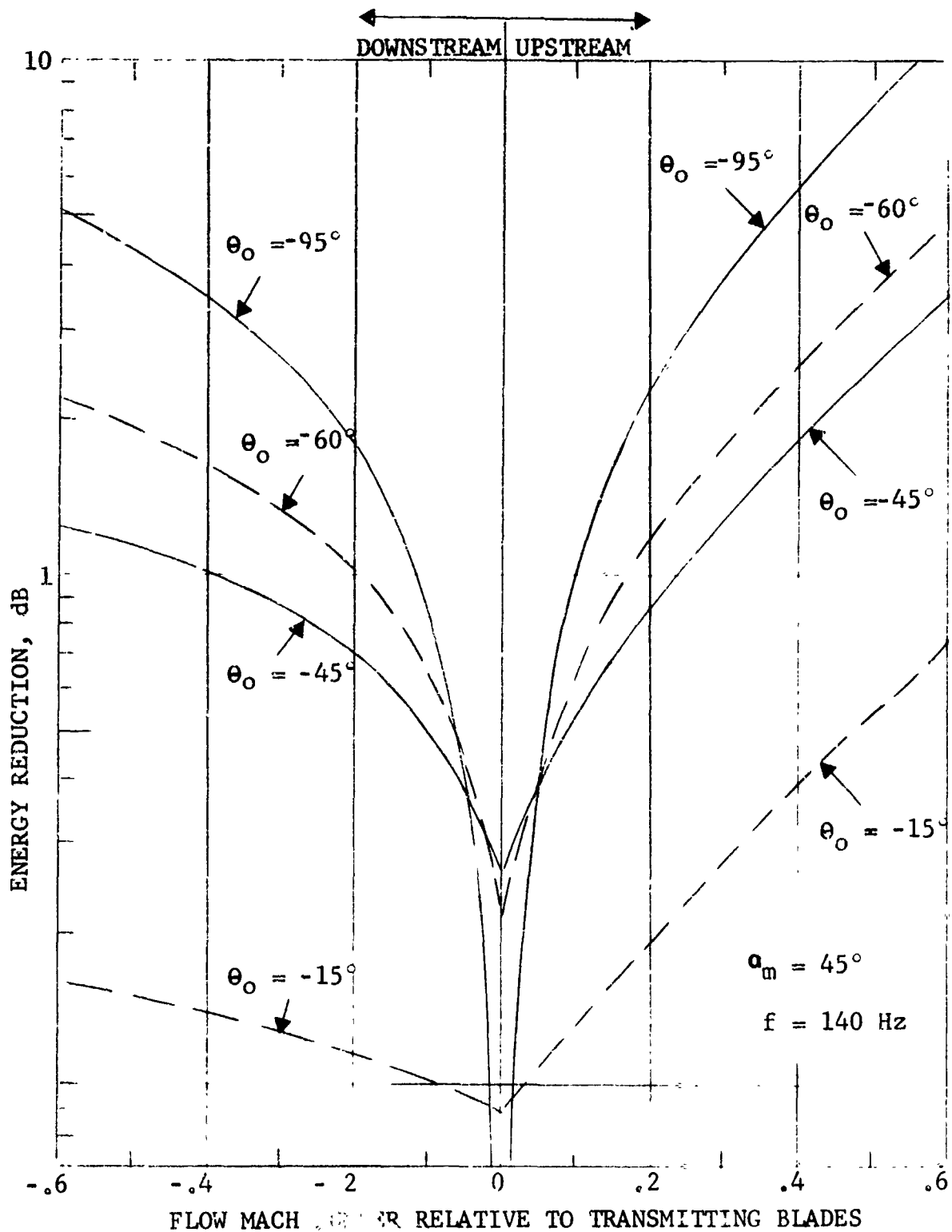


FIGURE III-B6

SOUND ENERGY REDUCTION BY A BLADE ROW AS A FUNCTION OF SOUND WAVE ANGLE OF INCIDENCE AND FLOW MACH NUMBER.

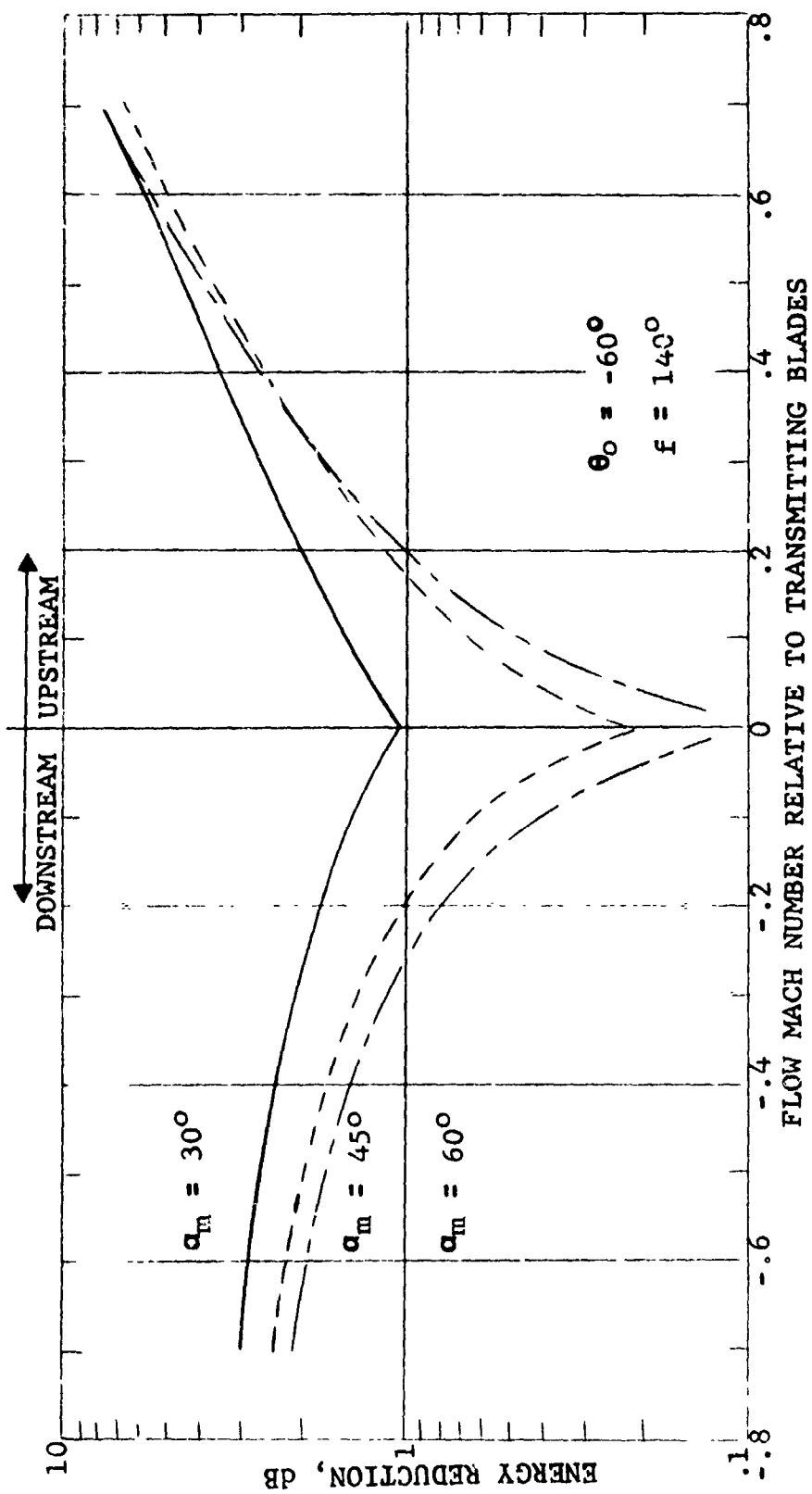


FIGURE III-B7 SOUND ENERGY REDUCTION BY A BLADE ROW AS A FUNCTION OF STAGGER ANGLE AND FLOW MACH NUMBER.

NOMENCLATURE SECTION III-B

c	Airfoil chord
f	Frequency
M	Flow Mach number
s	Circumferential Spacing
α_m	Angle between the blade plane and circumferential direction (Compliment of stagger angle) (See Figure III-B3)
θ_o	The angle of incidence of the incident wave (see Figure III-B3)
σ	Solidity (airfoil chord/circumferential spacing).
$\phi_{I,T,R}$	Incident transmitted, reflected wave (see Figure III-B3)
α	Stagger

REFERENCES SECTION III-B

1. Mani, R., Harvay, G., "Sound Transmission Through Blade Rows," General Electric Class 1 Report No. 69-C-104, February 1969.
2. Chesnutt, D., "Noise Reduction by Means of Inlet Guide Vane Choking in an Axial Flow Compressor," NASA TN D-4682, July 1968.
3. Benzakein, M.J., Kazin, S.B., "A Theoretical Prediction of Aerodynamically Generated Noise in Fans and Compressors," November 1968, ASME Meeting.

(C) Refraction Effect on Sound Directivity. The airflow in the ducts of the turbofan affects the effect speed of propagation. Sound propagating against the airflow is effectively slower, while that propagating with the flow is effectively faster than the propagation speed in still air. So when the noise generated by a rotating blade row stage reaches the inlet or the exhaust plane, the propagating wave must experience a change in effective propagation speed.

The transition occurs rather abruptly in the discharge because the airflow velocity gradients are contained entirely within the exhaust jet mixing zone, and this zone is geometrically restricted to a relatively small volume. In the inlet, on the other hand, the transition is distributed over a relatively large volume more or less according to the distribution given by the potential flow lines into a sink.

Therefore, it is to be expected that refraction of the sound rays will occur for the noise propagating out the exhaust. Furthermore, the amount of the refraction will depend upon the exhaust velocity and the temperature of the exhaust stream, since both affect the speed of sound propagation. Thus, sound from a high velocity, high temperature turbine exhaust should be refracted more than that from a low velocity, moderate temperature fan exhaust. But, even in the fan exhaust, typical exhaust velocities are sufficiently high for the refraction effect to be a very strong, if not the dominant influence on the far-field directivity of aft-radiated internally generated (turbomachinery) noise.

For the inlet radiated noise, qualitative evaluation of the potential flow lines into the engine inlet indicate that there may be some slight shifting of the radiation pattern because of refraction, but the effect is minor as compared with the conditions that exist in the exhaust. The modal patterns that exist in the inlet duct appear to be the dominant variable.

The effects involved are discussed in the following, based upon the assumption that the noise propagates along ray paths like light waves. The trends indicated are that aft-radiated noise is redirected by refraction toward the sideline, so that the noise received by a ground observer during an aircraft flyover is increased.

(1) Basic Mechanism of Refraction. Refraction of sound occurs between two regions of air if there is a difference in the velocities or a difference in the sonic speed between the two regions. This effect is well known in the case of light rays, for example, passing from air into water (see Figure III-C1). The index of refraction as defined by Snell's Law is:

$$\mu = \frac{\sin \theta_i}{\sin \theta_r} = \frac{C_{\text{air}}}{C_{\text{water}}}$$

C_{air} = speed of propagation in air

C_{water} = speed of propagation in water

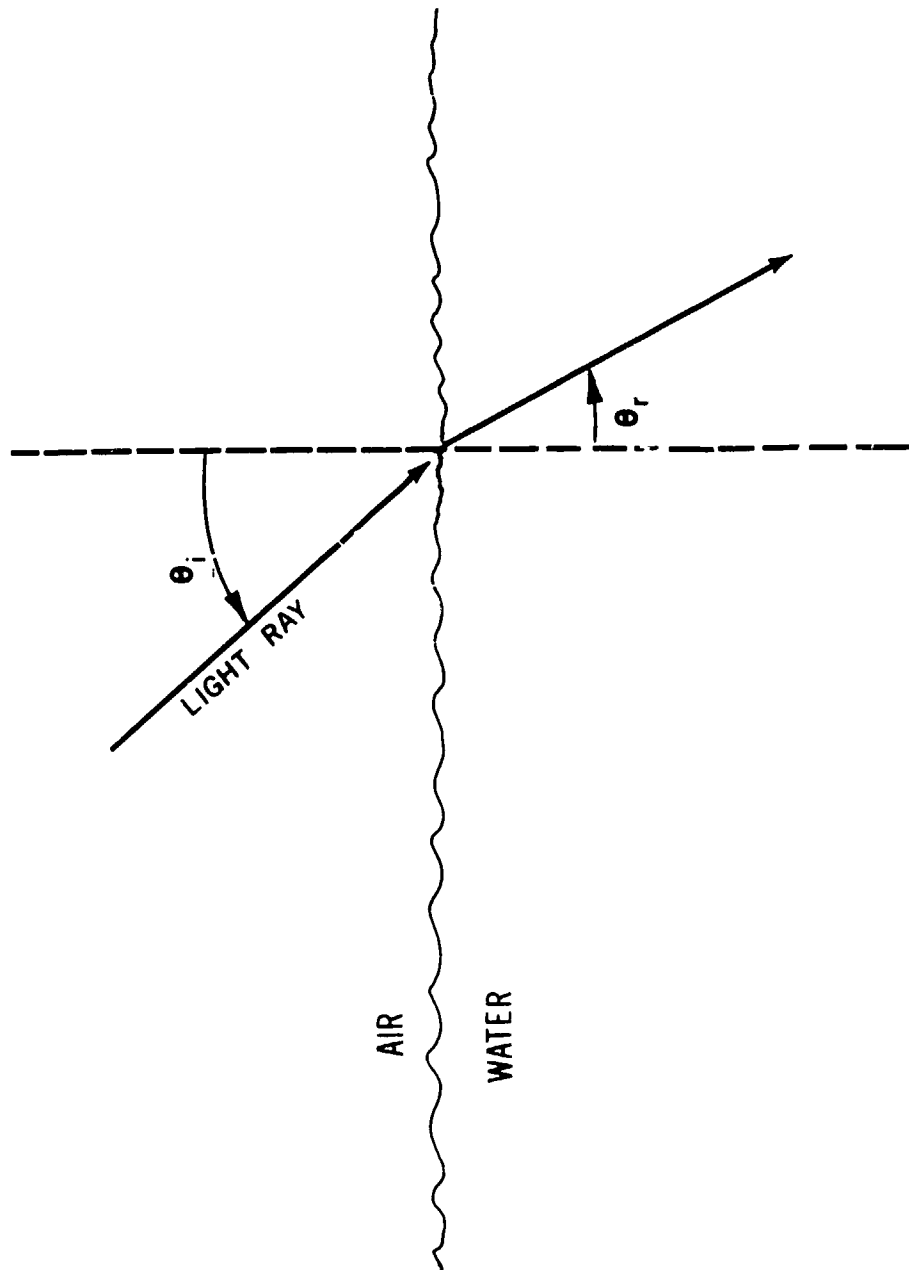


FIGURE III-C1 SIMPLE MODEL OF SNELL'S LAW OF REFRACTIVE INDEX USING AIR AND WATER AS AN EXAMPLE

The same thing happens with acoustic waves if the two layers are both air but at different temperatures, since the speed of sound depends upon temperature. Likewise, the same thing appears with acoustic waves if the two layers are both air but at different velocities since the apparent speed of sound is the sum of the sonic velocity within the medium and of the velocity of the medium, itself. (See Figure III-C2). Morse and Ingard (Reference 1) have published the applicable derivation for the case of current interest, with the results as given below (nomenclature changed):

$$\frac{c_1}{\sin \theta_i} + V_1 = \frac{c_2}{\sin \theta_r} + V_2 \quad (\text{III-C1})$$

If the angle of incidence, θ_i , is known, then the angle of refraction, θ_r , can be calculated.

Simplifying the equation for the case in which the air in each region is the same temperature and the velocity in region 2 is zero (ambient), then:

$$\frac{1}{\sin \theta_r} = \frac{1}{\sin \theta_i} + M$$

where: M = Mach number of the flowing airstream.

It should be noted that the interface need not be sharply defined. If the velocity or temperature gradient extends over an extended width, the ray bends locally according to the local conditions, so that it may proceed on a curved path, but the exit refraction angle will be the same as if the interface were sharp. Also, of course, the location at which the ray exits will be displaced, depending upon the width of the transition region. At far field distances of interest in regard to engine noise, this effect is of secondary importance.

The consequences of the above equations are discussed in the following to provide an appreciation of the manner in which refraction can be expected to modify predictions made without this effect.

(a) For the exhaust, using the simplified case:

$$\text{When} \quad 0 \leq \theta_i \leq 90$$

$$\text{then} \quad 0 \leq \sin \theta_i \leq 1$$

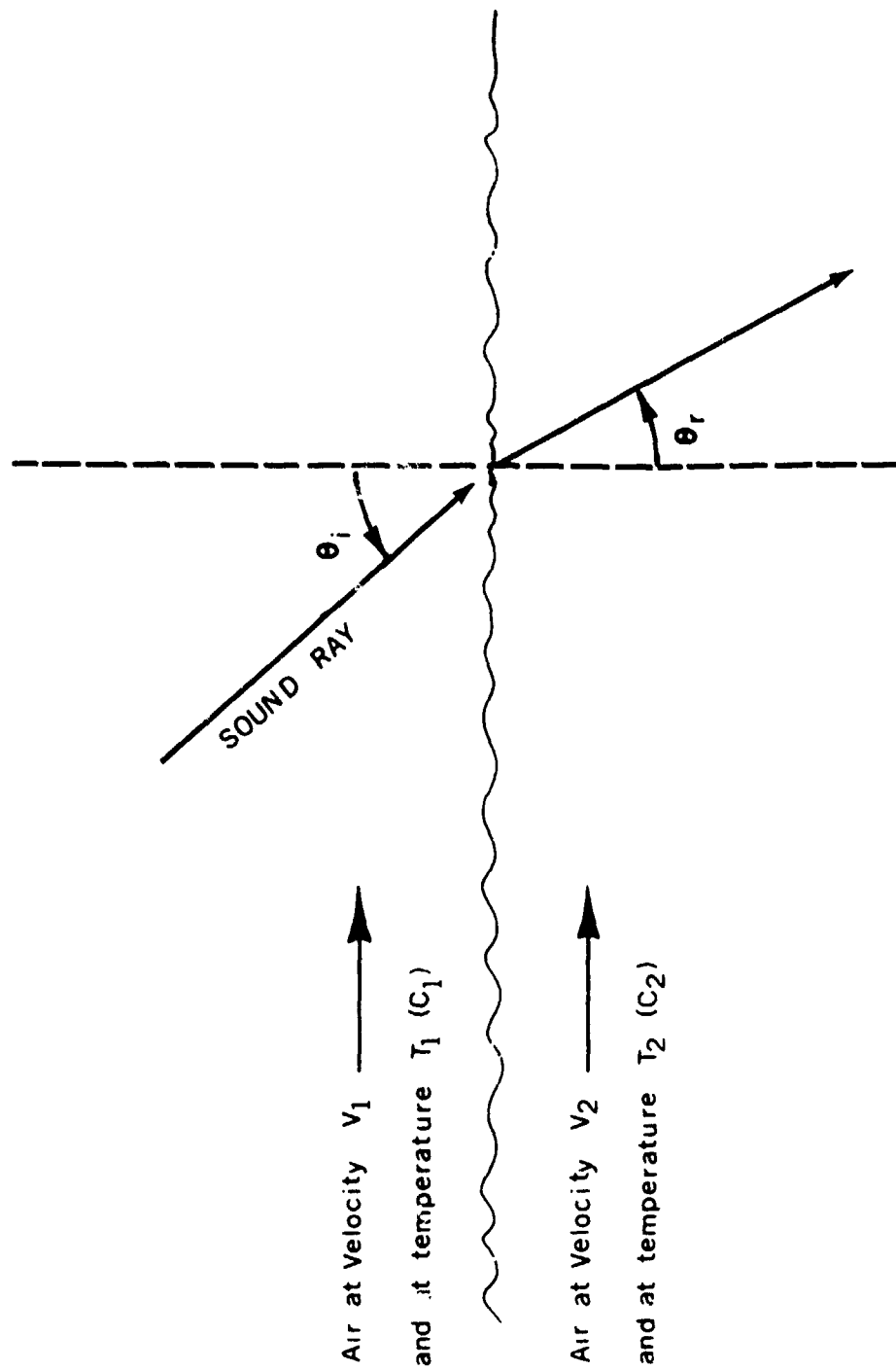


FIGURE III-C2 SIMPLE MODEL FOR SNELL'S LAW ACROSS THE SHEAR ZONE OF TWO AIRSTREAMS OF DIFFERENT VELOCITY AND TEMPERATURE

$$\text{and} \quad 0 \leq \sin \theta_r \leq \frac{1}{1+M}$$

In this case, the refracted sound reaches the far field in an angle extending between 0° and $\theta_r = \sin^{-1} \left(\frac{1}{1+M} \right)$ (See Figure III-C3).

A shadow region occurs in the aft-end, the angle of the shadow depending upon the Mach number of the exhaust:

M	=	0	.25	.5	.75	1
$\theta_{r \max}^1 = 90 + \theta_{r \max}$	=	180	143	132	125	120
θ_r^1	=	Angle measured from engine inlet				

According to this, at $M = 0.75$, the shadow is shown in Figure (III-C4).

Thus, any sound ray leaving the engine between 125° and 180° has been refracted forward of 125° . (This applied for the fan generated noise, not necessarily for jet noise.)

Further appreciation of the trend of the directivity pattern is obtained by noting the angle of refraction for various angles of incidence:

M = 0.75												
θ_i^1	=	$90 + \theta_i$	=	90	100	110	120	130	140	150	160	170 180
θ_r^1	=	$90 + \theta_r$	=	90	99	106	111	116	119	122	123	124 125

This shows, for example, that all sound originally directed between 140° and 180° has been redirected to between 119° and 125° ; that sound energy within a 40° arc has been collapsed within a 6° arc. Qualitatively, this indicates that the region between 110° and 125° of a polar noise plot should have the highest sound pressure level.

The directivity index change as a result of this effect is derived later in this section.

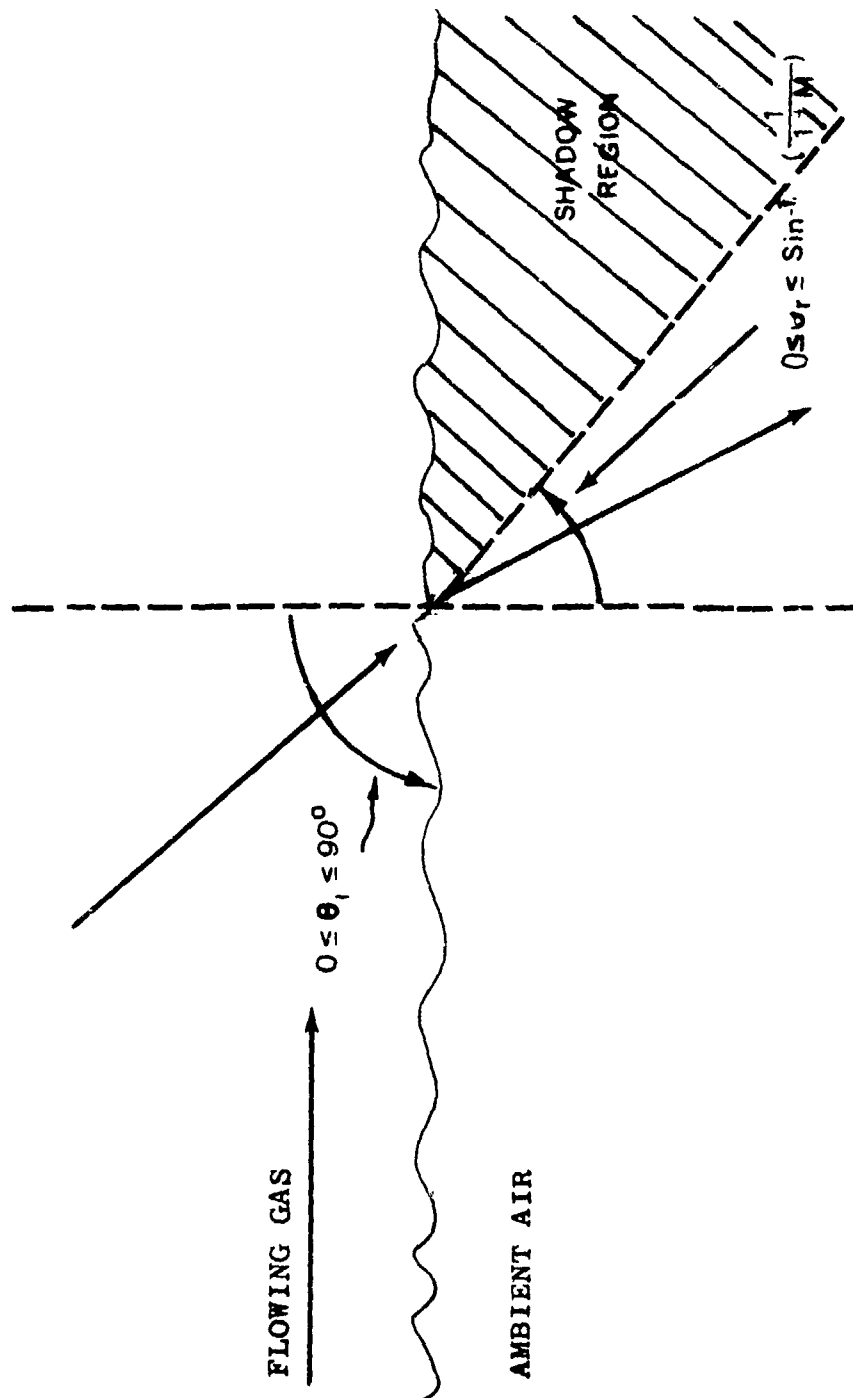


FIGURE III-C3 POSSIBLE ANGLES OF REFRACTION AND OCCURRENCE OF SHADOW REGION

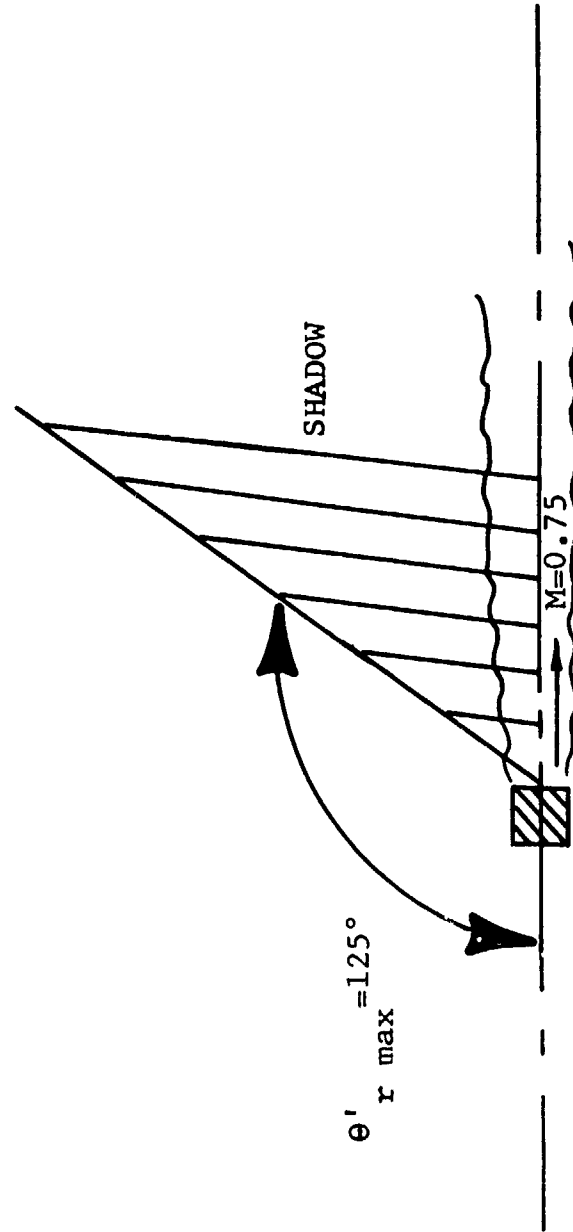


FIGURE III-C4 SHADOW ANGLE WHEN THE FAN JET EXHAUST MACH NUMBER IS 0.75

(b) For the inlet, potential flow lines and lines of constant velocity potential for static test operation are of the character illustrated in Figure III-C5 (Reference 2).

The dotted lines represent lines of constant velocity and the spacing between them is a measure of the velocity gradient. It is noted that these lines are non-spherical so that sound rays emanating from the inlet plane on the axis will generally intersect them, at an angle of incidence which, as sketched in Figure III-C6 cause a deflection toward the sideline, away from the axis.

The angle of incidence, θ_1 , is with respect to the normal to the velocity contour (this direction also being the local direction of the flow streamline). This can be visualized more easily by comparing the process with the refraction of light from a point source inside a transparent ellipsoid such that there is an abrupt increase in the propagation speed at the surface. If the ellipsoid were oriented with the major dimensions on the axis, refraction would tend to deflect the rays away from the sideline instead of toward it as shown in the above. The contour lines of constant velocity are such, however, that the trend is to cause sidewise deflection. And, of course, the velocity gradient is gradual, not abrupt change of direction suggested by the sketches in Figure III-C7.

The shape of the constant-velocity contours changes rapidly in close proximity to the inlet plane. Thus, it is necessary to consider the details of the sound source distribution over the surface of the inlet plane. This, combined with the fact that turbulence in the inlet is relatively low as compared with the mixing zone in the exhaust, indicates that the far field directivity will be determined to a large extent by the modal patterns in the inlet duct. Refraction effects appear to be secondary for inlet radiated noise. Therefore, the remainder of the discussion of refraction effects is concerned with aft radiated noise.

(2) Refraction Control of Exhaust Radiated Noise. Since the exhaust radiated noise is increased toward the sideline because of the refraction effect of airflow-convected sound waves, there is the possibility that by changing the basic parameters, some control of this effect might be achieved to advantage. Specifically, if the discharge air is shrouded with a gas with higher effective speed of propagation, channeling of the sound by internal reflections is possible. This effect has been demonstrated by E. Grande at the University of Toronto (Reference 3) using a cold nitrogen jet to contain pure tone noise injected into it through a hypodermic needle.

If the exhaust flow is surrounded by a shroud of higher velocity and/or higher temperature air, for example, there will be a critical angle of incidence within which the sound will be completely reflected from the interface at the shroud. (See Figure III-C8).

Using equation (III-C1) let :

V_1 = Velocity of fan discharge air

C_1 = Sonic speed of fan discharge air

V_2 = Velocity of hot shroud air

C_2 = Sonic speed of hot shroud air

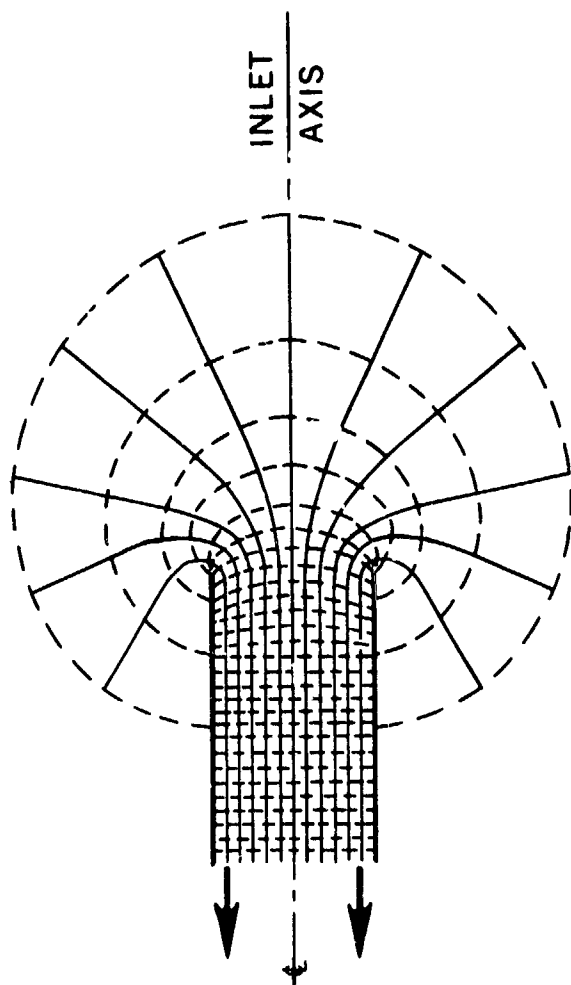


FIGURE III-C5
TYPICAL INLET POTENTIAL FLOW LINES AND
CONSTANT VELOCITY CONTOURS

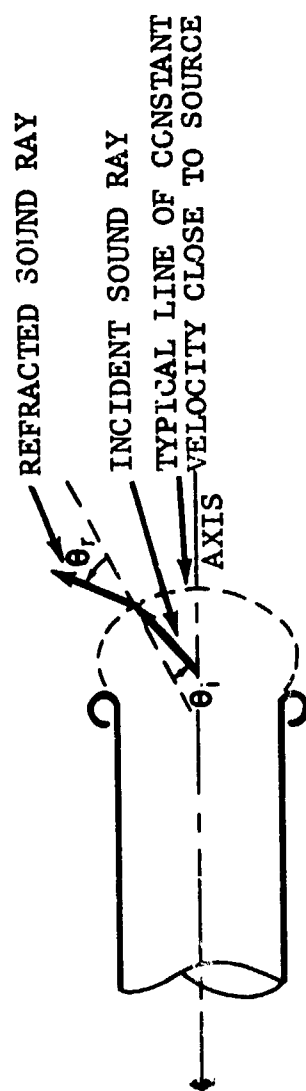


FIGURE III-C6 CHARACTERISTIC REFRACTION EFFECT FOR THE INLET

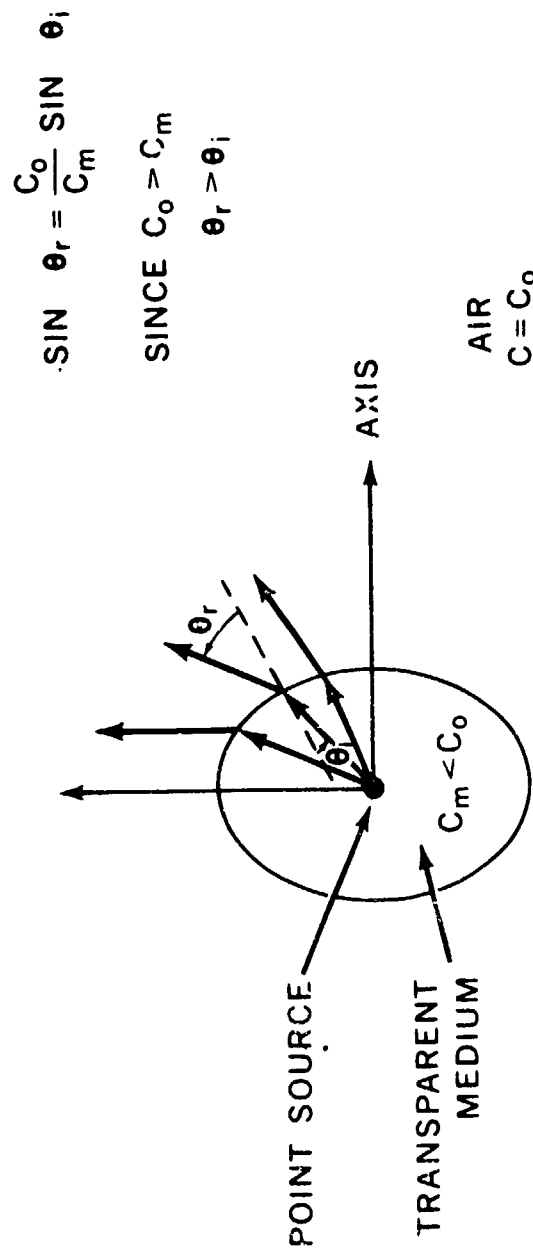


FIGURE III-C7 SIMPLIFIED ILLUSTRATION OF CHARACTERISTIC REFRACTION EFFECT AT THE INLET

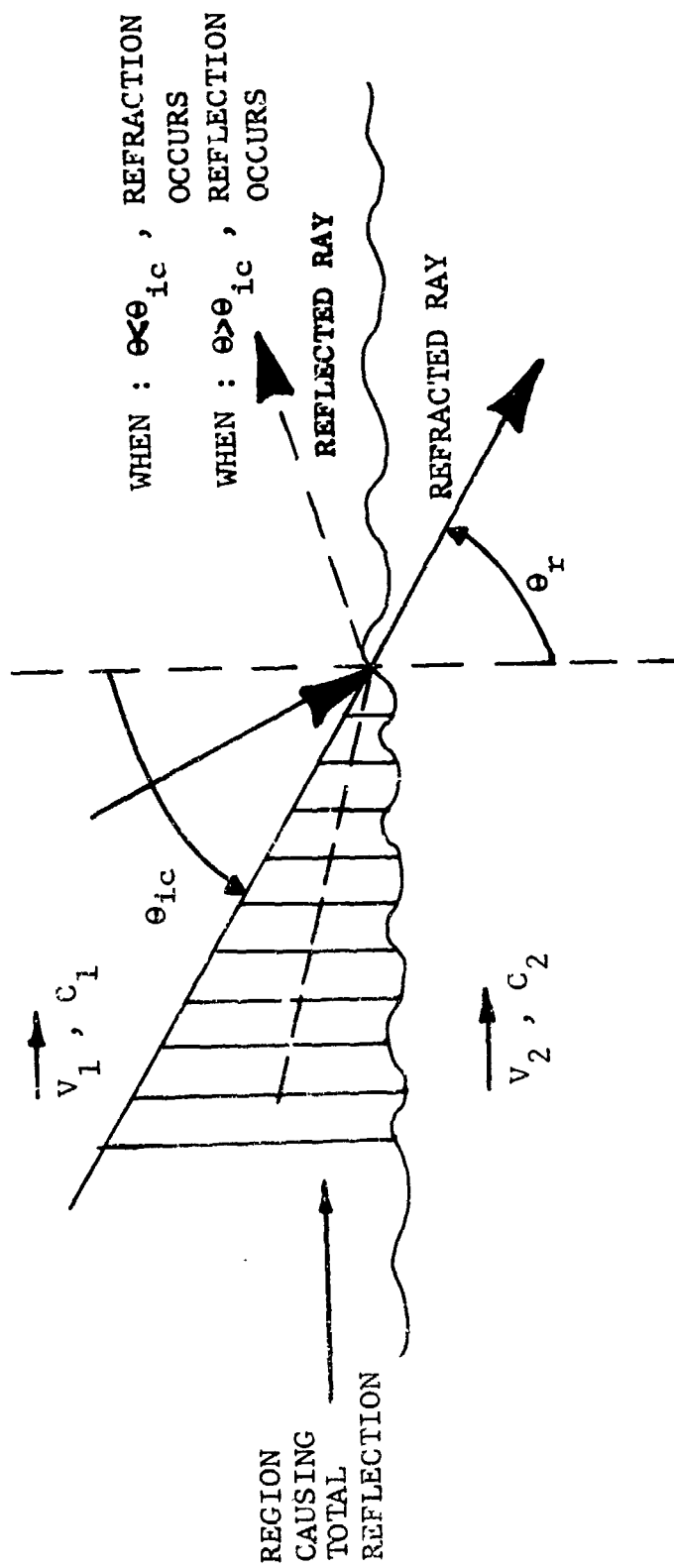


FIGURE III-C8 CRITICAL ANGLE FOR INTERNAL REFLECTION

One could make $V_2 > V_1$ and $C_2 > C_1$, and determine the critical angle of incidence, θ_{ic} , knowing it occurs when $\theta_r = 90^\circ$:

$$\frac{C_1}{\sin \theta_{ic}} + V_1 = \frac{C_2}{\sin 90^\circ} + V_2$$

$$\text{or } \sin \theta_{ic} = \frac{C_1}{C_2 + (V_2 - V_1)}$$

For example, using temperature only to affect C_2 and letting the two streams have the same velocity yield:

$$\sin \theta_{ic} = \sqrt{\frac{T_1}{T_2}}$$

So, for

$\frac{T_2}{T_1}$	= 1	2	3	4
θ_{ic}	= 90	45.0	35.2	30°

This shows that at $T_2/T_1 = 4$, all sound with an angle of incidence between 30° and 90° will be internally reflected and contained inside the shroud so as to be directed along the axis of the jet within the mixing zone.

The angle of incidence yielding complete internal reflection is shown in Figure III-C9 as a function of the air shroud temperature for three cases of interest:

- (a) $V_1 = V_2$ (effect of temperature only)
- (b) $V_1 = C_1$ and $V_2 = C_2$ (effect of shroud temperature when the Mach number of both streams is the same)
- (c) $V_2 = C_2$, $V_1 = 0$ (maximum effect, combining both the temperature and velocity effects)

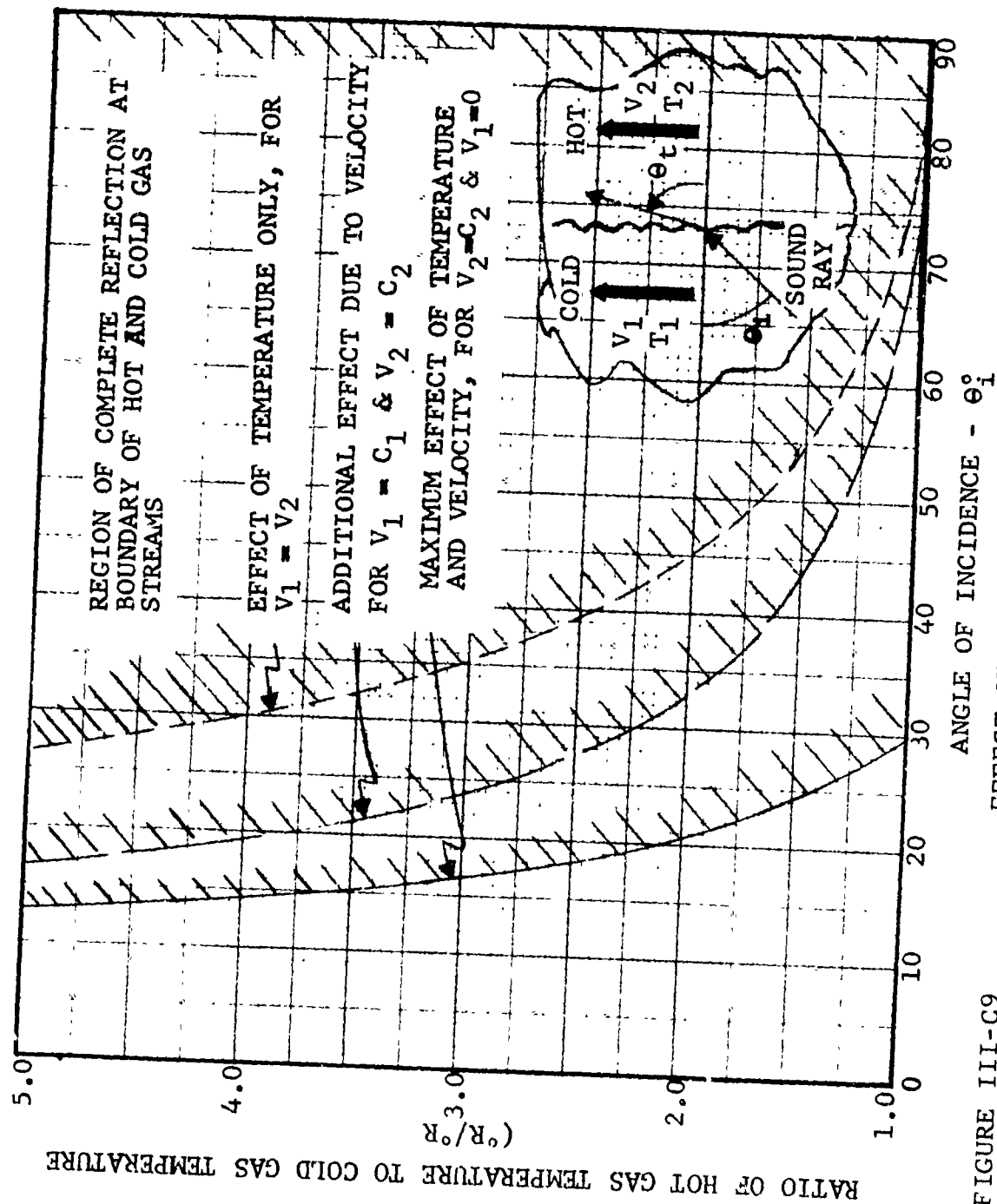


FIGURE III-C9

EFFECT OF TEMPERATURE AND VELOCITY DIFFERENCE IN TWO ADJACENT GAS STREAMS ON ACOUSTIC TRANSMISSION

Case (b) above is of most practical interest since it is achievable by having the same exhaust pressure ratio for both streams.

(3) Predicted Directivity Index Resulting from Refraction. The directivity index at angle θ is defined as:

$$D I_{\theta} = SPL_{\theta} - \overline{SPL}$$

$$\text{where } \overline{SPL} = 10 \log_{10} \left[\frac{W}{A} / \left(\frac{W}{A} \right)_{\text{ref}} \right]$$

$$SPL_{\theta} = 10 \log_{10} \left[\left(\frac{W_{\theta}}{A_{\theta}} \right) / \left(\frac{W}{A} \right)_{\text{ref}} \right]$$

$$\text{So } DI_{\theta} = 10 \log \frac{W_{\theta}}{W} - 10 \log \frac{A_{\theta}}{A}$$

where DI = Directivity Index, dB

SPL = Sound Pressure Level

W = Sound Power

A = Area over which the sound power, W , is distributed

Before refraction the directivity index of the incident sound energy is:

$$D I_{\theta i} = 10 \log W_{\theta i} - 10 \log \Delta A_{\theta i} - \text{const}$$

After refraction it is:

$$D I_{\theta r} = 10 \log W_{\theta r} - 10 \log \Delta A_{\theta r} - \text{const}$$

where ΔA_{θ} is a small increment of area associated with the direction θ .

Then

$$D I_{\theta r} = D I_{\theta i} + 10 \log \frac{W_{\theta r}}{W_{\theta i}} - 10 \log \frac{\Delta A_{\theta i}}{\Delta A_{\theta r}}$$

$$= D I_{\theta i} - 10 \log \frac{\Delta A_{\theta i}}{\Delta A_{\theta r}}$$

$$\text{because } W_{\theta r} = W_{\theta i}$$

(4) Refraction from a Simple Engine Exhaust. Thus the directivity index of the refracted sound depends upon the directivity of the incident sound rays and upon the area into which the incident sound has been refracted. The incremental area of a hemisphere measured from the exhaust axis, is:

$$\Delta A_{\theta} = 2\pi R^2 (\sin \theta_2 - \sin \theta_1)$$

So, the incremental area of the hemisphere for the incident sound is:

$$\Delta A_{\theta i} = 2\pi R^2 (\sin \theta_{i2} - \sin \theta_{i1}).$$

and for the refracted sound:

$$\Delta A_{\theta r} = 2\pi R^2 (\sin \theta_{r2} - \sin \theta_{r1}).$$

Solving Equation (III-C1) for $\sin \theta_r$ gives for the exhaust radiated noise in the aft quadrant:

$$\sin \theta_r = \frac{\sin \theta_i}{\frac{C_1}{C_0} + \frac{V_1 - V_p}{C_c} \sin \theta_i}$$

then

$$\Delta A_{\theta r} = 2\pi R \left[\frac{\sin \theta_{i2}}{\frac{C_1}{C_o} + \frac{V_1 - V_p}{C_o} \sin \theta_{i2}} - \frac{\sin \theta_{i1}}{\frac{C_1}{C_o} + \frac{V_1 - V_p}{C_o} \sin \theta_{i1}} \right]$$

$$= 2\pi R \left[\frac{\frac{C_1}{C_o} (\sin \theta_{i2} - \sin \theta_{i1})}{\left(\frac{C_1}{C_o} + \frac{V_1 - V_p}{C_o} \sin \theta_{i2} \right) \left(\frac{C_1}{C_o} + \frac{V_1 - V_p}{C_o} \sin \theta_{i1} \right)} \right]$$

or

$$\Delta A_r = \frac{\frac{C_1}{C_o} \Delta A_{\theta i}}{\left(\frac{C_1}{C_o} + \frac{V_1 - V_p}{C_o} \sin \theta_i \right)^2} \quad \text{or } \theta_{i1} \rightarrow \theta_{i2}$$

Therefore

$$\frac{\Delta A_{\theta i}}{\Delta A_{\theta r}} = \frac{\left(\frac{C_1}{C_o} + \frac{V_1 - V_p}{C_o} \sin \theta_i \right)^2}{C_1/C_o}$$

So

$$DI_{\theta r} = DI_{\theta i} + 20 \log \left[\frac{C_1}{C_o} + \frac{V_1 - V_p}{C_o} \sin \theta_i \right] - 10 \log \frac{C_1}{C_o} \quad (\text{III-C2})$$

where

- C = Sonic speed
- V_1 = Exhaust velocity
- V_p = Plane velocity
- subscript 1 = Engine exhaust
- 0 = Ambient

The angle at which this directivity index applies is the refraction angle, θ_r , given by:

$$\theta_r = \sin^{-1} \left[\frac{\sin \theta_i}{\frac{C_1}{C_o} + \frac{V_1 - V_p}{C_o} \sin \theta_i} \right] \quad (\text{III-C3})$$

So, given DI_{θ_i} and θ_i , then DI_{θ_r} and θ_r are determined. Note that the angle as measured from the engine inlet, ϕ , is:

$$\phi = \theta + 90^\circ$$

These equations simplify to the following for the case of fan discharge noise under static test conditions ($C_1 \approx C_o$, $V_p = 0$)

$$DI_{\theta_r} = DI_{\theta_i} + 20 \log (1 + M \sin \theta_i)$$

$$\theta_r = \sin^{-1} \left[\frac{\sin \theta_i}{1 + M \sin \theta_i} \right], \quad M = \frac{V_1}{C_o}$$

The directivity index for the simple case has been plotted in Figure III-C10 for various exhaust Mach numbers. If the directivity index without flow, DI_{θ_i} , can be determined by analysis, then the directivity index with refraction, DI_{θ_r} , is established.

In general, accumulated data on turbofan engine exhausts suggest that, to a first approximation, it may be assumed that:

$$DI_{\theta_i} \approx 0 \quad \text{for aft-end radiated noise}$$

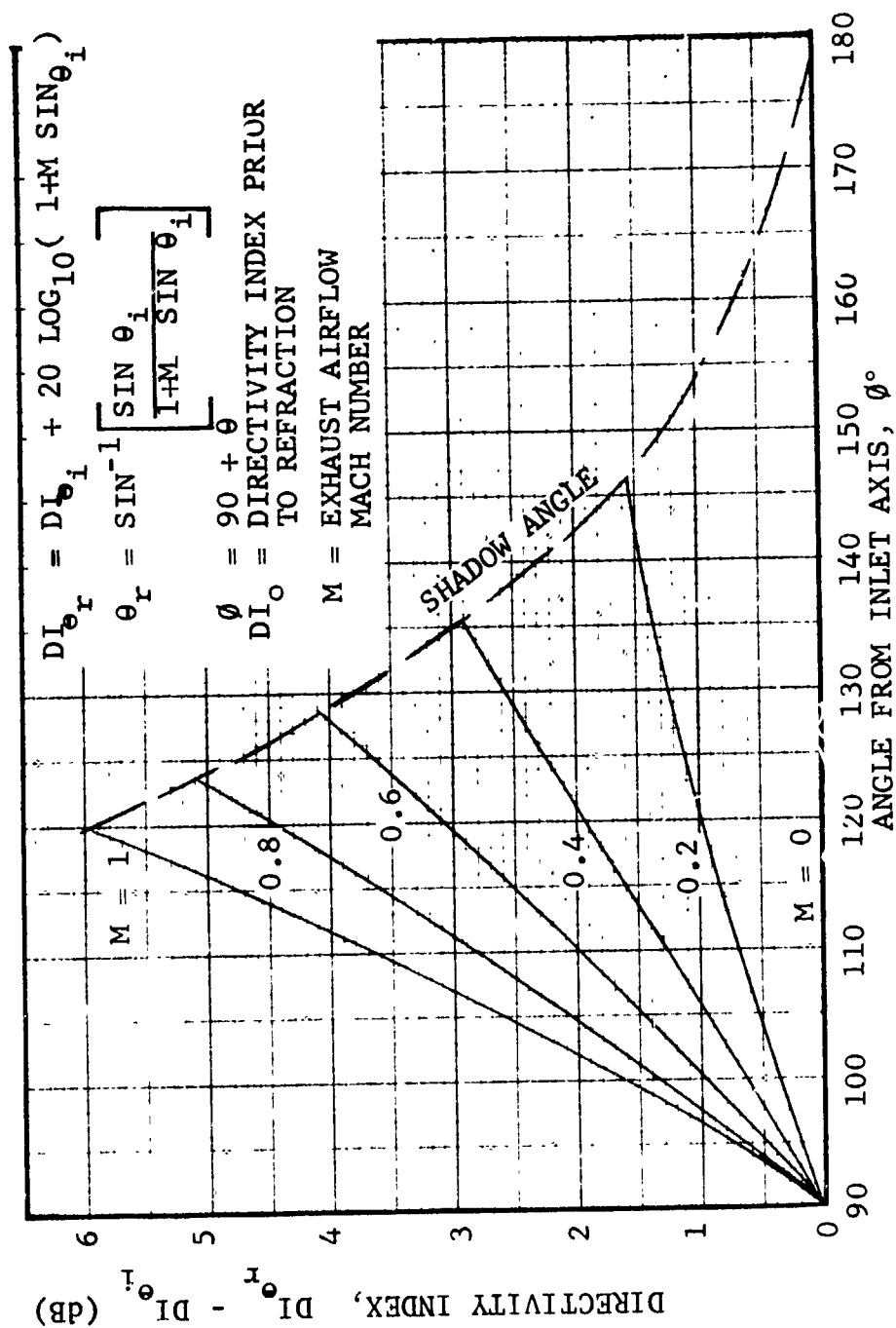


FIGURE III-C10 EFFECT OF AIRFLOW MACH NUMBER ON AFT QUADRANT DIRECTIVITY INDEX

So, then $DI_{\theta r} = 20 \log (1 + M \sin \theta_1)$

This assumption is valid for a monopole source. Such an assumption is in conflict with the idea of lobes caused by the phasing relationships for the modes generated by turbomachinery blade rows. These phase relationships are derived, however, on the assumption of wave propagation in a stationary, homogeneous, non-turbulent medium. In the actual case, the mixing zone of the jet exhaust is very turbulent, causing random disruption to phase reinforcement and cancellation in the far field. Also, such turbulence introduces scattering of the sound energy not only in terms of geometrical distribution but also, in terms of the frequency spectral distribution. Since lobes occur as a result of phase reinforcement and cancellation, which is quite dependent on the particular sound wave length, even the frequency spreading caused by scattering has the effect of causing the sound energy to be of more uniform spatial distribution.

This is particularly true in the sense of time-averaged sound pressure levels. Instantaneously, these lobe patterns might well exist, even after refraction, but they can be expected to sweep back and forth across a far field receiver point so that from turbofan engines with strong pure tone content, the listener senses a warbling sound.

An exception to this general rule may occur for low frequency sound in which the wave length is an appreciable fraction of the distance from source to receiver. This is well known from ground reflection cancellation and reinforcement effects. For a hard surface, nearly perfect reflector, low frequency sound pressure is doubled by reinforcement, leading to 6 dB increase in sound power level. In this case, the phasing is coherent, and any lobe patterns as might exist for such low frequencies should be stable.

At high frequencies, however, the waves are scattered by air currents or turbulence in a random way so that the net result is the same as having two independent, uncorrelated sources, leading to only 3 dB increase in sound power level; such a result can occur only after periodic cancellation and reinforcement of the wave -- the period of this effect may be very long compared with the period of one acoustic wave cycle. Experience has shown that, in many cases, an averaging time of the order of 30 seconds is desirable to obtain repeatability of engine acoustic data. This is interpreted as an averaging of the back-and-forth sweeping of the lobes, which tends to equalize the far field radiation pattern insofar as aft-end lobes are concerned. Thus the remaining effect, refraction, becomes dominant for typical aft-end engine radiated noise as compared with any calculated initial directivity index based on lobe patterns.

(5) Effect of Adding a Hot Shroud . When internal reflections occur, such reflected sound is redirected primarily along the axis of the jet within an included angle essentially that given by the jet exhaust. That portion of the sound energy which is not internally reflected still reaches the far field. In passing through the hot shroud it is refracted on entering and re-refracted on leaving, as indicated in Figure III-C11.

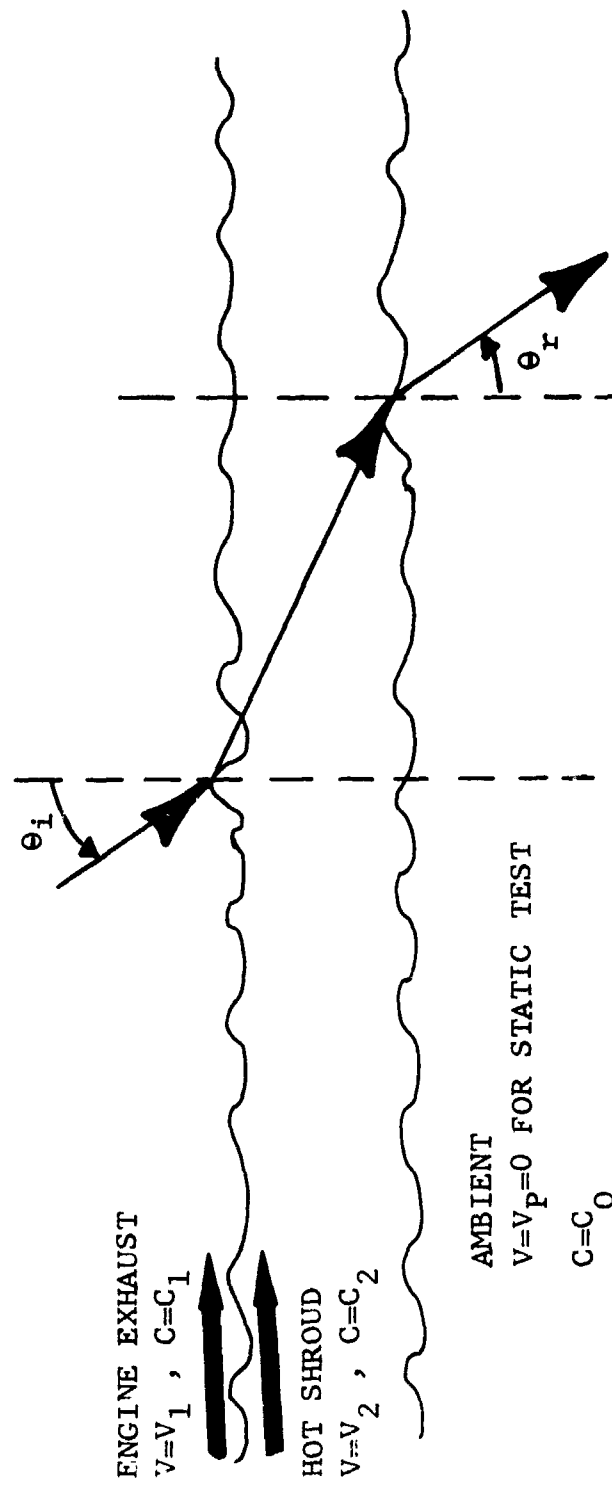


FIGURE III-C11 TYPICAL RAY PATH THROUGH SHROUD WHEN INTERNAL REFLECTION DOES NOT OCCUR

The shroud thickness must be at least one-quarter wave length in order for ray analysis to apply. Its thickness will be so small, however, as compared with far field distances at which engine noise is measured that the axial displacement inside the shroud can generally be ignored. Therefore, the Equations (III-C2 and C3) can be used for determining the effect of the hot shroud on the far field directivity where:

$$0 \leq \theta_i \leq \theta_{ic} = \sin^{-1} \left[\frac{c_1}{c_2 + (v_2 - v_1)} \right]$$

This has been evaluated with the results as shown in Figure III-C12 for a case in which the shroud is air at various elevated temperatures and surrounds the fan-discharge air which is essentially at ambient temperature. The dashed lines of constant temperature ratio in Figure III-C12 show how the data in Figure III-C10 are modified by the use of the hot-air shroud. For a fan discharge Mach Number of 1.0, for example, use of a shroud with an absolute temperature three times that of the fan air temperature (instead of unity) yields a change in the directivity index from a maximum of 6.0 to a maximum of 3.0, or a net reduction of 3.0 dB.

It should be noted that as the fan discharge Mach Number is reduced it is necessary to use higher shroud air temperatures to obtain this beneficial effect. For example, Figure III-C12 shows that for an exhaust Mach Number of 0.4, a shroud temperature of twice the exhaust air temperature has no effect; this happens because the critical angle of incidence for internal reflection is so large that none of the sound is reflected. In that case, however, further increase of the shroud temperature will result in a sideline noise reduction.

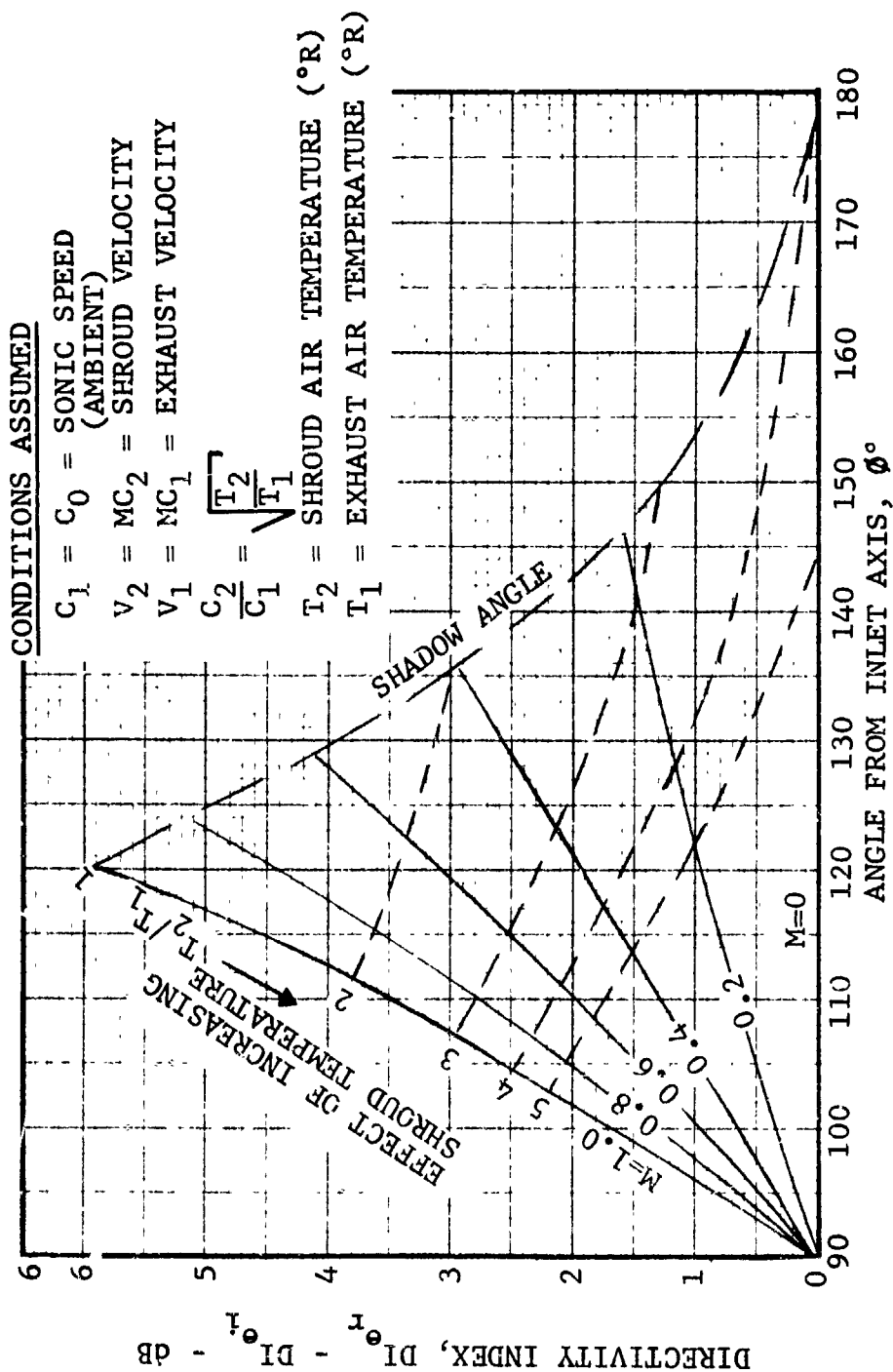


FIGURE III- C12
EXAMPLE OF EFFECT ON DIRECTIVITY INDEX OF
ENCLOSING EXHAUST WITH HOT SHROUD

NOMENCLATURES SECTION III-C

c	Speed of propagation
DI	Directivity Index
M	Mach number of flowing airstream defined as, V/C
SPL_{θ}	Sound pressure level at angle θ
W	Acoustic power
V	Speed of flowing airstream
θ	Wave angle
$\theta_{r,i}^1$	Angle measured from engine inlet (refraction, or incident wave angle)
ϕ	Angle measured from engine inlet
μ	Index of refraction
	Subscripts
i	incident
ic	critical angle of incidence
r	refracted
P	Plane

REFERENCES SECTION III-C

1. Morse, P.M., Ingard, K.U., Theoretical Acoustics, pp. 708-710, McGraw-Hill Book Co. (1968).
2. Sokolnifoff, I.S., Redheffer, R.F., Mathematics of Physics and Modern Engineering, pp. 594 - 595, McGraw-Hill Book Co. (1958).
3. Grande, E., "Refraction of Sound by Jet Flow and Jet Temperature," UTIAS Technical Note No. 110, 1966.

(D) Propagation Effects. In order to interpret the results of acoustic tests in the field, especially in comparing data from one site to another, or from ground to flight it is necessary to consider the mechanism associated with the propagation of sound in the atmosphere.

The phenomena considered in this section are:

- Change in amplitude due to inverse square law divergence.
- Absorption of energy by the atmosphere.
- Additional absorption of energy by the ground boundary layer.
- Reflection of sound waves by the ground.

All four effects must be considered prior to evaluation of data for either the purposes of comparison and/or prediction. The first three will have a major effect on the levels of sound energy reaching an observer; the fourth will have significant effect on the spectral signature of the source.

(1) Inverse Square Law. The basic assumption on propagation of sound energy considers a point source of sound in free space with constant total power output. The power flux (power per unit area) is proportional to the amplitude squared of the acoustic pressure wave. The total power passing through the surface of any sphere (with the acoustic source at its center) must be equal to the total power output of the source. Since the surface area at radius r is proportional to r^2 , the amplitude squared of the acoustic wave is proportional to $1/r^2$ (Inverse Square Law).

(2) Atmospheric Absorption. The phenomena of atmospheric absorption of acoustic energy are associated with power lost due to irreversible work done by the wave on the atmosphere. The losses are due to viscosity, heat transfer, and molecular absorption of energy. For an acoustic wave, these losses are functions of temperature, humidity, and the frequency of the sound.

Reference 1 presents atmospheric absorption coefficients for full and 1/3 octave bands over a wide range of meteorological conditions, based on a combination of analytical models and empirical laboratory testing, and modified in the high frequency range to account for observed spectral shape as it affects measurements taken with proportional bandwidth filters.

These coefficients are still based on the premise of uniform atmospheric properties along the propagation path, and results will vary in actual test conditions depending on the extent of non-uniformity present, or on the variations along the propagation path from measurements of the controlling parameters.

(3) Ground Boundary Layer Absorption. For source and receiver, or observer, both near the ground, additional losses are observed which are a combination of effects of the turbulent boundary layer of the air mass moving along the ground, and the refraction of sound caused by temperature and wind gradients along the propagation path. Reference 2 provides the results of a number of empirical studies into these effects. For measurements or predictions

over relatively short distances, the acoustic shadow effect shown in Figure 1 and 2 can be neglected, but the losses due to the turbulence of the ground boundary layer (illustrated in Figure 3, Reference 2) are present in the real test situation and must be taken into account. For the studies of Section VI-B of this report, the levels of ground boundary layer losses shown in Figure 4, Reference 2 have been used.

(4) Reflection of Sound Waves by the Ground. It is not possible to conduct acoustic tests in the field without a reflecting surface in the vicinity.

Analytical considerations of the acoustic field for a point source in the vicinity of a reflecting surface as well documented (see for sample Reference 3).

The reflection problem is illustrated in Figure III-D1. As indicated in the Figure the problem may be treated by considering the total signal received to be the sum of the direct signals at the receiver and at an image receiver.

For an ideal reflecting surface there is no loss in amplitude of the reflected signal and the reflection occurs with no phase shift in the signal. For a real surface (no diffuse reflection) a certain portion of the incident energy is absorbed. Thus, the signal to the image receiver has a reflection coefficient, Q , which is:

$$Q = \frac{P_{\text{reflected}}}{P_{\text{incident}}}$$

The amplitude of the two components (direct and image) of the signal will be different due to three effects:

- Atmospheric absorption and ground boundary layer absorption.
- The effect of square law divergence over different path lengths.
- Absorption of part of the incident waves by the surface.

The effect of atmospheric and ground boundary layer are negligible (with regards to differences in amplitude).

In addition, there will be a time delay between the two signals, τ .

$$\tau = \frac{\Delta r}{c} = \frac{\Delta c}{\lambda f}$$

where:

- Δr = difference in path length (reflected minus direct)
- c = acoustic velocity
- λ = wave length
- f = frequency

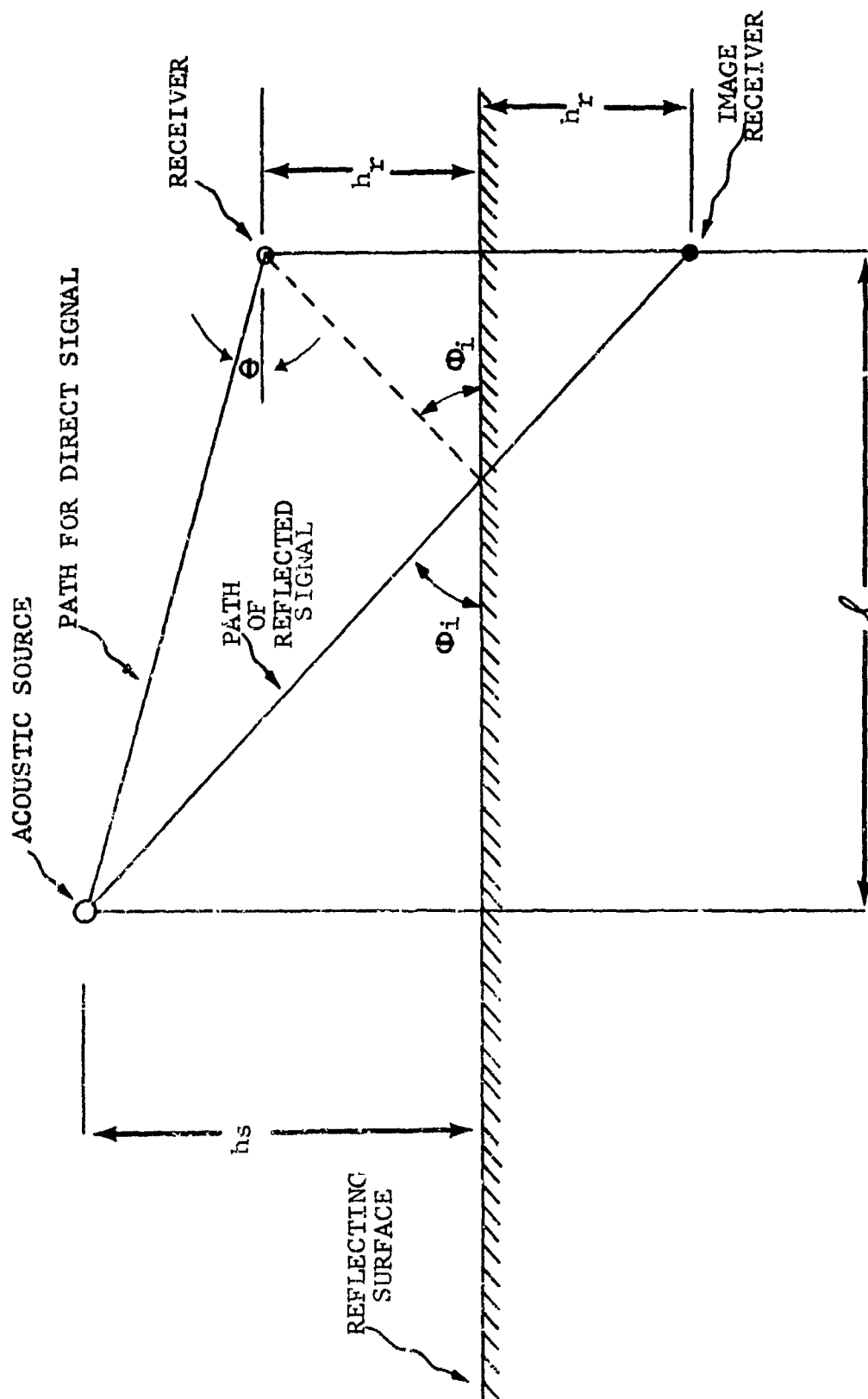


FIGURE III-D1 ILLUSTRATION OF REFLECTION PROBLEM

If C_r is defined as follows:

$$C_r = \left(\frac{P_o}{P_d} \right)^2$$

where:

P_o = rms value of pressure at microphone.

P_d = rms value of pressure due to direct signal
(i.e., signal that would be received in free field)

and with the sound pressure level (SPL) defined as:

$$SPL = 10 \log_{10} \left(\frac{P}{P_{ref}} \right)^2$$

where

P = pressure (rms value)

P_{ref} = reference pressure

then the value of sound pressure level at a microphone (including reflection becomes:

$$SPL = 10 \log_{10} \left(\frac{P_d^2}{P_{ref}^2} \times C_r \right)$$

or

$$SPL = SPL_{free \text{ field}} + 10 \log_{10} (C_r)$$

i.e., $10 \log_{10} C_r$ may be interpreted as a delta to be added to the free field sound pressure level in order to account for reflection.

Now, C_r may be written (Reference 3)

$$C_r = 1 + \left(\frac{P_r}{P_d} \right)^2 + 2 \left(\frac{P_r}{P_d} \right) \cdot \left(\frac{P_{ri} \times P_{di}}{P_r \times P_d} \right)$$

where i denotes instantaneous value, and

P_r = rms value of reflected signal

P_d = rms value of direct signal

$\frac{P_{ri} \times P_{di}}{P_r \times P_d}$ is defined as the autocorrelation function $(R_{r, r + \Delta r})$ which is given by Reference 3 as:

$$(R_{r, r + \Delta r}) = \cos \left[\sqrt{1 + \left(\frac{\Delta f}{2 f_c} \right)^2} 2\pi f_c \tau \right] \cdot \frac{\sin \left[\frac{\Delta f}{2 f_c} 2\pi f_c \tau \right]}{\frac{\Delta f}{2 f_c} 2\pi f_c \tau}$$

where

Δf = bandwidth of noise

f_c = geometric center frequency of band

τ = time delay between points

Now P_r/P_d is (using the inverse square law and reflection coefficient):

$$\frac{P_r}{P_d} = Q \times \frac{r_d}{r_r} = \frac{Q}{Z}$$

where Z equals the ratio between the reflected path length and the direct path length.

Making the necessary substitutions yields:

$$C_r = 1 + \frac{Q^2}{Z^2} + \frac{2Q}{Z} \frac{\sin \left(\alpha \frac{\Delta r}{\lambda} \right)}{\alpha \frac{\Delta r}{\lambda}} \cos \left(\frac{\beta \Delta r}{\lambda} \right)$$

where

$$\alpha = 2\pi \left(\frac{\Delta f}{2 f_c} \right)$$

$$\beta = 2\pi \sqrt{1 + \left(\frac{\Delta f}{2 f_c} \right)^2}$$

To this point the analysis has considered acoustic waves travelling in a homogeneous medium (at rest) with reflection from a plane surface that may change the amplitude of the wave (Q) but does not affect the phase of the reflected wave. In general, the atmosphere is neither uniform nor at rest. In addition, the surface may introduce a phase angle and it may be considered smooth only if $\lambda \gg$ surface roughness.

All of these factors tend to create an effective path length differential, $\Delta r'$, greater than the geometric difference, Δr .

Defining the phase factor to be:

$$\phi = \frac{\Delta r}{\Delta r'}$$

The actual time delay, τ' , becomes

$$\tau' = \frac{\Delta r}{\lambda f \phi}$$

or

$$\tau' = \tau / \phi$$

Making the substitution in the equation for C_r yields:

$$C_r = 1 + \frac{Q^2}{Z^2} + \frac{2Q}{Z} \frac{\sin \frac{\alpha}{\phi} \frac{\Delta r}{\lambda}}{\frac{\alpha}{\phi} \frac{\Delta r}{\lambda}} \cos \left(\frac{\beta}{\phi} \frac{\Delta r}{\lambda} \right)$$

The condition for a minimum value of C_r (null) is

$$\Delta r' = \lambda \frac{2n+1}{2} \quad n = 0, 1, 2, 3 \dots$$

or for fixed geometry:

$$\phi = \frac{2}{(2n+1)} \frac{\Delta r}{\lambda_{\text{null}}} = \frac{2f_{\text{null}}}{(2n+1)} \frac{\Delta r}{c} \quad n = 0, 1, 2 \dots$$

The above relationship allows for experimental determination of the phase factor.

For an ideal reflector and a homogeneous atmosphere $\phi = 1$, and

$$f_{\text{null ideal}} = \frac{2n + 1}{2} \frac{c}{\Delta r}$$

Thus, the phase factor may be expressed as

$$\phi = \frac{f_{\text{null actual}}}{f_{\text{null ideal}}}$$

Summarizing:

$$\text{SPL}_{\text{recorded}} = \text{SPL}_{\text{free field}} + 10 \log_{10} (C_r)$$

where

$$C_r = 1 + \left(\frac{Q}{Z}\right)^2 + 2 \frac{Q}{Z} \frac{\sin\left(\frac{\alpha}{\phi} \frac{\Delta r}{\lambda}\right)}{\left(\frac{\alpha}{\phi} \frac{\Delta r}{\lambda}\right)} \cos\left(\frac{\beta}{\phi} \frac{\Delta r}{\lambda}\right)$$

where:

Q = fraction of incident wave that is reflected (coefficient of reflection)

$Z = r_r / r_d$

$\Delta r = r_r - r_d$

r_r = path length reflected signal

r_d = path length direct signal

λ = wave length of geometric mean frequency of the bandwidth considered

$\beta = 2\pi \sqrt{1 + (\Delta f / 2f_c)^2}$

$\alpha = 2\pi \frac{\Delta f}{2f_c}$

Δf = bandwidth

f_c = geometric mean frequency

and $\phi = \frac{f_{\text{null actual}}}{f_{\text{null ideal}}}$

Analytical determination of the phase factor (ϕ) and the coefficient of reflection is for all practical purposes impossible. The studies of Section VI B of this report involve the determination of ϕ and Q experimentally (as functions of frequency, surface, and geometry).

For broadband noise analysis using proportional bandwidth filters (such as 1/3 octave) the relationship $\Delta f/2f_c$ remains constant. Thus, at high frequencies (small wave lengths) the last term in C_r is damped out due to the $1/\lambda$ term in the denominator. As an illustration of this, $10 \log_{10} C_r$ for 1/3 octave bands is presented for an ideal reflector ($Q = 1, \phi = 1$) and for a reflecting surface with $Q = .6$ and $\phi = 0.9$ in Figure III-D2. For this illustration the following geometric values were used: $h_s = h_r = 12'$ and $L = 50'$.

When pure tones ($\Delta f \rightarrow 0$) are being analyzed the equation for C_r may be simplified to:

$$C_r = 1 + \frac{Q^2}{Z} + 2 \frac{Q}{Z} \cos \left(\frac{\Delta r}{\phi \lambda} \right)$$

Since $\alpha \rightarrow 0$ and $\beta \rightarrow 1$.

In this equation, there is no damping term associated with the last term in C_r . For the same conditions used previously, $10 \log_{10} C_r$ is plotted in Figure III-D3 for pure tones.

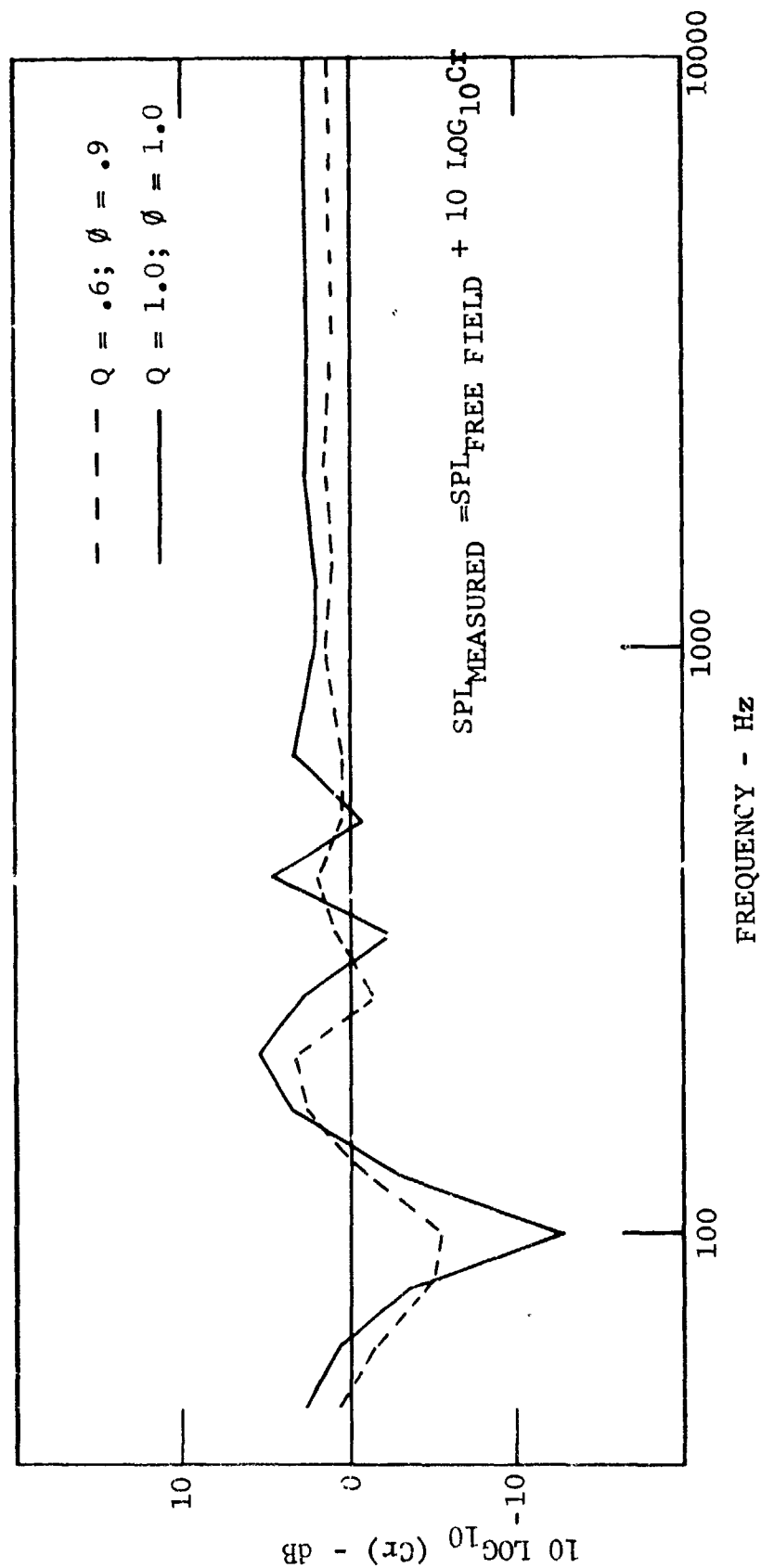


FIGURE III-D2
ILLUSTRATION OF THE EFFECT OF REFLECTION ABSORPTION ON SOUND
PRESSURE LEVEL FOR 1/3 OCTAVE BAND ANALYSIS

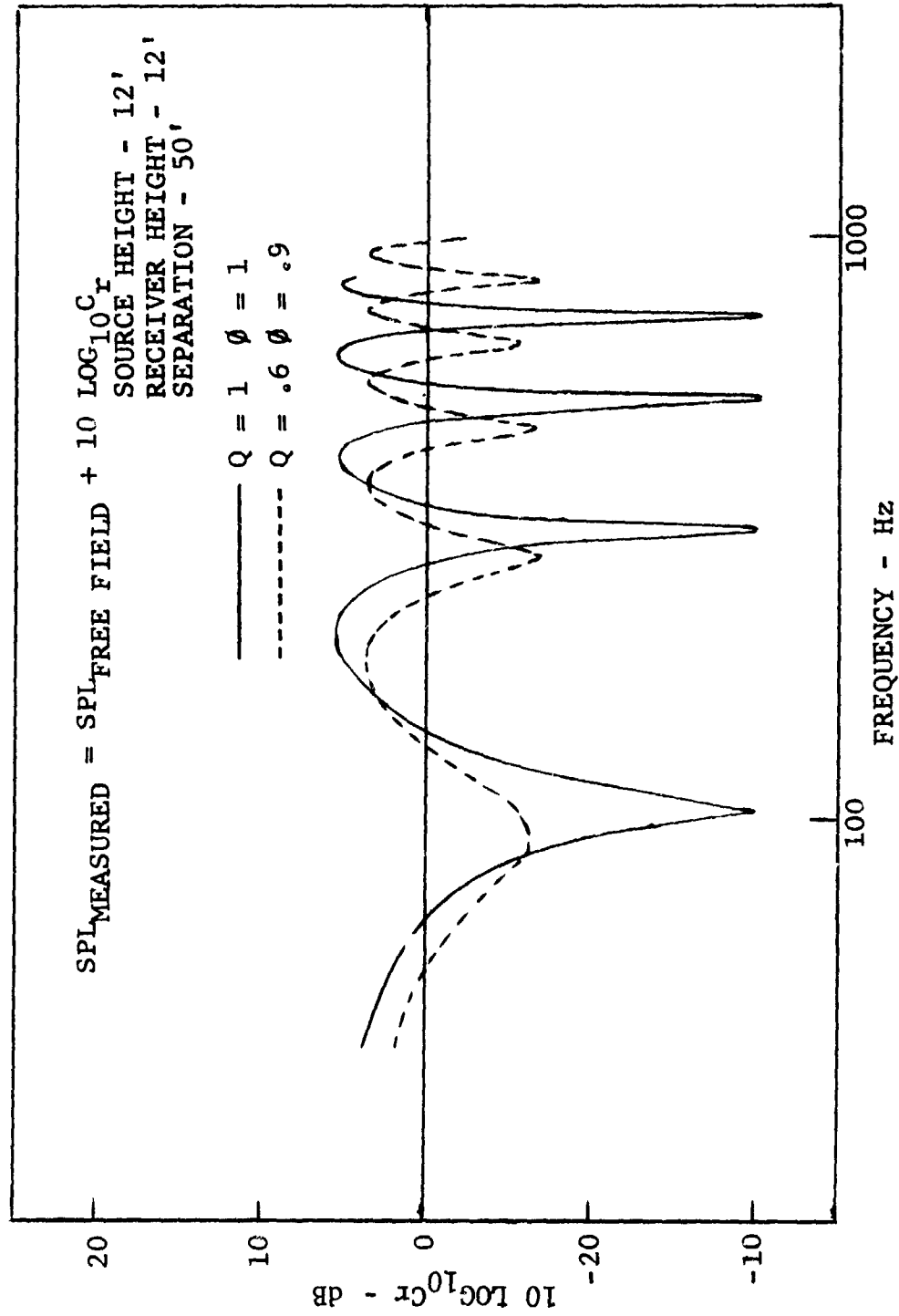


FIGURE III-D3
 ILLUSTRATION OF THE EFFECT OF REFLECTION ON
 MEASUREMENT OF PURE TONES

NOMENCLATURE SECTION III-D

c	Acoustic velocity
C_r	Defined as, $(P_o/P_d)^2$
f	Frequency
f_c	Geometric center frequency of band
P	RMS value of pressure
P_d	RMS value of pressure due to a direct signal
P_o	RMS value of pressure at the microphone
Q	Reflection coefficient defined as, $P_{\text{reflected}}/P_{o\text{incident}}$
r_r	Path length of reflected signal
r_d	Path length of direct signal
Z	Defined as, r_r/r_d
α	Defined as, $2\pi (\Delta f/2f_c)$
β	Defined as, $2\pi [1 + (\Delta f/2f_c)^2]$
λ	Wave length
Δf	Bandwidth of noise
Δr	Difference in path length ($r_r - r_d$)
τ	Time delay between two signals
τ'	Defined as, τ/ϕ
ϕ	Phase factor defined as, $f_{\text{null actual}}/f_{\text{null idea}}$

REFERENCES SECTION III-D

1. SAE ARP 866, "Standard Values of Atmospheric Absorption As A Function Of Temperature and Humidity For Use In Evaluating Aircraft Flyover Noise", August 31, 1964.
2. SAE AIR 923, "Method for Calculating the Attenuation of Aircraft Ground to Ground Noise Propagation During Takeoff and Landing", August 15, 1966.
3. WADD Technical Report 61-178, Morgan et.al, "The Use of Acoustic Scale Models For Investigating Near Field Noise Of Jet and Rocket Engines", April 1961.

IV. EXPERIMENTAL INVESTIGATION OF VANE/BLADE NUMBER EFFECTS

(A) Vehicle and Test Descriptions. An experimental investigation was pursued to determine the effects of vane/blade ratio on fan generated and transmitted noise. To perform a meaningful investigation, two aerodynamically optimized configurations were tested on a fan vehicle.

The vehicle (Development Vehicle I) used for baseline comparison purposes was a scale model of a modern, high tip speed, high bypass ratio front fan (Figure IV-A1). The main-stage rotor consisted of 38 blades, and was 35 inches in diameter; there were 80 outlet guide vanes (OGV's) and no inlet guide vanes. The inner termination of the OGV's was a circumferential island which was located approximately 80% of the span in from the rotor tip. Below this island were the IGV's, rotor, and OGV's of a small fan stage designed to provide the proper flow characteristics along the inner portion of the fan flowpath. This stage utilized less than 30% of the fan flow, and operated at a very low tip speed, generating very low levels of noise. The main rotor design tip speed was 1388 feet per second, the design bypass ratio was 6:1 and the average bypass pressure ratio was 1.617:1.

A new system of main-stage OGV's, incorporating only 48 vanes, was employed on the vehicle (D/V II) for the second series of tests (Figures IV-A2, 3, and 4). The chord length of these OGV's was increased proportionately, to maintain the solidity of the original design; otherwise, the vehicle was very similar to the baseline configuration. Rotor tip speed, pressure ratio, etc., remained as before. Figure IV-A5 compares the operating line data actually measured from the two vehicles; as can be seen, they are almost identical in performance.

Acoustic tests were carried out on the two vehicles at a Peebles, Ohio, Test Facility. The far field tests employed microphones arranged in two concentric arcs, centered around the fan axes (see Figure IV-A6). The outer arc, of 250 ft. radius, consisted of 15 microphones placed in 10 degree incremental angles from 20 to 160 degrees. (Angles are measured relative to the fan axial centerline, with the inlet equal 0°.) The inner arc (D/V II only) had 8 microphones placed at a 150 ft. radius, at angles of 50 through 120 degrees. Probe microphones were also employed in the fan inlet, fan nozzle, and fan exhaust (for readings at certain selected speeds). Several test runs were made at different fan speeds. The sound data obtained from the microphones was recorded on magnetic tape for later reduction, employing standard one-third octave band and 50 Hz narrowband techniques. The two sets of reduced data obtained on D/V I and II are tabulated respectively in Appendix A and B.

It is noted that the acoustic comparisons between D/V I and D/V II are performed entirely on the basis of the 250 ft. arc data. The 150 ft. arc data, taken only with D/V II, was used for substantiation of reflection phenomena involving propagation of noise to different distances from a fixed location noise source. The reflection phenomena data is shown in Section VI-B, Figures VI-B67 through VI-B70.

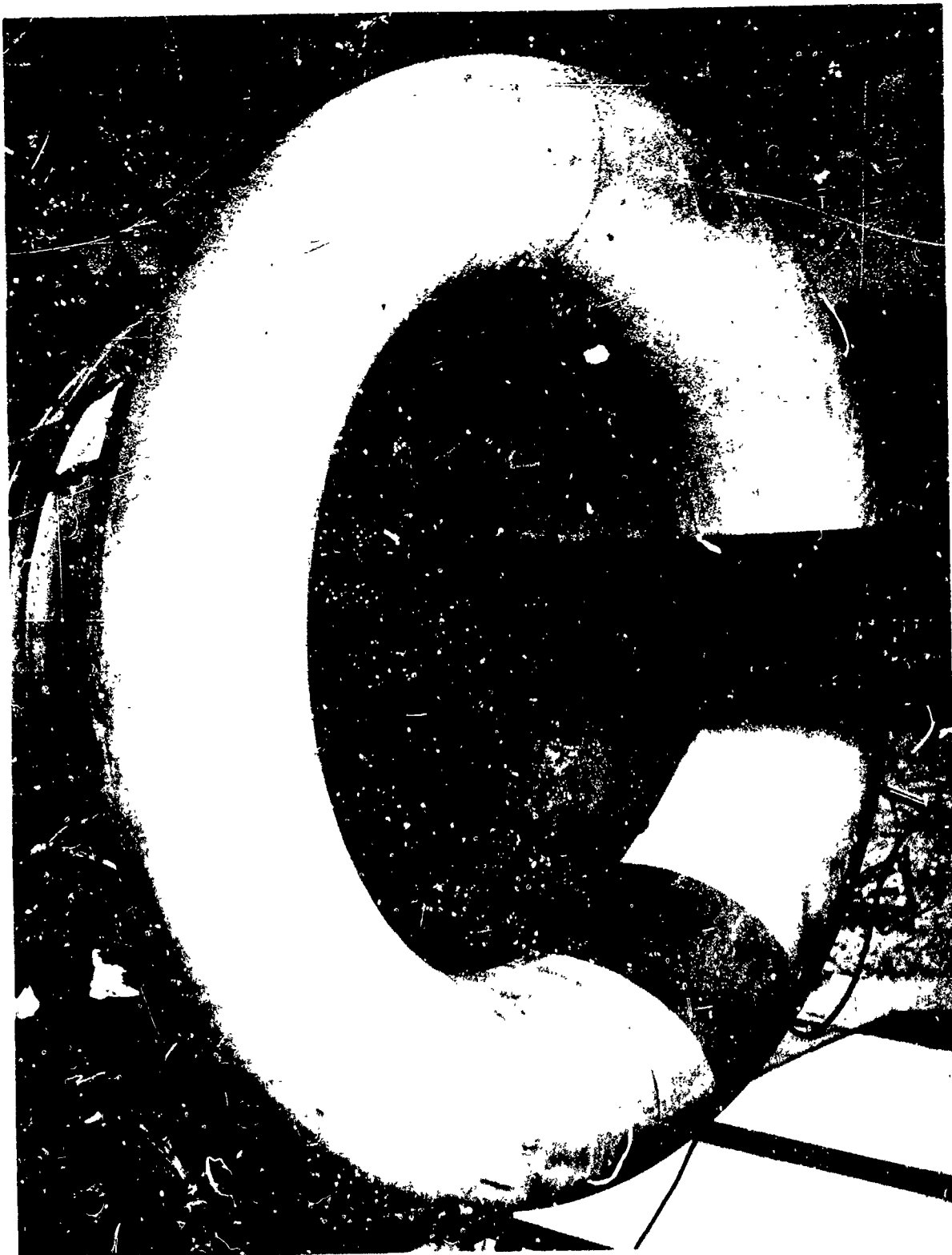


FIGURE IV-A1 80 - OGV VEHICLE (D/V I)

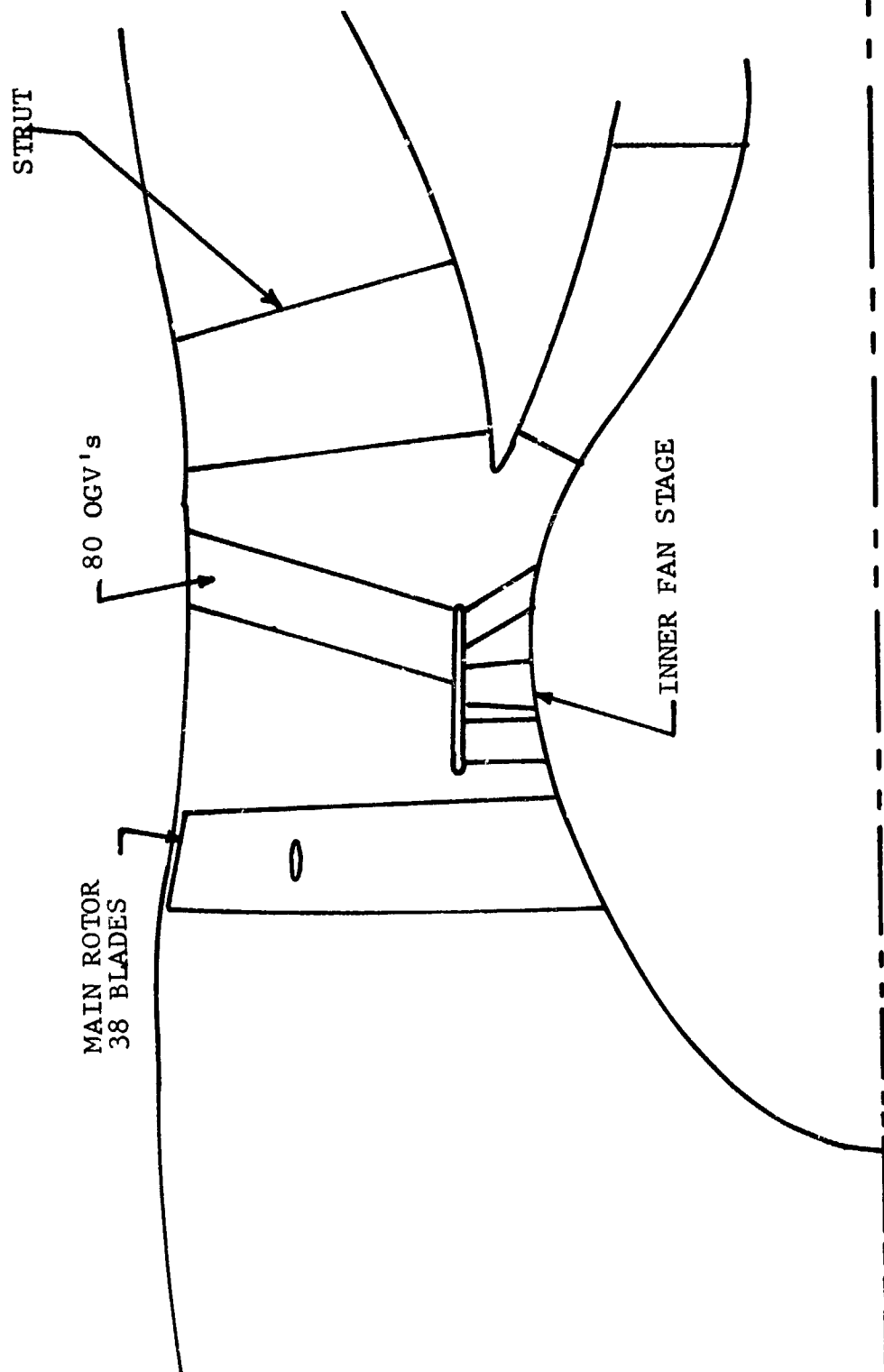


FIGURE IV-A2 CONFIGURATION SKETCH - D/V I



FIGURE IV-A3 OGV FOR D/V II FRONT VIEW

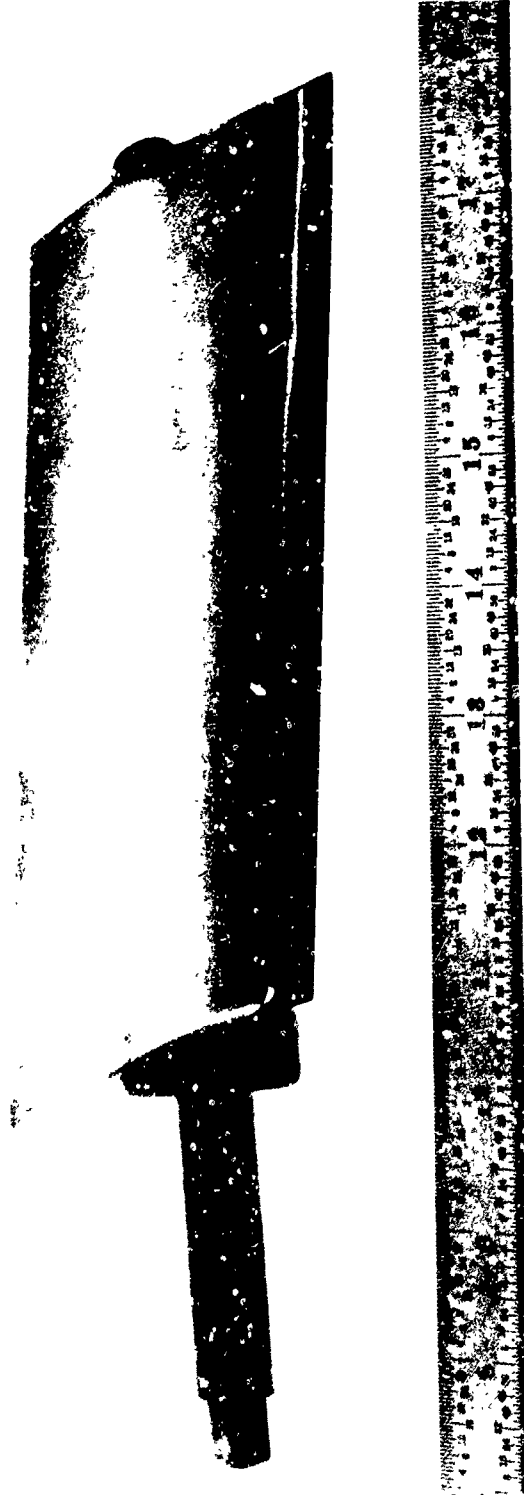


FIGURE IV-A4 OGV FOR D/V II REAR VIEW

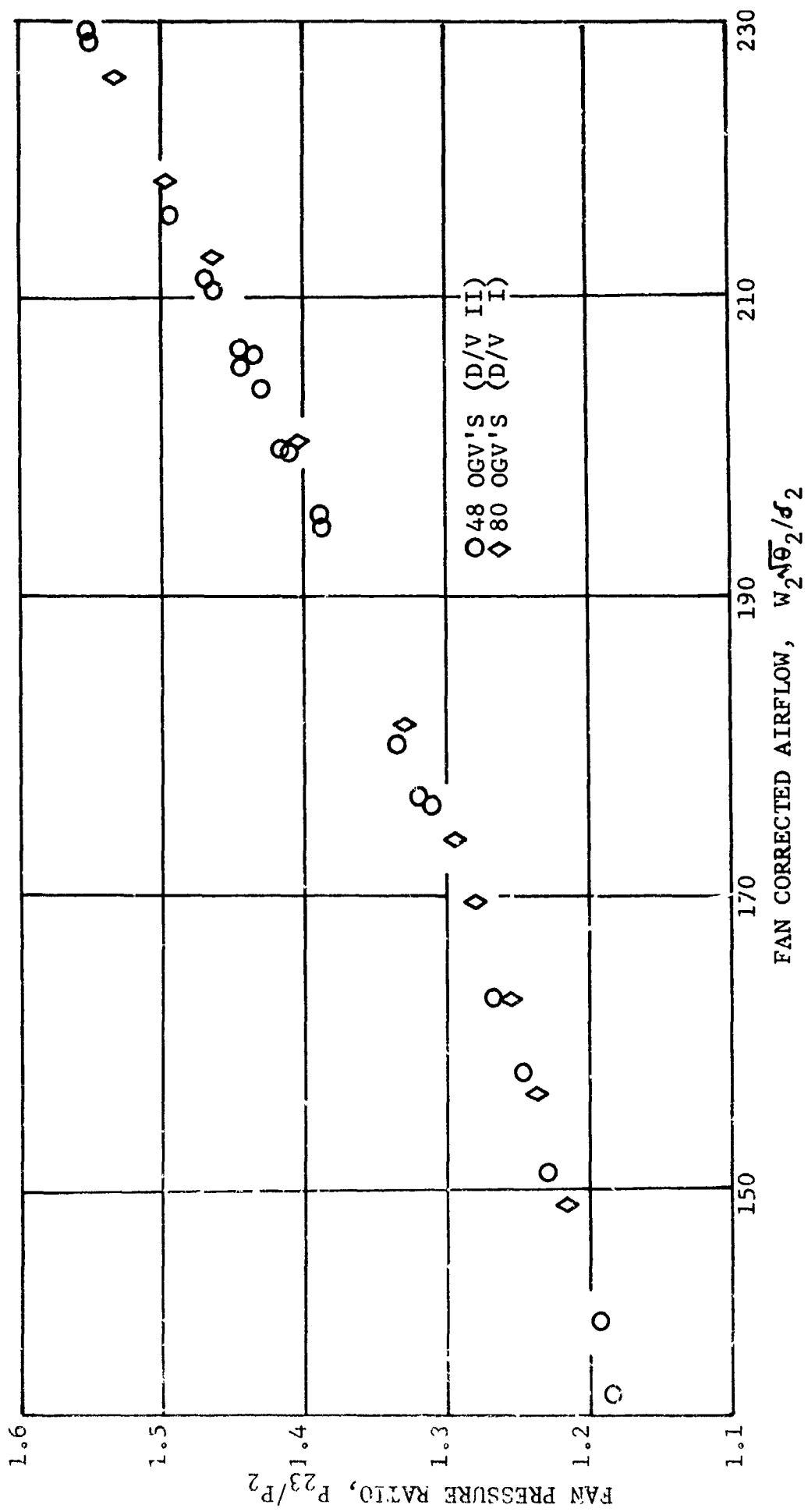


FIGURE IV-A5 FAN OPERATING MAP D/V I and D/V II COMPARISON

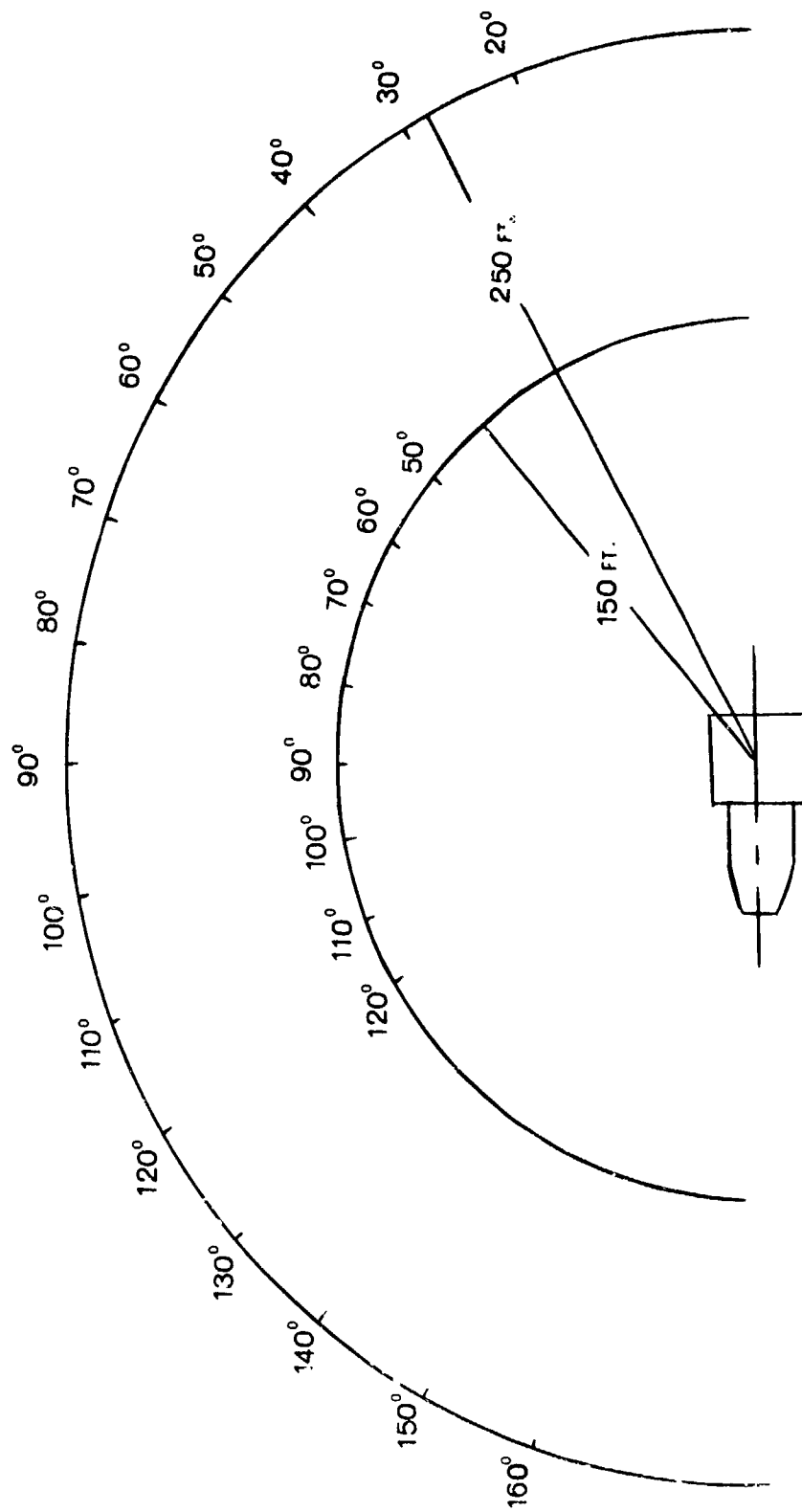


FIGURE IV-A6 D/V II TEST FARFIELD ACOUSTIC TEST MICROPHONE LOCATIONS

(B) Discussion of the Test Results. In Section II-A1 an equation was derived for the acoustic pressure of the blade passing frequency. For zero steady duct flow that equation can be expressed as:

$$P = \sum_{n=-\infty}^{\infty} \sum_{m=-\infty}^{\infty} A_{nm} \rho C^2_{nw} e^{in(\theta - t)} R_n(\lambda nmr) e^{i\beta Z}$$

This equation has the following mathematical properties:

- When β is imaginary the mode is "cutoff"
- Series convergence in m decreases the energy in successive radial modes
- Series convergence in n decreases the energy in higher order lobe numbers

In the case under consideration the test vehicles D/V I and D/V II had 38 blades and respectively 80 and 48 vanes. That is, except for the vane numbers the two tests were done on identically performing test configurations. The cutoff speeds and mode numbers for each configuration are shown in Table IV-B1. Table IV-B1 also shows that the lowest two lobe numbers generated in, respectively, the 48 and 80 vane configurations are 10 and 38, and 38 and 42. From equation II-A18, D/V I should generate 5 dB less noise at 5750 RPM and 2 dB less noise at 8500 RPM. These are within 1 dB of the measured reductions.

Figure IV-B1 shows the blade passing frequency (BPF) power level (PWL) versus tip Mach number for the two vane numbers. It is clear that at tip Mach numbers less than one that the higher vane/blade ratio results in less noise. These data were constructed from narrowband analyses of far field arc data corrected to the source.

At higher tip Mach numbers the noise reduction is not as great as at lower speeds. This suggests that the cutoff mechanism (to whatever extent it exists) is no longer functioning and/or that another noise source (other than rotor wake-stator interaction) is making a significant contribution to BPF PWL. In either case the high vane/blade ratio is seen to reduce noise in the important low tip Mach number range which is encountered at aircraft approach and power cutback engine speeds.

Figure IV-B2 presents the 2nd harmonic data. No major difference between the two configurations was expected (similar lobe number at the 2nd harmonic frequency). There has been a slight increase at low speeds and a slight decrease at high speeds with 48 vanes.

The 1/3 octave power spectrum at low speed shown in Figure IV-B3 clearly indicates the BPF PWL decrease and that no appreciable broadband noise increase has occurred with D/V II.

<u>Vane Configuration</u>	<u> n *</u>	<u>m</u>	<u>Corresponding Cutoff Speeds (RPM)</u>
48 Vanes	10	0	2320
	10	1	3135
	10	2	4111
	10	3	4648
48 and 80 Vanes	38	0	8057
	38	1	9344
	38	2	10313
	38	3	11166
80 Vanes	42	0	8866
	42	1	10189
	42	2	11183
	42	3	12067

* $|n| = 38 - KV$ - Where $V = 48$ and 80

TABLE IV-B1
Fundamental Blade Passing Frequency Cutoff
Speeds with 48 and 80 Vane Stators

BLADE PASSING FREQUENCY PWL, dB (re: 10^{-13} WATTS)

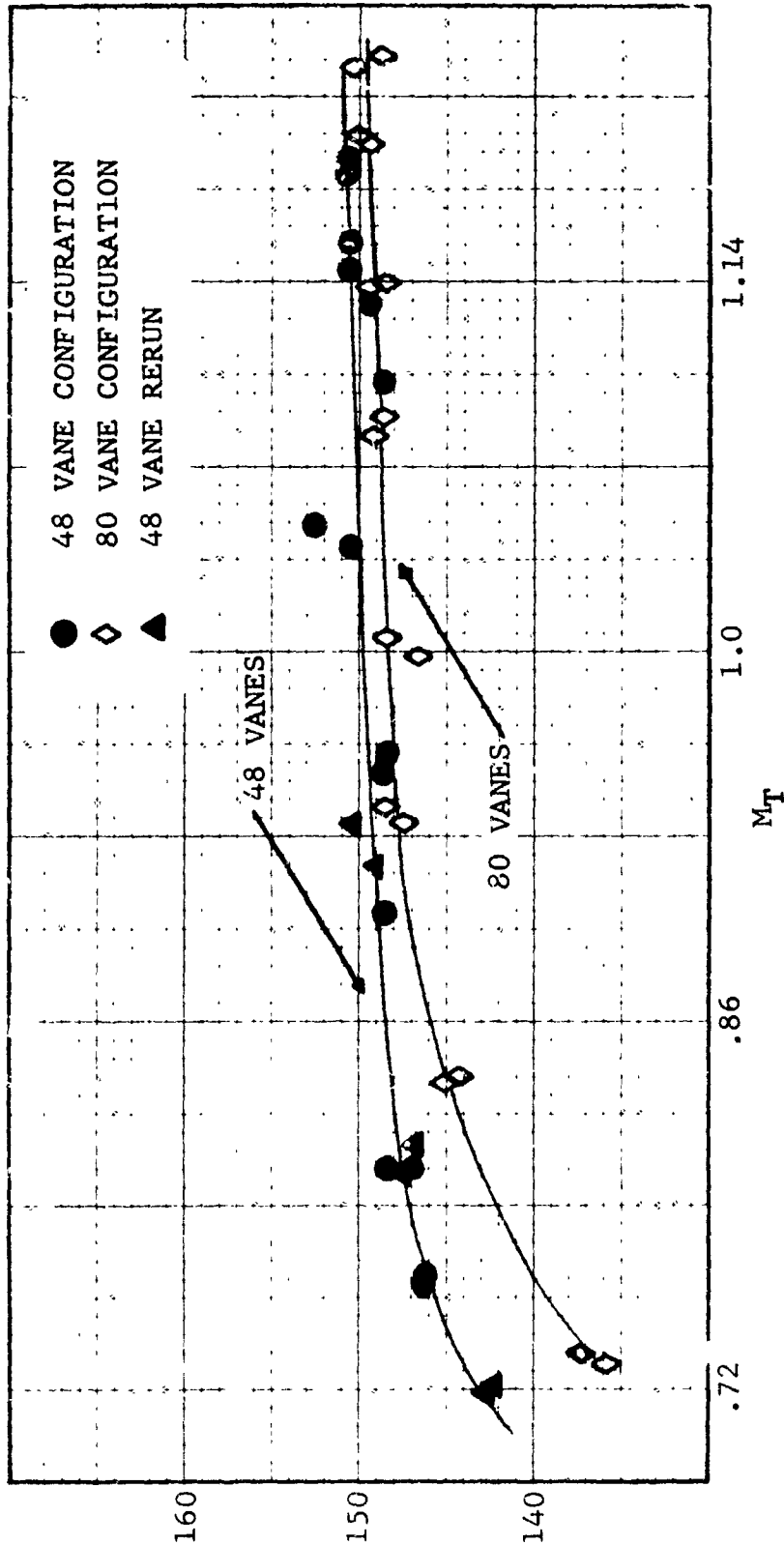


FIGURE IV-B1

COMPARISON OF FUNDAMENTAL PWL'S FROM 50-CYCLE NARROWBANDS 80-VANE CONFIGURATION VS. 48-VANE CONFIGURATION

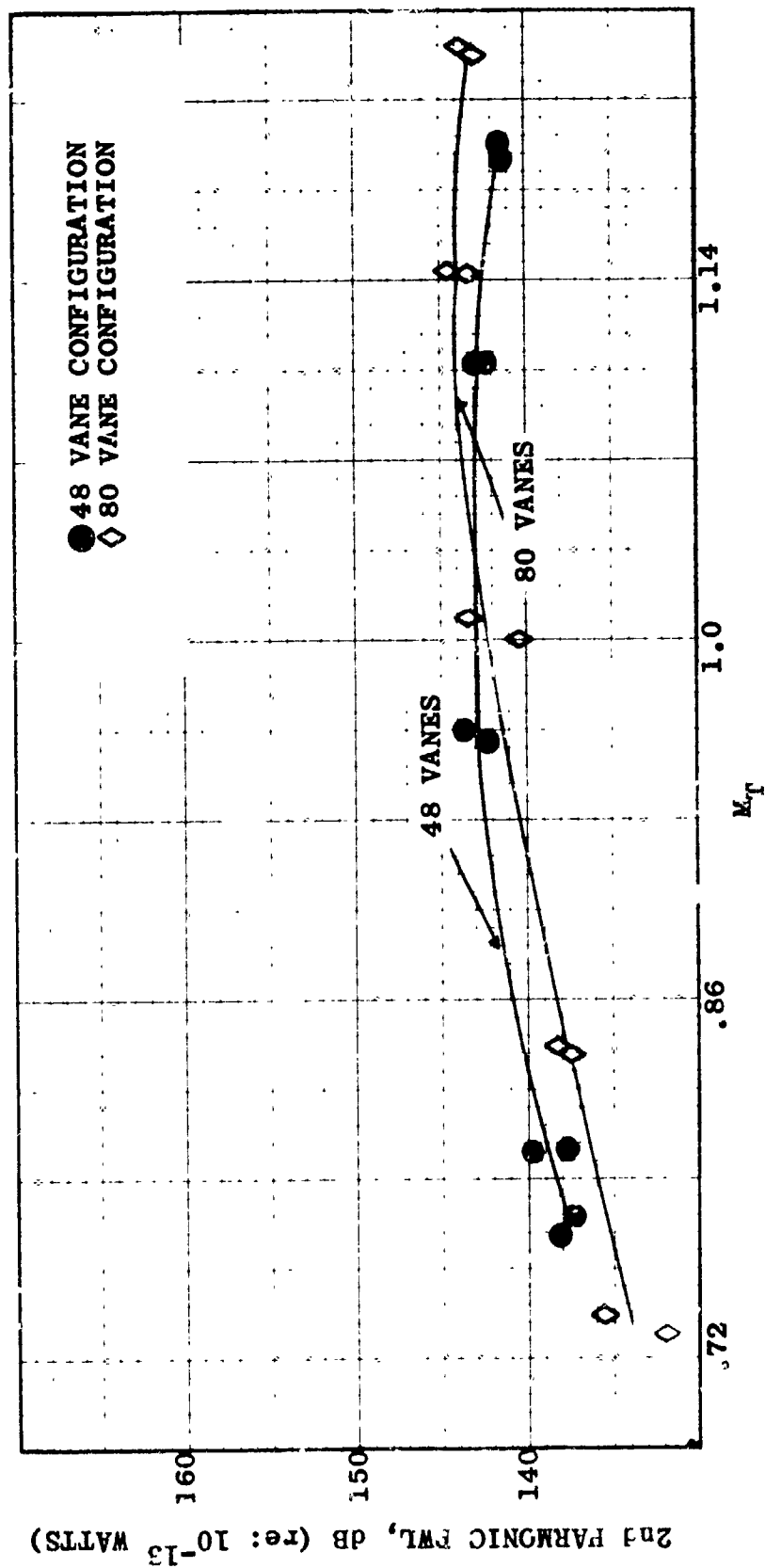


FIGURE IV-B2
2nd HARMONIC PWL'S FROM 50 CYCLE NARROW AND 80 VANE AND 80 VANE CONFIGURATIONS

1/3 OCTAVE POWER LEVEL db (re:10⁻¹³ WATTS)

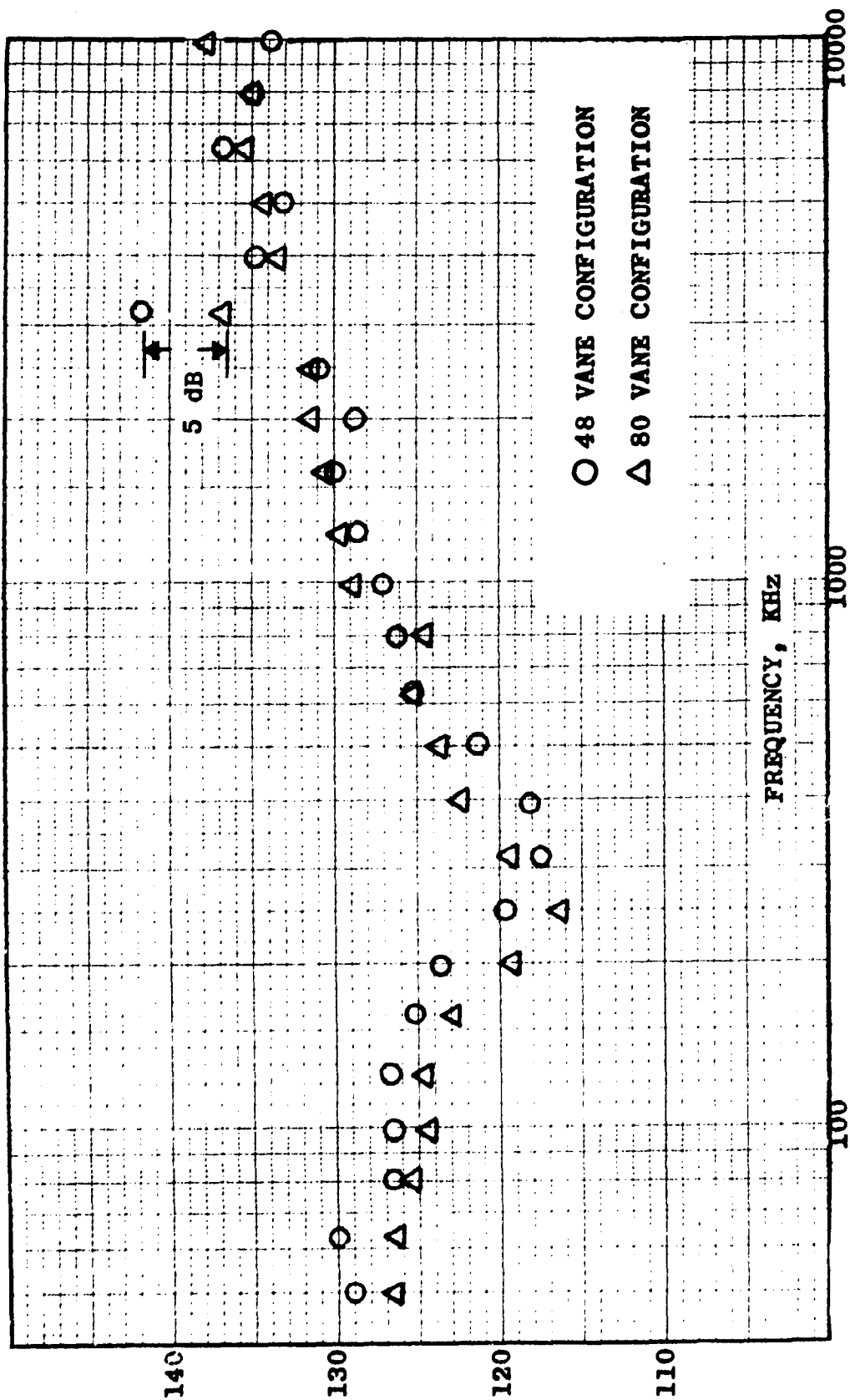


FIGURE IV-B3 COMPARISON OF 1/3 OCTAVE POWER SPECTRUM FOR 48-VANE AND 80-VANE VEHICLES. (5089 RPM.)

The BPF and second harmonic directivities at low and high speeds are shown in Figures IV-B4 through IV-B7. The low speed BPF directivity (Figure IV-B4) indicates noise reduction at most locations around the arc, particularly in the aft quadrant. The directivity of BPF at high speed shows, as did the BPF PWL of Figures IV-B1, little change in BPF SPL.

The second harmonic curves, Figures IV-B5 and IV-B7, show almost no change at low speeds and a slight increase in second harmonic level with 80 vanes at high speed probably due to the lobe pattern ($80 - 2 \times 38 = 4$) present on this configuration.

Figures IV-B8 through IV-B11 represent narrowband data at 5750 rpm for 110 and 120 degree far field angles for the two OGV configurations. These data have not been corrected for atmospheric conditions and cannot be compared directly. However, the relation of the tone content of the spectrum with respect to the broadband background noise gives an indication of the tone reduction obtained with 80 OGV's. For example, on Figures IV-B8 and IV-B10 for 48 vanes the BPF tone (at 3600 Hz) has a greater signal (tone) to noise (broadband) ratio than for the 80 vane vehicle shown in Figures IV-B9 and IV-B11.

In summary, the high vane to blade ratio has been shown to reduce BPF noise generation, particularly at subsonic rotor tip speeds.

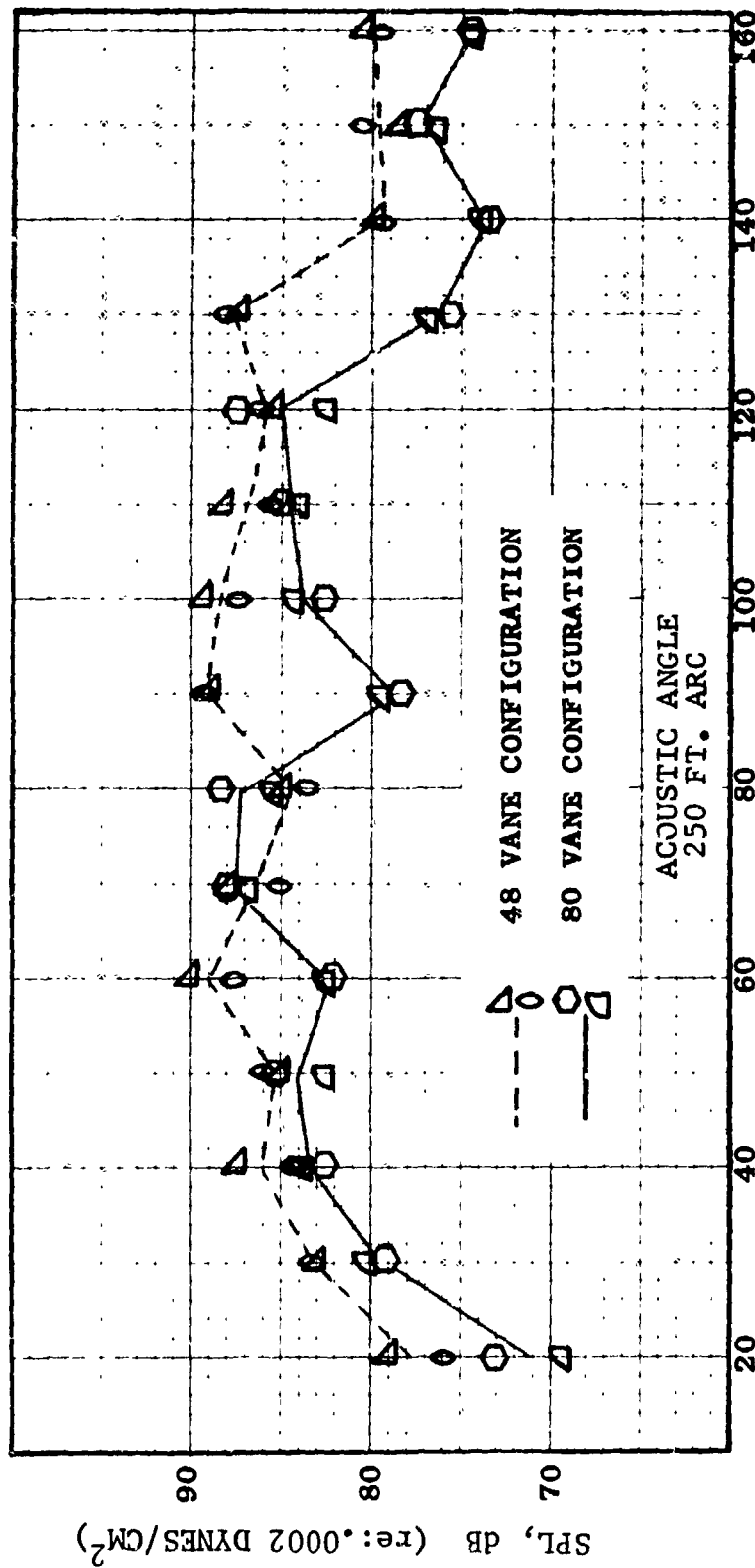


FIGURE IV-B4
COMPARISON OF BLADE PASSING FREQUENCY ARC SPL FOR 48 OGV AND
80 OGV VEHICLES - 5750 RPM

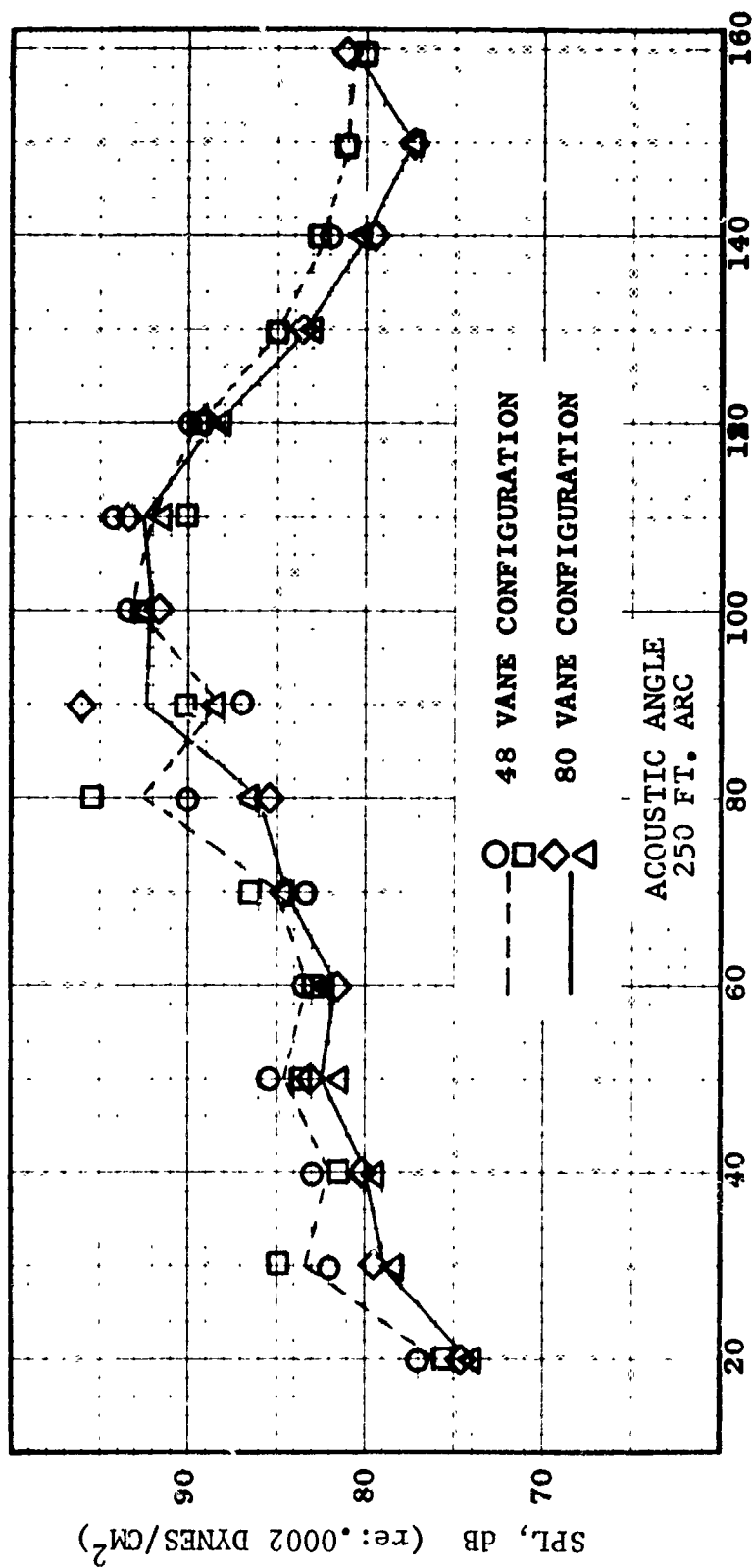


FIGURE IV-B5
COMPARISON OF BPF ARC SPL FOR 48 OGV AND 80 OGV VEHICLES -
8500 RPM

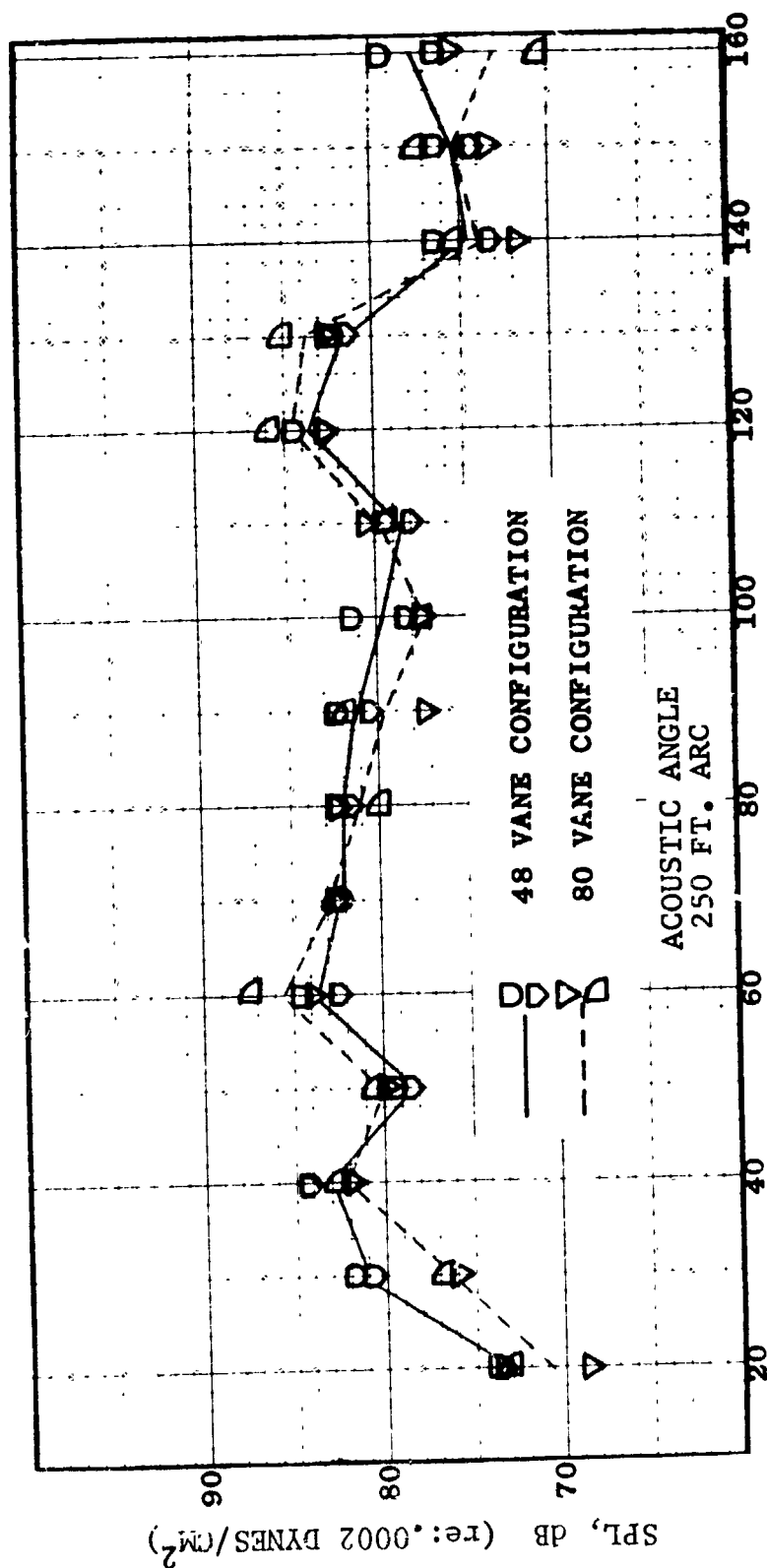


FIGURE IV-B6
COMPARISON OF 2nd HARMONIC ARC SPL FOR 48 OG AND 80 OG
VEHICLES - 5750 RPM

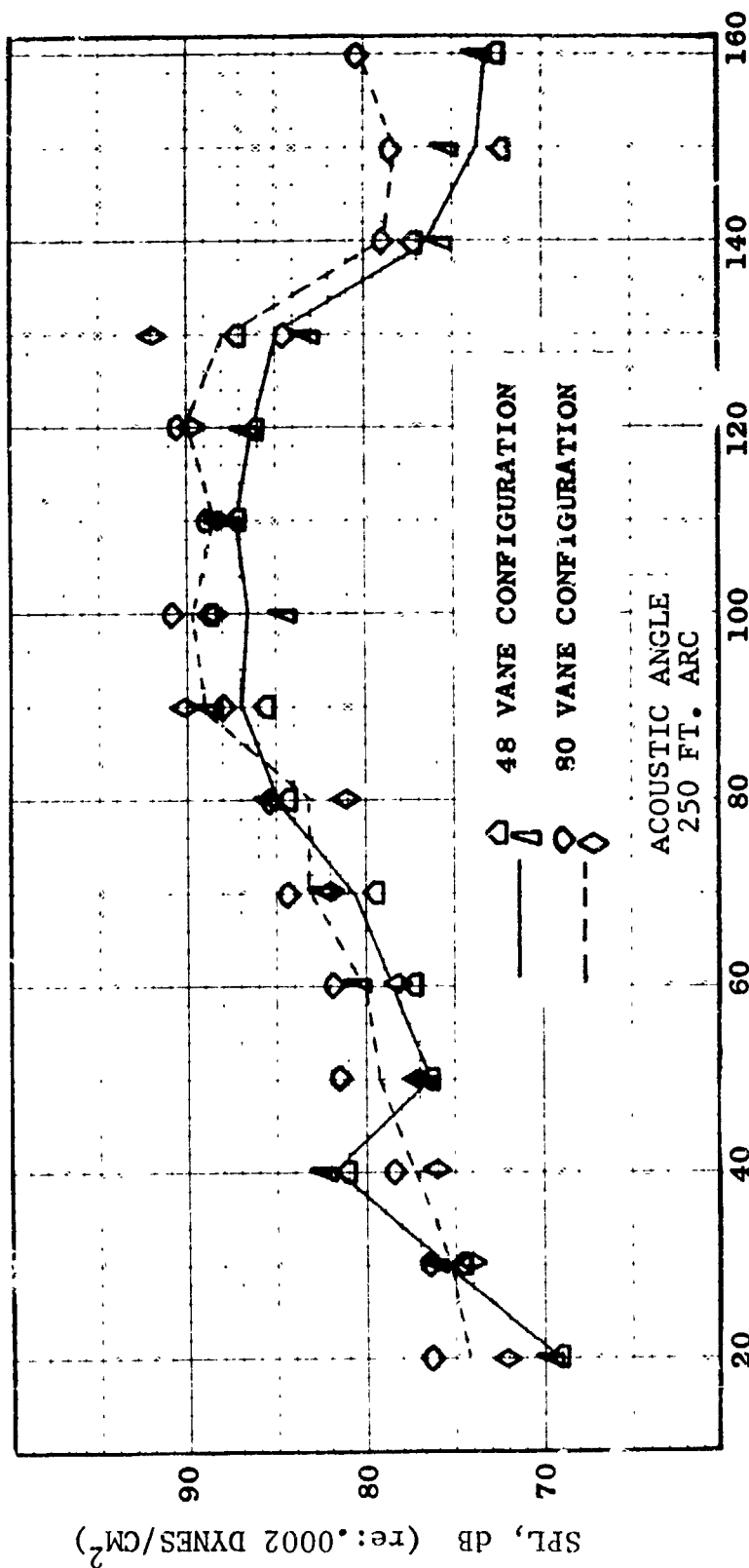


FIGURE IV-B7
COMPARISON OF 2nd HARMONIC ARC SPL FOR 48 OG V AND 80 OG V
VEHICLES - 8500 RPM

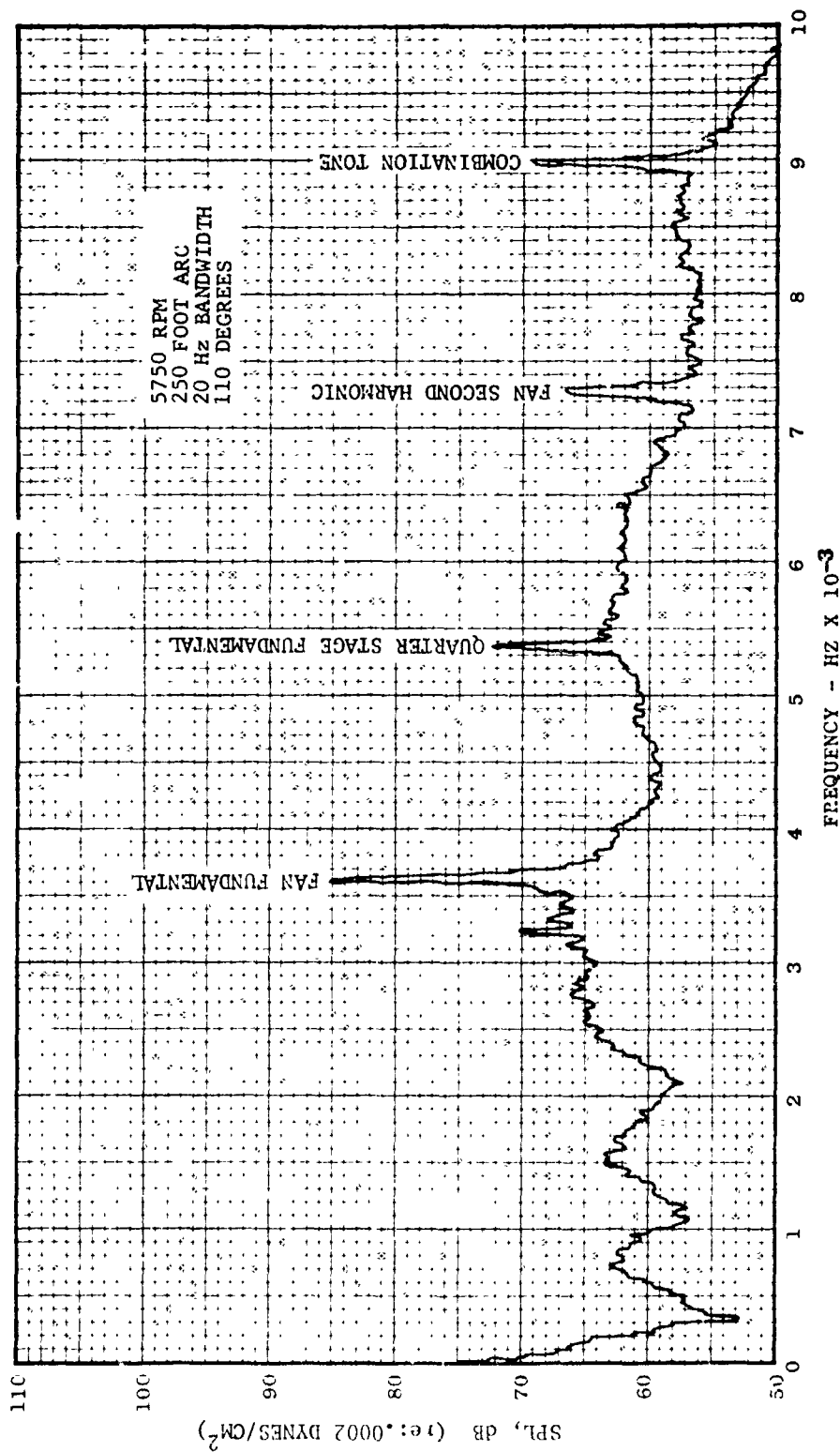


FIGURE IV-B8 NARROWBAND ANALYSIS OF 48 OGV VEHICLE FARFIELD DATA

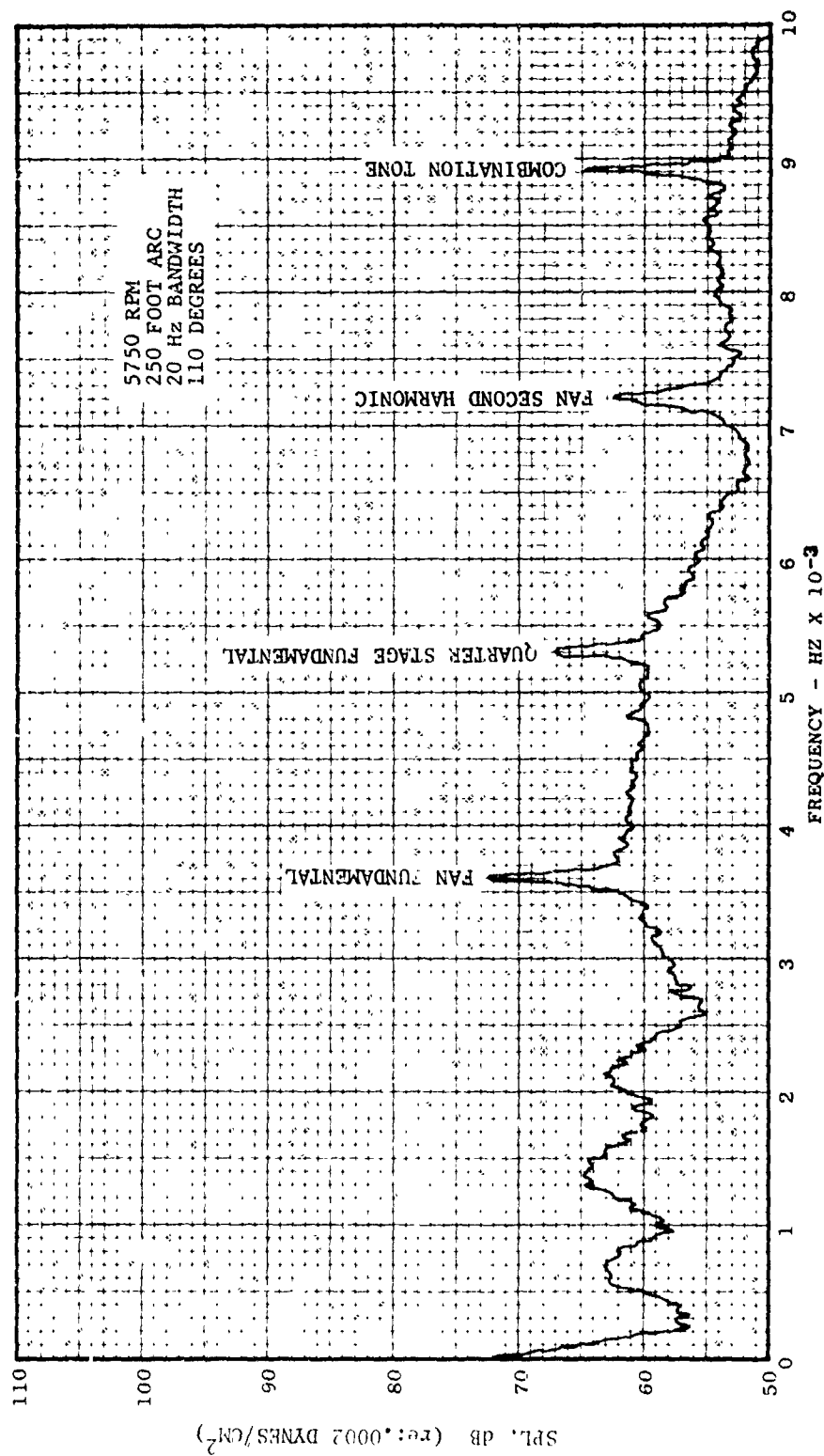


FIGURE IV-B9
NARROWBAND ANALYSIS OF 80 OGV VEHICLE FARFIELD DATA

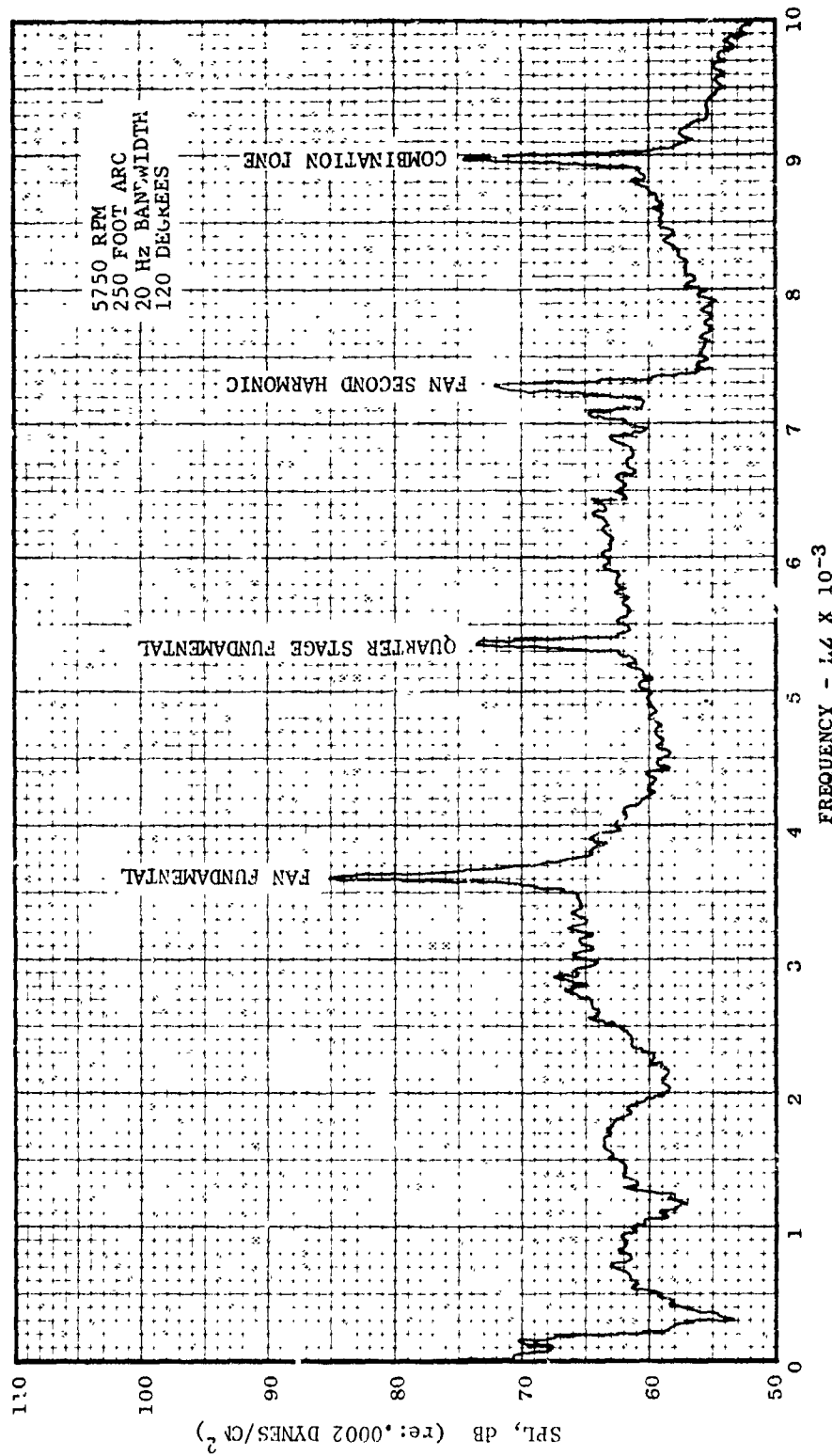


FIGURE IV-B10 NARROWBAND ANALYSIS OF 48 OGV VEHICLE FARFIELD DATA

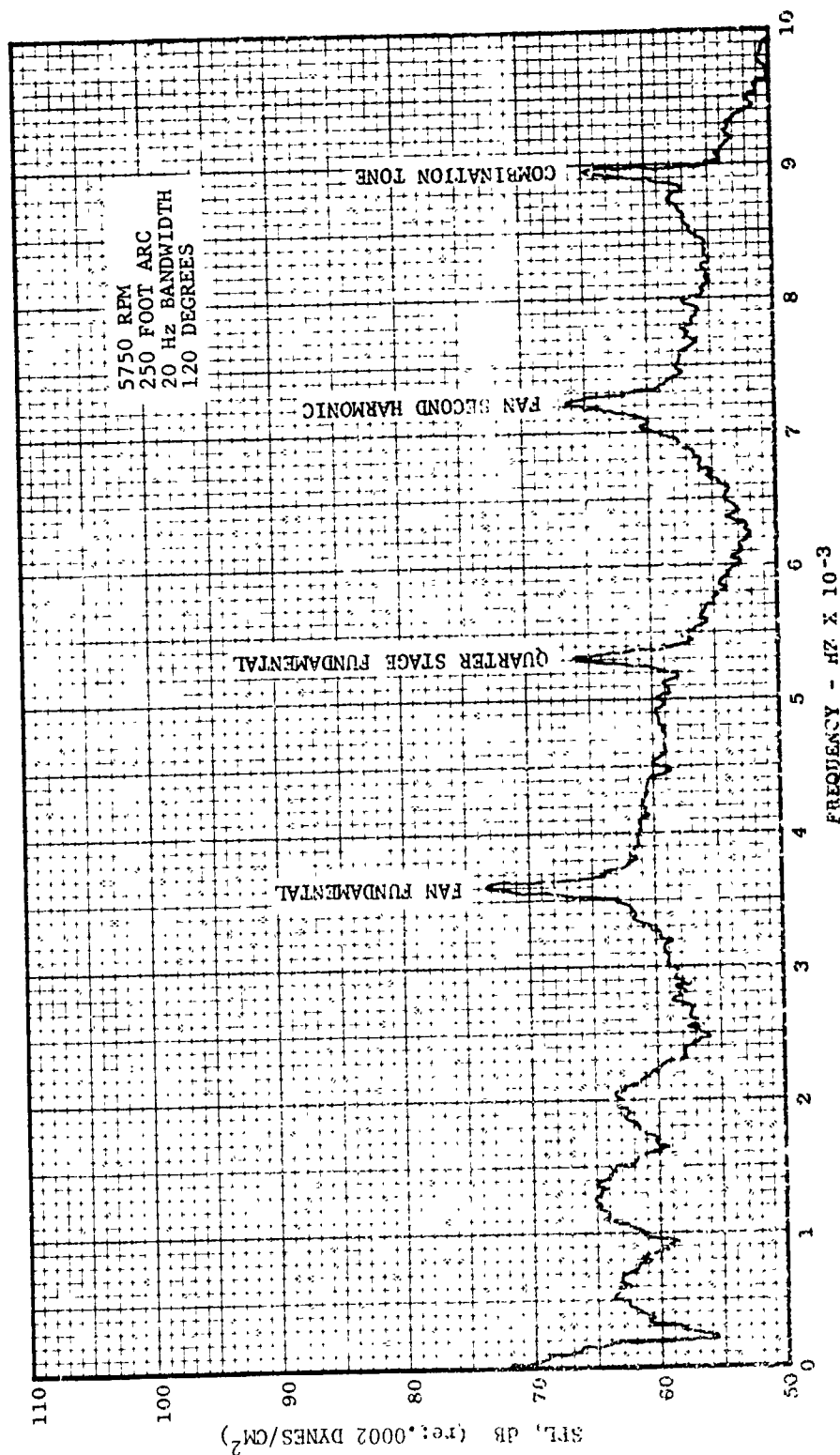


FIGURE IV-B11
NARROWBAND ANALYSIS OF 80 OGV VEHICLE FARFIELD DATA

V. EXPERIMENTAL INVESTIGATION OF IGV VS. NO IGV FAN

(A) Vehicle and Test Descriptions. Previous tests conducted in order to determine the effects of IGV's on fan noise have been done in a rather crude manner. A set of IGV's would be placed arbitrarily on a vehicle designed for operation without IGV's, and acoustic test data would be taken, for comparison to no-IGV data. The fallacy in this procedure is that addition of the IGV's alters the fan performance; the vehicles being compared thus differed in performance as well as IGV configuration.

A new fan vehicle was designed, in order to permit the determination of the acoustic effect of IGV's versus no IGV's on fans having essentially the same performance. The new fan (Figures V-A1 and 2) was similar to the reduced-number-of-OGV's test fan, which was used as a baseline. It had the same dimensions, rotor blade and OGV numbers, etc. Seventy-two inlet guide vanes (Figure V-A3) were added. The IGV's extended to about 75% of the rotor span, since the lower portion of the fan rotor did not require preswirl. Also, since the far greater part of the noise is generated at, and transmitted from, the upper portion of the rotor, the region of the fan which was most important from an acoustic standpoint was affected by these IGV's. The small inner stage again remained unchanged.

In order to achieve the same performance (and stall margin) as the IGV-less fan, it was necessary to design a new set of rotor blades (Figure V-A4) and OGV's (Figure V-A5), and to increase rotor tip speed by less than 2.5%. The OGV was designed with 15° preswirl at the tip and the rotor redesigned accordingly. Pertinent comparisons between the two fans are listed below.

	<u>IGV-less Fan (D/V II)</u>	<u>IGV Fan (D/V III)</u>
No. of rotor blades	38	38
No. of OGV's	48	48
No. of IGV's	--	72
Inner Stage	-----Common-----	
Rotor-IGV Spacing	--	2 OGV chords
Des. Pt. Rotor Tip Mach No.	1.275	1.305
Des. Pt. Tip Relative Mach No.	1.371	1.253
Des. Pt. Pressure Ratio	1.617	1.617
Des. Pt. Fan Weightflow (lb/sec)	244	244
Diffusion "D" factor		
Hub	.284	.256
Pitch	.505	.489
Tip	.359	.398
Work Coefficient -		
Hub	1.849	1.7663
Pitch	0.964	0.9478
Tip	0.6284	0.6004



Reproduced from
best available copy.



FIGURE V-A1 IGV - VEHICLE (D/V III)

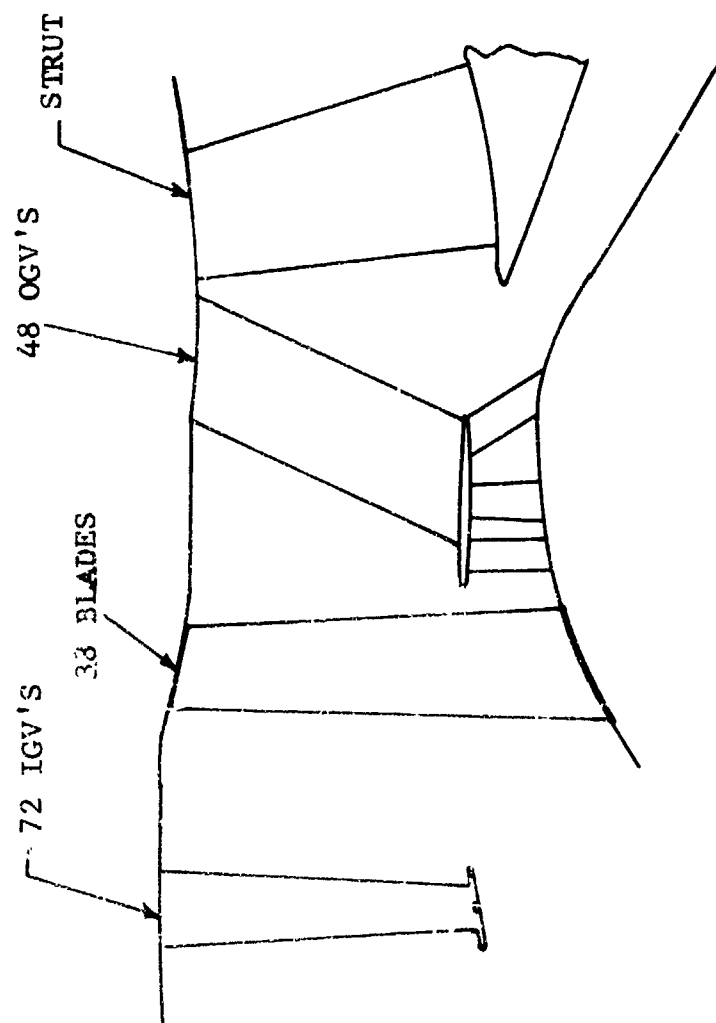
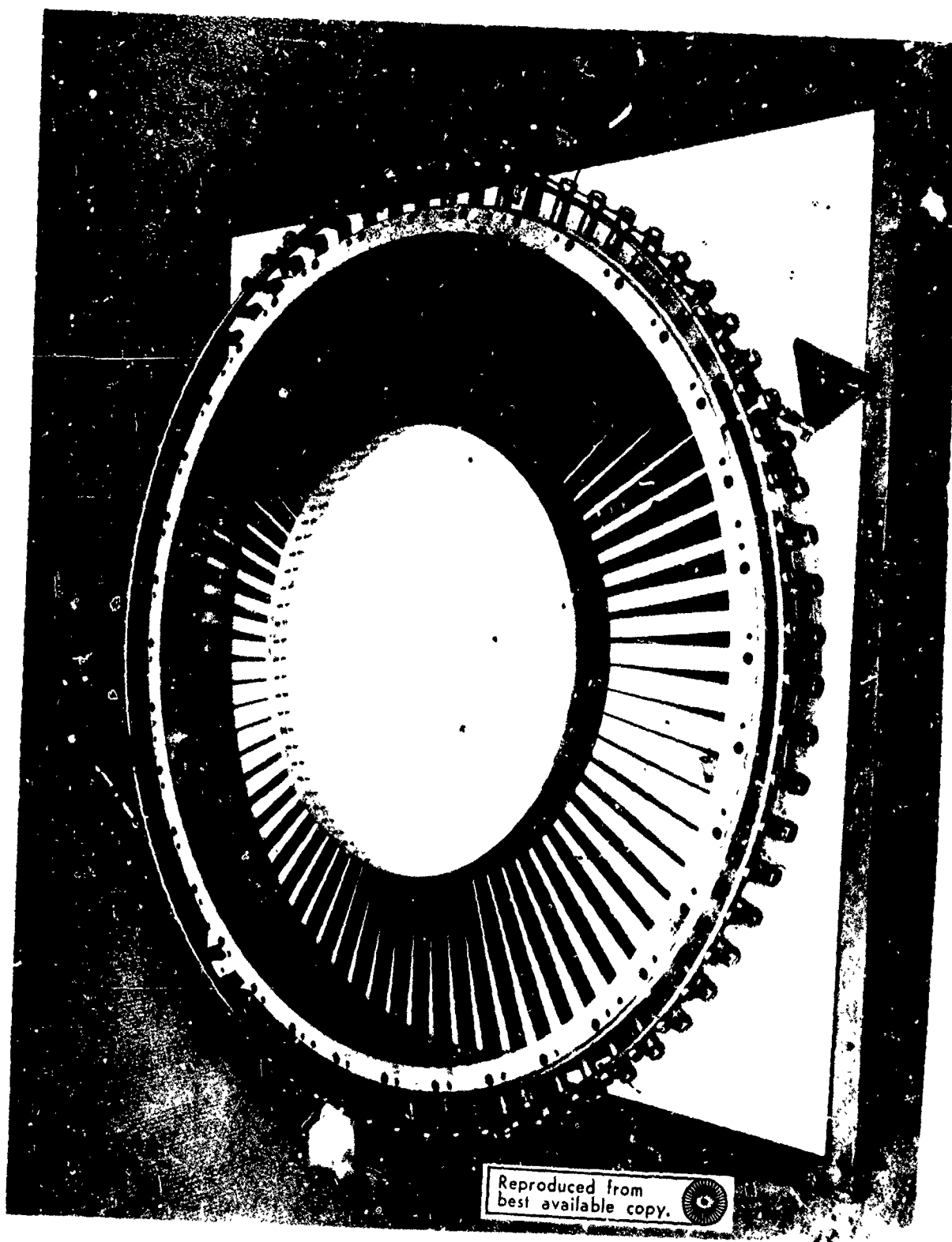


FIGURE V-A2 SCHEMATIC OF IGV TEST VEHICLE (DV III)



Reproduced from
best available copy.



FIGURE V-A3 IGV FOR D/V III

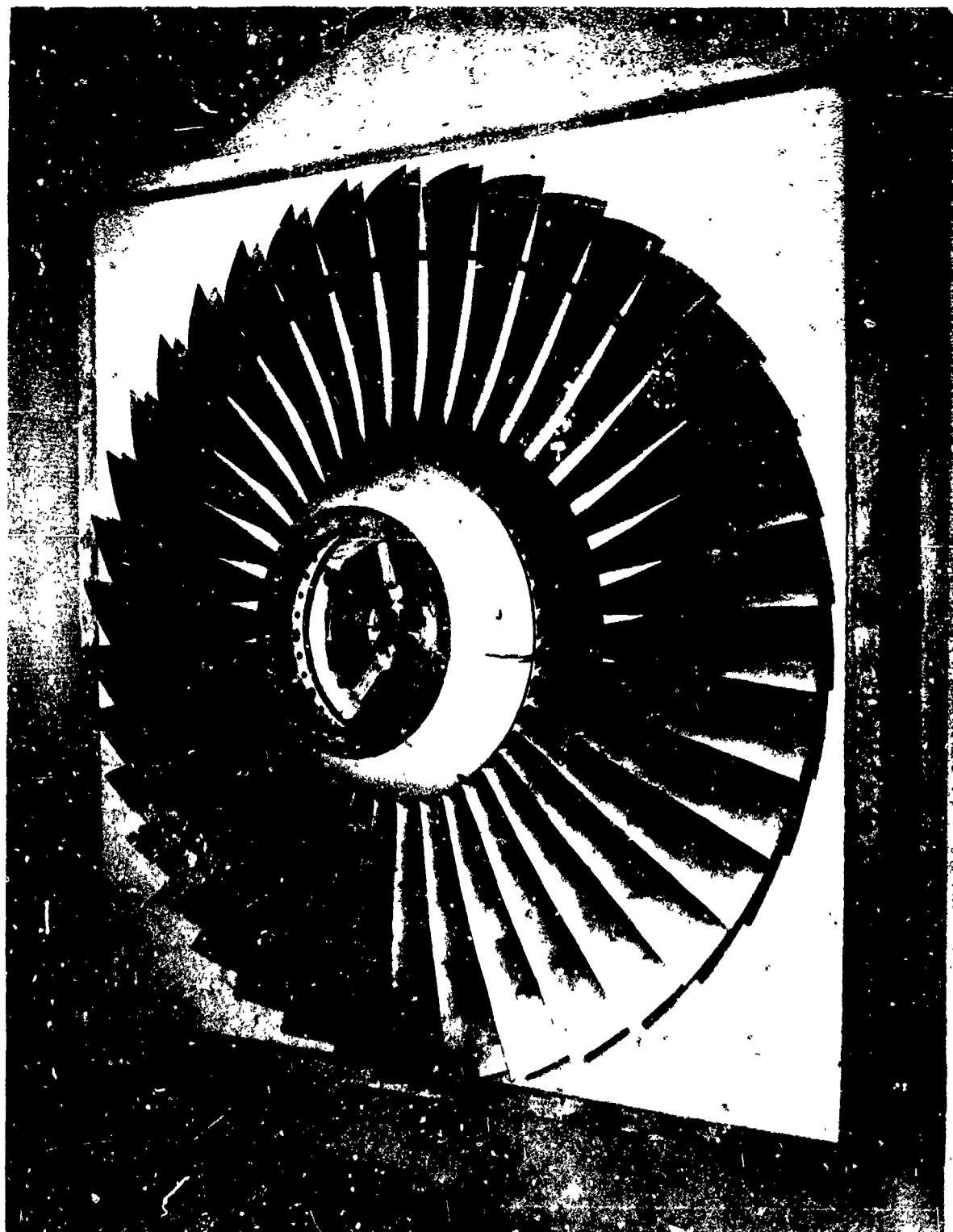


FIGURE V-A4 ROTOR FOR D/V III)

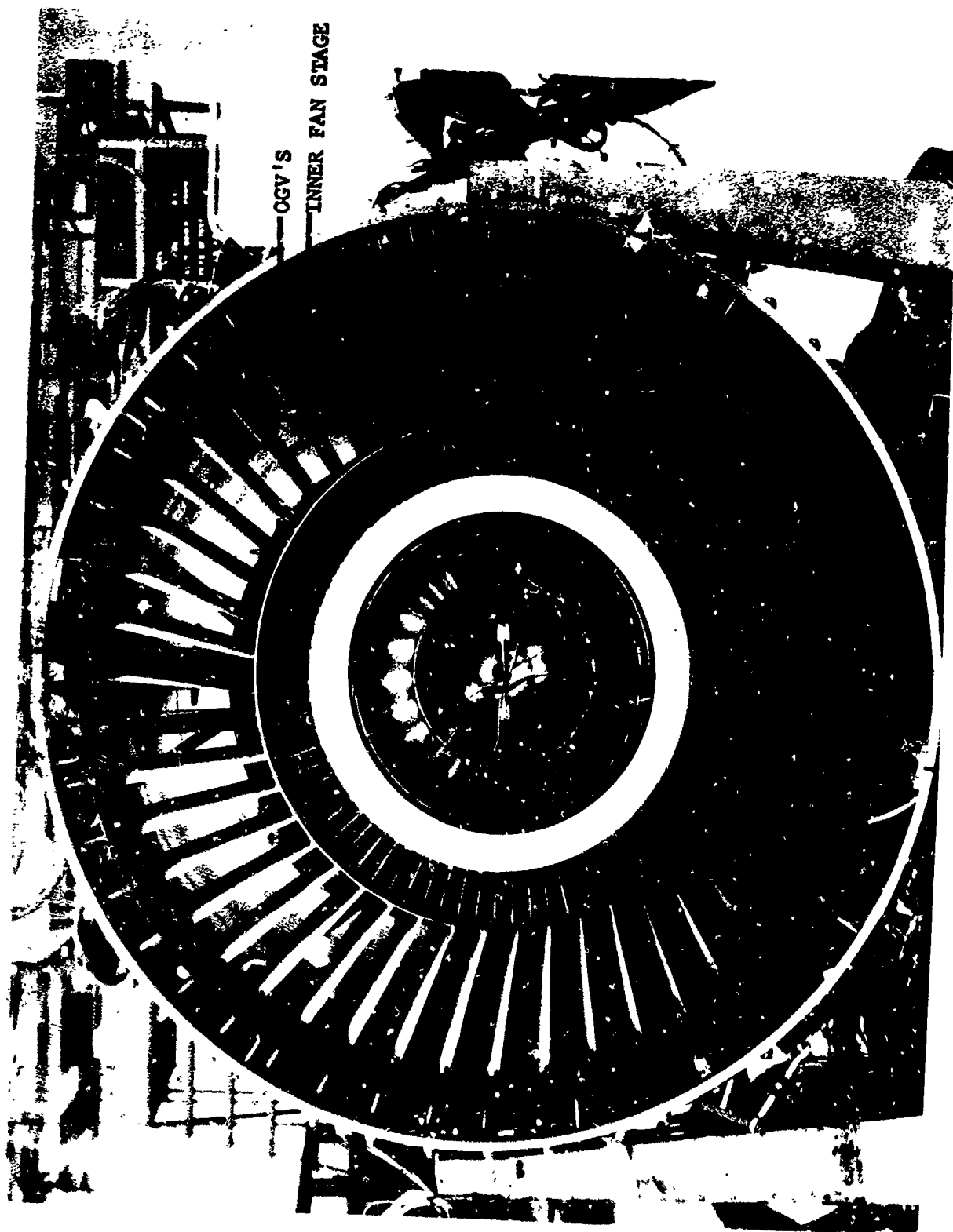


FIGURE V-A5 OGV'S AND INNER FAN STAGE

The key goal was to maintain the blade loading as closely as possible. With the small increase in tip speed, the tip loading did increase, but the pitchline and hub loadings actually decreased compared to the IGV-less fan. Spanwise, the average hub-tip loadings were essentially the same. With regard to work coefficient, the higher tip speed of the IGV fan caused only a slight decrease, as compared to the IGV-less fan. The net loadings of the two fans were thought to be close enough to provide a direct comparison on the basis of equivalent loading.

Data recorded from performance tests of the two fans indicates that they were, indeed, almost identical in performance. Figure V-A6 compares the two configurations on the basis of fan weight flow versus percentage of fan speed; Figure V-A7 compares their operating line data.

Acoustic testing, identical to that described for the IGV-less vehicle in Section IV, was conducted on the IGV fan. The two sets of data were then compared, to determine the effects of the IGV's on noise generation and transmission.

The IGV's were installed in such a manner that their incidence angle could be varied. As an extension of the previous study, two further sets of tests were run, in which the IGV's were set at "off-design" angles. Specifically, the two settings employed were 9 degrees to either side of the nominal angle. Comparison of the data from these tests with that from the nominal incidence angle tests allowed a determination of the acoustic effects of IGV incidence angle variations.

(B) Discussion of Test Results. This test sequence had the following objectives:

- To test theoretical prediction.
- To quantify noise generation changes with IGV's.
- To identify the effects of opening and closing the IGV's.
- To examine the effects of IGV's on MPT propagation.

With regard to the first objective, the theoretical work done in Section II-A predicts the curves of Figure V-B1. The prediction shows the difference in blade passing frequency noise generation for the IGV fan and the no IGV fan at various blade row spacings. At wide IGV-Rotor spacing (greater than about .75 IGV chords) the difference between the two configurations remains essentially constant for both inlet and exhaust noise. The inlet noise shows less than one decibel increase with the IGV, but a more than two decibel increase is predicted in the exhaust.

Figure V-B2 shows the blade passing frequency (BPF) power level (PWL), as derived from 1/3 octave data, versus tip Mach number. There is no discernible trend; i.e., both configurations are producing the same noise. Figures V-B3 and V-B4 show the corresponding directivity of the BPF at, respectively, 6150 and 7600 rpm. At the lower speed the aft quadrant BPF Sound Pressure Level has increased with the addition of IGV's. The inlet level, in fact, shows a decrease. This decrease is most likely due to the attenuating effect of the noise passing through the IGV's. At higher speeds (Figure V-B4) these effects have been washed out and both vehicles are producing approximately the same BPF levels.

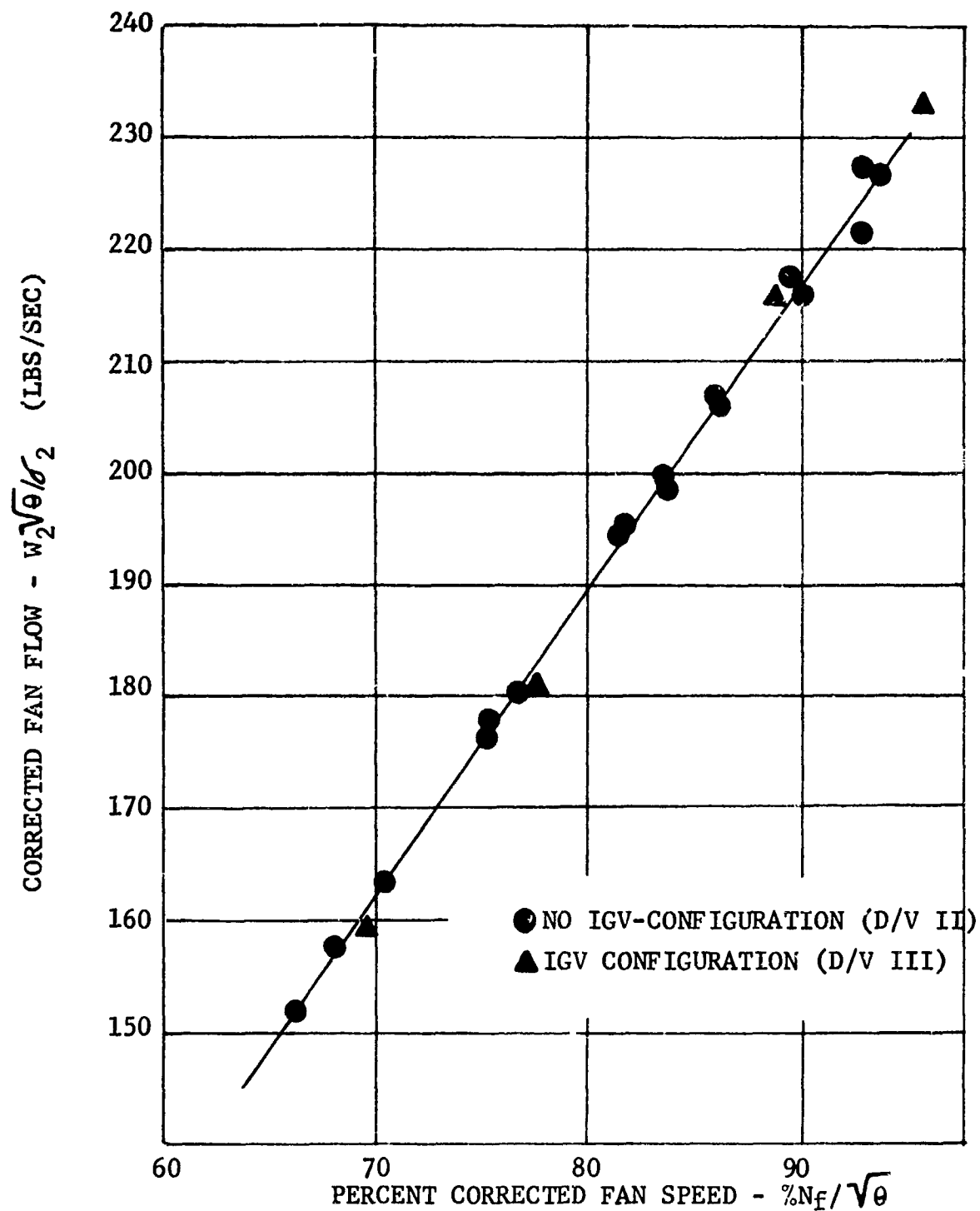


FIGURE V-A6

COMPARISON OF D/V II AND D/V III WEIGHT FLOW
vs. SPEED

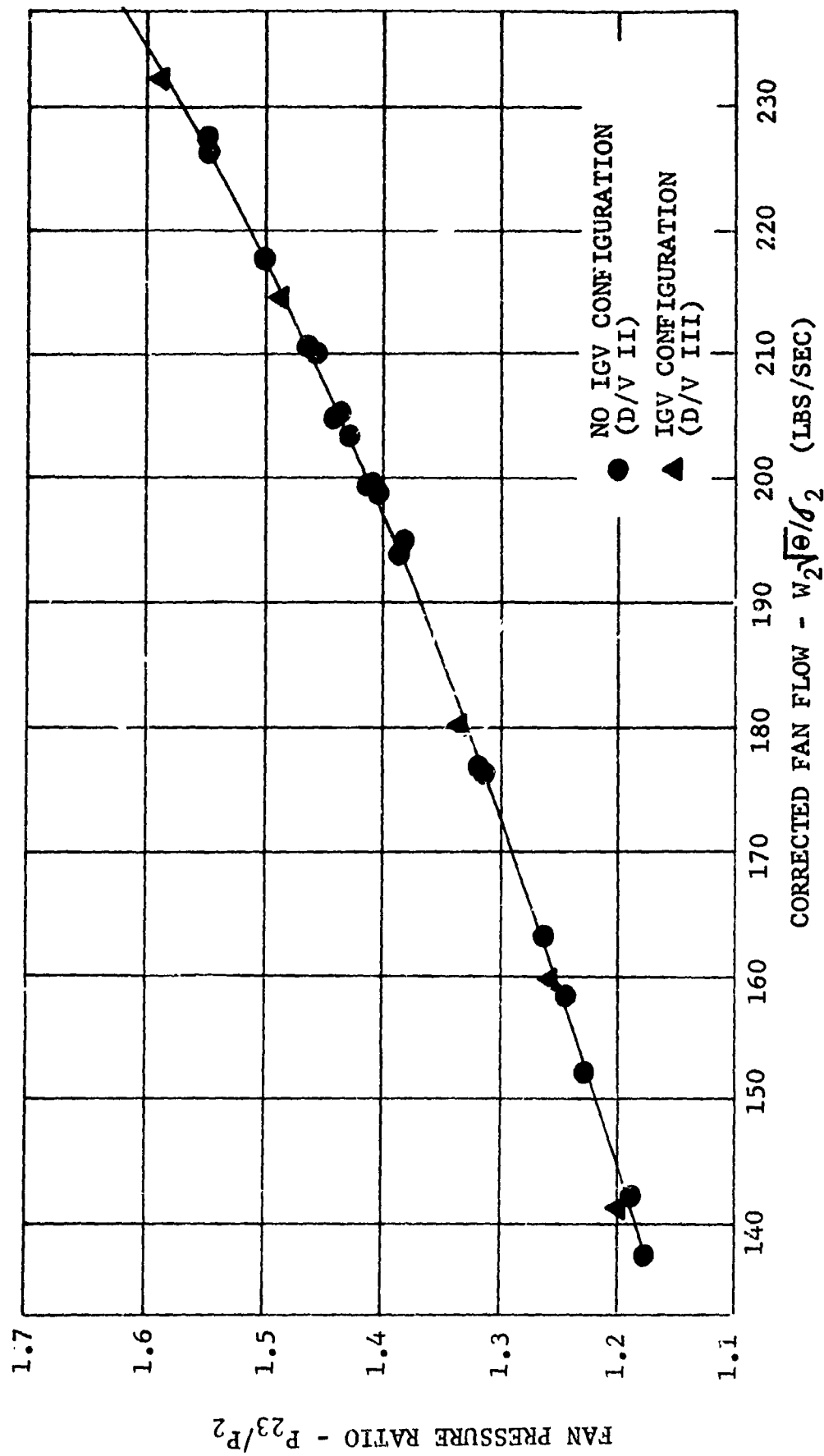


FIGURE V-A7 COMPARISON OF D/V II AND D/V III OPERATING LINE DATA

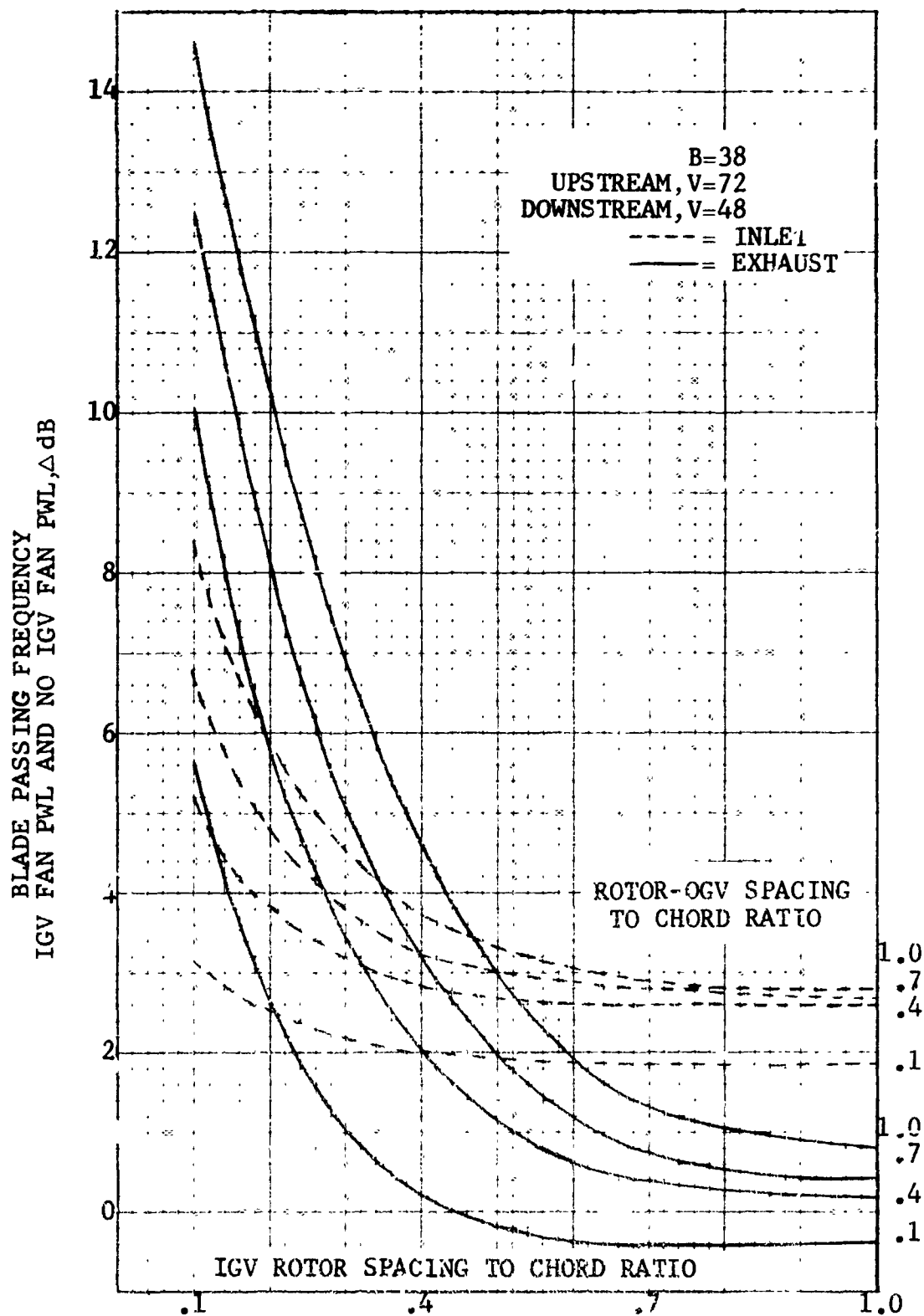


FIGURE V-B1 COMPARISON OF IGv AND NO IGv FANS WITH VARIABLE ROTOR-STATOR SPACING

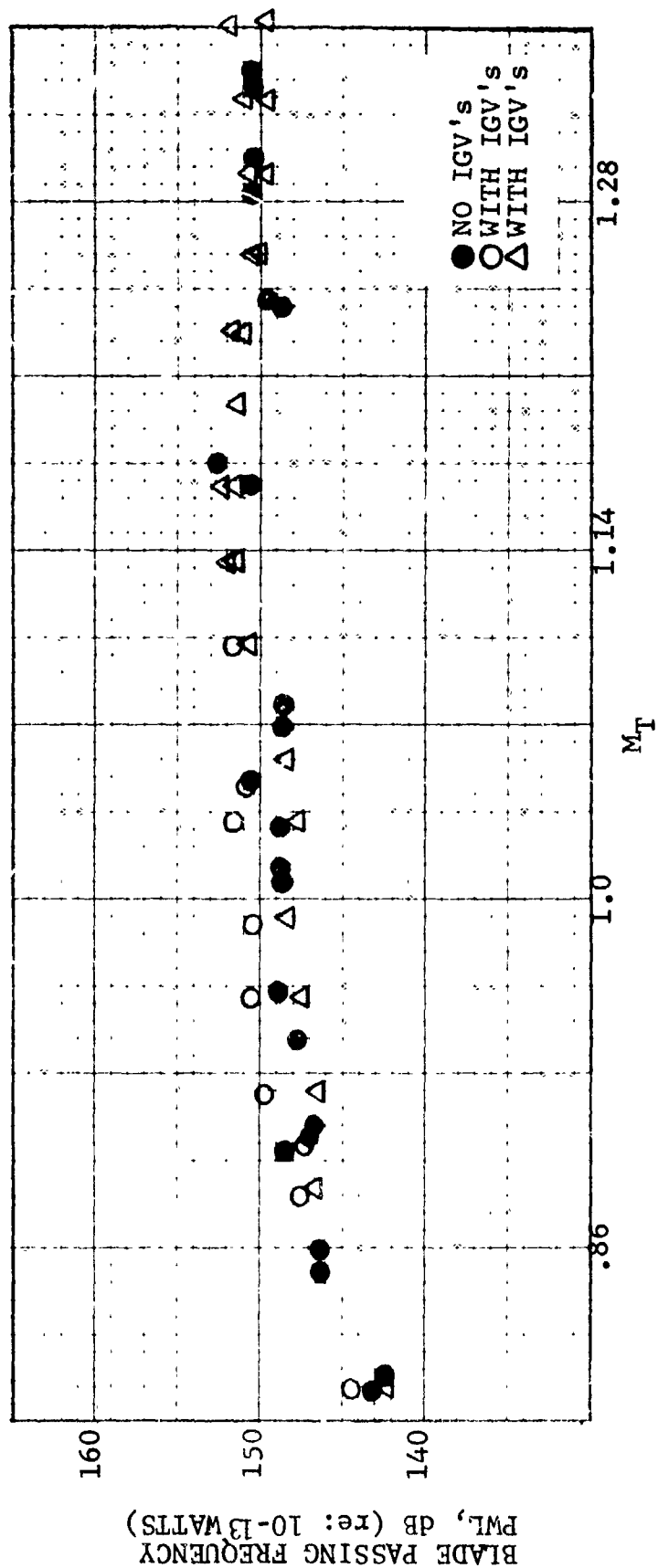


FIGURE V-B2 COMPARISON OF FUNDAMENTAL FWL IGV AND NO IGV VEHICLES

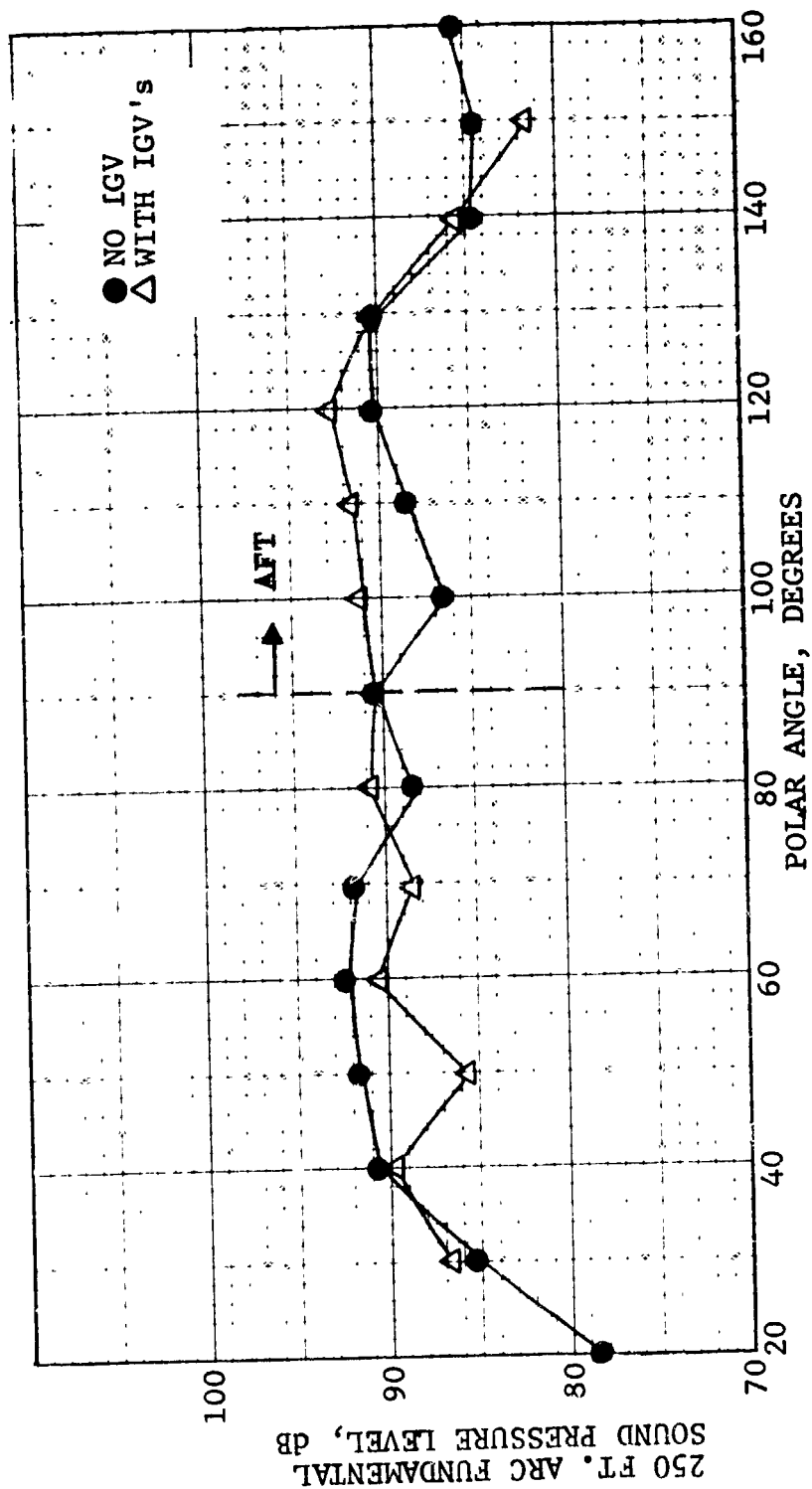


FIGURE V- B3 BLADE PASSING FREQUENCY DIRECTIVITY COMPARISON IGV AND NO IGV VEHICLES - 6150 RPM CORRECTED SPEED

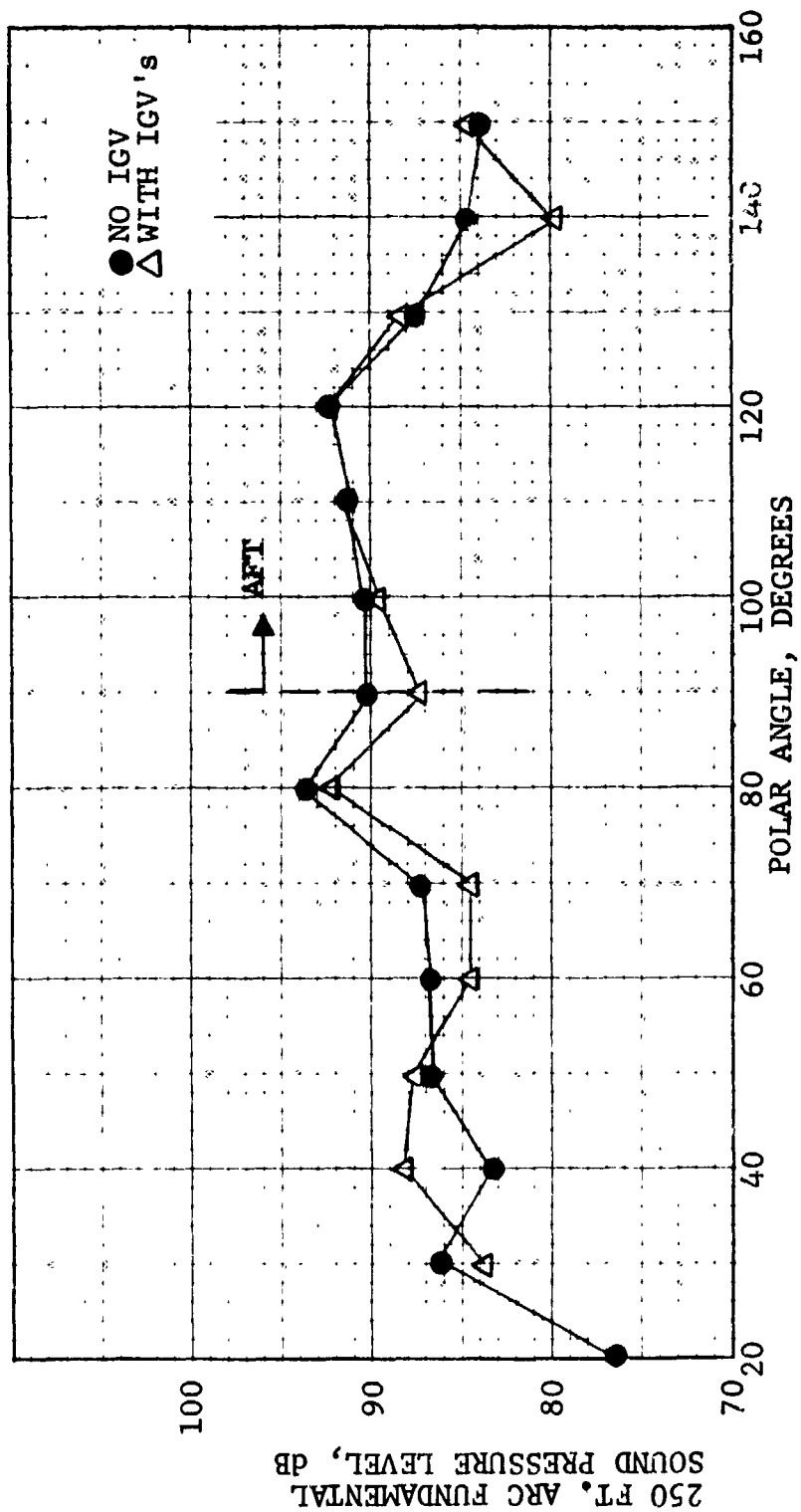


FIGURE V-B4 BLADE PASSING FREQUENCY DIRECTIVITY COMPARISON IGV AND NO IGV VEHICLES - 7600 RPM CORRECTED SPEED

Figures V-B5 and V-B6 are the 1/3 octave source power spectra at 6150 and 7600 rpm. Figure V-B5 shows the BPF PWL (4 KHz center frequency band) to be equal; however there is an increase in broadband noise with IGV's. This increase is probably due to the increase in turbulence level of the air entering the rotor due to the IGV wakes. The increased turbulence results in random fluctuations of rotor lift which manifest themselves in random (broadband) noise. At higher speeds a significantly opposite effect has occurred. At high speed the multiple pure tone (MPT) content of the power spectra has decreased reducing the noise at frequencies below the BPF significantly (See Section II-D). This reduction is due primarily to the "blocking" effect of the IGV's. There are also secondary effects associated with the change in rotor aerodynamic loading although none of these effects are thought to be significant.

Figures V-B7 and V-B8 are the resulting PNL directivities for the two speeds. At the lower speed the aft arc PNL has increased while the front is essentially unchanged. At high speed, however, (Figure V-B8) a decrease in front quadrant PNL has occurred with no significant change in the aft quadrant. The inlet noise decrease is important since inlet wall area available for acoustic treating is limited and, in some instances, an inlet acoustic splitter may be the only method of obtaining significant inlet noise reduction. In the exhaust, on the other hand, there is usually more treatment area available which can minimize the exhaust noise increase at low speeds.

As previously noted (Section V-A) the 72 IGV's were variable; i.e., their stagger could be changed. Tests were run with the IGV's restaggered 9 degrees open and 9 degrees closed. The closing of the IGV's decreases the rotor's aerodynamic loading; while the loading increases as the IGV's are opened. Opened IGV's (Figure V-B9) show small increases in BPF PWL: particularly at low speed. Thus, increasing rotor loading has increased the BPF noise. The power spectra at 7900 rpm shown in Figure V-B10 shows small increases in broadband noise with the IGV's opened although there appears to be no MPT increase.

Closed IGV's had no effect transonically and caused small decreases at low speeds (Figure V-B11). Figures V-B12 and V-B13 show the 1/3 octave power spectra at, respectively, 5750 and 6900 rpm. Within the data scatter there is little change in noise at the low speed. At the higher speed there appears to be a noise decrease over much of the spectrum. Figures V-B14 and V-B15 are comparisons of the 9° closed IGV and the no IGV data. The BPF PWL shows no discernible increase over the operating speed range. The 7900 rpm power spectra shown in Figure V-B15 shows a small BPF PWL increase, a significant decrease in MPT level, and no appreciable broadband noise increase.

In summary, the IGV configuration has been shown to decrease MPT levels at the expense of small increases in BPF SPL in the aft quadrant and in broadband noise. Opening the IGV's (loading the rotor) increased noise while closing the IGV's brought broadband noise levels down to the no IGV levels.

Test data on D/V III is tabulated in appendices C, D and E for the 3 IGV settings.

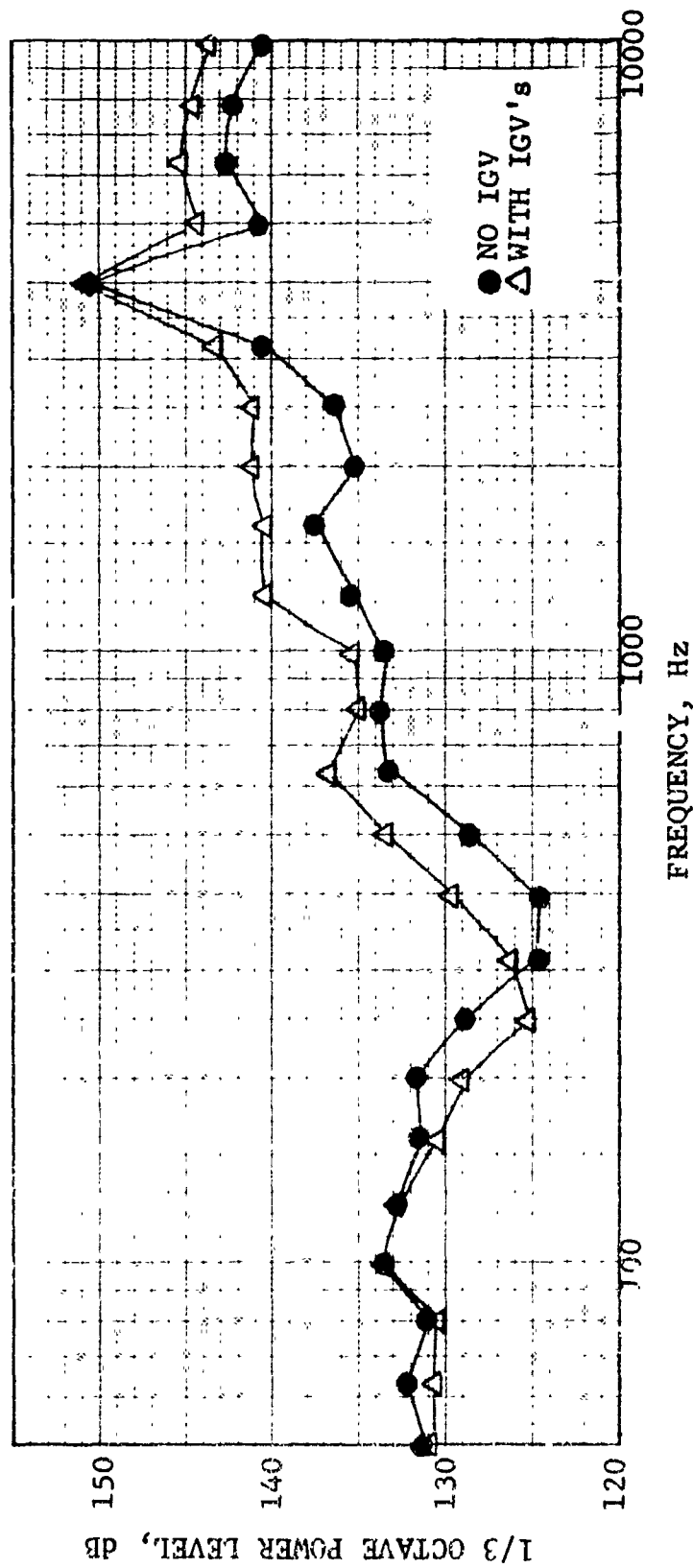


FIGURE V- B5 1/3 OCTAVE POWER LEVEL SPECTRA COMPARISON IGV AND NO IGV VEHICLES-
6150 RPM CORRECTED SPEED

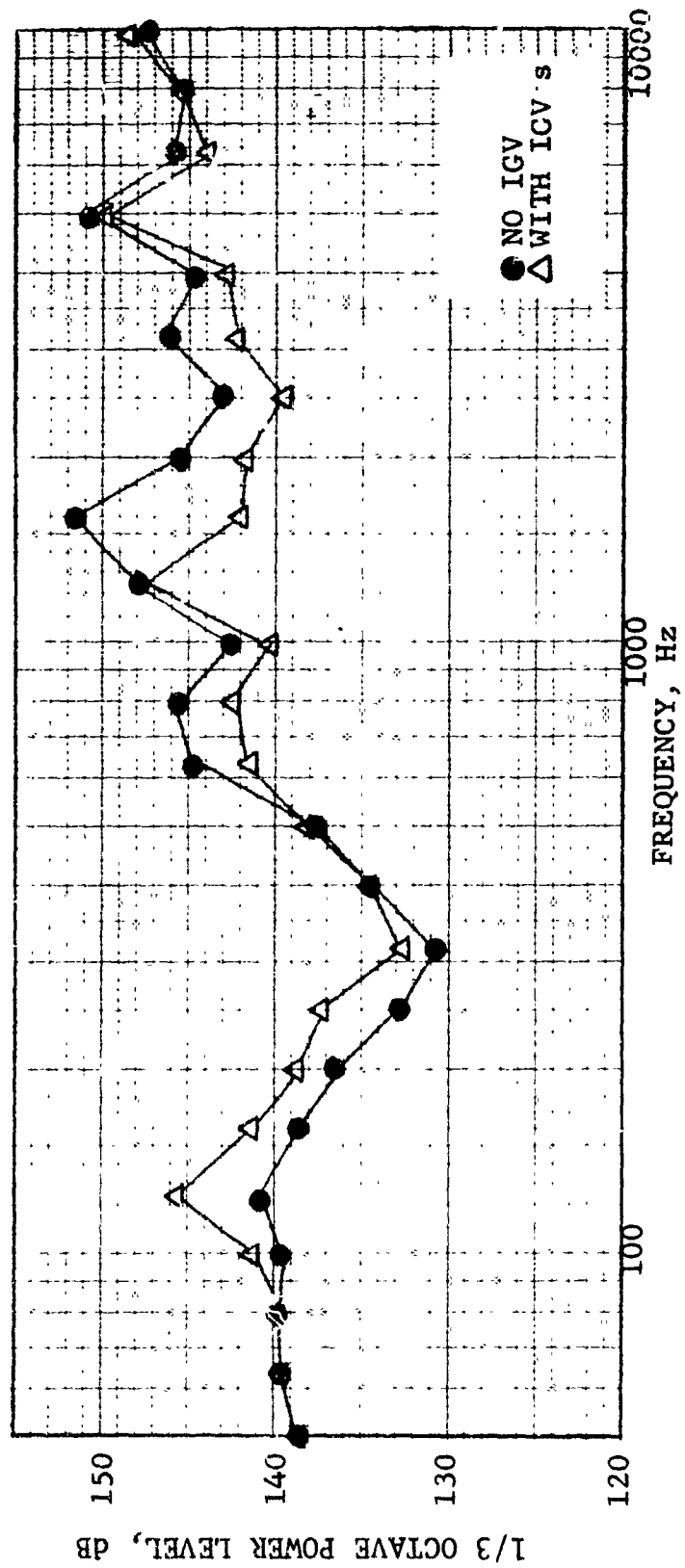


FIGURE V-B6 1/3 OCTAVE POWER LEVEL SPECTRA COMPARISON IGV AND NO IGV VEHICLES-
7600 RPM CORRECTED SPEED

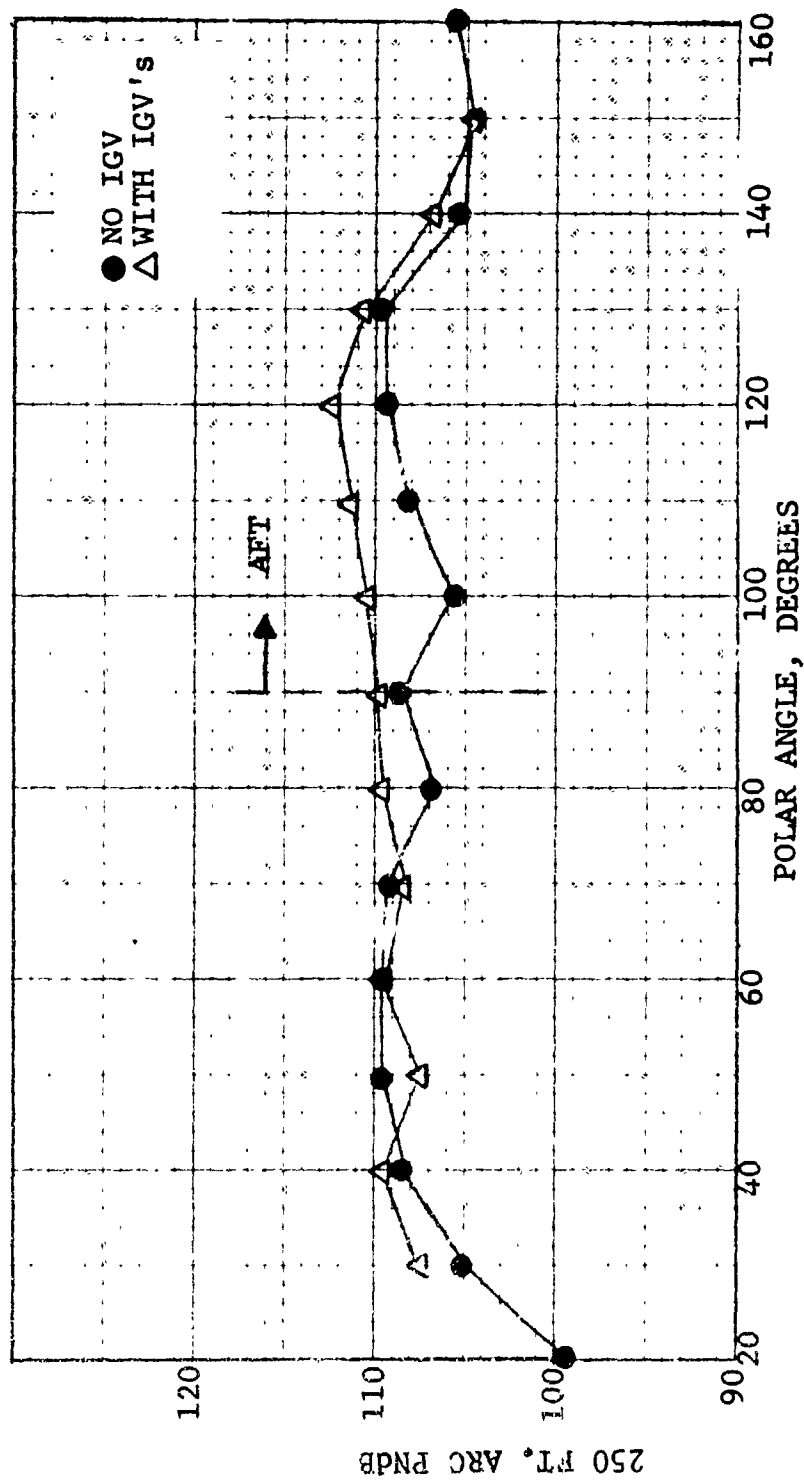


FIGURE V-B7 PNdB DIRECTIVITY COMPARISONS IGV AND NO IGV VEHICLES -
 6150 RPM CORRECTED SPEED

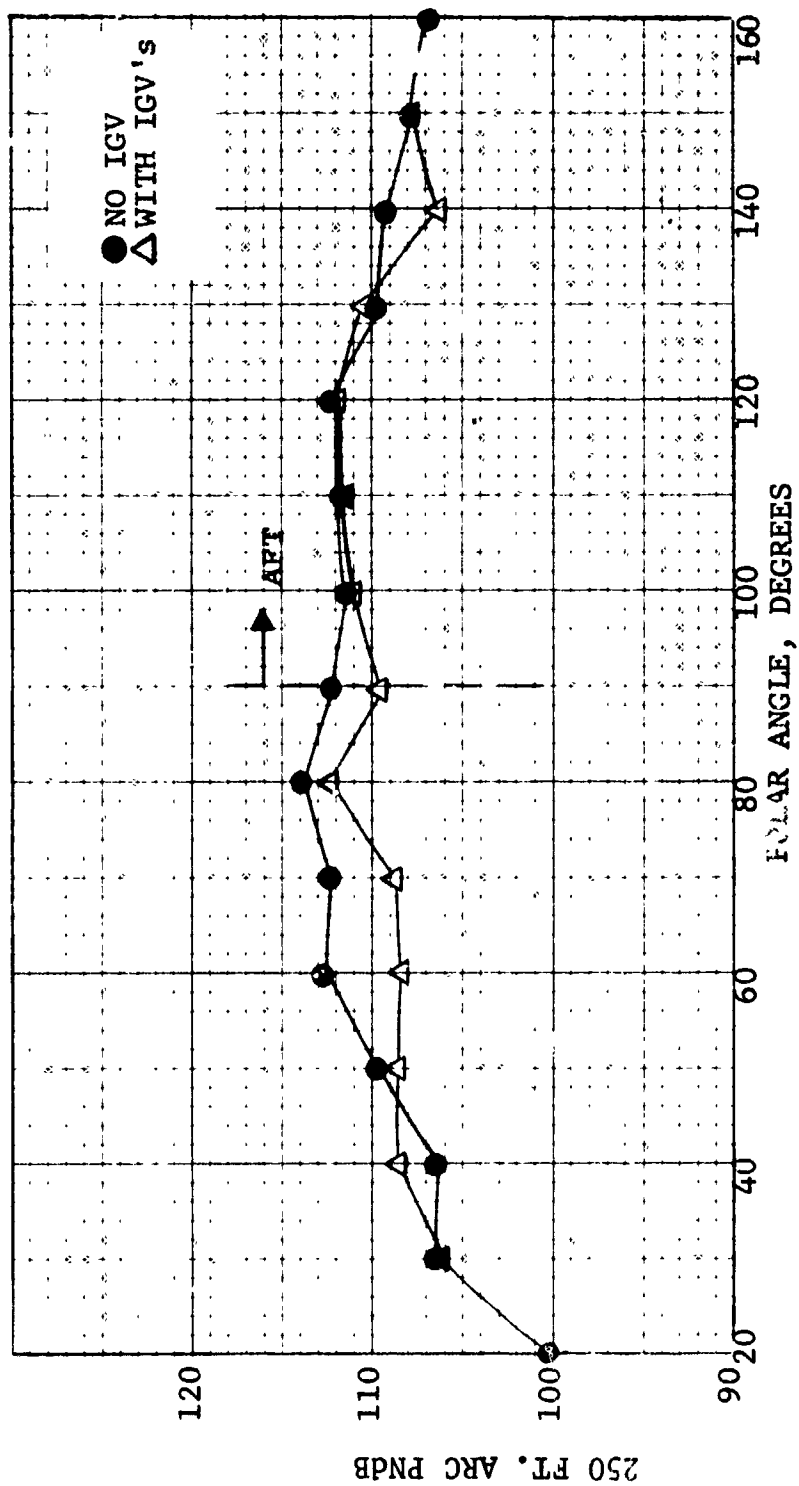


FIGURE V- B8 PNdB DIRECTIVITY COMPARISONS IGV AND NO IGV VEHICLES -
7600 RPM CORRECTED SPEED

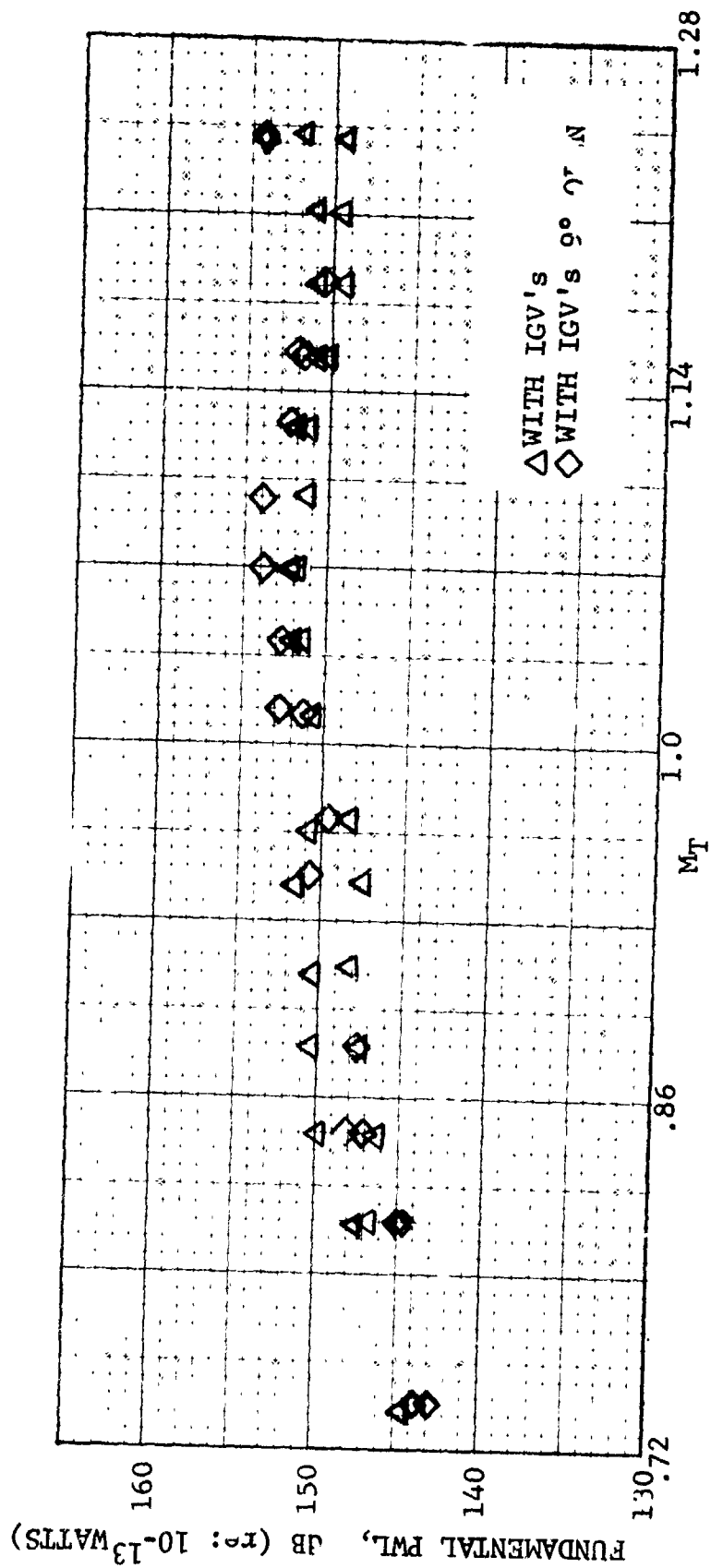


FIGURE V-B9 COMPARISON OF BLADE PASSING FREQUENCY PWL - IGV's NOMINAL AND IGV's 9° OPEN

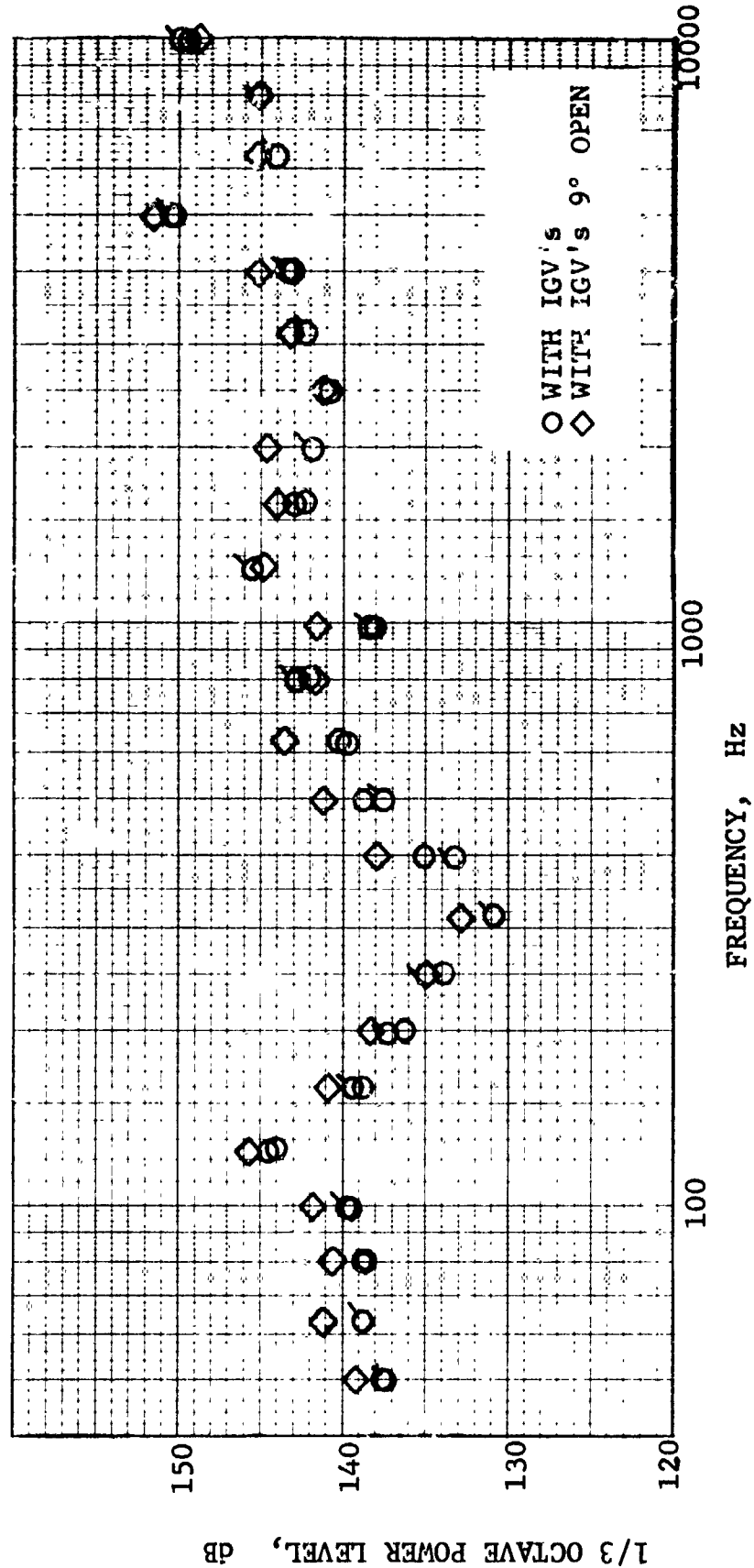


FIGURE V-B10

COMPARISON OF 1/3 OCTAVE POWER LEVEL SPECTRA IGV's NOMINAL AND IGV's 9° OPEN -7900 RPM

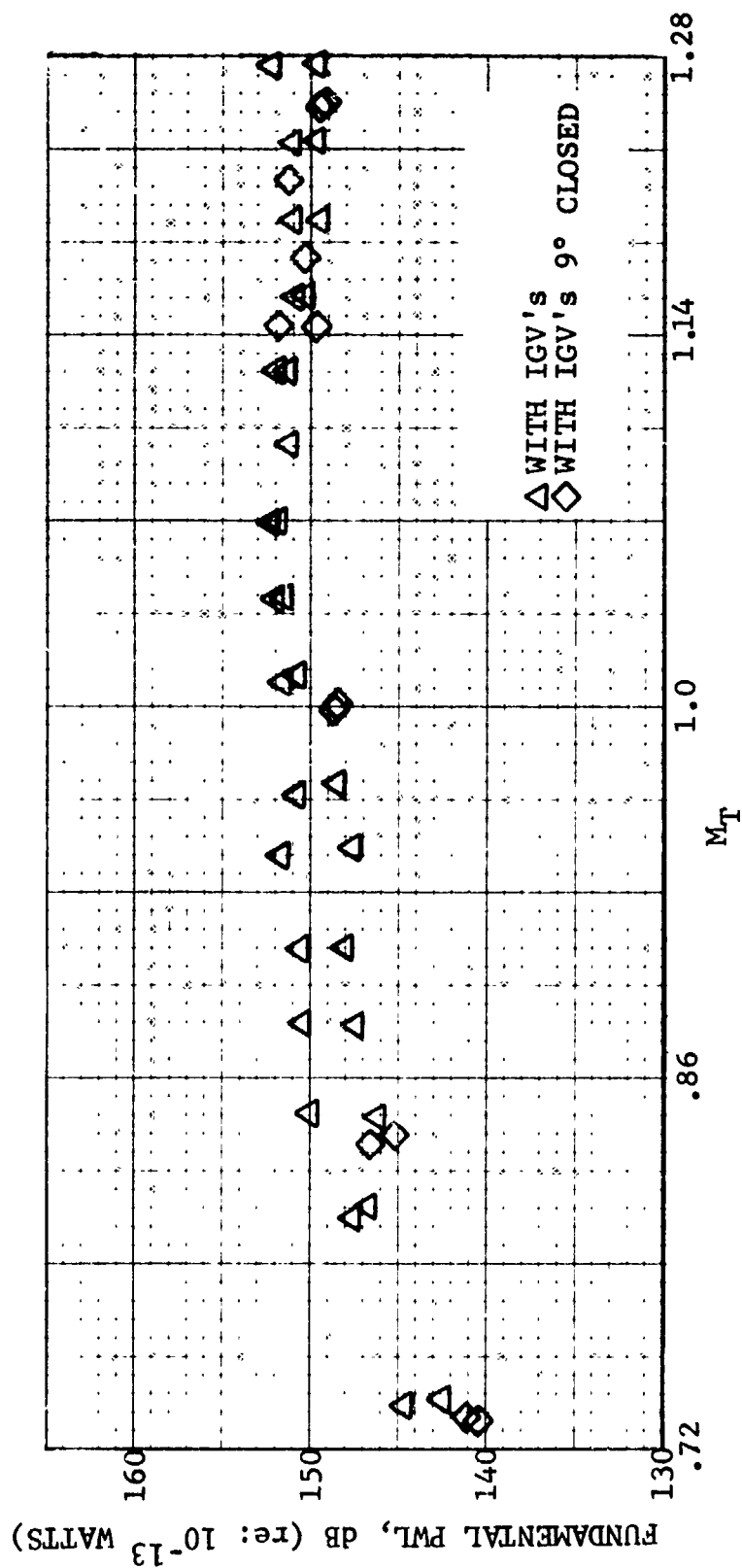


FIGURE V-B11 COMPARISON OF BLADE PASSING FREQUENCY PWL - IGV's NOMINAL AND IGV's 9° CLOSED

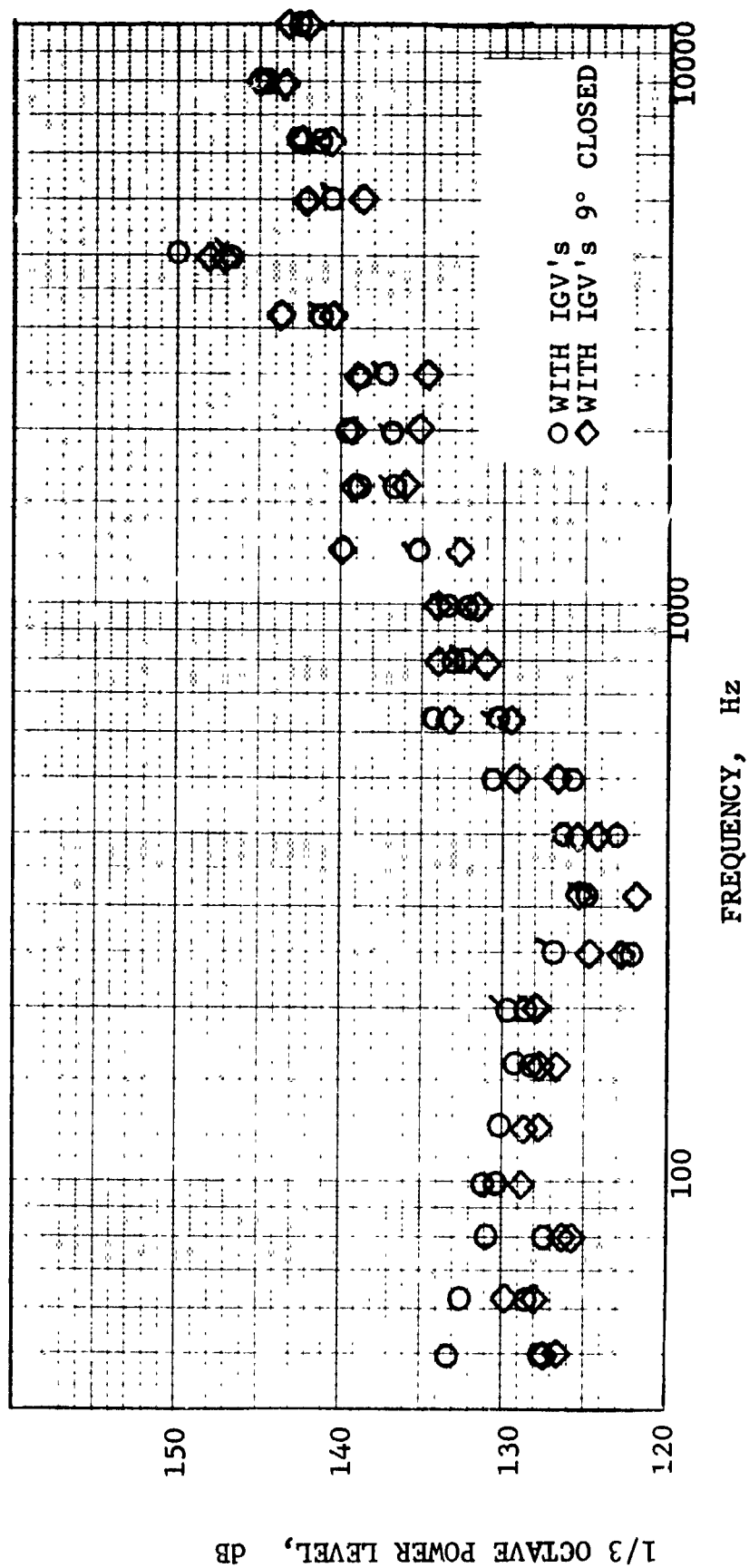


FIGURE V-B12 COMPARISON OF 1/3 OCTAVE POWER LEVEL SPECTRA IGV's NOMINAL AND IGV's 9°CLOSED - 5750RPM

FIGURE V-B13
COMPARISON OF 1/3 OCTAVE POWER LEVEL SPECTRA IGV's NOMINAL AND IGV's
9° CLOSED - 6900 RPM

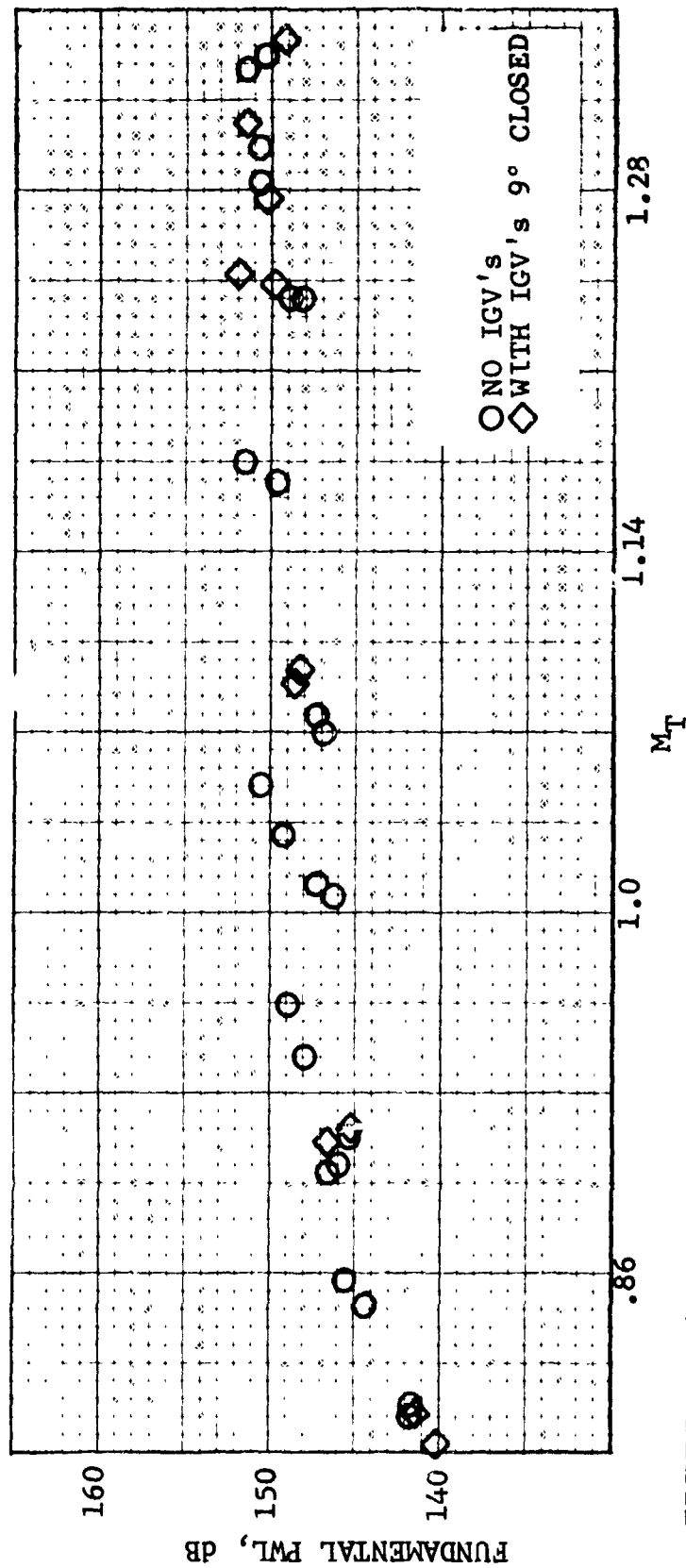


FIGURE V-B14 COMPARISON OF BLADE PASSING FREQUENCY PWL NO IGV's AND IGV's 9° CLOSED

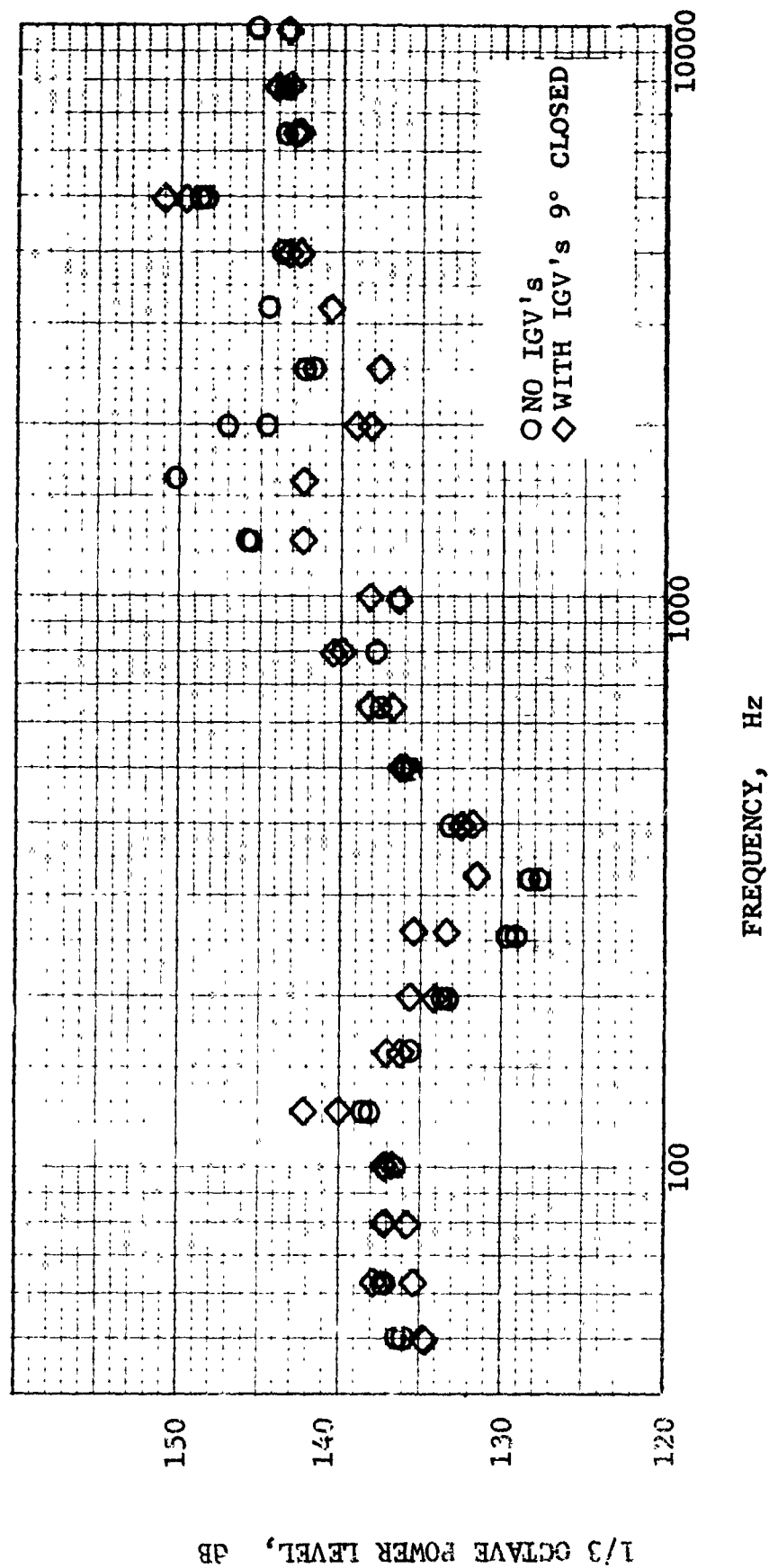


FIGURE V-B15 COMPARISON OF 1/3 OCTAVE POWER LEVEL SPECTRA NO IGV's AND IGV's
9° CLOSED - 7900 RPM